



Max-Planck-Institute für Festkörperforschung

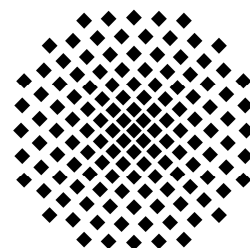
Stuttgart

**New ternary alkaliometallates of the first-row
transition-metal elements through the
Azide Nitrate Route**

Naveed Zafar Ali

Dissertation an der Universität Stuttgart

Stuttgart, 2011



New ternary alkalioxometallates of the first-row transition-metal elements through the Azide Nitrate Route

Von der Fakultät Chemie der Universität Stuttgart
zur Erlangung der Würde eines
Doktors der Naturwissenschaften (Dr. rer. nat.)
genehmigte Abhandlung

Vorgelegt von

Naveed Zafar Ali

aus Islamabad, Pakistan

Hauptberichter:	Prof. Dr. Dr. h. c. mult. Martin Jansen
Mitberichter:	Prof. Dr. Robert E. Dinnebier
Mitprüfer und Prüfungsvorsitzender:	Prof. Dr. Thomas Schleid

Tag der Einreichung der Arbeit: 26.01.2011

Tag der mündlichen Prüfung: 02.03.2011

Max-Planck-Institut für Festkörperforschung, Stuttgart

2011

Dedicated to: My Adorable Family.

Table of contents

Contents

1: Introduction	1
2: Methods and instrumentation	14
2.1 Working Methodology.....	14
2.1.1 Working under inert atmosphere.....	14
2.1.1.1 Vacuum and inert gas glass apparatus.....	14
2.1.1.2 Glove box.....	16
2.1.1.3 Schlenk technique.....	17
2.1.2 Investigation under high pressure.....	18
2.1.3 Azide-Nitrate/Nitrite Route.....	20
2.1.4 Crystal growth.....	22
2.1.5 High – temperature laboratory furnaces.....	23
2.2 Analytical Techniques.....	24
2.2.1 X-ray diffraction methods.....	24
2.2.2 Powder X-ray diffraction.....	24
2.2.3 Precession technique.....	30
2.2.4 Single crystal diffraction.....	31
2.2.5 Raman spectroscopy.....	33
2.2.6 Energy dispersive X-ray spectroscopy (EDX+SEM)	33
2.2.7 Thermal analysis.....	34
2.2.8 Temperature dependence of the specific heat (Cp)	36
2.2.9 Conductivity measurements.....	36
2.2.10 Magnetic measurements.....	37
2.2.11 Mössbauer spectroscopy.....	40
2.2.12 Synchrotron radiation.....	43
2.2.13 Neutron diffraction.....	44
2.2.14 MAPLE calculations.....	46
2.2.15 Bilbao crystallographic server.....	47
2.3 References.....	47

Table of contents

3: Synthesis of (active) starting materials	50
3.1 Synthesis of alkali azides (AN ₃)	50
3.1.1 Lithium, potassium, rubidium and cesium azides.....	50
3.1.2 Drying Assembly.....	54
3.2 Synthesis of (active) transition metal binary oxides.....	55
3.2.1 Iron(III)-oxide, Fe ₂ O ₃	55
3.2.2 Cobalt(II-III)-oxide, Co ₃ O ₄	57
3.2.3 Copper (II)-oxide, CuO.....	58
3.2.4 Chromium (III)-oxide, Cr ₂ O ₃	59
3.3 References.....	60
4: The AFeO₂ (A = K, Rb and Cs) family	
<i>Three-dimensional magnetic iron oxides</i>	61
4.1 Introduction.....	62
4.2 Experimental.....	67
4.2.1 Synthesis.....	67
4.2.2 X-ray single crystal diffraction.....	68
4.2.3 High-resolution synchrotron powder diffraction.....	73
4.2.4 Neutron diffraction experiments.....	73
4.2.5 Thermal analysis and magnetic susceptibility measurement.....	75
4.2.6 Mössbauer Spectroscopy on RbFeO ₂ and CsFeO ₂	75
4.3 Results and discussion.....	76
4.3.1 Single crystal X-ray diffraction.....	76
4.3.2 Thermal analysis and magnetic susceptibility characterization.....	87
4.3.3 High-resolution synchrotron powder diffraction.....	90
4.3.4 Neutron scattering experiments.....	102
4.4 Discussion and Conclusions.....	116
4.5 Mössbauer Spectroscopy on RbFeO ₂ and CsFeO ₂	122
4.6 Parametric Rietveld refinement.....	129
4.7 References.....	132

Table of contents

5: New two-dimensional layered magnetic oxides	136
5-A: Synthesis, crystal structure and magnetic properties of CsCoO ₂ , a new two dimensional layered structure.....	137
5.1 Introduction.....	137
5.2 Experimental Details.....	139
5.3 Results and discussion.....	144
5.3.1 Single crystal X-ray diffraction.....	144
5.3.2 Structural phase transitions in CsCoO ₂	150
5.3.3 The result of a temperature-dependent resistivity.....	154
5.3.4 Thermal analysis and magnetic characterization.....	156
5.4 Conclusion.....	159
5-B: Synthesis, crystal structure and magnetic properties of β-KCrO ₂	161
5.5 Introduction.....	161
5.6 Experimental.....	162
5.7 Results and discussion.....	168
5.7.1 Description of crystal structure.....	168
5.7.2 MAPLE calculations.....	170
5.8 Structural phase transitions.....	171
5.9 A comparison of α-KCrO ₂ to β-KCrO ₂	174
5.10 Magnetic properties.....	175
5.11 The specific heat for KCrO ₂	178
5.12 Conclusion.....	179
5.13 References.....	180
6: One-Dimensional Alkali-oxocuprates	186
6.1. Synthesis, structure and magnetic properties of the new Wigner crystallized chain cuprate Na ₅ Cu ₃ O ₆	187
6.1.1 Introduction.....	187
6.1.2 Experimental details.....	191
6.1.2.1 Material synthesis.....	191

Table of contents

6. 1.2.2 Structure determination.....	193
6.1.2.3 The X-ray investigation on powder samples.....	194
6.1.2.4 The differential scanning calorimetry (DSC).....	194
6.1.2.5 Temperature dependence of the specific heat (C_p).....	195
6.1.2.6 The magnetic susceptibility measurement.....	195
6.1.2.7 Computational methods.....	196
6.1.3 Results and discussion.....	196
6.1.3.1 Crystal Structure and Structure Comparison.....	196
6.1.3.2 Thermal analysis and magnetic characterization.....	199
6.1.4 Theoretical investigation of the magnetic properties.....	202
6.1.5 Conclusion.....	208
6.2. Reinvestigation of physical properties of the Wigner crystallized chain cuprate $\text{Na}_3\text{Cu}_2\text{O}_4$	209
6.2.1 Experimental details.....	209
6.2.1.1 Material synthesis.....	209
6.2.1.2 The X-ray investigation on powder samples.....	211
6.2.1.3 Temperature dependence of the specific heat (C_p).....	211
6.2.1.4 The magnetic susceptibility $\chi(T)$	211
6.2.2 Results and discussion.....	213
6.3 Crystal Structure and Raman Spectroscopic Study of $\text{K}_5[\text{CuO}_2][\text{CO}_3]$	216
6.3.1 Introduction.....	216
6.3.2 Experimental Section.....	217
6.3.2.1 Synthesis.....	217
6.3.2.2 X-ray Analysis.....	218
6.3.2.3 Raman Spectroscopy and Chemical Analysis.....	220
6.3.3 Results and Discussion.....	221
6.4 References.....	224

Table of contents

7: Summary and Outlook.....	230
8: Zusammenfassung.....	241
9: Addendum.....	250
List of tables and figures.....	256
Acknowledgements.....	270
Curriculum Vitae.....	271

Introduction

Multinary oxides, especially the oxides of first row transition metals constitute a remarkably versatile and prolific class of materials of technological importance. The interest which they have aroused in the recent past is evidenced by the zeal and zest of experimentalist and theoretician publishing wealth of experimental and theoretical results and conferences dealing solely with these compounds and their properties [1-5]. The alkaliometallates have continued to play a major role in the fields of high temperature superconductivity (HTSC) [6] and colossal magneto resistivity (CMR) [7], or, more recently, multiferroics, thermoelectricity and spintronics [8]. Yet, despite the wealth of information that has resulted from these investigations, many of their properties are not at all well understood, for example the phenomena of HTSC in cuprates [9] and of CMR in manganates. In the first place, this unpleasant state is due to the high complexity of the problems resulting among others from strong electron correlation, and coupled charge, spin and orbital ordering in collective systems. Furthermore, virtually all oxide materials showing HTSC or CMR include severe structural disorder, even decay into multiphase systems (phase separation, stripe formation [10-12], a fact that has impeded theoretical analyses commonly relying upon translational invariance, and blurred experimental observations by inhomogeneous signal broadening effects. Thus, it would be highly desirable to employ fully periodic and chemically well defined materials as model systems for studying charge spin and orbital ordering, either coupled or independent.

1. Introduction

Solid state chemists relentlessly try to obtain structure-property relations of solids so as to be able to design better materials towards desired properties. Synthesis, structural characterization and alongwith measurement of intrinsic properties of pristine sample has always remained the candid strategy of solid state chemists. The work described in this thesis is based on such an excelsior approach of solid state chemist towards synthesis coupled with understanding and realization of novel materials properties among the family of new ternary metal oxides.

The magnetic properties of these materials depend strongly on the arrangement of magnetic ions in the crystal structure. The existence of long-range ordering depends on the dimensionality (D) of the system, i.e. on whether the interaction takes place in one, two or three directions of space. Changing the dimensionality of a magnetic lattice has a dramatic effect upon the thermodynamic properties. This has been clearly illustrated throughout the study by considering the specific heat and magnetic susceptibility behaviour of the magnetic system particularly at low temperature.

In principle, the two fundamental quantities which characterize a magnetic material are the ordering temperature and the exchange integral. A magnetic interaction between two nearest neighbour ions i and j is described best by the Heisenberg-Dirac Hamiltonian.

$$\mathcal{H} = -2J \sum_{i>j} [aS_i^z S_j^z + b(S_i^x S_j^x + S_i^y S_j^y)]$$

where S_i and S_j are spin operators. The exchange integral \mathbf{J}_{ij} has the dimension of energy and falls off rapidly with the increasing distance between the neighbouring atoms i and j . Summation is taken over nearest neighbouring spins with exchange

1. Introduction

constant (J). If we put $a = b = 1$ we obtain the *Heisenberg model*, in which the interaction is wholly isotropic. The other extreme, the anisotropic *Ising interaction*, is obtained by setting $a = 1$ and $b = 0$. The third case $a = 0, b = 1$, is called the *XY model*, or the *planar Heisenberg model* if one puts the additional requirement that the spins are constrained to lie within the xy plane [13].

Another scale to measure the amount of ordering present in a system below the critical temperature is the Order parameter ($n = \text{spin-dimensionality}$). The ordering parameter are $n = 1$ for an Ising model, $n = 2$ for the xy model, and $n = 3$ for a Heisenberg model.

Whereas the sign of exchange constant (J) is another variable beckoning quantity. When J is positive, the interaction is ferromagnetic (F); when it is negative, the interaction is antiferromagnetic (AF).

Additionally in order to estimate the magnetic ordering temperature precisely, the magnetization data is fitted normally to the empirical equation:

$$M(T) = M_0 * \left[1 - \left(\frac{T}{T_N} \right)^\alpha \right]^\beta$$

where M_0 is the saturated magnetic moment at $T=0$, T_N is the Néel temperature, α and β are the refineable exponential parameters. The important feature here is the estimated “critical exponent” parameters β describing the vanishing of the magnetization at T_c and has value around $\beta = 1/8$ for 2-dimensional system, whereas for 3-dimensional systems, for instance, the observed - β values are all near $1/3$ [13]. The numerous theoretical calculations of critical exponent parameters to characterize 2D or 3D magnetic systems

1. Introduction

have resulted ultimately in the emergence of a so-called “*Universality law*” devised by DeGennes [14].

Obviously a determination of the magnetic structure with neutron diffraction is a most valuable tool. On the other hand, one can go a long way by simply combining specific heat and susceptibility measurements, and if possible by moessbauer spectroscopy. The height of the specific heat maximum C_{\max} , the ratio of the temperatures at which the maxima in C_m and χ occur and the quantity $(1/g)^2 \chi_{\max} T (\chi_{\max})$ together provide a handy set of criteria for the determination of the model appropriate to the investigated compound [13].

The study of low-dimensional magnetic systems has been quite pleasing and rewarding for theoretical physicists, since they provided the means of obtaining exact solutions of cooperative phenomena involved. Some well known many body problems that have defied solution in three dimensions can be solved exactly in one or two dimensions. The alkalioxocuprates have continued to play a major role in the fields of high temperature superconductivity (HTSC). Yet, despite the wealth of information that has resulted from these investigations, many of their properties are not at all well understood, for example the phenomena of HTSC in cuprates. In good and successful collaboration with the theoretician, we exercised the freedom to study new one dimensional Wigner crystallized chain cuprate and reported our findings

Transition metal oxides with two dimensional layered structures became the subject of interest for scientific community after the discovery of superconductivity ($T_c = 5K$) in $Na_xCoO_2 \cdot yH_2O$ [15]. In addition to high-temperature superconductivity, they also

1. Introduction

exhibit a multitude of exotic phenomenon like, thermoelectricity, multiferroic behaviour, metalinsulator transition, colossal magnetoresistance (CMR) effect, cathode materials in solid oxide fuel cells, spin (up/down) and charge degrees of freedom, which shifts the attention of the scientific community entangled to find reason of superconductivity in cuprates related compound.

However a layered transition-metal oxide NaCo_2O_4 first identified by Jansen and Hoppe [16], became the focus of interest after 23 years of its discovery when I-Terasaki *et. al.* in 1997 reported high thermoelectric (TE) performances in NaCo_2O_4 and reported it as a potential thermoelectric material [17]. Layered structures are considered superior to other structures according to the concept of a phonon glass and an electron crystal [18]. Optimizing electronic structure by adjusting crystal structure is a way to improving TE performances, which provides theoretical sustainment for the choice of material.

Now, researchers begin to study the effects of various cations substitutions on TE performances [19-20]. Ag substitution among Na-site substitutions shows a remarkable enhancement of the power factor [21]. Cations substitutions mainly change the carrier concentration, and then affect the electrical conductivity and Seebeck coefficient. Furthermore, a key facet of cobalt oxides that distinguish them clearly from its counterpart is the spin state degree of freedom of the Co^{3+} —ions: it can be low spin (LS, $S=0$), high spin (HS, $S=2$) and even intermediate spin (IS, $S=1$) [22]. For the archetypal LaCoO_3 compound, for instance, various early studies accredited the low temperature spin state change to be of LS-HS nature, while studies in the last decade put a lot of effort to propose a LS-IS scenario instead. Various spectroscopic studies unearthed spectacular results in recent past about the spin state of Co^{3+} ions in different local coordination [22].

1. Introduction

However, in contrast to octahedral coordination of transition metal, a less common coordination geometry observed is the tetrahedron where the weaker crystal field splitting of energy levels [$10Dq$ (Td) = $4/9 * 10Dq$ (Oh)] favours the high spin complexes. In the present investigation the crystal and magnetic structure of recently identified new two dimensional layered cobaltate, $CsCoO_2$ will be discussed with Co^{3+} in a unique tetrahedral coordination.

Geometrically frustrated systems are being widely studied due to the possibility of unconventional ground states and their susceptibility to weak perturbations. The two dimensional triangular lattice Heisenberg antiferromagnet (TLHAF) is a prominent example where exotic magnetic phenomena have been observed [23]. In this context $ACrO_2$ [A=Li, Na and K] are the extensively studied family of compounds that crystallize in the α - $NaFeO_2$ layer structure (space group R-3m). In these 2-D oxochromates, the increase in the interlayer Cr-Cr distances with increasing the size of alkali cation (A^+), compare to intralayer distances results in significant reduction of the ordering temperature [24]. Various theoretical model and formula were proposed to construct a model for the spin interactions in 2-D Heisenberg antiferromagnet and to estimate the intralayer exchange integral J using the series expansion coefficients computed by Rushbrooke and Wood and similarly mostly used Stanley and Kaplan formula to derive the Curie temperature of a 2-D Heisenberg ferromagnet with good accuracy. In the $ACrO_2$ family, the magnetic structure is built by stacking well-separated, triangular planes of Cr^{3+} with spin $S = 3/2$ in an ABCABC sequence. In this study, we present results on yet another high temperature polymorph of the $ACrO_2$ family (A = Li, Na, K), namely β - $KCrO_2$, built by stacking well-separated, triangular planes of Cr^{3+} ($S = 3/2$)

1. Introduction

with oxygen ion stacking sequence of ABBAAB with unusual trigonal prismatic coordination of K^+ cation, in contrast to ABCABC sequence observed in its alpha analogues.

In retrospect, different phenomenological parameters were proposed in order to systematize the statistics on the high Néel temperatures observed in various magnetic oxides, and even to predict them. For example, in [25], the T_N in $RFeO_3$ (R= rare earth) was found to be proportional to the average cosine of the Fe-O-Fe angles, ranging from ~630 to ~740 K for the $\cos(\text{Fe—O—Fe})$ changing from ~0.78 to ~0.92. Likewise, In [26], a value of T_c / n , where T_c is an antiferromagnetic transition temperature, and n is the effective coordination number of Fe in different simple and mixed iron oxides was found to be on average equal to 115K (ranging from 106 K to 132 K). Apart from the mentioned above empirical quantities, also other possibilities have been explored. For example in [27], for the case of the $RMnO_3$ manganites (R= rare earth), a puzzling $T_N \sim \langle \cos^2 \phi \rangle$ proportionality has been established, reporting the variation of the Néel temperature T_N with decreasing bending of the $(180^\circ - \phi)$ Mn-O-Mn bond angles. In our present neutron scattering experiments on iron based magnetic sub-system ($AFeO_2$) wherein we observed unexpectedly strong superexchange interactions between the Fe ions leading to the exceptionally high values of Neel temperatures ($T_N=1055K$ in $CsFeO_2$). We discussed the various possibilities of origin of such a high Neel temperature in the family of $AFeO_2$ compounds and tested various theoretical models.

The "azide/nitrate route" has proven to be an efficient approach in present work for the solid state synthesis of new magnetic oxides covering the whole dimensionality,

1. Introduction

starting from 3-dimensional oxoferrates, two dimensional oxochromate and oxocobaltate respectively, and also new intrinsically doped one dimensional cuprates. As a particular strength of this procedure, the oxygen content, and thus the valence state of the transition metal, can be precisely fixed by the alkali azide/nitrate ratio weighed in. The basis of the reaction is the Zintl and Baumbach's concept [28] of mixing of sodium azide with sodium nitrate or nitrite, however their proposal is not frequently exercised for the synthesis of Na_2O because of explosion danger. Nonetheless, with the incorporation of respective transition metal binary oxide, in situ production of the alkali metal oxide that react with the corresponding transition metal oxide (diluting the azide/nitrate mixture) to give the desired product in pure amount [29]. The main advantage of this route is the simplification of the preparative work and wide variety of systems that can be handled. In addition to the acid-base reactions, it is possible to perform redox reactions with simultaneous reduction or oxidation of the counter cation, so just like “to kill two birds with one stone”.

Later in order to construct a model for the spin interactions in these alkali oxometallates, the intrinsic magnetic properties have been measured and the resulting magnetic properties were later justifiably analysed by employing various theoretical models.

The dissertation is structured as follows: *Chapter 1* is introductory giving historical perspective on the overall properties of alkalioxometallates, more focused on the aspects that have been central to current experimental work. *Chapter 2* refers to the instrumentation and methodology employed throughout the study. Whereas *Chapter 3*

1. Introduction

shed light on the importance of active material (high surface area) and their in house synthesis procedures, which play a pivotal role in solid state chemistry.

Chapter 4 deals with the comparative study of crystal structures, structural phase transitions, twinning, lattice dynamics and spin Ordering Phenomena in the $A\text{FeO}_2$ (A: K, Rb and Cs) Family. Which are among the simplest stuffed variants of the cristobalite type of structure, whereby the alkali metals enforce a specific tilting pattern of the tetrahedral framework structure. We've studied in great detail by state of the art techniques including single crystal diffractometry, high resolution synchrotron X-ray powder diffraction coupled with neutron scattering experiments that this fully ordered orthorhombic structure is undergoing a structural phase transition to a cubic modification with a dynamically disordered $\text{MO}_{4/2}$ -framework. The mechanism of phase transition into cubic phase is explained in detail by synchrotron data (time and space averaged structure) with the strongly anisotropic character of the atomic thermal vibrations of the oxygen atoms, and in the split atom model based on neutron investigation. The magnetic ordering phenomenon has also been investigated in detail by neutron powder diffraction technique reporting the highest ever reported Neel temperature of 1055 K in case CsFeO_2 , in Fe oxides. The origin of the high Neel temperatures in KFeO_2 and RbFeO_2 and CsFeO_2 has been addressed by employing different phenomenological theoretical parameters and empirical quantities.

Chapter 5 introduces two new two dimensional magnetic oxides with layered structure with special focus in terms of their strong magnetic interactions, and the respective structural phase transitions at higher temperature. Single crystal X-ray

1. Introduction

analysis of the CsCoO_2 reveals a first and unique structure of its kind in the field of ternary oxide chemistry which consists of pairs of CoO_4 tetrahedra edge-linked to form bow-tie-shaped Co_2O_6 dimer (butterfly-motif) which share vertexes to form layered structure. In order to construct a model for the spin interactions in CsCoO_2 , the magnetic properties of CsCoO_2 have been measured and further endorsed by specific heat measurements. Also the structural phase transition to a new cubic modification (Fd-3m) at $T \sim 500\text{K}$ has been observed and reported. *In the second part of Chapter 5*, a new two dimensional oxochromate, $\beta\text{-KCrO}_2$, is reported for the very first time. Single crystal X-ray analysis reveals the unique trigonal-prismatic arrangement of K^+ ions entrenched between the layers of edge-shared CrO_6 octahedra perpendicular to [001]. In the last part of the chapter the thermodynamics of phase transitions systematically investigated by high resolution X-ray powder diffraction and DSC techniques is presented, showing transitions to occur at $\sim 629\text{ K}$ from low temperature $\alpha\text{-KCrO}_2$ (R-3m) to high temperature $\beta\text{-KCrO}_2$ (P-31c). Magnetic measurements were performed and the Néel temperature (T_N) of 26K is confirmed here for the very first time by Magnetic susceptibility and further endorsed by specific heat measurement.

Chapter 6 introduces the enduringly interesting subject in the field of low-dimensional magnetic oxides, i.e charge ordering, Wigner crystallization. The solid state chemistry of low dimensional materials has both experimental and theoretical interest particularly in connection with their physical properties. In here, we report $\text{Na}_5\text{Cu}_3\text{O}_6$, the first charge ordered compound where the importance of virtual excitations across the Wigner gap has been convincingly demonstrated. The crystal structure description as well as the results for the magnetic susceptibility and specific heat are discussed. $\text{Na}_5\text{Cu}_3\text{O}_6$,

1. Introduction

represents a new member of the family of mixed valent chain cuprates with a hole filling factor of $1/3$. From the effective one-dimensional spin $1/2$ Heisenberg model used to analyze the magnetic properties of $\text{Na}_3\text{Cu}_2\text{O}_4$ and $\text{Na}_8\text{Cu}_5\text{O}_{10}$ the magnetic structure of $\text{Na}_5\text{Cu}_3\text{O}_6$ is expected to be particularly simple: the spin-bearing divalent copper ions on next-nearest lattice sites within the chain should form dimers which are only weakly coupled among each other. *Surprisingly*, this is not the case. We discuss the reasons for the unexpected magnetic properties and present a quantitative theoretical analysis of the susceptibility data. Also we developed the theoretical model to describe the magnetism and discuss the differences to the previously synthesized chain cuprates showing Wigner crystallization, with special note on importance of virtual excitations across the Wigner gap. In the second part of chapter 6, we presented a new potassium copper oxycarbonates $\text{K}_5[\text{CuO}_2][\text{CO}_3]$ prepared along the azide nitrate route. In retrospect, such an option of including carbonate anions in perovskite related multinary oxides is widely exercised and has proven to be a versatile measure, not only to modify the stacking modes encountered [30], but also to improve the performance of cuprate based superconductors [31]. *The last section* is devoted to outline of results with eventual conclusions.

References:

- [1] M. Jansen, J.C. Schön: „Design“ in der chemischen Synthese – eine Fiktion, *Angewandte Chemie*, **118**, 3484-3490 (2006).
- [2] M. Jansen: Anorganische Festkörperchemie im Konzert der Materialforschung *Nachr. Chem. Techn. Lab.* **55** 622-6 (2007).

1. Introduction

- [3] J. B. Goodenough, *Magnetism and the Chemical Bond* (John Wiley & Sons, New York, (1963).
- [4] C. N. R. Rao, Transition metal oxides, *Annu. Rev. Phys. Chem.* **40**, 291-326 (1989).
- [5] A. K. Cheetham and Peter Day, *Solid State Chemistry: Techniques*, Oxford Science Publication (1987).
- [6] T. Mayer, M. Eremin, I. Eremin, and P. F. Meier, *J. Phys.: Condens. Matter* **19**, 116209 (2007).
- [7] C. N. R. Rao, R. Mahesh, A. K. Raychaudhuri, and R. Mahendiran, *J. Phys. Chem. Solids* **59** (4), 487, (1998).
- [8] C. Felser, G. H. Fecher, and B. Balke, *Angew. Chem. Int. Edn.* **46**, 668, (2007).
- [9] H. Takagi, *Nature Materials* **6**, 179, (2007).
- [10] V.V. Moshchalkov, L. Trappeniens, and J. Vanacken, *Physica C: Superconductivity* **887**, 341-348, (Part 2), (2000).
- [11] J. M. Tranquada, B. J. Stemlieb, J. D. Axe, Y. Nakamura, and S. Uchida, *Nature (London)* **375**, 561 (1995).
- [12] N. Kumar, and C. N. R. Rao, *ChemPhysChem.*, **4** (5), 439, (2003).
- [13] L. J. de Jongh and A. R. Miedema, *Advances in Physics*, **50** (8), 947—1170 (2001).
- [14] P. G. De Gennes, *La Recherche* **51**, 1022 (1974).
- [15] K. Takada, H. Sakurai, E. Takayama-Muromachi, F. Izumi, R. A. Dilanian, and T. Sasaki, *Nature* **422**, 53 (2003).
- [16] M. Jansen and R. Hoppe, *Z. Anorg. Allg. Chem.* **408**, 104, (1974).

1. Introduction

- [17] I. Terasaki, Y. Sasago: Phys. Rev. B. **56**, 12685, (1997).
- [18] K. Takahata, Y. Iguchi, D. Tanaka: Phys. Rev. B **61**, 12551 (2000).
- [19] T. Kawata, Y. Iguchi, T. Itoh: Phys. Rev. B. **60**, 10584, (1999).
- [20] R. Kitawaki, I. Terasaki: J. Phy: Condens. Matter. **14**, 12495, (2002).
- [21] H. Yakabe, K. Fujita, K. Nakamura: 17th Inter. Conf. Thermoelectrics, 551, (1998)
- [22] http://www.nsrrc.org.tw/NsrrcWebSystem/UPLOADS%5CCHINESE%5CPUBLISH_YEARLY%5C2003~2004/03.pdf
- [23] A. Olariu, P. Mendels, F. Bert, L. K. Alexander, A. V. Mahajan, A. D. Hillier and A. Amato, Physical Review B **79**, 224401, (2009).
- [24] C. Delmas, F. Menil, G. Le Flem, C. Fouassier and P. Hagemuller, J. Phys. Chem Solids, **39**, 55, (1978).
- [25] D. Treves, M. Eibschütz and P. Coppens, Phys. Lett. **18**, 216-217 (1965).
- [26] M. A. Gilleo, Phys. Rev. **109**, 777-781 (1958).
- [27] J.-S. Zhou and J. B. Goodenough, Phys Rev. B **68**, 054403 (2003).
- [28] E. Zintl u H. H. Baumbach, Z. Anorg. Chem., **198**, 98, (1931).
- [29] D. Trinscheck, M.Jansen, Angew. Chem. **111**, 234-235 (1999); Angew. Chem.. Int. Ed. Engl. **38**, 133-135 (1999).
- [30] K.S. Aleksandrov and V. V. Beznosikov, Phys. Solid State, **39**, 785-808, (1997).
- [31] K. Kinoshita and T. Yamada, Nature, **357**, 313-315, (1992).

Chapter-2

Methods and instrumentation

2.1 Working methodology

2.1.1 Working under inert atmosphere

2.1.1.1 Vacuum and inert gas glass apparatus

Inert conditions are a prerequisite for the preparation of most of alkaliometalates because of the sensitivity of not only starting active (high surface area) precursors but also the end products towards moisture and air. Normally, argon is used as an inert gas media under which these moisture and air sensitive samples are handled. The apparatus (vacuum line) as shown in **Figure 2.1** is made from borosilicate duran glass and is attached to a rotary valve oil pump (Type: RD4, Vacuubrand GmbH). The quality of vacuum is controlled by a Pirani manometer (Thermovac TM 20, Company: Leybold) within a range of 10^{-3} - 10^3 mbar. The vacuum assembly is filled with dried argon gas. Before use, the Argon gas from source is passed through four successive drying towers of blue gel, potassium hydroxide, molecular sieve (mesh size 3 Å) and phosphorous pentaoxide(P_4O_{10}) on an inert substrate (Sicapent with $CaCl_2$ as an indicator, Merck), respectively. This arrangement is used to remove the humidity and traces of O_2 and N_2 from the gas. And later after passing through the whole setup finally the gas is passed through the “titanium oven” operated at 1023 K into the vacuum line assembly for further usage. Equipments/tubes connected by glass spirals or angled glasses (L-shaped angled glasses connectors) can be evacuated and filled with dried argon by opening the concerned valve. The joints are sealed with silicon grease (Wacker Chemie AG). Before

2. Experimental

use, the necessary glassware is heated under vacuum 3-5 times and is simultaneously rinsed with dried argon. The process of evacuating, heating, and refilling with argon is repeated a couple of times to ensure that the apparatus is completely inert and free from moisture. The flow rate can be controlled as per the requirement. To find leakage in the glass tubes and throughout the whole vacuum assembly, a high frequency vacuum examiner (VP 201, Company G. Lauer) is used. The whole assembly is firstly evacuated and then filled with helium gas throughout the assembly.

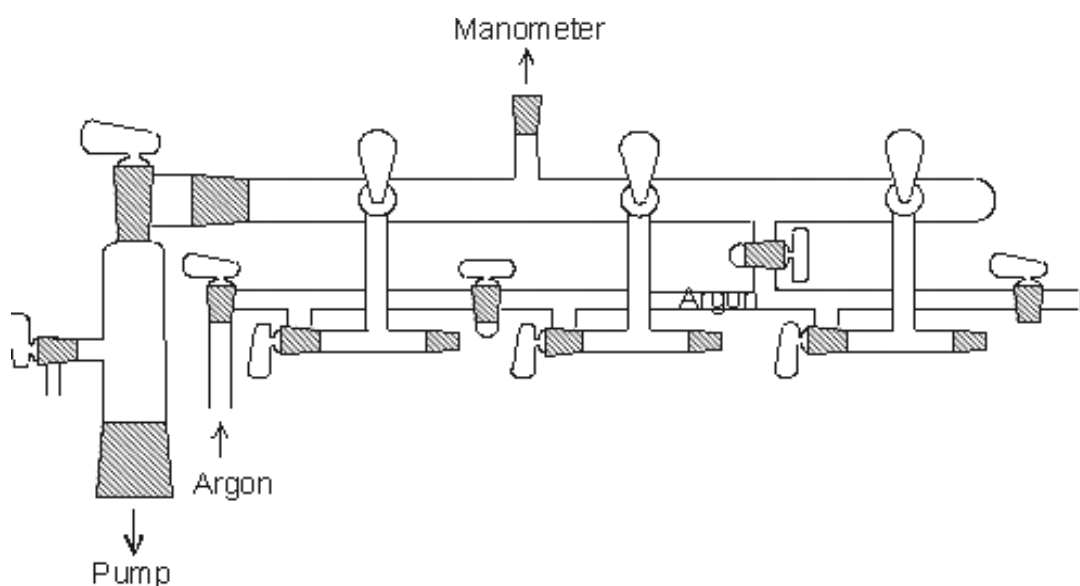


Figure 2.1: Schematic representation of vacuum assembly

Later apparatus with special nozzle (sensitive Helium sensors) are used to detect the leakage in the assembly line. This whole procedure is inevitable, if the “titanium oven” is intended to be used at 1023 K.

2. Experimental

Hazards: The presence of moisture or oxygen may cause a severe exothermic reaction (oxidation of titanium blocks into titanium oxides) which may burn the whole set up if handled not professionally!!

2.1.1.2 Glove box

In the whole duration of work starting from day one, different kinds of glove boxes were used extensively. The glove box apparatus is normally used for picking single crystals, preparing pellets for various reactions and also for preparing the reaction mixtures when the active reactants (with high surface area) are sensitive to moisture and/or oxygen. Pellets of such reaction mixture can also be grinded, mixed in mortar pestle and later pressed inside the glove box. These things are not possible with the inert gas setup shown in **figure 2.1**, while they can be mastered effortlessly in the glove box compartment (MT 200 - M. Braun). The cleaning of the inert gas (Argon) is done by passing it over the molecular sieve. The quality of the inert gas (Ar-5.0, 99.9995%) and moisture contents can be automatically controlled by special sensors. The water content inside the glove box compartment is maintained below 0.1ppm and the oxygen content below 0.1 ppm. Apparatus (e.g. evacuated Schlenks / tubes etc) or samples can be taken inside or outside the glove box compartment through airtight evacuation chambers (big and small). The chambers are filled with argon and evacuated simultaneously three times (big chamber automatically for 20 minutes and small chamber manually five times for 10 minutes) to ensure the inert atmosphere inside the respective chamber and the whole glove box. For certain samples even the long duration open storage in glove box is not advisable due to high sensitivity of sample to moisture. The glove box is a perfect tool for working and

2. Experimental

handling the moisture and air sensitive samples, it should not be recommended as storage medium for ternary alkaliometallates investigated in the present study. For long term storage the sealed ampoule under dried argon using Schlenk technique is, however, recommended.

2.1.1.3 Schlenk technique

Although latest glove boxes are good enough for short term handling of the compounds but for long term storage purposes, the Schlenk technique is mostly used and is ideal for handling such substances. The schematic representation of the Schlenk apparatus is shown in **figure 2.2**.

This technique was developed by Schlenk [1], especially for handling air sensitive substances. This equipment also allows for homogenization of the substances by pulverizing it into powder with the use of a dried glass rod. The apparatus also helps in filling the substances into glass or quartz capillaries of various diameters (under flow of argon), which are further used for X-ray analysis. The remaining substance is sealed in small glass ampoules under the flow of dried argon for further magnetic and other physical measurements. The Oxroehr (oxygen tube) as displayed in **fig. 2.2 (right panel)** below are used for drying the substances overnight under vacuum.

2. Experimental

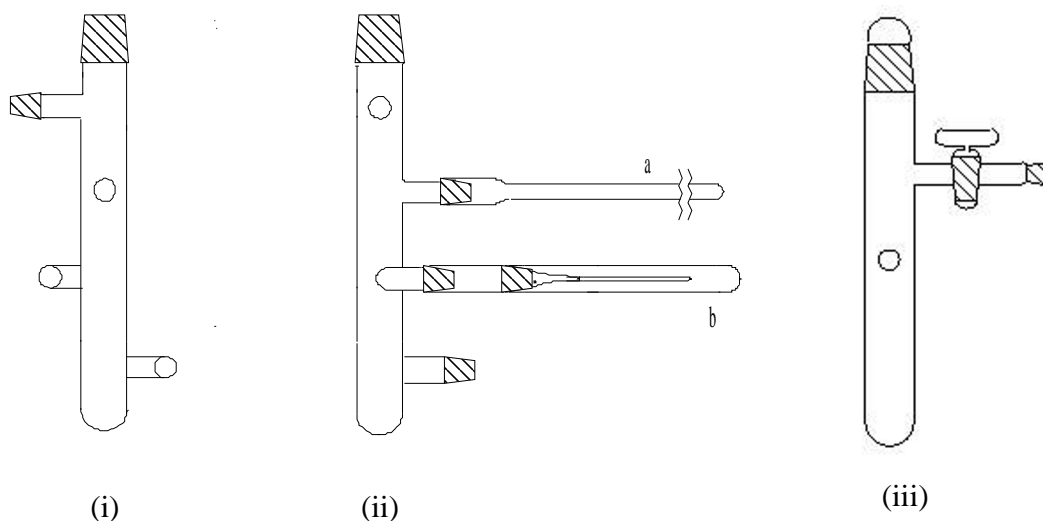


Figure 2.2: **i and ii**) Schlenk tubes (upper cross section: LV of 29, remaining cross section LV 14.5:
a) = ampoules sealing unit and b) = capillary filling unit. **iii**) A common drying tube (ox-Rohr).

2.1.2 Investigation under high pressure

For applying hydrostatic pressures during synthesis and for inducing phase transitions, a belt press and a multi anvil press were utilized [2]. The basic principle involved is the generation of force by a hydraulic ram, that is further transmitted via suitable anvils to a miniaturized sample volume in order to generate large pressures (*c.f.* $P = F/A$). A belt press (PUS 300A, Diefenbacher GmbH) is capable of attaining sample pressures up to 8 GPa and temperatures of 1200 °C. The sample is located in a sealed pot (volume=45-50 mm³), which can be made of different materials (BN, Au, Pt, Pd, Al₂O₃). The central part comprises of a two conical dies of tungsten carbide wherein the pressure cell is built up. This is surrounded by two conical steel support rings and a hollow outer ring that allows for cooling water circulation.

The press is powered using a fluid medium (hydraulic oil pump) and sample compression is achieved by a pair of opposed conical tungsten carbide anvils. The hydraulic pump

2. *Experimental*

forces the assembled module upwards onto the upper anvil. The uniaxial load generated is transmitted to the sample via the pyrophyllite assembly that surrounds it. Pyrophyllite is a layered silicate that begins to flow under pressure and in this manner allows for the exertion of a quasi-hydrostatic pressure (tangential forces) on the sample. An electrically heated thin graphite tube serves as the furnace around the sample capsule attached to a Ni-Cr/Ni thermocouple. Whereas in case where higher pressure is solicited, a '6/8 type' multi-anvil press (1000-Tonne, Voggenreiter & Söhne GmbH) equipped with a steel Walker module was employed. The material was preground and compacted into gold capsules (diameter: 4 mm). The sample capsules were loaded into MgO/Cr₂O₃ octahedron. Sample pressure was determined on the basis of predetermined pressure/load calibration curves and sample heating accomplished via a LaCrO₃ resistance heater and temperature monitored/controlled by an in-situ thermocouple. Experimental conditions employed were typically $p=16$ GPa, $T= 1173$ K, and $t=0.5$ h. Experiments were terminated by rapidly quenching the sample to ambient temperature and slow pressure release 15 h. Moreover, since at higher the pressure, the 'damping' effect due to the elastic response of the anvil material to the applied load is pronounced, thereby require the use of calibration curves (applied load vs sample pressure) is inevitable.

2. Experimental

2.1.3 Azide-nitrate / nitrite route

Azide-Nitrate route is a very prospective route to synthesize ternary oxides of alkali metals. In all the cases, the experimental procedure remains the same. The weighed reactants: respective alkali metal azide, nitrate, nitrite are blended carefully with the corresponding oxides of the transition metals. Then they were finely ground in a ball-mill, pressed in the form of pellet (6-13 mm diameter) under 10^5 N, dried under vacuum (10^{-3} mbar) at 423 K overnight, and placed under argon in a tightly closed steel container provided with a silver / copper inlay. This reaction crucible is shown in **fig. 2.3**.

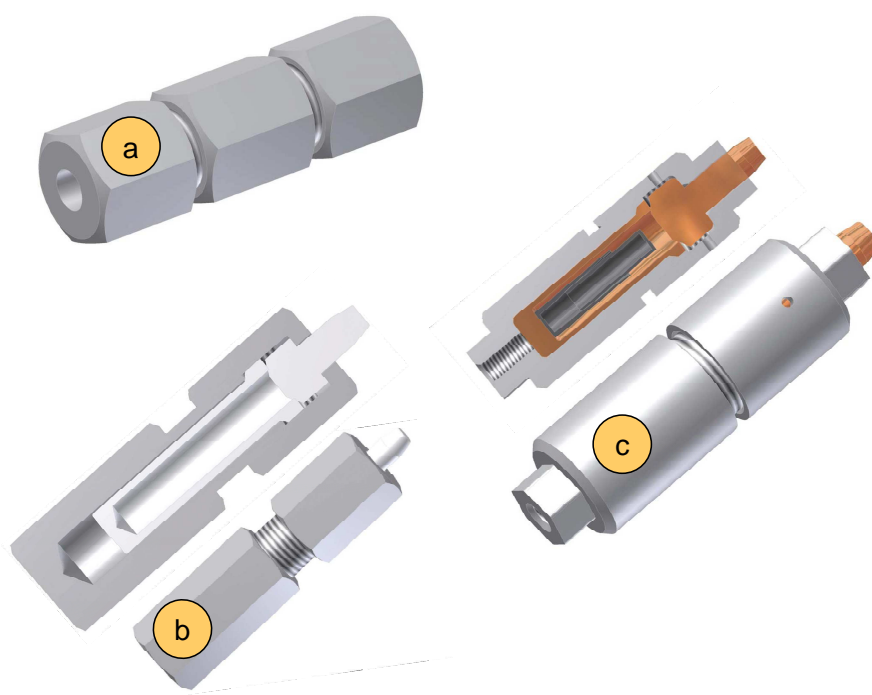
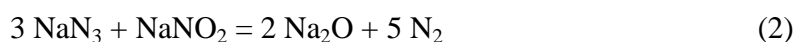
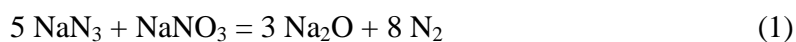


Figure 2.3: Reaction crucibles specially designed for the azide nitrate route (hexagonal, steel 9S29-K) with Ag, Cu inlays. (a) Double hole Crucible, (b) Single hole crucible (c) Single hole with double lining.

2. Experimental

Special temperature regime was applied for the reactants that are kept in the crucibles. Rapid heating of the mixture may cause some explosion as the nitrogen pressure shoots up inside the crucible because of presence of azide in it. It was found to be safe when the temperature was increased at the rate of 5 K/h till the complete decomposition of the corresponding alkali azide, particularly in the temperature regime of 533 K till 653 K. After the decomposition of the azide, the rate of temperature can be varied. Silver inlays can be used for the reactions in which the final temperature does not exceed 1023 K. Above this temperature, there may be a possibility of these silver inlays getting damaged or melted. Molybdenum or platinum crucibles were used for carrying out the reactions above 1023 K. Or preferably Alumina (Corundum) crucibles were also used.

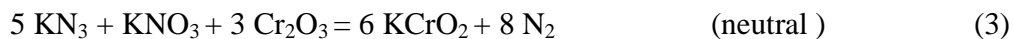
As a particular strength of this procedure, the oxygen content, and thus the valence state of the transition metal, can be precisely fixed by the alkali azide/nitrate ratio weighed in. At various illustrative examples, the "azide/nitrate route" has been proven to be rather versatile in providing highly defined materials showing interesting structural and physical properties [3-6]. The basis of the reaction is the Zintl and Baumbach's concept of mixing of sodium azide with sodium nitrate or nitrite (Eq. 1 und Eq. 2).



The method is not frequently used for the synthesis of Na_2O because of explosion danger with uncontrolled pressure of N_2 generated within the closed crucible. However with the incorporation of respective transition metal binary oxide as explained in detail by [3], in situ production of the alkali metal oxide that react with the corresponding transition metal oxide (diluting the azide/nitrate mixture) to give the desired product in pure amount.

2. Experimental

The main advantage of this route is the simplification of the preparative work and wide variety of systems that can be handled. In addition to the acid-base reactions, it is possible to perform redox reactions with simultaneous reduction or oxidation of the counter cation which is as shown in the following equations.



2.1.4 Crystal growth

Crystals were grown by high temperature annealing of pressed pellets of powder sample welded in silver crucibles particularly designed for annealing. Because of sensitivity to air and moisture, pellets were prepared inside the glove box. This silver crucible was then transferred into a quartz tube, which was sealed further in the form of ampoules under the flow of dry argon as seen in **Fig. 2.4** below. Later the sample was annealed between 500 to 1000 hours at a selected temperature inside the round tube furnace. Depending upon the thermal behaviour of sample at higher temperature as seen by DSC, the respective annealing profile was used. After long annealing time, the suitable crystals were separated in the glove box compartment under the microscope and picked up using a 0.1 mm sharp edged glass capillary and inserted into a 0.3 mm capillary. This zipped capillary is finally sealed under dry argon using heating filament, to be finally used for single crystal analysis.

2. Experimental

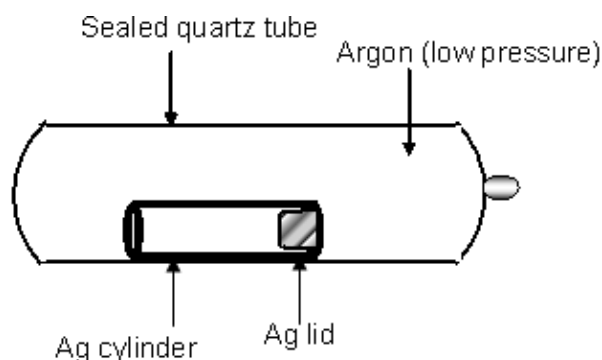


Figure 2.4: Schematic of commonly used quartz tube for crystal growth.

2.1.5 High – temperature laboratory furnaces

The key in high temperature synthesis in solid state chemistry is the well calibrated single zone furnaces that can be operated at higher temperature conditions with temperature difference of less than 5 K. The high temperature syntheses in present study were conducted in tube furnaces (LOBA type, HTM Reetz GmbH, Berlin) featuring KANTHAL heating wire and capable of achieving temperatures up to ~1273 K).

The temperature is monitored using Ni-Cr/Ni thermocouples and regulated by Eurotherm controls. Normally the quartz tube were placed inside the furnace whereby the streaming argon was required, however for annealing the sample at higher temperature, an encapsulated sealed quartz tube was placed inside the corundum tube in the furnace with automated central temperature control unit.



Figure 2.5: Single zone furnace (HTM Reetz GmbH, Berlin) used for synthesis in present this study.

2. *Experimental*

2.2 Analytical techniques

2.2.1 X-ray diffraction methods

The close scrutiny and knowledge of atomic structure of materials plays a pivotal role in order to understand and improve the properties of these materials. An effective way to do this is by means of diffraction techniques using *neutrons* from nuclear reactors and particle accelerators or X-rays from X-ray tubes and *synchrotrons*. The *single crystal* diffraction technique, using relatively large crystals of the material, gives a set of separate data from which the structure can easily be obtained. However, most materials of technical interest cannot grow large crystals, so one has to resort to the *powder* diffraction technique using material in the form of very small crystallites. The drawback of this conventional *powder* method is that the data grossly overlap, thereby preventing proper determination of the structure. The "Rietveld Method" creates an effective separation of these overlapping data, thereby allowing an accurate determination of the structure.

2.2.2 Powder X-ray diffraction

The variety of diffractometers that were frequently used throughout the present research study for recording the X-ray diffractogram to ascertain the phase purity and for identification of the component phases of polycrystalline powder samples are listed in Table-1.

2. Experimental

Table 2.1: The specification of various diffractometers used in present investigation at Max Planck Institute for solid state research (FKF) Stuttgart

X-ray radiation	Sample geometry	Detector
Stoe Stadi-P: Cu- K- α_1 ($\lambda=1.54060 \text{ \AA}$)	Capillary (Debye-Scherrer) or Transmission mode	Image Plate PSD 2 θ angle range:140° ($\Delta 2\theta=0.1^\circ$)
Stoe Stadi-P: Cu- K- α_1 ($\lambda=1.54060 \text{ \AA}$)	Capillary (Debye-Scherrer) or Transmission mode	Linear PSD 2 θ range:6° ($\Delta 2\theta=0.08^\circ$)
Stoe IPDS: Mo- K- α_1 ($\lambda=0.70930 \text{ \AA}$)	Capillary (Debye-Scherrer) or Transmission mode	Linear PSD 2 θ range: 6° ($\Delta 2\theta=0.06^\circ$)
Stoe IPDS: Ag- K- α_1 ($\lambda=0.55941 \text{ \AA}$)	Capillary (Debye-Scherrer) or Transmission mode	2 θ range: ($\Delta 2\theta=0.1^\circ$)
Brucker D8: Cu K- α_1 ($\lambda=1.54060 \text{ \AA}$)	Debye-Scherrer mode	2 θ range: 6° ($\Delta 2\theta=0.0001^\circ$) Väntag-1 PSD opening angle (2 $\theta = 6^\circ$) and resolution $\Delta 2\theta = 0.009^\circ$.
Brucker D8: Mo K- α_1 ($\lambda=0.70930 \text{ \AA}$)	Debye-Scherrer mode	2 θ range: 3.5° ($\Delta 2\theta=0.1^\circ$) LynxEye PSD Detector

X-ray diffraction is based on the principal of constructive interference of monochromatic X-rays and a crystalline sample satisfying the Braggs law. These X-rays are generated by a cathode ray tube (Cu, Mo, Ag) and consist of several components [K_{α_1} , K_{α_2} , and K_{β}]. K_{α_1} has a slightly shorter wavelength and twice the intensity as K_{α_2} . K_{α_1} and K_{α_2} are sufficiently close in wavelength such that a weighted average of the two is used. However in advanced Brucker machine the monochromatic K_{α_1} line is isolated by the Vario-1 Johansson monochromator at the X-Ray tube. No more need to numerically subtract out the K_{α_2} from your data. These rays are further filtered by using Ge(220)-single crystal as a monochromator, collimated to concentrate, and directed toward the sample. These diffracted X-rays are then detected, processed and counted. By scanning

2. Experimental

the sample through a range of 2θ angles, all possible diffraction directions of the lattice should be achieved due to the random orientation of the powdered material. The geometry of an X-ray diffractometer is such that the sample rotates on goniometer head in the path of the collimated X-ray beam at an angle θ while the X-ray detector is mounted on an arm to collect the diffracted X-rays. When the geometry of the incident X-rays impinging the sample satisfies the Bragg Equation, constructive interference occurs and a peak in intensity occurs. The unique set of d-spacing derived from this pattern can be used to 'fingerprint' the compound under investigation. For typical powder patterns, data is collected at 2θ from $\sim 2^\circ$ to 90° (Cu diffractometer), and from $\sim 2^\circ$ to 40° (Mo and Ag diffractometer). The material to be analyzed is finely ground, homogenized, and average bulk composition is determined. Air sensitive samples were sealed inside the borosilicate glass capillaries [outside diameter from 0.1 to 0.5 mm respectively (glass number: 14, Hilgenberg)] inside the glove box. Whereas the air stable samples were stuck by means of silicon grease on plastic foils for the recording of the radiographs using flat disc. To collect the diffractograms at higher temperatures the quartz capillary was placed in round furnace attached to respective D8 diffractometer. This instrument was also equipped with a water-cooled heater stage (mri Physikalische Geräte GmbH), with a temperature stability < 1 K that could be used for high-temperature measurements. The correction of measured raw data (zero shift in 2θ values, if any) was achieved by using elemental Si standard (cubic, Fd-3m, $a = 543.08(8)$ pm) or the NIST line profile standard SRM 660a (LaB₆, Pm-3m, $a = 415.695$ pm).

2. *Experimental*

2.2.2.1 **Structure solution and refinement from powder diffraction**

Precise structure determination from crystalline powder data has become more demanding in recent years, particularly in the field of material sciences. Unfortunately not all phases can be grown as single crystals and as a consequence the usage of X-ray powder methods becomes inevitable. Scattering of the powder samples gives one-dimensional projections of the reciprocal lattice, in contrast to three dimensional data of the reciprocal space in single crystal diffractometry. Owing to the limited resolution of the involved detectors while recording powder patterns, the information about the intensity of some reflections can be lost due to the systematic and accidental peak overlap of symmetrically non-equivalent reflections particularly in the case of crystal structure with low symmetry and large lattice parameters. Consequently, structure solution and refinement methods based on structure factors derived from extracted reflection intensities usually cannot be employed in such cases. However, if a crystal structure model is already available then this problem can be circumvented by a method developed by Hugo Rietveld [7, 8].

In certain cases where the structural model is incomplete or calculated intensities might deviate significantly from observed ones, the Le Bail refinement is in fact a right choice to get good fit. It's a structure free approach whereby the refinement of lattice parameters (space group and unit cell parameters, alongwith the 2θ correction) results in good match between the generated profile and experimental one. The Le Bail method is in fact a peak extraction method used to refine the background (Chebychev polynomials), lattice parameters and the peak profiles (Voigt approximation). The lattice parameters obtained via Le Bail refinement can be used further for whole profile refinement.

2. Experimental

The structure refinement should be carried out with correct starting structural model with all atomic positions. However if some atomic position are missing, the aid of difference Fourier map (difference in electron density) can be used to calculate the missing atomic position and complete the structural model. However, in the case where totally no structure model is available, the method of simulated annealing based on global optimization algorithms is extensively employed, to attempt to solve the structural model from powder data. Careful monitoring of results (decrease in GOF (goodness of fit) values) after every least square refinement cycles shows the right progress of refinement, and refinement should be carried out until the extent of agreement between the observed profile and calculated profile (as determined via least squares fitting) is optimized.

Once the initial crystal structure is solved, various steps can be done to attain the best possible fit between the observed and calculated crystal structure. The final structure solution will be presented with an *R* value (the reliability factor), which gives the percent variation between the calculated and observed structures. Quality of a solution is assessed by the values of R_1 , wR_2 , and GooF.

The reliability factor of the refined data was defined as follows:

- **R_1** , often called the **R-value**, is the agreement between the calculated and observed models. The formula for this value is $R_1 = \frac{|\sum |F_o| - |F_c| |}{|\sum |F_o| |}$. Ideal solutions would have R-values of 0, however, due to random errors, this is never achieved. R-values (listed as percents) of less than 5% are considered good solutions; high quality samples will often result in R-values lower than 2.5%.

2. Experimental

- **wR₂** is similar to R1, but refers to squared F-values. This results in wR2 always having a higher value than R1.
 - The final value, **GOF**, refers to the "goodness of fit" of the solution. In addition to the difference in F values, the GOF also takes into account the number of observed reflections and the parameters used.
-
- *The Profile R-factor.....* $R_p = \sum (|F_o| - |F_c|) / \sum |F_o|$
 - *The weighted R_{wp}.....* $wR_2 = \sqrt{\sum [w (F_o^2 - F_c^2)^2] / \sum [w (F_o^2)^2]}$
 - $R_{exp} = \sqrt{(N-P) / \sum_i w_i y_i (obs)^2}$
 - *The goodness of fit.....* $GOF = \sqrt{\sum [w(F_o^2 - F_c^2)^2] / (N-P)}$

For all stages of crystal structure determination from powder diffraction data (x-ray or neutron) starting with indexing of powder pattern, Le-Bail/Pawley fitting to solution of crystal structures (via a simulated annealing approach) till the final Rietveld refinement, the commercial program TOPAS (Version 4.1 or 3.0, Bruker AXS GmbH, Karlsruhe, Germany) was employed. For all other work with powder diffraction data the Stoe-WinXPow software package (Version 1.2, 2001, Stoe & Cie GmbH, Darmstadt) was used. This encompasses the powder patterns visualization using Graphics-interface, raw data handling, zero-point correction alongwith peak calibration, calculation of theoretical

2. *Experimental*

powder diffraction patterns as well as routine qualitative phase analysis of measured patterns with the aid of powder diffraction databases (“Search/Match” utility, PCPDFWIN Version 1.2, JCPDS-ICSD, ICDD, USA). All pictorial representations of crystal structures depicted in this thesis were created using the program Diamond (Version 3.1b 2006, Klaus Brandenburg, Crystal Impact GbR, Bonn, Germany) and Atoms (Shape Software, USA) whilst all graphical plots were made using the program Origin (Version 7.5 SR4 2004, OriginLab Corporation, Northampton, USA). Microsoft Office 2003 Professional Software is gratefully acknowledged.

2.2.3 Precession technique

This method is used to quickly test the quality of the single crystals, prior to sending it to single crystal X-ray diffractometer (IPDS). Crystals were selected inside a glove box with the aid of an optical microscope and appropriate micro-tools, mounted on the drawn-out tip of a thin glass capillary (0.1 or 0.3 mm) via vacuum grease and sealed inside a wider capillary (0.3 or 0.5 mm) using a heating filament and then mounted into tubular steel split pins (spannstift) using molten wax. The single crystals glass capillary is mounted on the goniometer head and Laue photographs were taken using precession cameras (Huber Diffraktionstechnik GmbH & Co. KG, Rimsting) equipped with a Mo source plus zirconium filters ($\lambda = 0.71073 \text{ \AA}$) and image plate detector systems in order to select the best crystals.

2. *Experimental*

2.2.4 Single crystal diffraction

Single-crystal X-ray Diffraction is a non-destructive analytical technique which provides precise determination of the lattice parameters, positions of atoms within the lattice (atomic coordinates), bond-lengths, bond-angles, and details of site-ordering (thermal displacement parameters). X-rays from the respective source are collimated and directed at the crystal. Diffracted rays at the correct orientation for the configuration are then collected by the detector. Modern single-crystal diffractometers use CCD (charge-coupled device) technology to transform the X-ray photons into an electrical signal which are then sent to a computer for processing. Molybdenum is the most common target material for single-crystal diffraction, with MoK α radiation = 0.7107Å. However the CuK α radiation = 1.54060 Å are also used depending upon the intervening elements involved. Single-crystal diffractometers use either 3- or 4-circle goniometers. These circles refer to the four angles (2θ , χ , ϕ , and Ω) that define the relationship between the crystal lattice, the incident ray and detector. In our present study the three circle goniometers were used.

Single crystal sample are carefully picked inside the glove box under argon using pre dried grease and are mounted on thin glass capillary (0.1mm) tip which is later further pushed in 0.3mm capillary and sealed under argon. The zipped glass capillary containing the single crystal of interest after quality control via precession technique is further processed for single crystal X-ray diffractometry, where it is mounted onto goniometer heads. Diffraction experiments on single crystals collect the reflexes in the three-dimensional area individually and thus make a simpler task to solve crystal structures in contrast to powder diffraction.

2. *Experimental*

The centering of the single crystal is done by adjusting of the x, y and z orthogonal directions by viewing the sample under an attached microscope or video camera until the sample is completely centered under the cross-hairs for all crystal orientations within the X-ray beam. There are however certain limitations, that the crystal quality should be good enough (single crystal), the sample should be stable and of reasonable size (between 50microns—1mm in size).The twinned samples can be handled with difficulty using softwares like TWINABS [9]. Data is typically collected between 4° and 60° 2θ for molybdenum radiation. A complete data collection may require anywhere between 6-24 hours, depending on the specimen and the diffractometer. Exposure times of 10-30 seconds per frame for a hemisphere of data will require total run times of 6-13 hours. After the data collection; corrections for instrumental factors, polarization effects, X-ray absorption and (potentially) crystal decomposition must be applied to the entire data set. Later assignment of phase to strong reflections and iterating to produce a refined fit using direct methods and least-squares, gives unique set of phases that can be combined with the structure factors to determine the electron density map. Elements can be assigned to intensity centers, with heavier elements associated with higher intensities. Distances and angles between intensity centers can also be used for atom assignment based on likely coordination and chemical knowledge. If the sample is of a known material, a template is normally used for the initial solution.

Single crystal diffraction data were collected on a three circle diffractometer (Bruker AXS, Karlsruhe, Germany) equipped with a SMART-CCD (APEX I), at 293 K. The collection and reduction of data were carried out with the Bruker Suite software package [10]. Intensities were corrected for absorption effects applying a multi-scan method [11].

2. Experimental

The structure was solved by direct methods and refined by fullmatrix least-squares fitting with the SHELXTL software package [12].

2.2.5 Raman spectroscopy

Raman spectra of a single crystal were collected on Laser Raman spectrometer (LabRAM system, Horiba Jobin-Yvon) with a laser excitation source at 784 nm (20 mW diode laser) coupled with the optical filters and a multichannel CCD detector. There are, however, laser excitation sources of 532 nm (4mW diode laser) and 633 nm (4mW He-Ne laser) also available, which can be used depending on sample composition and structure. The microscope allowed for measurement of spot sizes on the micrometer range. The spectra were taken in the range of 400–1200 cm^{-1} with the single crystal zipped in the glass capillary, at room temperature (298K).

2.2.6 Energy dispersive X-ray spectroscopy (EDX+SEM)

The atom ratio of the heavy elements was confirmed with a (SEM) scanning electron microscope (XL 30 TMP, Philips, Holland, tungsten electrode, 25 kV), equipped with an integrated EDAX (EDAX, Traunstein-Neuhof) with an S-UTW-Si(Li) (Super Ultra Thin Window) detector (polymer window, active detector surface area = 10 mm^2). The images of the single crystals were taken using SEM. Observations of the shapes of crystals, the crystal morphology, can suggest the regular external form of a crystal and shape can be an expression of internal order. Energy Dispersive X-ray Spectroscopy (EDX) is mostly used to probe the presence of heavier elements in the sample. Mostly this is not a quantitative technique, but it is used to probe the crystals composition and morphology.

2. *Experimental*

The principle involved in EDX is the interaction of incident electrons (electron beam) with inner-shell electrons of the sample. When the sample is bombarded with fast moving electrons the characteristic X-rays are produced. During the ionization process, a high-energy electron ejects an electron from the inner-shell of the atom, leaving a vacancy in the shell. The excited atom returns to its initial state filling the vacant place with an electron from an outer-shell (recombination). Because of the difference in bonding-energy, the recombination process results in the emission of characteristic X-rays. The intensity and the wave length of this X-rays yield quantitative and qualitative information on the elements present in the sample.

2.2.7 Thermal analysis

As the name implies it is the measurement of chemical and physical properties of a substance as a function of temperature. In this work thermogravimetric analysis (TGA), differential thermal analysis (DTA), and differential scanning calorimetry (DSC) were employed to study the phase transitions and respective decomposition temperature of the substance of interest. The difference thermal analysis (DTA) and thermogravimetry (TG) were performed simultaneously, up to a temperature of 1673 K with a Thermoanalyser STA 409 C (Company: Netzsch, Selb). Using a Skimmer coupling (Netzsch) the volatile decomposition products can be directed to a quadruple mass spectrometer (QMS 421, Balzers) and their mass up to 1024 m/e can be measured.

A differential scanning calorimeter (DTA 404, Netzsch) equipped with a NiCr / NiCu-thermoelement (type E, Argon) was used. As a sample holder, cylindrical Pt/Rh/Al

2. *Experimental*

crucibles (external diameter 7 mm, height 2.5 mm) with lid were applied. The change in the mass of the sample due to its decomposition was studied by heating the sample to a controlled temperature program in oxygen/argon atmosphere. The decomposition products were detected with a coupled quadrupole mass spectrometer QMS 421 (Company: Balzers, Hudson, NH, USA).

DSC technique was extensively used for study of phase transition in various compounds. Two different instruments were used for the said purpose. For routine or more qualitative purposes, a DSC 404 Cell instrument (Netzsch) utilizing a NiCr / NiCu thermocouple (Type E) and argon carrier gas was used starting from room temperature till 1473 K. For measurements below 873 K, powder was pressed into sealed aluminum crucibles, whereas for temperature above 873 K the substance was weighed into a corundum crucible and compared with the measurement of an empty blank reference.

However for more precise measurements, with the added possibility of low temperature scans till 100 K, a Perkin Elmer Pyris 1 instrument operating in power compensation mode was employed. In this case cooling is achieved via liquid N₂ and the sample measured in an inert atmosphere of He gas (Helium 4.6, purity > 99.996 vol. %). Samples were housed in 50µl Al crucibles (Perkin Elmer) with an empty one serving as a blank. Sapphire served as an external standard. The sample measurement range on this Perkin Elmer machine is from 100K till 950K.

2. Experimental

2.2.8 Temperature dependence of the specific heat (Cp)

Specific heat as a function of temperature of a polycrystalline sample of almost all the mentioned compounds were measured between 2 and 350 K using a commercial PPMS (Physical Property Measurement System, Quantum Design, 6325 Lusk Boulevard, San Diego, CA.) employing the relaxation method [13, 14]. To thermally fix the sample tablet ($\varnothing = 5$ mm and thickness 1mm) to the sapphire sample platform, a minute amount of Apiezon N vacuum grease was used. The heat capacity of the sample holder platform and grease was individually determined in a separate run and subtracted from the total measured heat capacities.

2.2.9 Conductivity measurements

The conductivity σ (S m^{-1} , or $\Omega^{-1} \text{m}^{-1}$) of a material differs and depends upon the investigated substances around several orders of magnitude. For metals it is about $10^6 - 10^4 \text{ S m}^{-1}$ (Ag: $62.5 \cdot 10^6 \text{ S m}^{-1}$) [15], for semiconductors around $100 - 10^{-6} \text{ S m}^{-1}$ (Si: $4.3 \cdot 10^{-4} \text{ S m}^{-1}$) [15] and for insulator below $10^{-10} \text{ S m}^{-1}$ [16]. A further unique characteristic is the temperature dependence of the conductivity. For metals the conductivity decreases during rise in temperature, and for semiconductors the resistivity drops down (positive and/or negative temperature coefficient). The total conductivity of a solid sample comprises of ionic (cationic, anionic) and electronic parts. Ionic conductivity measurements were carried out for polycrystalline sample using ion-blocking silver (or gold) electrodes by means of impedance spectroscopy. For this purpose the sample was pressed in the form of compact tablet ($\varnothing = 6$ mm, thickness = 0.8 mm) using pressure of 350 MPa. The sample disc was placed into a quartz glass cell [17] and the measurements

2. Experimental

were performed under argon atmosphere at a rate of 1K min^{-1} both heating and cooling cycles. The temperature dependent AC impedance spectra were recorded with a Novocontrol Alpha-A 4.2 Analyzer in combination with the impedance interface ZG 4 in a 2-wire arrangement in the frequency range of $\nu = 0.5$ to 20 MHz. Measurements and data recording were carried out with the WinDeta program [18]. The bulk conductivities were determined by non linear mean square deviation curve fitting of the impedance spectra using the WinFit program [19]. A programmable DC voltage source (TR 6142, Advantest Corporation) was used for collecting DC conductivity data (electrical conductivity). The current was measured by a digital multimeter (195 A, Keithley) serving as a serial switched ampere meter. The voltage was measured by another digital multimeter (HM 8112-2, Hameg Instruments) which was parallely switched as a voltmeter. The conductivity is determined afterwards according to the four probe “van der Pauw method” [20, 21] with an in-built measuring system.

2.2.10 Magnetic measurements

The temperature dependent measurement of the magnetic susceptibility of any substance gives an idea about the presence of the unpaired electrons in that substance. The magnetic moment values gives the information about the compound whether it is diamagnetic, paramagnetic, ferromagnetic, antiferromagnetic or ferrimagnetic substance. The temperature dependence of the magnetic susceptibility was measured on a spin quantum interference device: SQUID magnetometer (Superconducting Quantum Interference device) MPMS 5.5, (Company: Quantum Design, San Diego, CA, USA). This device allows Investigations in the temperature range of 1.7-800 K in a homogeneous magnetic

2. Experimental

field up to 7 T. The samples were sealed in supra-seal quartz ampoules under high grade helium atmosphere. For measurements above 350 K the sample was contained in warily dried SUPRASIL ampoule ($\varnothing = 3$ mm) that was long enough to extend over the coils of the magnetometer inside the oven. To avoid any reaction of the pristine sample with the quartz tube, use of gold crucible is recommended as shown in **Fig. 2.6**. However, prior to measurement empty gold crucible correction ought to be performed.

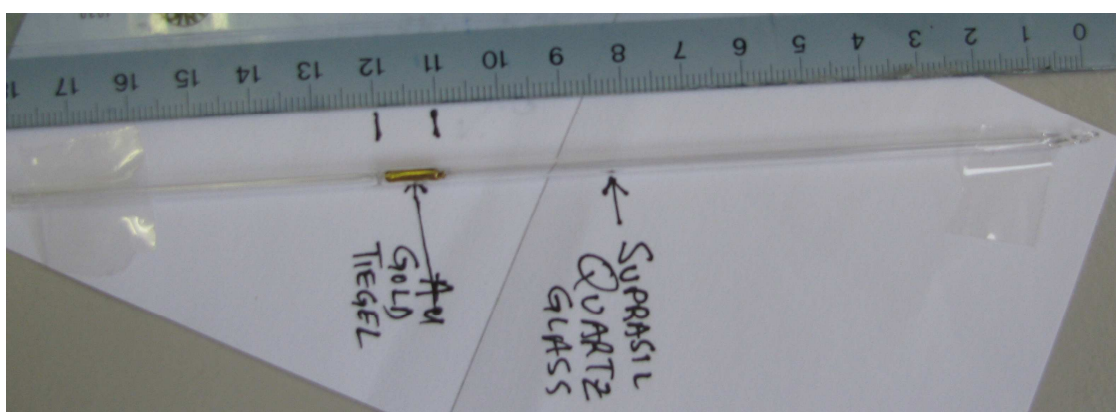


Figure 2.6: A standard supraseal quartz tube ($\varnothing = 3$ mm) with gold crucible used for high temperature magnetic susceptibility measurement.

On contrary for low temperature measurement 4 mm or 5 mm quartz ampoules were used. For non-air sensitive samples, special gelatin capsules can also be used.

2. Experimental

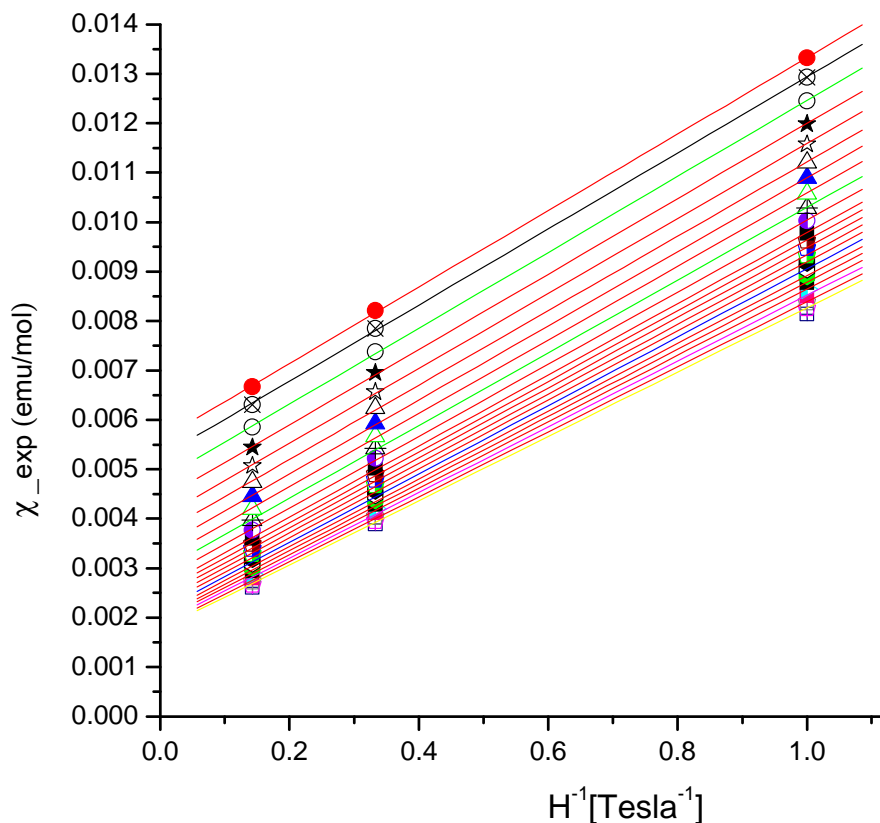


Figure 2.7: The common Honda Owen plot of $\chi_{\text{mol}}(\text{exp})$ vs $H^{-1}(\text{Tesla}^{-1})$ at various temperatures at magnetic field approaching infinity [$H^{-1}=0$].

In order to nullify the contribution to the raw data, whatsoever, from spurious ferro- and paramagnetic impurities the Honda Owen correction [22, 23] was made to the whole raw data obtained at 1, 3 and 7 Tesla, at magnetic field approaching infinity [$H^{-1} = 0$] as displayed in **Fig. 2.7**. Later the data is further corrected for core electron diamagnetic and van Vleck contributions [24] to get the original spin susceptibility χ_{spin} . The diamagnetic contribution of the core electrons in closed shell can be estimated by incremental method of all the ions as tabulated, e.g, by Selwood [25, 26].

2. Experimental

The plot of χ^{-1} vs T gives a lucid view of the temperature dependent magnetic susceptibility of a given sample and grows almost linearly with increasing temperature particularly at higher temperature ($T \gg T_N$) at various applied magnetic fields, whereby the data can be fitted applying Curie-Weiss law [$\chi_{\text{mol}} = C/(T-\theta) + \chi_0$], with curie constant (C), Curie-Weiss temperature (θ). χ_0 comprises all the extra contributions to the original sample susceptibility: i.e: Temperature Independent Magnetic Susceptibility [TIP], Van Vleck, Diamagnetic susceptibilities contribution, which must be subtracted. The curie constant (C) is related to effective magnetic moment, $\mu_{\text{eff}}/\mu_B = g[S(S+1)]^{1/2}$ of the respective metal cation as per following equation:

$$\chi = \frac{C}{T} = \frac{M}{H}$$
$$\frac{C}{T} = \frac{N\mu_0 g^2 j(j+1) \mu_B^2}{3KT}$$
$$\mu_{\text{eff}} = g \sqrt{j(j+1)} \mu_B$$

Finally, the data handling using different models were performed using Microcalc Origin (Version 7.5 SR4 2004, OriginLab Corporation, Northampton, USA) program.

2.2.11 Mössbauer spectroscopy

It is a powerful technique for extracting very precise information about the valence state, coordination environment around central atom, charge distribution, magnetic and time-dependent properties of a material. The essence of this technique is the recoil free emission and absorption of γ -rays by nuclei called as 'Mössbauer Effect'. The technique

2. *Experimental*

of Mössbauer spectrometry has been extensively used for the investigation of iron-containing systems [^{57}Fe isotope] and apart from that the other systems that can be studied include ^{119}Sn , ^{151}Eu , ^{121}Sb , and ^{161}Dy . A typical ^{57}Fe Mössbauer spectrum consists of sets of peaks (usually doublets and sextets), depending on what the Fe nucleus "sees" in its environment. The nuclear environment depends on a number of factors including the number of electrons (Fe^0 , Fe^{2+} , Fe^{3+}), the number of coordinating anions, the symmetry of the site, and the presence/absence of magnetic ordering (which may be temperature-dependent). Thus the spectrum of a given sample may consist of a superposition of doublets and sextets. The experimental setup for Mössbauer spectrometry includes a radioactive source [^{57}Co] sample, detector, and a drive to move the source or absorber. For this case, ^{57}Co is used as the radioactive source. By a spontaneous electron capture, the source changes to a metastable state of ^{57}Fe and then decays to the ground state, emitting γ -rays, particularly a 14.41 keV Mössbauer γ -rays. The emitted rays are passed through the sample, where some of them are absorbed, and then the remaining rays continue on to a detector as can be seen in Fig. 2.8. To investigate the energy levels [nuclear] in the sample, the energy of the γ -rays beam is varied through the energies for resonant absorption. The energy modification is performed by moving the source relative to the absorber, thus shifting energy as a result of "the first-order relativistic Doppler effect". For example, for ^{57}Fe , moving the source at a velocity of 1 mm/sec toward the sample increases the energy of the emitted photons by about ten natural line widths. Very small energy shifts of nuclear levels [of the order of 10^{-8} eV] caused by hyperfine interactions between the nucleus and its surrounding

2. Experimental

electrons can be measured. These shifts can be achieved by Doppler shifting the energy of the photon.

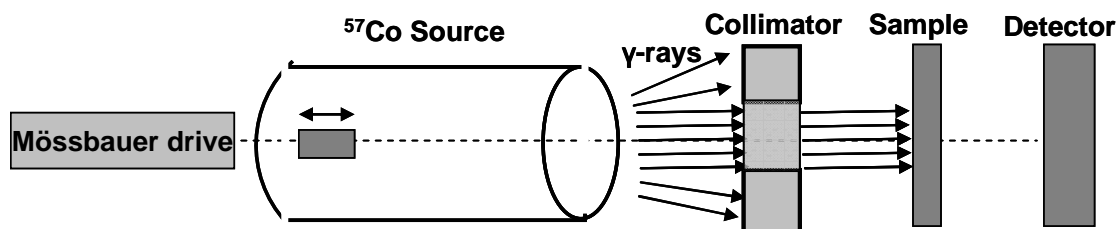


Figure 2.8: Setup for Mössbauer spectrometry measurements.

For the 14.41 keV ray of ⁵⁷Fe, the velocities needed are on the order of several mm/s. An energy range of ± 10 mm/s would give an energy shift of 4.8×10^{-7} eV to a 14.41 keV γ -ray, which is usually sufficient to investigate the Mössbauer energy spectrum for ⁵⁷Fe. There are three main hyperfine interactions corresponding to the nuclear moments determining the nuclear levels: isomer shift (δ) (electric monopole interaction), which arises from the difference in s electron density between the source and the absorber [⁵⁷Fe²⁺ has a larger isomer shift than ⁵⁷Fe³⁺], quadrupole splitting (the electric quadrupole interaction, Δ which is a shift in nuclear energy levels that is induced by an electric field gradient caused by nearby electrons, and the nuclear Zeeman effect (hyperfine splitting due to magnetic dipole interaction for magnetic materials only). Graphically, quadrupole splitting is the separation between the two component peaks of a doublet, and isomer shift is the difference between the midpoint of the doublet and zero on the velocity scale. The combination of all three parameters is usually sufficient to identify the valence state and site occupancy of Fe in a given site and individual sample. Since Iron atoms

2. Experimental

[Mössbauer atom] in different local environments and with different oxidation states absorb at different, diagnostic energies. Also because of low ^{57}Fe natural abundance (2.19%) enriched sample is preferred.

2.2.12 Synchrotron radiation

Synchrotron radiation is the name given to radiation, which is produced when charged particles are accelerated in a curved path or orbit by magnetic field. Under acceleration charged particles emit electromagnetic radiation, which in the case of relativistic charged particles and acceleration by magnetic fields is called synchrotron radiation. In contrast to X-rays, the intense synchrotron light beams are sharply focused like a laser beam. Basically it works on the principle of 'cyclotron accelerator' where the electrons are accelerated in an alternating electric field with a certain frequency, and rotated in a uniform magnetic field. But however, if we change the frequency of the electric field or the magnetic field during the acceleration process, it is the synchro-cyclotron, and if both the magnetic field and electric field are changed, it is synchrotron. The radiated energy is proportional to the fourth power of the particle speed and is inversely proportional to the square of the radius of the path. For an accelerator like a synchrotron, the radius is fixed after construction, but the inverse dependence of synchrotron radiation loss on radius argues for building the accelerator as large as possible. At synchrotron radiation laboratories electrons are induced via linear accelerators [Tandem Linac] into a bunches inside a vacuum storage ring and forced to travel in a closed loop by strong magnetic fields. The bending of traveling charged particle beam is achieved by a magnet (bending

2. *Experimental*

magnet) as the Lorentz force. To altering the magnetic field, undulator is designed by construct a periodical structure of many dipole magnets. The synchronization of undulator and the wiggler in synchrotron cause to increase the magnetic flux by orders, and thus the energy of the particle beam increased. According to the emitted energy, synchrotron radiations can be at different wavelength, from Infrared to soft and hard X-rays. The high purity, high stability, collimated, pulsed, narrow, brightly intense linearly polarized electromagnetic beam are the special properties of the synchrotron radiation. In our investigation of high temperature structural phase transitions the synchrotron diffraction patterns were collected at Swiss light source (SLS) Paul Scherrer Institute (PSI), Switzerland.

2.2.13 Neutron diffraction

The neutron powder diffraction patterns were obtained from the SINQ spallation source of Paul Scherrer Institute (PSI), Laboratory for Neutron Scattering, ETHZ & PSI, CH-5232 Villigen PSI, Switzerland. Neutron diffraction is an effective tool to obtain information on both, the structure and the dynamics of condensed matter, especially in studying the magnetic structure of compounds. As neutrons are not charged but carry spin thereby they do not interact with the intervening electron cloud surrounding the nucleus (unlike X-rays), rather they interact only with the nucleus of the atom thus having a unique ability to probe the magnetic structure of the compound thereby unraveling the direction and magnitude of the magnetization inside a solid. The moment carried by the neutron gives rise to the magnetic Bragg scattering in a magnetic field produced by unpaired electrons. The difference between X-ray (̄electron scattering) and neutron

2. Experimental

(nuclear scattering) technique is in fact in the scattering process. The scattering factor for X-rays increases linearly with number of electrons in the atom, so that heavy atoms are much more effective at scattering than lighter atoms. Since the neutron scattering factor is almost invariant with $\sin\theta/\lambda$, therefore the intensity of data points do not drop off at higher angles of θ (in contrast to X-rays) thereby give more information about the structure and dynamics involved, particularly in locating the exact position of light atoms in the unit cell which otherwise is not possible with X-ray diffraction. In neutron scattering experiments, the diameters of the circles representing the atoms (e.g. for CsFeO_2) are proportional to the coherent neutron scattering lengths of 5.42, 9.45 and 5.80 fm (10^{-15}m) for Cs, Fe and O, in contrast to X-ray, where it is proportional to the charges of 55, 26 and 8 for Cs, Fe and O respectively. Thus the contrast for “seeing” oxygen ions is therefore much better via neutron than X-ray, particularly the details of the oxygen site disorder at the structural transition points.

In our investigations a total of about ~4 g of polycrystalline samples of the respective compounds were sealed inside cylindrical vanadium containers of 6 mm diameter for neutron studies. The neutron diffraction data were collected at the neutron powder diffractometer HRPT [27] with the neutron wavelength $\lambda = 1.886 \text{ \AA}$, using the closed-cycle refrigerator for the low temperature (10...300 K) and evacuated radiation-type furnace for the high temperature (up to 1080, 1030 and 1100 K for $A=\text{K, Rb and Cs}$, correspondingly) measurements. All the measurements were carried out on heating the samples from low to high temperatures. The crystal structure determination was carried out on the data collected from the high-resolution HRPT1 diffractometer [27] while the data on the magnetic ordering were obtained by means of the DMC powder

2. Experimental

diffractometer situated at a super mirror coated guide for cold neutrons at SINQ ($\lambda = 2.567 \text{ \AA}$). The symmetry analysis of the possible magnetic structures has been carried out with the program SARAh-2k, and the refinements of the parameters of both the crystal and magnetic structure parameters were done with the Fullprof suite of programs with the use of its internal scattering lengths and magnetic scattering form-factors for the Fe^{3+} ion.

2.2.14 MAPLE calculations

The Madelung constant alongwith related Madelung energy is one of several factor used to predict the plausibility of crystal structure. For calculation of the Madelung part of the lattice energy, MAPLE program [28—30] was used. The MAPLE value of a compound depends on the electrical charges of the cations and anions, their inter-ionic separations and the way they are arranged in three dimensions with respect to each other within crystal structure and it gives an indication of the thermodynamic stability of the structure. The calculated value (kcal mol^{-1}) for ternary compound and the sums of the calculated partial Madelung energies derived from respective binary oxides were compared. The deviation of $< 3\%$ testifies the quality of the structure refinements and suggests that the energetics of the crystal is in order. Inspection of bond lengths and angles gives a lucid picture of the coordination sphere.

Throughout the present study both MAPLE values as well as mean fictive ionic radii (MEFIR), effective coordination numbers (ECoN) and inter-atomic distances were calculated using the program MAPLE (Version 4.0, Rainer Hübenthal, Leihgestern, Germany, 1993).

2. Experimental

2.2.15 Bilbao crystallographic server

The Bilbao Crystallographic Server (www.cryst.ehu.es) is a unique combination of crystallographic databases and programs [31]. The program SUBGROUPGRAPH was employed for problems involving group-subgroup relations (Wondratschek & Mueller, 2004; Mueller, 2004) between the aristotype high symmetry and lower symmetry structures space groups and how they arise from those of the aristotype, includes consecutive steps of symmetry reduction of the type *translationengleich* and *klassengleich*, alongwith the construction of Baernighausen–Stammbaum (relation tree). Also other problems related to structural phase transitions, infrared and Raman selection rules etc can easily be solved using the program [32].

2.3 References:

- [1] W. Schlenk, A. Thal, Ber. Dtsch. Chem. Ges., **46**, 2840 (1913).
- [2] Stefan A. Ghedia, Ph.D. Dissertation, Max-Planck-Institut für Festkörperforschung, Stuttgart (2010).
- [3] D. Trinschek, M. Jansen, Angew. Chem. 1999, 111, 234; Angew. Chem. Int. Ed. Engl., **38**, 133 (1999).
- [4] M. Sofin, Ph.D. Dissertation, Max-Planck-Institut für Festkörperforschung, Stuttgart, (2003).
- [5] N Arumugam, Ph.D. Dissertation, Max-Planck-Institut für Festkörperforschung, Stuttgart, (2005).

2. Experimental

- [6] Steffen Pfeiffer, Ph.D. Dissertation, Max-Planck-Institut für Festkörperforschung, Stuttgart, (2009).
- [7] H. M. Rietveld, *Acta Crystallogr.*, **22**, 151-152 (1967).
- [8] H. M. Rietveld, *J. Appl. Crystallogr.*, **2**, 65-71 (1969).
- [9] G. M. Sheldrick, *TWINABS—Bruker AXS scaling for twinned crystals*, version 2008/4, University of Göttingen, Germany (2008).
- [10] Bruker Suite, Version 2008/3, Bruker AXS Inc., Madison, USA, (2008).
- [11] G. M. Sheldrick, *SADABS*, Bruker AXS area detector scaling and absorption, Version 2008/1, University of Göttingen, Germany, (2008).
- [12] G. M. Sheldrick, *Acta Crystallogr.* **A64**, 112, (2008).
- [13] R. Bachmann, F. J. DiSalvo Jr., T. H. Geballe, R. L. Greene, R. E. Howard, C. N. King, H. C. Kirsch, K. N. Lee, R. E. Schwall, H. U. Thomas, and R. B. Zubeck, *Rev. Sci. Instrum.* **43**, 205 (1972).
- [14] J. S. Hwang, K. J. Lin, and C. Tien, *Rev. Sci. Instrum.* **68**, 94, (1997).
- [15] C. J. Smithells, *Metals Reference Book*, Butterworth & Co, London, (1967).
- [16] A. Wert, R. M. Thomson, *Physics of Solids*, McGraw-Hill, New York, (1964).
- [17] U. Kohler, Ph. D. Dissertation, Univ. Hannover, Germany, (1987).
- [18] Novocontrol GmbH, *WinDeta* Version 4.5, Hundsangen, Germany (1995).
- [19] Novocontrol GmbH, *WinFit* Version 2.9, Hundsangen, Germany (1996).
- [20] L. J. Van der Pauw, *Philips Res. Rep.*, **13**, 1 (1958).
- [21] J. P. Suchet, *Electrical Conduction in Solid Materials*, Pergamon Press, Oxford, (1975).
- [22] K. Honda, *Ann. Phys.* **32**, 1027, (1910).

2. *Experimental*

- [23] M. Owen, *Ann. Phys.* **37**, 657, (1910).
- [24] H. Lueken, *Magnetochemie*, Teubner, Leipzig, (1999).
- [25] Landolt-Börnstein, *Zahlenwerte und Funktionen aus Naturwissenschaften und Technik; Neue Serie, Gr. II, Bd. 2*, Springer, Berlin, (1966).
- [26] P. W. Selwood, *Magnetochemistry*, 2nd ed. Interscience, New York, p. 78, (1956).
- [27] P. Fischer et al., *Physica B* **276-278**, 146 (2000)
- [28] Hoppe R., *Angew. Chem. Int. Ed. Engl.* **5**, 95 (1966).
- [29] Hoppe R., *Angew. Chem. Int. Ed. Engl.* **9**, 25 (1970).
- [30] Huebenthal R., ‘‘MAPLE, Program for the Calculation of the Madelung Part of Lattice Energy,’’ University of Giessen, Germany, (1993).
- [31] M. I. Aroyo, J. M. Perez-Mato, D. Orobengoa, *Acta Crystallogr., Sect. A: Found. Crystallogr.*, **64**, C633, (2008).
- [32] M. I. Aroyo, J. M. Perez-Mato, C. Capillas, E. Kroumova, S.Ivantchev, G. Madariaga, A. Kirov & H. Wondratschek. *Z. Kristallog.*, **221**, 1, 15-27 (2006).

Chapter 3

Synthesis of (active) starting materials

3.1 Synthesis of alkali azides (AN_3)

3.1.1 Lithium, potassium, rubidium and cesium azides

Single phase powders in gram amounts (~ 10 g / single lot) of LiN_3 , KN_3 , RbN_3 and CsN_3 were prepared from hydrazoic acid (HN_3) condensate. HN_3 (colorless, toxic, volatile, and extremely explosive liquid at room temperature) is produced by reaction between aqueous solution of NaN_3 (99.5%, from Johnson Matthey) with very controlled gentle heating (heating mantle) under the continuous drops of 20% H_2SO_4 (99.9%, Merck) in flask (i) as shown schematically in Fig. 3.1 below.

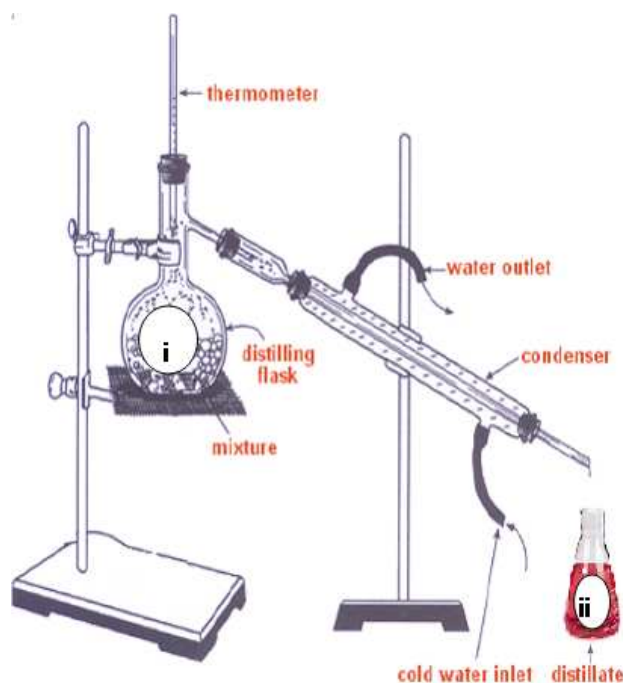
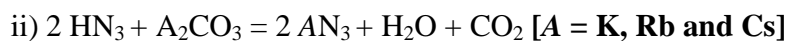
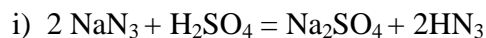


Fig. 3.1: A schematic view of assembly used for the preparation of alkali azides

3. Material synthesis



The nascent volatile HN_3 vapours are passed through the water condenser where it liquefies and later gently pour into the respective solution of potassium (99%, Sigma-Aldrich) or rubidium (99%, Johnson Matthey) and cesium carbonate (99%, Sigma-Aldrich) according to equation (ii) [1].

Within the flask (ii) the respective carbonate slurry reacts with effervescence upon addition of HN_3 drops. The absence of CO_2 bubbles formation confirms the completion of reaction which can be counterchecked with neutrality of pH. After completion of the reaction the solution of MN_3 (M = K, Rb or Cs) is further dried on sad bath at 393 K till the white precipitate settles down. The respective white precipitates are finally dried under vacuum at 423 K overnight. For the purity control of azides, X-ray powder diffraction patterns were taken (**Fig. 3.2**). However, the above mentioned drying procedure should not be carried out in case of lithium azides, otherwise the LiN_3 will blow up.

For the synthesis of all the akali metal azides AN_3 [A =Li, K, Rb and Cs] purchased sodium azide (Sigma Aldrich, 99,9%) is used as one of the starting precursor. However, in literature, the most common synthesis method for NaN_3 synthesis is Wislicenus procees [*c.f ref.* Brauer book / [2]].

3. Material synthesis

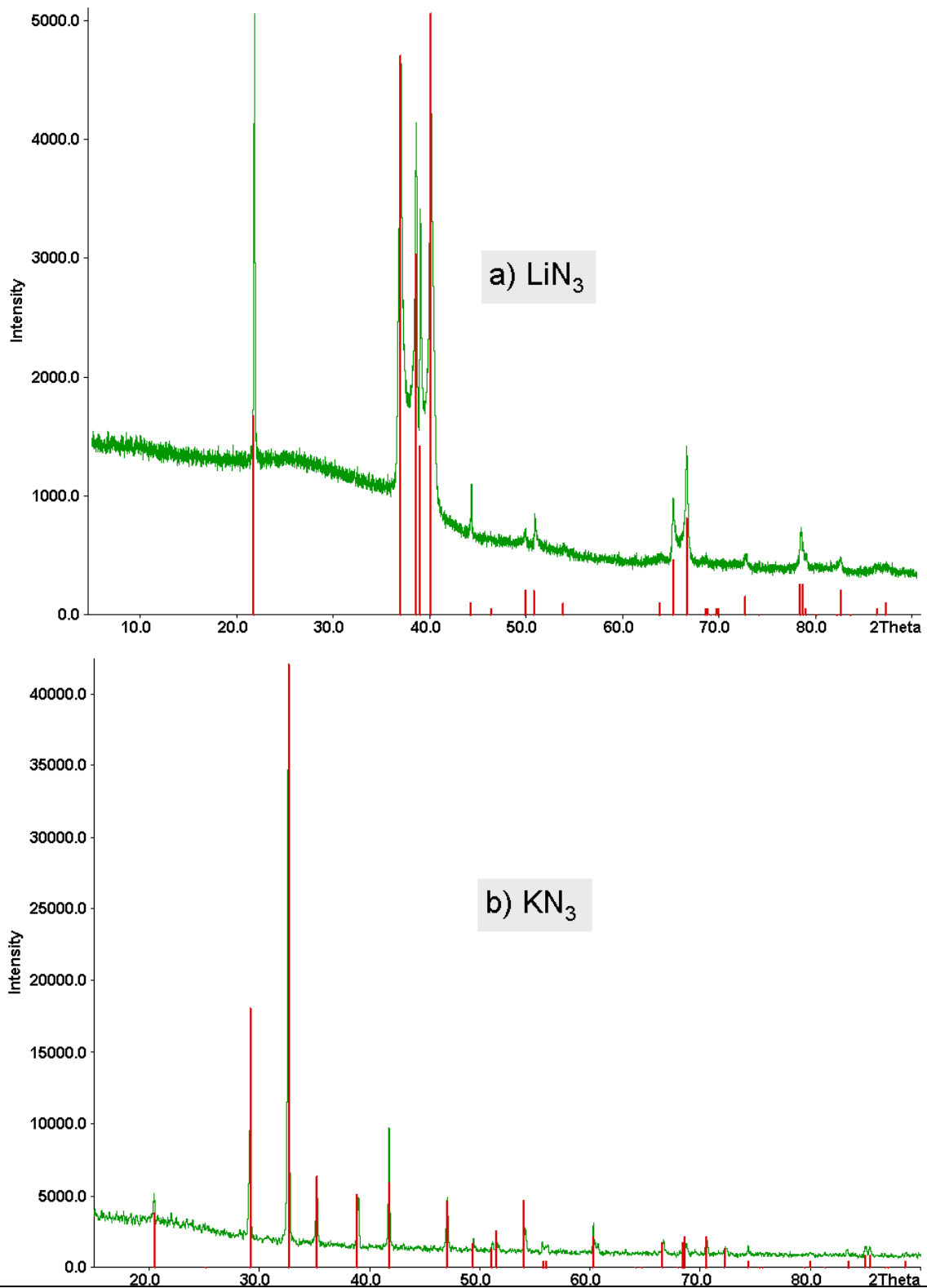


Fig. 3.2 (i). Measured Powder diffractograms (green) and the calculated literature data (red-line) for (a) LiN₃^[3] (b) KN₃^[4]

3. Material synthesis

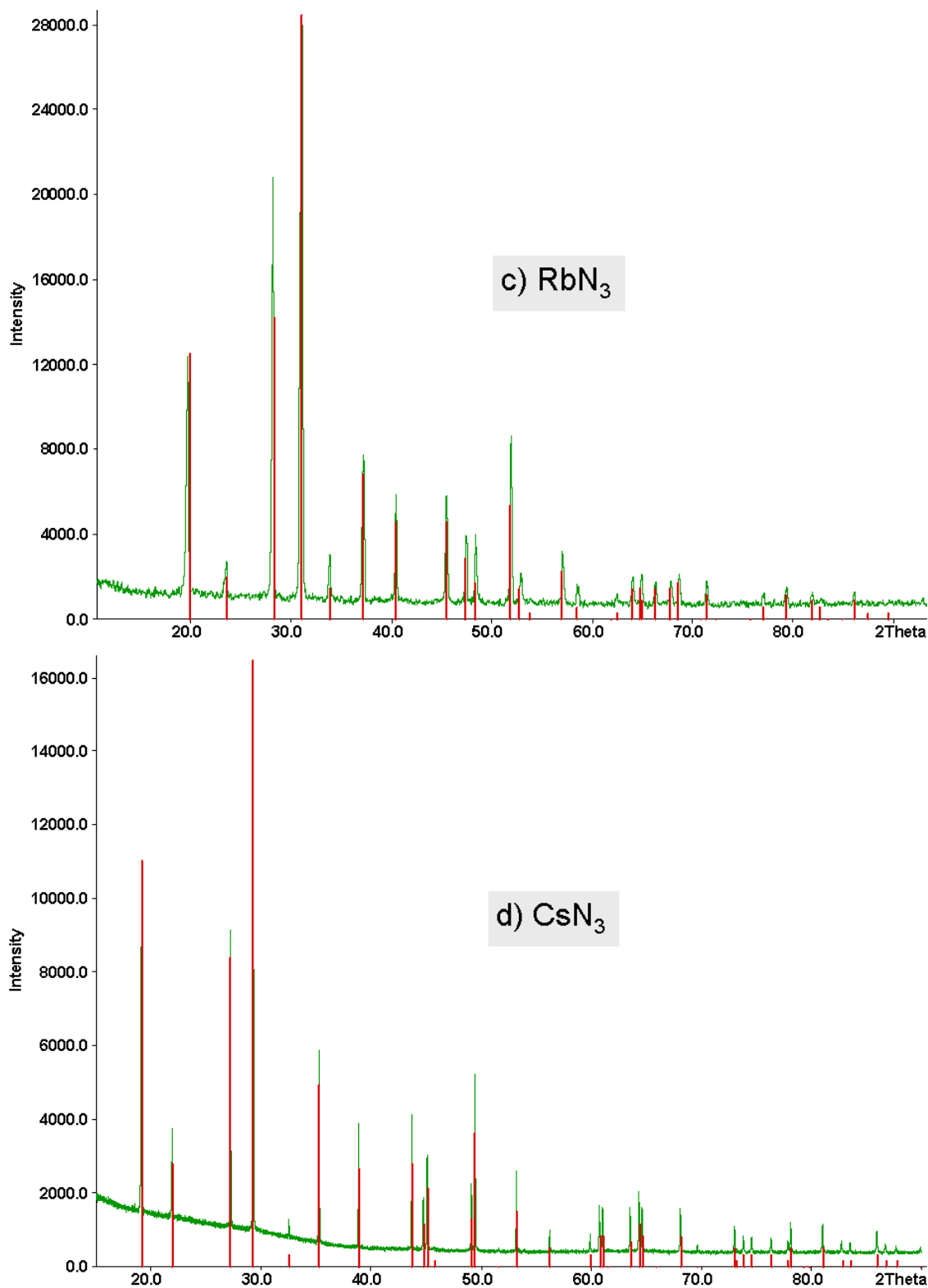


Fig. 3.2 (ii). Measured Powder diffractograms (green) and the calculated literature data (red-line) for (c) RbN₃^[5] (d) and CsN₃^[6]

3. Material synthesis

3.1.2 Drying Assembly ('Troockenpistole'):

In order to dry the small amount of substances and for the materials that are stable at higher temperatures, the use of drying gun is a suitable option and is exercised in our investigations too. One can evaporate by heating the moisture and other desired volatile impurities from the sample. The overview of the drying gun is shown in **Fig. 3.3**. The sample to be dried is placed in corundum boat and later this boat is pushed in to the drying kiln (A). The drying kiln (A, Gun Barrel) is equipped with a cylindrical bulb (B, Gun-Handle), which carries the drying agent (P_4O_{10} with indicator). From here the exit to the vacuum pump is attached. Normally the drying gun is preferred, where use of completely dried precursor is the prerequisite in a chemical reaction, as the moisture completely hinders the reaction or changes the path of reaction.



Fig. 3.3. The Drying Gun. (*Trockenpistole*) **A**) Glass round bottom flask with the dessicant / drying agent (Sicapent with indicator). **B**) Cotton ball for preventing turbulence and to prevent the worst case of mixing the two substances during evacuation. **C**) Corundum crucible (boat) containing substance to be dried. **D**) Round glass test tube to be placed finally in the furnace.

Normally during distillation it is inevitable mostly to keep the sample free from water contact, in particular, in case of moisture sensitive precursors like LiN_3 , where the use of

3. Material synthesis

“Drying Gun” is obligatory. On contrary to rest of alkali azides , in case of LiN_3 , one cannot do open drying on sand bath etc, because as soon as the temperature comes back to room temperature, it absorbs moisture quickly and turned from white to pink within a couple of minutes. During drying the sample in drying gun the sample should be ground thoroughly and preferably be placed in Corundum boat. The sample should not be heated above its flash point. So prior knowledge of boiling point and flash point in case of explosives is mandatory. To avoid any increase in internal pressure inside the drying gun, during drying process, the sample must be slowly evacuated every 3 hours and later after evacuation the vacuum valve should be closed, to have a constant vacuum condition inside the Pistol. After the drying process of almost 24 hours, the evacuated drying pistol should be transported to glove box carefully.

3.2 Synthesis of transition metal binary oxides

3.2.1 Iron (III)-oxide, Fe_2O_3

Active iron(III)-oxide Fe_2O_3 with high surface area was prepared by thermal decomposition of $\text{Fe}(\text{C}_2\text{O}_4) \cdot 2\text{H}_2\text{O}$ in a flow of dry oxygen at 623 K for 20 hours. The phase purity of the precursors was monitored by X-ray powder analysis as is displayed in **Figure 3.4(a)**. The schematic representation of temperature profile employed for the synthesis of active powder of Fe_2O_3 is shown in **Figure 3.4(b)**.

3. Material synthesis

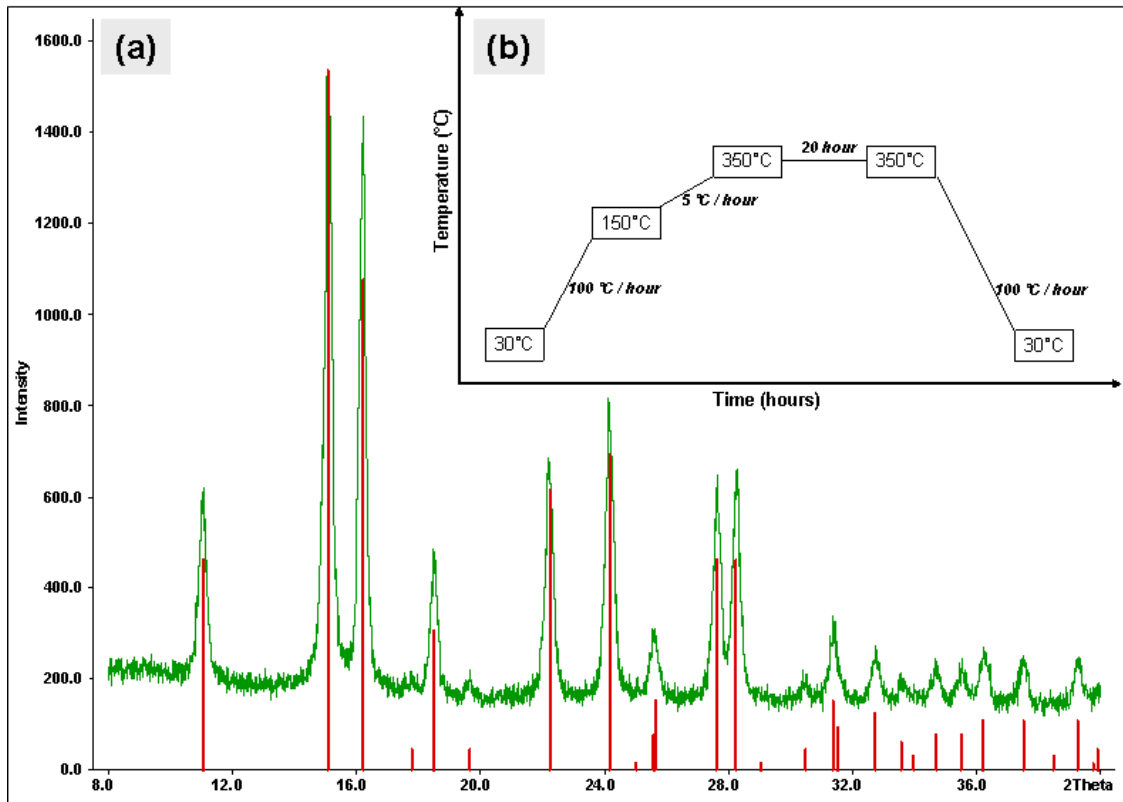


Figure 3.4. a) Measured Powder diffractogram (green) and the calculated literature data ^[7] (red-line) from Fe_2O_3 . b) Standard schematic view of temperature profile used for the synthesis of Fe_2O_3 active powder.

3. Material synthesis

3.2.2 Cobalt (II/III)-oxide, Co_3O_4

Active cobalt(II-III)-oxide, Co_3O_4 with high surface area was prepared by thermal decomposition of $\text{Co}(\text{C}_2\text{O}_4)\cdot 2\text{H}_2\text{O}$ at 623 K (20 hours) under streaming oxygen. For the phase purity the X-ray diffractogram was taken as can be seen in Figure 3.5(a). The temperature profile employed is schematically represented Figure 3.5(b).

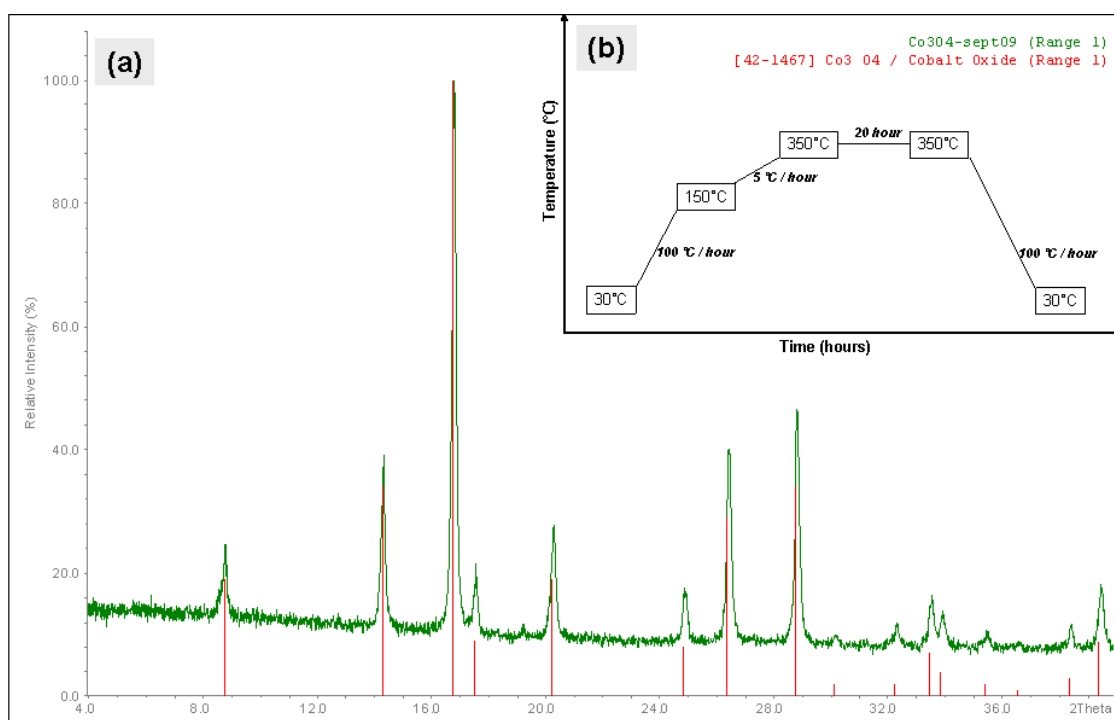


Figure 3.5. **a)** Measured Powder diffractogram (green) and the calculated literature data ^[8] (red-line) for Co_3O_4 . **b)** Standard schematic view of temperature profile used for the synthesis of Co_3O_4 (active) powder.

3. Material synthesis

3.2.3 Copper(II)-oxide, CuO

Active black colored copper (II) oxide (CuO) with high surface area was prepared by thermal decomposition of $\text{Cu}(\text{C}_2\text{O}_4)\cdot 0.5\text{H}_2\text{O}$ at 623 K for 20 hours under streaming oxygen. For the phase purity the X-ray diffractogram was taken as shown in Figure 3.6(a). The schematic representation of temperature profile employed for the synthesis of active powder of CuO is shown in Figure 3.6(b).

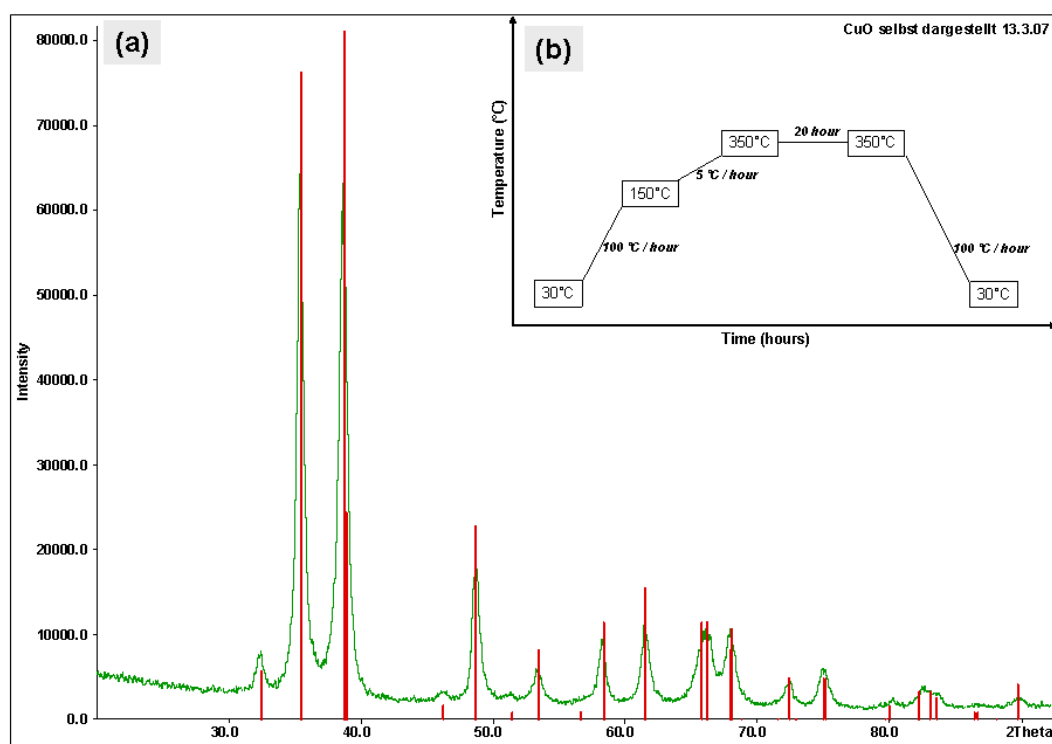


Figure 3.6. a) Measured Powder diffractogram (green) and the calculated literature data^[9] (red-line) for CuO. b) Standard schematic view of temperature profile used for the synthesis of CuO (active) powder.

3. Material synthesis

3.2.4 Chromium (III)-oxide, Cr₂O₃

Active green colored single phase powder of chromium (III)-oxide, Cr₂O₃ with high surface area was prepared by thermal decomposition of ((NH₄)₂Cr₂O₇) at 923 K (24 hours) under streaming oxygen. For the phase purity the X-ray diffractogram was taken as can be seen in **Figure 3.7(a)**. Whereas the schematic representation of temperature profile employed for the synthesis of active powder of Cr₂O₃ is shown in **Figure 3.7(b)**.

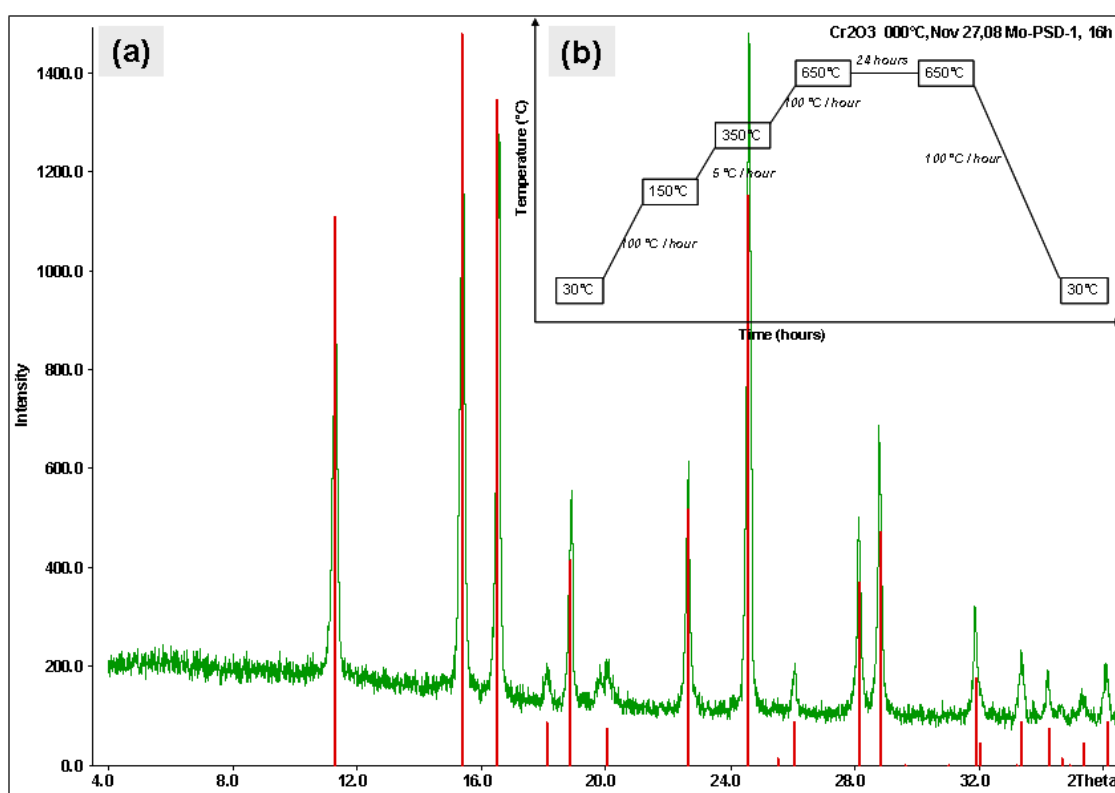


Figure 3.7. a) Measured Powder diffractogram (green) and the calculated literature data^[10] (red-line) from Cr₂O₃ b) Standard schematic view of temperature profile used for the synthesis of Cr₂O₃ (active) powder.

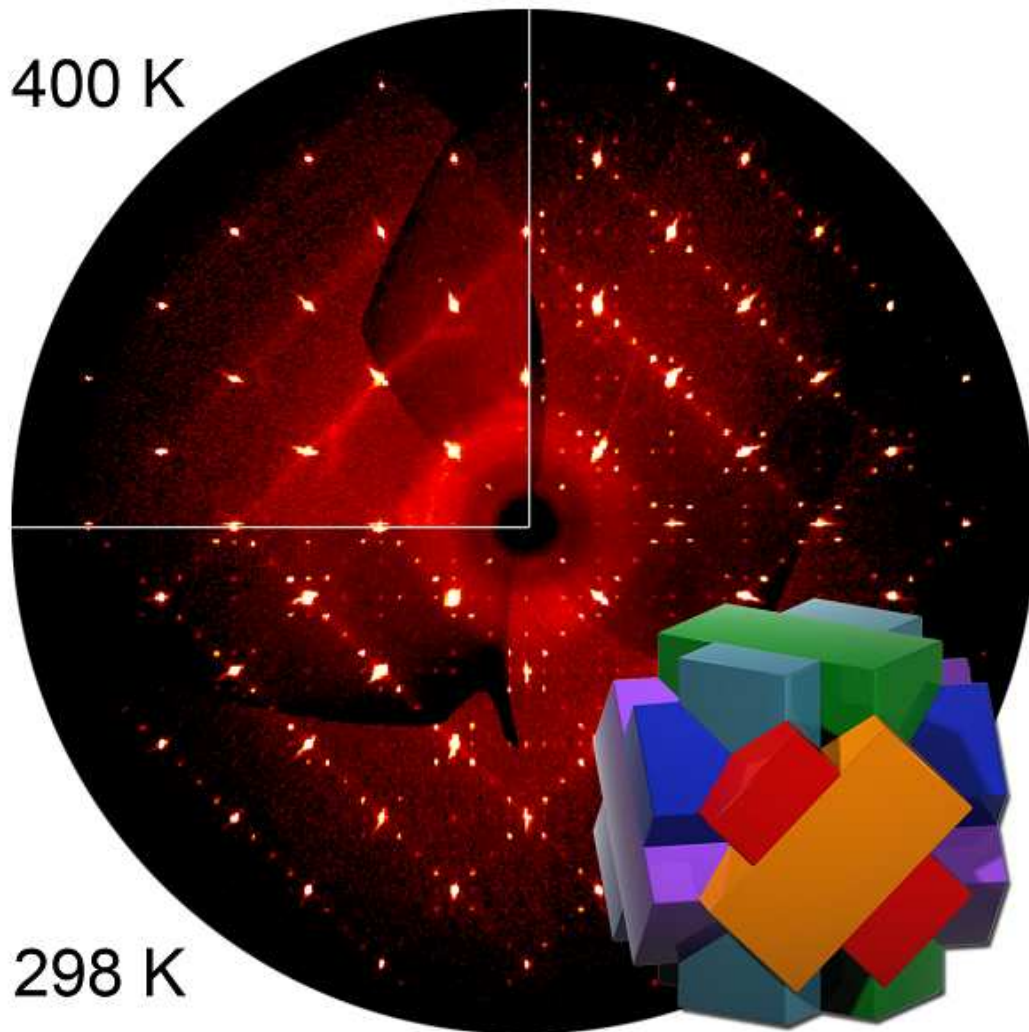
3. Material synthesis

3.3 Reference:

- [1] H. D. Fair and R. F. Walker, Energetic Materials, vol. **1**. (pp 30-38) *Physics and chemistry of inorganic azides*, Plenum press, New York and London (1977).
- [2] G. Brauer, in *Handbuch der präparativen anorganischen Chemie*, 1st ed., F. Enke Verlag, Stuttgart, p. 457 (1975).
- [3] G. E. Pringle, D. E. Noakes, Acta Crystallogr. B. **24**, 262, (1968). [ICDD=76 773- LiN₃]
- [4] U. Mueller, ZAAC, **392**, 159, (1972). [ICDD=73 2426 KN₃]
- [5] C. S. Choi, E. Prince, J. Chem. Phys. **64**, 4510 (1976). [ICDD=76 590 RbN₃]
- [6] U. Mueller, ZAAC, **392**, 159, (1972). [ICDD=73 2428—CsN₃]
- [7] L. R. Blake, R. E. Hessevick, T. Zoltai, L. W. Finger, Am. Mineral. **51**, 123 (1966).
- [8] X. Liu, C.T. Prewitt, Phys. Chem. Miner., **17**, 168 (1990).
- [9] S. Asbrink, A. Waskowska, J. Phys. Condens. Mater., **3**, 8173 (1991).
- [10] H. Saalfeld, Z. Kristallogr. , Kristalloggeom., Kristallphys., Kristallchem., **120**, 342 (1964).

Chapter 4: The $AFeO_2$ (A = K, Rb and Cs) family

Three dimensional magnetic Iron oxides.



Chapter 4: The $AFeO_2$ ($A = K, Rb$ and Cs) family

4.1. Introduction

The cristobalite type of structure serves as the aristotype for many important synthetic and naturally occurring materials. In particular when including stuffed and substituted structure variants of general formula AMo_2 , a vast family of solids is resulting that imposes intriguing challenges for science. Besides the multifaceted phenomena related to cation substitution and ordering on both, the A and M cation sites, the disorder transitions even of the parent cristobalite (SiO_2) continue to attract high interest. The exact nature of the room temperature (α -type) and high temperature (β -cristobalite) form and the microscopic transition mechanism involved has been a subject of great debate in the last decades [1-22].

The structure of α -cristobalite studied earlier by Barth and Nieuwenkamp [1, 2] was later well established from single crystal X-ray diffraction studies (tetragonal, $P4_32_12$ or its enantiomorph $P4_12_12$; $a = 4.98 \text{ \AA}$, $c = 6.95 \text{ \AA}$) showing that the crystal structure is a distortional derivative of the high temperature polymorph, β -cristobalite [3, 4].

The “ideal” $C9$ type structure (space group $Fd\bar{3}m$) formerly proposed for β -cristobalite by Wyckoff [5] was soon discovered to be physically inconsistent. Barth [6] observed several reflections not allowed by space group $Fd\bar{3}m$, and concluded that the correct space group is $P2_13$. He proposed that the oxygen atoms of the ideal $C9$ structure may either be dynamically disordered and precessing about the [111] direction in an annulus normal to the local Si—O—Si axes. β -cristobalite is now understood to be a time and space averaged structure [7-10].

4. The $AFeO_2$ ($A = K, Rb$ and Cs) family

Table 4.1: An overview of $\alpha \rightarrow \beta$ transformation in the cristobalite family

Chronological view of the ($\alpha \rightarrow \beta$) transformations in Cristobalite in analogy with $AFeO_2$ family	
<p>α-CRISTOBALITE orthorhombic (Pbca) $a\sqrt{8} = b\sqrt{2} = c$</p> <ul style="list-style-type: none"> • Barth (1932b) • Nieuwenkamp (1935) • Dollase (1965) and Peacor (1973).....(tetragonal, $P4_32_12$ or its enantiomorph $P4_12_12$) • $a = 4.98\text{\AA}$ $c = 6.95\text{\AA}$ • Si-O = 1.601—1.608Å • Si-O-Si = 146.8 <div style="border: 1px dashed black; padding: 2px; width: fit-content; margin-left: 20px;"> <p>♦ The crystal str. distorted derivative of high cristobalite</p> </div>	<p>β-CRISTOBALITE cubic, Fd-3m $a = 7.14\text{\AA}$</p> <ul style="list-style-type: none"> • Wyckoff (1925)...High Temp. Powder XRD... C9 type structure.. Si-O-Si (180°) and Si-O = 1.54 Å • Barth (1932a)... $P2_13$.. Si-O-Si ($\neq 180^\circ$) & • Si-O (1.58-1.69 Å) • Nieuwenkamp (1937)... oxygen atoms are displaced from 16(c) position and are randomly placed on circle of radius=0.3-0.55Å with circle plane \perp Si-Si axis • Peacor (1973).... domains are dynamically changing configuration • Wright and leadbetter (1975)... I-42d • O'Keefe and Hyde (1976)... I-42d it's a partially collapsed form of C9 str., thereby reducing the symmetry from Fd-3m to I-42d by tilting of tetrahedron • Hatch and Ghose [1991] recommended that the α-to β-transition is a fluctuation-induced first-order transition and that the β-phase is a dynamic average of α-type domains of $P4_12_12$ symmetry.

It has taken many years to achieve a more realistic structure model for β -cristobalite and to better understand the microscopic phenomena involved [Table 4.1] in the thermally induced reversible displacive structural phase transition ($\alpha \rightarrow \beta$ cristobalite) that can be described via coupled rotations of the MO_4 tetrahedra around mutually orthogonal [110] rotation axes (in such a way that the corner-connected polyhedra remain as close to rigid as possible and/or minimizing the cavities in the tetrahedral framework [11-22]).

Alkali metal oxoferrates(III) are known to form the family of composition $AFeO_2$ with $A = Li$ [23], Na [24], K [25], Rb [26], and Cs [27]. With the exception of $LiFeO_2$ and α - $NaFeO_2$ all of them crystallize in stuffed structure variants of β -cristobalite. They thus belong to the structure family of feldspars that is displaying an intriguing richness of twinning and disorder phenomena [28, 29].

In another study the β (low temperature, $Pn2_1a$) to γ (high temperature $P4_12_12$) phase transformation in $NaFeO_2$ has been studied by Rietveld refinement of neutron powder diffraction, showing cooperative rotation of FeO_4 tetrahedra in the cristobalite related

4. The $AFeO_2$ ($A = K, Rb$ and Cs) family

$FeO_{4/2}$ -framework [30]. Order-disorder phase transitions among different polymorphs of $LiFeO_2$ obtained at different temperature have been systematically studied using X-ray powder diffractometry, neutron diffraction, Moessbauer spectroscopy and transmission electron microscopy [31, 32].

Among the most simple stuffed variants of the cristobalite type of structure are the alkali metallates AMo_2 , where A represents an alkali metal preferably K, Rb or Cs, while M is a trivalent cation, like Al, Ga, Mn, Fe or Co. In these cases the alkali metals enforce a specific tilting pattern of the tetrahedral framework structure, which has been revealed correctly for the first time by E. Vielhaber and R. Hoppe [33, 34]. They found out that $KGaO_2$ and $RbGaO_2$ are pseudo-cubic, with the actual structure being orthorhombic, with $a:b:c \approx 1:2:3$. In correspondence to the similarity between the ionic radii of Fe^{3+} and Ga^{3+} , $KFeO_2$ also has this structure and one would expect $RbFeO_2$ and $CsFeO_2$ to be isostructural, too. For all the representatives known this fully ordered orthorhombic structure is undergoing a structural phase transition to a cubic modification with a dynamically disordered $MO_{4/2}$ -framework.

In this report we address the iron based subset $AFeO_2$ with $KFeO_2$ [35], $RbFeO_2$ [36], and $CsFeO_2$ [37]. In retrospective, the first member of the isostructural series, $KFeO_2$, was erroneously reported to have the filled $C9$ structure with space group $Fd\bar{3}m$ ($CsAlO_2$ structure type) with $a = 7.99 \text{ \AA}$ [38], but was later known to have a lower symmetry ($KGaO_2$ type) structure [33]. Recently the crystal structure of $RbFeO_2$ was investigated on a six domain twin single crystal and was found to be isostructural to $KGaO_2$ [36], while $CsFeO_2$ was reported to crystallize cubic in the $CsAlO_2$ type of structure (Fig. 4.1) [37].

These alkali metal ferrates obviously offer the attractive opportunity for a comparative study of the implications as displayed by stuffed cristobalites. As a common feature, these structures display a three-dimensional network of corner sharing tetrahedra, $FeO_{4/2}$, providing space for including further cations for the sake of charge compensation.

4. The $AFeO_2$ ($A = K, Rb$ and Cs) family

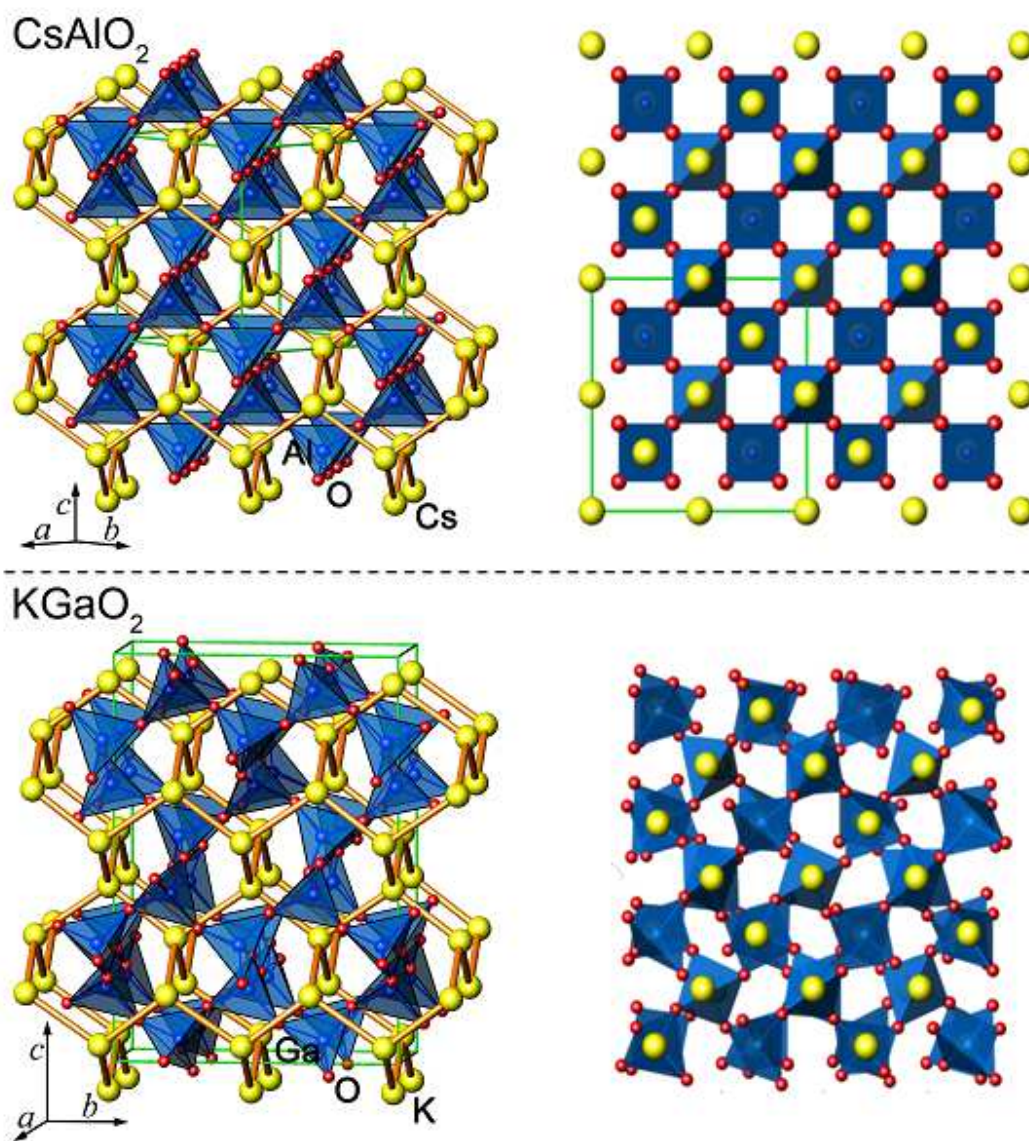


Fig. 4.1. Crystal structure of cubic $CsAlO_2$ (top) and orthorhombic $KGaO_2$ (below), with unit cells drawn in.

4. The $AFeO_2$ ($A = K, Rb$ and Cs) family

All of the three ferrates show static disorder at low temperatures, frozen in by twinning, and a transition to dynamically disordered polymorphs of average cubic symmetry at rising temperature [*c.f.* section 4.3.3].

As the tetrahedral framework can easily undergo collective tilting motions, it is adaptable to accommodate cations of various sizes. This flexibility, however, introduces a complex variety of static and dynamic disorder, and the above mentioned ferrates are particularly well suited for studying the related structural order-disorder transitions in comparison [21].

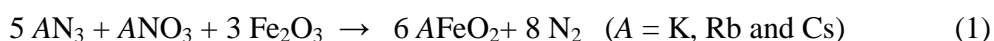
Since the tilting Fe-O-Fe angles and the transition temperatures vary systematically with the size of the alkali ions. So from such structural features one would deduce strong, non-frustrated antiferromagnetic ordering, which, however, is expected to be modulated by the systematic variations in the Fe-O-Fe angles as caused by the counter-cations, and possibly by the librational degrees of freedom. Thus, the title compounds appear to be an appropriate reference system for studying interrelations between structural and magnetic order-disorder transitions.

We have thus investigated the structural changes with temperatures and the structural phase transitions of $KFeO_2$, $RbFeO_2$, $CsFeO_2$ using X-ray single crystal diffraction, synchrotron powder diffraction and differential scanning calorimetry. And simultaneously the effect of systematic variations in the Fe-O-Fe angles as caused by the counter-cations on the magnetic ordering phenomenon is also systematically studied by neutron scattering experiments for the whole family of respective potassium, rubidium and cesium ferrates.

4.2. Experimental

4.2.1 Synthesis

All the samples of the isostructural series $AFeO_2$ ($A = K, Rb, Cs$) were prepared using the “azide nitrate route” [39, 40] from KNO_3 (E. Merck, 99%), $RbNO_3$ (E. Merck, 99%) and $CsNO_3$ (Sigma Aldrich, 99%) respectively, the respective alkali metal azide (AN_3) and active iron oxide (Fe_2O_3) according to equation (1).



The alkali metal azides were synthesized from aqueous HN_3 and alkali metal carbonates [41]. Active iron(III) oxide, Fe_2O_3 , was prepared by heating $FeC_2O_4 \cdot 2H_2O$ in a flow of oxygen at 623 K for 20 h. The phase purity of the precursors was monitored by X-ray powder analysis.

The starting materials were mixed in the ratio required according to the equation (1), ground thoroughly in an agate mortar, pressed into pellets ($\varnothing = 6$ mm) under 10^5 N, dried in vacuum (10^{-3} mbar) at 400 K for 12 h and placed under argon into a tightly closed steel vessel, provided with a silver inlay [40]. In a flow of dry argon the following temperature profile was applied: 298-533 K (100 K h^{-1}); 533-653 K (5 K h^{-1}); 653- T_{max} (20 K h^{-1}) with subsequent annealing for 50 h at $T_{max} = 793$ K for $RbFeO_2$, 833 K for $CsFeO_2$ and 873 K for $KFeO_2$. The reaction vessels were cooled down slowly to 673 K (5 K h^{-1}) and then to room temperature at a rate of 100 K h^{-1} . The powders obtained are very sensitive to humid air and must be handled in an inert atmosphere.

4. The $A\text{FeO}_2$ ($A = \text{K}, \text{Rb}$ and Cs) family

4.2.2 X-ray single crystal diffraction

Single crystals of RbFeO_2 and CsFeO_2 have been grown by post annealing the reaction product at 783K (800 hours) and 773 K (500 hours) respectively. For this purpose, the microcrystalline primary product was pressed into pellets and placed in silver crucibles, closed with a silver stopper. The crucibles were sealed in glass ampoules under dried argon. Single crystals were selected in a dry box under an argon atmosphere ($\text{O}_2, \text{H}_2\text{O} < 0.1 \text{ ppm}$, M. Braun GmbH, Garching, Germany) and mounted in sealed glass capillaries. Diffraction intensities were collected with a SMART APEX I three-cycle diffractometer (Bruker AXS, Karlsruhe, Germany) with $\text{Mo-K}\alpha$ radiation ($\lambda = 0.71073 \text{ \AA}$) at room temperature (298 K). In case of CsFeO_2 because of the feasibility to achieve the transition temperature of 358 K, single crystal X-ray measurements were also performed at 100 K, 298 K, and 400 K, with a 700^{plus} Cryostream cooler [Oxford Cryosystems Ltd., Oxford, UK (80-500 K)]. The collection and reduction of data were carried out with the *Bruker Suite* software package [42]. A detailed analysis of the collected diffraction intensities at room temperature for all the three ferrates under investigation revealed the twinning phenomenon. The full pattern can be interpreted as a superposition of six differently oriented but identical diffraction patterns. The handling for data processing of this reticular pseudo-merohedrally twinned crystal is described in detail somewhere else [43]. An absorption correction was applied using *TWINABS* [44] for the room temperature and low temperature measurements; and *SADABS* [45] for the high temperature measurement, respectively. The room and high-temperature structures were refined by full-matrix least-squares fitting with the *SHELXTL* software package [46], within the space groups $Pbca$ and $Fd\bar{3}m$, whereby the atomic coordinates of KGaO_2 [33, 34] and CsAlO_2 [47] were used as starting models for the room temperature and high temperature modifications, respectively. Experimental details on crystallographic data and data collection of RbFeO_2 single crystal are given in Table 4.2, atomic coordinates and isotropic displacement parameters are given in Table 4.3, whereas selected bond distances (\AA) and angles ($^\circ$) are given in Table 4.4. Similarly, crystallographic data for single crystal of CsFeO_2 at different temperatures alongwith details about atomic coordinates and equivalent isotropic displacement parameters are displayed in Table 4.5 and Table 4.6 respectively.

4. The $AFeO_2$ ($A = K, Rb$ and Cs) family

Table 4.2: Crystallographic data for $RbFeO_2$ at 298 K (single crystal diffraction data).

Crystal data		Refinement			
Chemical formula	$RbFeO_2$	Refinement on	F^2		
M_r	173.32	$R[F^2 > 2\sigma(F^2)], wR(F^2), S$	0.053, 0.126, 1.17		
Cell setting, space group	Orthorhombic, $Pbca$	No. of reflections	14009 reflections		
Temperature (K)	298(2)	No. of parameters	78		
Lattice parameters (\AA)	$a = 5.7568(7)$	Twin volume fraction I	0.1728(6)		
	$b = 11.514(1)$	Twin volume fraction II	0.1970(6)		
	$c = 16.283(2)$	Twin volume fraction III	0.1565(6)		
V (\AA^3)	1079.2(2)	Twin volume fraction IV	0.1472(6)		
Z	16	Twin volume fraction V	0.1966(6)		
D_x (Mg m^{-3})	4.267	Twin volume fraction VI	0.1299(6)		
Radiation type	Mo $K\alpha$	Weighting scheme	Calculated $w = 1/[\sigma^2(F_o^2) + (0.0154P)^2 + 5.2299P]$ where $P = (F_o^2 + 2F_c^2)/3$		
μ (mm^{-1})	23.21	$(\Delta/\sigma)_{\max}$	0.002		
Crystal form, colour	Block, black	$\Delta\rho_{\max}, \Delta\rho_{\min}$ (e \AA^{-3})	1.70, -1.86		
Crystal size (mm)	$0.25 \times 0.20 \times 0.20$	Statistic of the measured reflections.			
Data collection					
Diffractometer	SMART APEX, Bruker AXS				
Data collection method	ω -scans				
Absorption correction	Multi-scan (based on symmetry-related measurements)				
T_{\min}	0.006	Domain I only	6940	785	1/4
T_{\max}	0.011	Domain II only	6960	785	—
No. of measured, independent and observed reflections	89193, 14009, 8087	Domain III only	6972	788	—
Criterion for observed reflections	$I > 2\sigma(I)$	Domain IV only	6948	785	—
θ_{\max} ($^\circ$)	37.3	Domain V only	6955	786	—
		Domain VI only	6954	785	—
		2 domains	30597	3654	3/8
		3 domains	13491	5286	1/4
		6 domains	3376	1328	1/8
		Sum	89193	14982	1

Computer programs: *APEX Suite* (Bruker AXS, 2005); *SHELXL-97* (Sheldrick, 1997); *TWINABS* (Sheldrick, 2007); *ATOMS* (Dowty, 2005).

4. The $AFeO_2$ ($A = K, Rb$ and Cs) family

Table 4.3: Atomic coordinates and equivalent displacement parameters (\AA^2) for $RbFeO_2$. U_{eq} is defined as one third of the trace of the orthogonalized U_{ij} tensor.

Atom	x	y	z	U_{eq}
Rb1	0.75227(7)	0.00989(4)	0.06235(3)	0.02215(8)
Rb2	0.29890(7)	0.25920(3)	0.31403(3)	0.02196(8)
Fe1	0.25374(6)	0.00565(4)	0.18853(4)	0.00900(7)
Fe2	0.78355(8)	0.25956(4)	0.43671(4)	0.01021(8)
O1	0.3035(7)	0.1540(3)	0.1481(2)	0.0320(7)
O2	0.1761(5)	0.1004(2)	0.6065(2)	0.0215(5)
O3	0.0764(4)	0.2144(3)	0.9816(2)	0.0279(7)
O4	0.9464(4)	0.9829(3)	0.2219(2)	0.0229(6)

Table 4.4: Selected bond distances and angles for $RbFeO_2$ (\AA , $^\circ$).

Fe1	— O1	1.853(3)	Rb1	— O1	3.373(4)
	— O2	1.854(3)		— O2	2.973(3)
	— O4	1.851(3)		— O4	2.845(3)
		1.869(3)	Rb2	— O1	2.961(3)
Fe2	— O1	1.843(3)			3.159(4)
	— O2	1.865(3)			3.207(4)
	— O3	1.861(3)		— O2	3.000(3)
		1.862(3)		— O3	3.030(3)
Rb1	— O2	2.865(3)		— O4	2.995(3)
	— O3	2.855(3)			3.321(3)
		3.279(3)			3.345(3)
		3.409(3)			
O1 – Fe1 – O2	108.5(1)		O1 – Fe2 – O3	113.0(2)	
O1 – Fe1 – O4	108.5(2)		O2 – Fe2 – O3	107.4(1)	
	112.3(2)			108.0(1)	
O2 – Fe1 – O4	110.1(1)		O3 – Fe2 – O3	110.2(1)	
	108.9(1)		Fe1 – O1 – Fe2	149.8(2)	
O4 – Fe1 – O4	108.6(1)		Fe1 – O2 – Fe2	140.2(2)	
O1 – Fe2 – O2	108.0(1)		Fe2 – O3 – Fe2	144.7(2)	
O1 – Fe2 – O3	110.1(2)		Fe1 – O4 – Fe1	140.9(2)	

4. The $AFeO_2$ ($A = K, Rb$ and Cs) family

Table 4.5: Crystallographic data for $CsFeO_2$ at different temperatures (obtained from single crystal diffraction data).

Temperature /K	100.0(2)	298.0(2)	400.0(2)
Formula weight	220.76		
Crystal system	orthorhombic	orthorhombic	cubic
Space group, Z	$Pbca$, 16	$Pbca$, 16	$Fd\bar{3}m$, 8
Lattice constants /Å	$a = 5.8876(6)$ $b = 11.855(1)$ $c = 16.733(2)$	$a = 5.9137(6)$ $b = 11.894(1)$ $c = 16.776(2)$	$a = 8.406(1)$
Volume /Å ³	1168.0(2)	1180.0(2)	593.9(1)
Density (calc.) /g·cm ⁻³	5.022	4.971	4.938
Diffractometer	SMART APEX I, Bruker AXS		
Radiation type		Mo- $K\alpha$, 0.7103 Å	
θ range /°	2.43-35.07	2.43-35.12	4.20-34.56
Absorption correction	Multi-scan (based on symmetry related measurements)		
	TWINABS [37]	TWINABS [37]	SADABS [38]
Reflections collected	12681	11953	2102
Independent reflections. R_{int}	—	—	84, 0.037
No. of parameters	79	79	5
$R_1[F^2 > 2\sigma(F^2)]$, $wR(F^2)$	0.094, 0.255	0.120, 0.362	0.154, 0.615
Twin volume fractions	0.175(1), 0.242(1), 0.170(1), 0.175(1), 0.117(1), 0.121(1)	0.180(2), 0.238(2), 0.174(2), 0.176(2), 0.117(2), 0.115(2)	—
Deposition no.	CSD-421171	CSD-421172	CSD-421173

4. The $AFeO_2$ ($A = K, Rb$ and Cs) family

Table 4.6: Atomic coordinates and equivalent isotropic displacement parameters $U_{eq} / \text{\AA}^2$ for $CsFeO_2$ at different temperatures (refined from single crystal diffraction data).

Temperature	Atom	Site	x	y	z	U_{eq}
100 K	Cs1	8c	0.75324(6)	0.00477(4)	0.06221(3)	0.0179(1)
	Cs2	8c	0.2897(1)	0.25518(3)	0.31295(3)	0.0197(1)
	Fe1	8c	0.2502(1)	0.00323(8)	0.18715(6)	0.0070(2)
	Fe2	8c	0.7737(2)	0.25474(7)	0.43551(6)	0.0077(2)
	O1	8c	0.306(1)	0.1414(5)	0.1373(4)	0.027(1)
	O2	8c	0.186(1)	0.1123(5)	0.6143(4)	0.020(1)
	O3	8c	0.0520(9)	0.2229(4)	0.9859(3)	0.0177(9)
	O4	8c	0.9617(8)	0.9899(4)	0.2323(3)	0.0158(8)
298 K	Cs1	8c	0.75287(9)	0.00263(5)	0.06220(4)	0.0295(2)
	Cs2	8c	0.2771(1)	0.25272(5)	0.31305(4)	0.0319(2)
	Fe1	8c	0.2501(1)	0.00234(7)	0.18713(6)	0.093(2)
	Fe2	8c	0.7681(2)	0.25289(8)	0.43569(6)	0.0093(2)
	O1	8c	0.313(2)	0.1383(6)	0.1354(5)	0.047(2)
	O2	8c	0.185(1)	0.1199(6)	0.6207(5)	0.040(2)
	O3	8c	0.0373(9)	0.2257(5)	0.9908(3)	0.024(1)
	O4	8c	0.9723(9)	0.9932(5)	0.2370(4)	0.028(1)
400 K	Cs	8b	3/8	3/8	3/8	0.059(4)
	Fe	8a	1/8	1/8	1/8	0.021(3)
	O	16c	0	0	0	0.071(9)

Table 4.7: Bond angles $Fe-O-Fe / ^\circ$ in the orthorhombic low temperature phases of $AFeO_2$ ($A = K, Rb, Cs$), describing the twisting of the FeO_4 tetrahedra.

Angle	$KFeO_2$ (Sync.) 298 K	$RbFeO_2$ (Sync.) 298 K	$CsFeO_2$ (Sync.) 298 K	$CsFeO_2$ (X-ray) 298 K	$CsFeO_2$ (X-ray) 100 K
Fe1—O1—Fe2	147.8(8)	152.8(1)	160.7(9)	156.3(6)	158.0(4)
Fe1—O2—Fe2	136.3(8)	141.5(1)	155.1(1)	152.2(5)	149.2(3)
Fe2—O3—Fe2	138.7(7)	146.5(1)	153.7(4)	158.5(4)	153.4(3)
Fe1—O4—Fe1	132.8(7)	140.9(1)	155.3(7)	161.6(4)	154.8(3)

4. The $AFeO_2$ ($A = K, Rb$ and Cs) family

4.2.3 High-resolution synchrotron powder diffraction

The synchrotron X-ray powder diffraction experiments were carried out at the powder diffraction station of the Materials Sciences (MS-Powder) beamline at the Swiss Light Source [SLS], with the use of the Microstrip Detector Mythen-II [48]. The diffraction patterns were collected on heating the powder samples enclosed in the Hilgenberg quartz-glass capillaries with a diameter 0.3 mm in the STOE oven, with an X-ray wavelength of 0.497 Å.

The Synchrotron patterns were measured in the range of $T = 298$ -1239 K with steps of 8 K for $KFeO_2$, in the range of $T = 298$ -783 K with steps of 5 K for $RbFeO_2$, whereas data collection for $CsFeO_2$ was done in the range of $T = 298$ -409 K with steps of 1 K. Upon heating the sample partial decomposition of the sample was observed particularly in the case of $KFeO_2$ and $RbFeO_2$ parallel to the evolution of the (high temperature polymorph) crystal structure [49—51]. It is grace to the high resolution of the synchrotron diffraction patterns collected which allowed for the phases identification, and for a multi component Rietveld refinement. The collected data were refined using the program Fullprof [52] based on the Rietveld procedure.

4.2.4 Neutron diffraction experiments.

A total of about 4 g of polycrystalline samples of the respective $AFeO_2$ compounds were prepared in several batches along the “azide nitrate route” [39—41], under argon stream as described in previous section [*c.f.* 4.2.1]. Each batch was checked with X-ray diffraction to confirm its purity as a single phase. The samples were sealed inside cylindrical vanadium containers of 6 mm diameter for neutron studies. The neutron diffraction data were collected at the neutron powder diffractometer HRPT [53] with the neutron wavelength $\lambda = 1.886$ Å, using the closed-cycle refrigerator for the low

4. The $AFeO_2$ ($A = K, Rb$ and Cs) family

temperature (10—300 K) and evacuated radiation-type furnace for the high temperature (up to 1080, 1030 and 1100 K for $A=K, Rb$ and Cs , correspondingly) measurements. All the measurements were carried out on heating the samples from low to high temperatures. We used the advantage of the previously carried out neutron diffraction experiments on exactly the same samples, Used for synchrotron study and though unlike in the synchrotron X-ray diffraction measurements, we did not observe any decomposition of the samples upon heating, probably because of use of vanadium container in the neutron diffraction experiments. The necessity for the use of both synchrotron X-ray and neutron diffraction was two-fold. On the one hand, we needed the high resolution of the synchrotron data in order to precisely monitor the structural parameters in the proximity of the phase transitions, where the splitting of diffraction lines due to the orthorhombic distortions is becoming really tiny. On the other hand, we intended to tackle the correlations between the magnetic ordering and the crystal structure in the title compounds, in particular the details of the oxygen site disorder at the structural transition points, thus the use of neutron diffraction for simultaneous crystal and magnetic structure study became indispensable.

The symmetry analysis of the possible magnetic structures has been carried out with the program SARAh-2k [54], and the refinements of the parameters of both the crystal and magnetic structure parameters were done with the Fullprof suite of programs [52] with the use of its internal scattering lengths and magnetic scattering form-factors for the Fe^{3+} ion.

4. The $AFeO_2$ ($A = K, Rb$ and Cs) family

4.2.5 Thermal analysis and magnetic susceptibility measurement

The differential scanning calorimetry (DSC) measurements were carried out with a DSC device (DSC 404 C, Netzsch GmbH, Selb, Germany) using a NiCr / NiCu thermocouple (Type E) operating in a heat flow mode. The samples were heated at a rate of 5 K min^{-1} in a corundum crucible under dry argon. Whereas for precise temperature dependence of the specific heat measurement of a polycrystalline sample of $AFeO_2$ a Perkin Elmer (*Pyris 1*) instrument operating in a power compensation mode, was employed with inert atmosphere of He gas (He 4.6, purity 99,996 vol. %). Background contributions were subtracted using external sapphire calibrations to give specific heat as a function of temperature.

The magnetic susceptibility $\chi(T)$ of polycrystalline single phase powder samples of $RbFeO_2$ and $CsFeO_2$ have been measured in the temperature range from 2 K to 800 K in magnetic fields up to 7 T using a SQUID-Magnetometer (MPMS 5.5, Quantum Design). For measurements above 350 K the sample was contained in warily dried SUPRASIL ampoule ($\varnothing = 3 \text{ mm}$) that was long enough to extend over the coils of the magnetometer inside the oven. Later the data is further corrected for core electron diamagnetic contribution to get the original spin susceptibility χ_{spin} [55].

4.2.6 Mössbauer Spectroscopy on $RbFeO_2$ and $CsFeO_2$

The samples with the chemical composition $RbFeO_2$ and $CsFeO_2$ have been investigated by Mössbauer spectroscopy at room temperature and high temperature. The Mössbauer spectrum was folded to 510 channels, fitted with the *Recoil* program (Lagarec K, Rancourt DG 1998, Recoil-Mössbauer spectral analysis software for windows version

4. The $A\text{FeO}_2$ ($A = \text{K}, \text{Rb}$ and Cs) family

1.02, Department of Physics, University of Ottawa, Ottawa, ON.) with Lorentzian lines, and decomposed into subspectra with parameters of the following meaning: isomer-shift (IS) relative to $\alpha\text{-Fe}$ (mm/s), half width Γ of the lines with Lorentzian shape (mm/s), quadrupole splitting QS (mm/s), internal magnetic field H (T), and area A (%) of the different subspectra. The convergence of the iteration and the χ^2 -value of the final fit served as an indication of the quality of the refinement.

The Mössbauer spectroscopic measurements were made in the velocity range of -10/10 mm/s because the peaks of the magnetic subspectra are located in this velocity range. The measuring time was very long for each measurement sometimes lasted upto 37 days because of the low intensity of the peaks caused by the low iron content in the sample.

4.3. Results and discussion

4.3.1. Single crystal X-ray diffraction

The diffraction intensities of the investigated crystals of RbFeO_2 and CsFeO_2 were collected, integrated and indexed, firstly (to a first approximation) on the basis of the cubic crystal system with $a_{\text{cubic}} = [16.283(2) \text{ \AA}, (R_{\text{int}} = 0.097)]$ for RbFeO_2 and $a_{\text{cubic}} = 16.784(2) \text{ \AA}$ at 298 K and $16.7123(2)$ at 100 K, for CsFeO_2 crystal respectively. This is an eightfold unit cell with doubled a axis compared with e.g. β -cristobalite type or CsFeO_2 [27]. The displacement parameters were found to be much too high, and no O-atoms could be localized in the difference-Fourier map.

4. The $AFeO_2$ ($A = K, Rb$ and Cs) family

No peak-splitting is observed with $MoK\alpha$ radiation; Figure 4.2 shows the zeroth and 1st layer of the reciprocal space of the $RbFeO_2$ crystal under investigation, constructed pixel by pixel from the original CCD-frames using the *Precession* module of

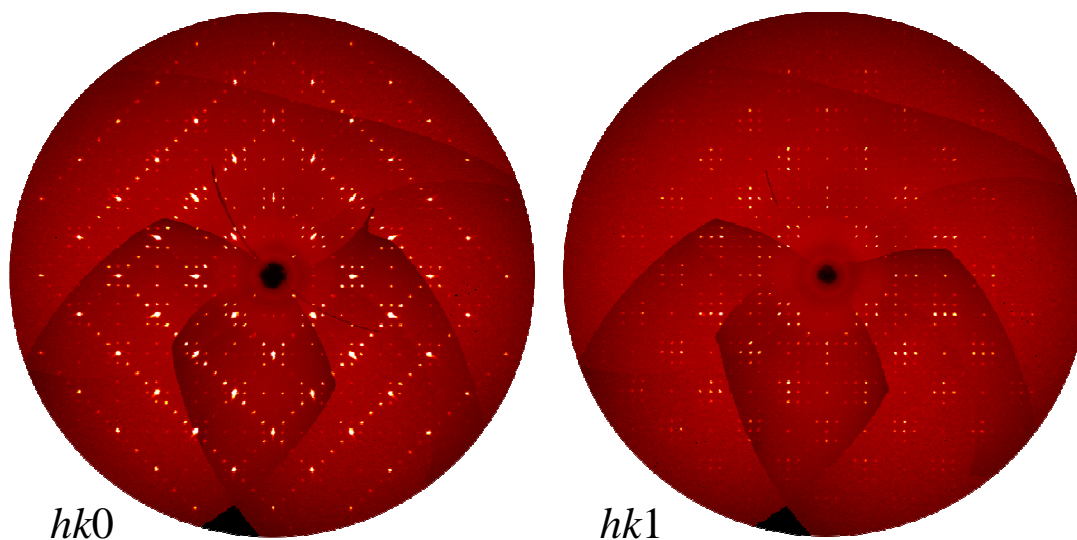


Fig. 4.2. Reciprocal layers $hk0$ and $hk1$ (refer to twin domain I) constructed pixel by pixel from the original CCD-frames. [RbFeO₂Cubic $P: m3m$ $a = 16.283(2)$ Å..... $R_{int} = 0.097$]

the *Bruker Suite* software package (Bruker AXS, 2005). For this procedure only the orientation matrix is taken into account, which allows a detailed exploration of the reciprocal space, independently from the lattice constants. The observed extinction rules $h00: h = 2n$; $0k0: k = 2n$; $00l: l = 2n$ leads to the space groups $P2_13$ (no. 198) and $P4_232$ (no. 208). Only in $P2_13$ the heavy atoms could be located, forming a 3D network of two interpenetrating diamond-like structures, consisting of respective alkali atom and iron, exclusively. By far too high thermal parameters were obtained during the structure refinement. The second crystal of $RbFeO_2$ under investigation with $R_{int} \approx 0.35$ for the cubic symmetry revealed that both crystals showed a special kind of twinning with different volume fractions of the twin individuals.

4. The $AFeO_2$ ($A = K, Rb$ and Cs) family

The structure of $KGaO_2$ [33, 34] is known to be an ordered variant of the $CsAlO_2$ type.

The latter one represents a stuffed undistorted β -cristobalite type ($a = 8.098 \text{ \AA}$, $Fd\bar{3}m$).

The structure of $KGaO_2$ is orthorhombic with the space group $Pbca$. The unit cell contains 16 formula units with lattice constants related to the $CsAlO_2$ type of structure according to equations (2).

$$a \approx a(CsAlO_2)/\sqrt{2}, b \approx a(CsAlO_2)\sqrt{2}, c \approx 2a(CsAlO_2) \quad (2)$$

Table 4.8: The twinning matrices to transform the orthorhombic unit cells.

(a)		(b)	
$\begin{pmatrix} 1/2 & 1 & 0 \\ -1/2 & 1 & 0 \\ 0 & 0 & 2 \end{pmatrix}$	$\begin{pmatrix} 1/2 & 1 & 0 \\ 1/2 & -1 & 0 \\ 0 & 0 & -2 \end{pmatrix}$	$\begin{pmatrix} 1 & 0 & 0 \\ 0 & 1 & 0 \\ 0 & 0 & 1 \end{pmatrix}$	$\begin{pmatrix} 0 & 2 & 0 \\ 1/2 & 0 & 0 \\ 0 & 0 & -1 \end{pmatrix}$
$\begin{pmatrix} 0 & 0 & 2 \\ 1/2 & 1 & 0 \\ -1/2 & 1 & 0 \end{pmatrix}$	$\begin{pmatrix} 0 & 0 & -2 \\ 1/2 & 1 & 0 \\ 1/2 & -1 & 0 \end{pmatrix}$	$\begin{pmatrix} 1/2 & -1 & 2 \\ -1/4 & 1/2 & 1 \\ -1/4 & -1/2 & 0 \end{pmatrix}$	$\begin{pmatrix} 1/2 & -1 & -2 \\ -1/4 & 1/2 & -1 \\ 1/4 & 1/2 & 0 \end{pmatrix}$
$\begin{pmatrix} 1/2 & 1 & 0 \\ 0 & 0 & 2 \\ -1/2 & 1 & 0 \end{pmatrix}$	$\begin{pmatrix} 1/2 & 1 & 0 \\ 0 & 0 & -2 \\ 1/2 & -1 & 0 \end{pmatrix}$	$\begin{pmatrix} 1/2 & 1 & -2 \\ 1/4 & 1/2 & 1 \\ 1/4 & -1/2 & 0 \end{pmatrix}$	$\begin{pmatrix} 1/2 & 1 & 2 \\ 1/4 & 1/2 & -1 \\ -1/4 & 1/2 & 0 \end{pmatrix}$

Starting from cubic lattice of $CsAlO_2$ there are six possible orientations (six transformation matrices) which can be chosen for the orthorhombic system [Table 4.8 (a)]. These matrices were used to create a multi-component hkl -file from the raw data set of the $RbFeO_2$ and $CsFeO_2$ crystals during the integration procedure with the *Bruker Suite* software package (Bruker AXS, 2005), which can be used with the HKLF5 option in

4. The $AFeO_2$ ($A = K, Rb$ and Cs) family

SHELXL (Sheldrick, 1997). The twinning matrices to transform the orthorhombic unit cells into each other are displayed in [Table 4.8 (b)].

The reflection intensities were corrected for absorption and analyzed with the program *TWINABS* (Sheldrick, 2007). The analysis of reflection for the case of $RbFeO_2$ indicates that from all reflections (I_{all}) of e.g. domain I, $I_{all}/4$ belong to this domain exclusively, $3I_{all}/8$ belong to two domains, $I_{all}/4$ belong to three domains and $I_{all}/8$ belong to all six domains. This confirms that the special relations of the lattice constants bring out a reticular pseudo-merohedral twin: only a partial number (*reticular*) of the reflections are overlapping completely in three dimensions (*merohedral*), there are either completely overlapping or non-overlapping reflections, there are no partial-overlapping ones by coincidence, like it is observed for e.g. dovetail twins. The twin lattice is *pseudo-cubic* because of the approximate equations $a\sqrt{8} = b\sqrt{2} = c$, and the twin lattice index is $[j] = V_{cubic}/V_{ortho} = 4$ ($V_{cubic} = 4137.2(2) \text{ \AA}^3$) [56].

Figure 4.3 shows the 1st reciprocal layer of $RbFeO_2$ twinned crystal with the reflections of each domain highlighted. It is shown that all visible intensities are indexed by at least one of the six twinning domains, and the 'empty' reciprocal space is left unindexed.

4. The $AFeO_2$ ($A = K, Rb$ and Cs) family

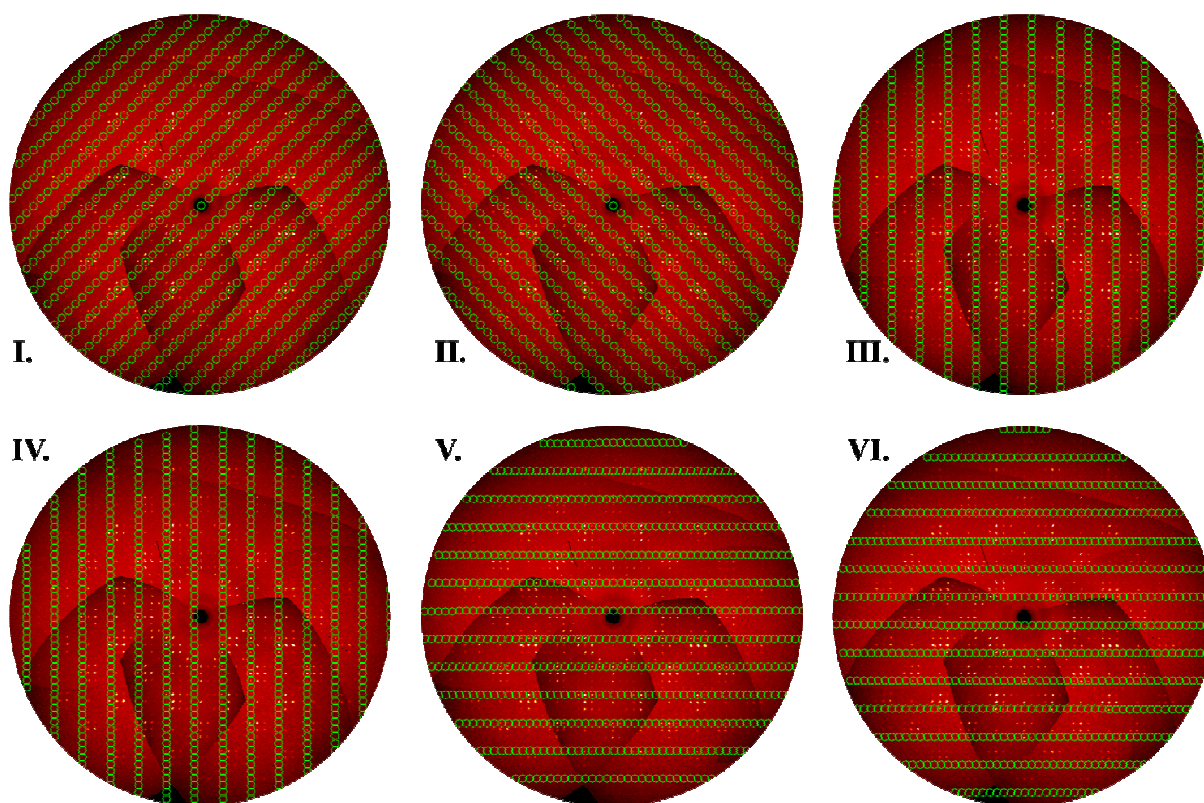


Fig. 4.3. Reciprocal layer $hk1$ (refer to twin domain I) of $RbFeO_2$ crystal. The reflections of the corresponding domains are emphasized by circles: $h k 1$ for domain I and II, $h -2h+1 l$ for domain III, $h 2h-1 l$ for domain IV, $h 2h+1 l$ for domain V and $h -2h-1 l$ for domain VI. The directions of the reciprocal axes of each domain are drawn in.

The intensities, belonging to one domain only, are not affected by the twinning and they have been used for structure solution. This solution yielded the positions of the heavy atoms Rb and Fe. With the complete data set, including all six domains, it was possible to locate the oxygen atoms via difference Fourier synthesis. All atoms were refined anisotropically, and the resulting twin volume fractions showed reasonable values in the order of magnitude of 1/6 for all six domains (see Table 4.2).

4. The $AFeO_2$ ($A = K, Rb$ and Cs) family

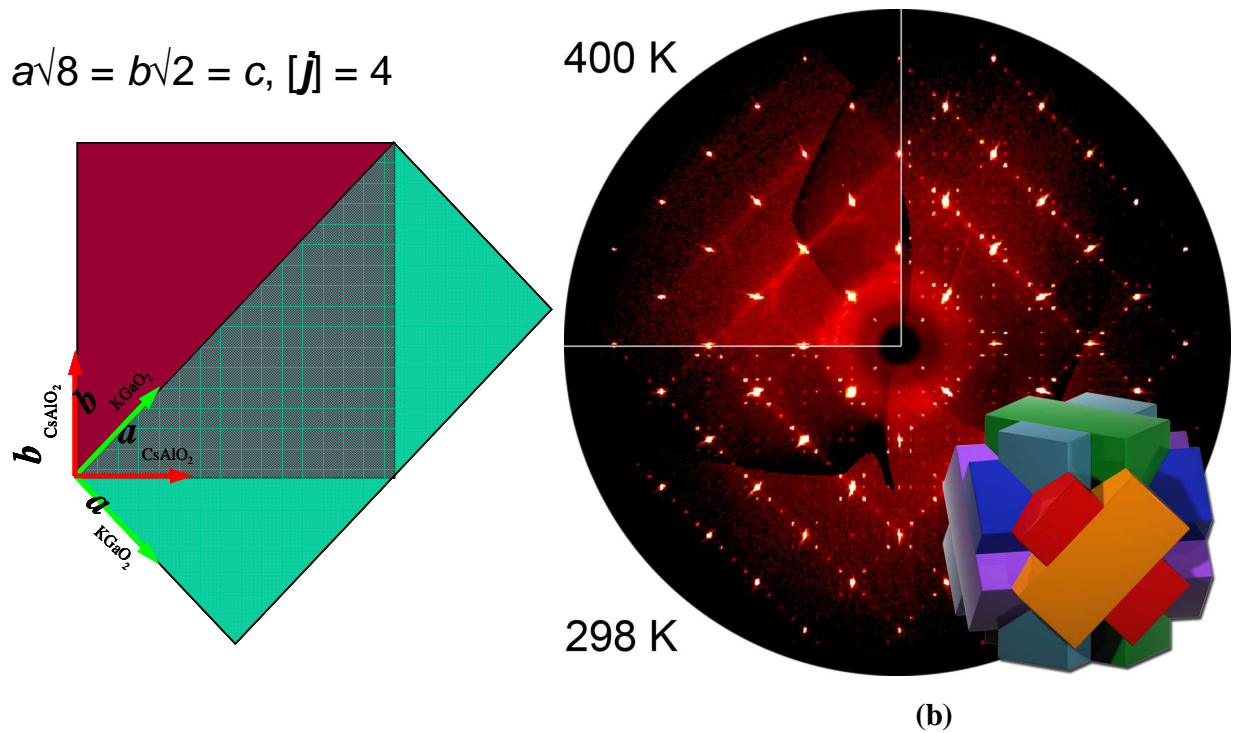


Fig. 4.4. a) The interrelation of lattice constants between the orthorhombic ($KGaO_2$) an ordered variant of the $CsAlO_2$ type (a_{cubic}). “[$a \approx a(CsAlO_2)/\sqrt{2}$, $b \approx a(CsAlO_2)\sqrt{2}$, $c \approx 2a(CsAlO_2)$]” b) Reciprocal layer $hk0$ for the orthorhombic room temperature phase, with pseudo cubic symmetry due to twinning, and the cubic high temperature phase of $CsFeO_2$. The polyhedron represents the six different orientations (six colors) of the six domains. Without paying attention to the colors, the polyhedron has the cubic symmetry $m\bar{3}m$, which also corresponds to the Laue group observed in the diffraction pattern.

In case of $CsFeO_2$ ‘single crystal’ because of the feasibility to achieve the transition temperature of 358 K, single crystal X-ray measurements were performed at 100 K, 298 K, and 400 K. The measurements confirm the occurrence of phase transition as depicted initially in DSC investigations. The disappearance of some of the intensity peaks at 400 K is clearly visible (Figure 4.4(b)). It has turned out, however, that like for $RbFeO_2$, in $CsFeO_2$ also the apparent cubic symmetry is an artifact caused by superposition of six,

4. The $AFeO_2$ ($A = K, Rb$ and Cs) family

differently oriented domains, resulting in a reticular pseudo-merohedrally twinned crystal. The orientations of the six domains are represented by the polyhedron shown in inset of Figure 4.4 (b), where each domain is shown in a different color. The twinning phenomenon is a result of the phase transition and thus a result of the synthesis procedure at high temperatures and the subsequent cooling to room temperature (transformation twin).

In Figure 4.5 (b), fragments of the crystal structures are shown on the example of $RbFeO_2$, with the illustration of the strongly anisotropic character of the atomic thermal vibrations of the oxygen atoms at high temperatures (Figure 4.5 (b), top).

4. The $A\text{FeO}_2$ ($A = \text{K}, \text{Rb}$ and Cs) family

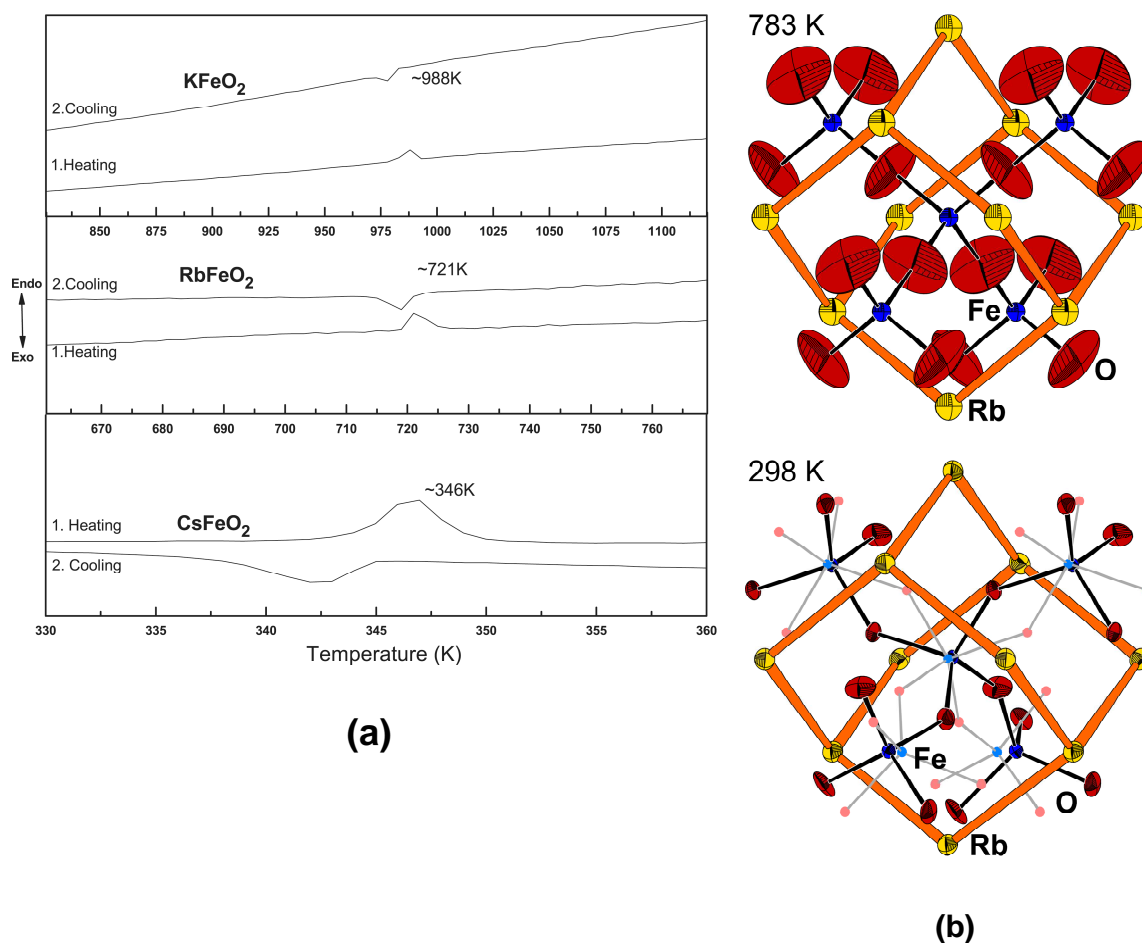


Fig. 4.5. a) Phase transitions detected by differential scanning calorimetry (DSC). b) Fragment of RbFeO_2 Structure with thermal motion of oxygen at high temperature.

These observations allow for tentative approach to rationalize the mechanism of phase transition. In fact, one may even think of the phase transition mechanism in such a way that as soon as with raising the temperature, increase in the atomic displacement parameters become large enough, the oxygen atoms “jump” from a given position with a well-defined Fe—O—Fe bond angle into a symmetrically related state illustrated in Figure 4.5 (b) (top) where these angles are of course also preserved. In time-average, all these equally possible orientations are observed in form of an apparently 180° Fe—O—Fe angle with unphysically-short Fe—O bond lengths and strongly anisotropic

4. The $AFeO_2$ ($A = K, Rb$ and Cs) family

displacement parameters for the oxygen atoms. Reversely the bending angles lock in, when lowering the temperature, and due to the symmetry relations (Figure 4.6), which is the origin of the observed twinning phenomenon; there are six possibilities of how this ordering can take place. Figure 4.5 shows, on the example of $RbFeO_2$, two of the six possible mutual orientations of the ${}^3_{\infty}[FeO_{4/2}]^-$ framework, with the displacement ellipsoids drawn for one of them, indicating a well ordered structure, but a twinned crystal.

The group-subgroup relation [57, 58] between the aristotype $CsAlO_2$ and $KGaO_2$ include two consecutive steps of symmetry reduction of type *translationengleich* ($t3$ and $t2$, Figure 4.6), which can be associated to multiple twinning in terms of 'twins by twins', and resulting in six (3×2) twinning fractions as observed. Figure 4.6 shows the

4. The $AFeO_2$ ($A = K, Rb$ and Cs) family

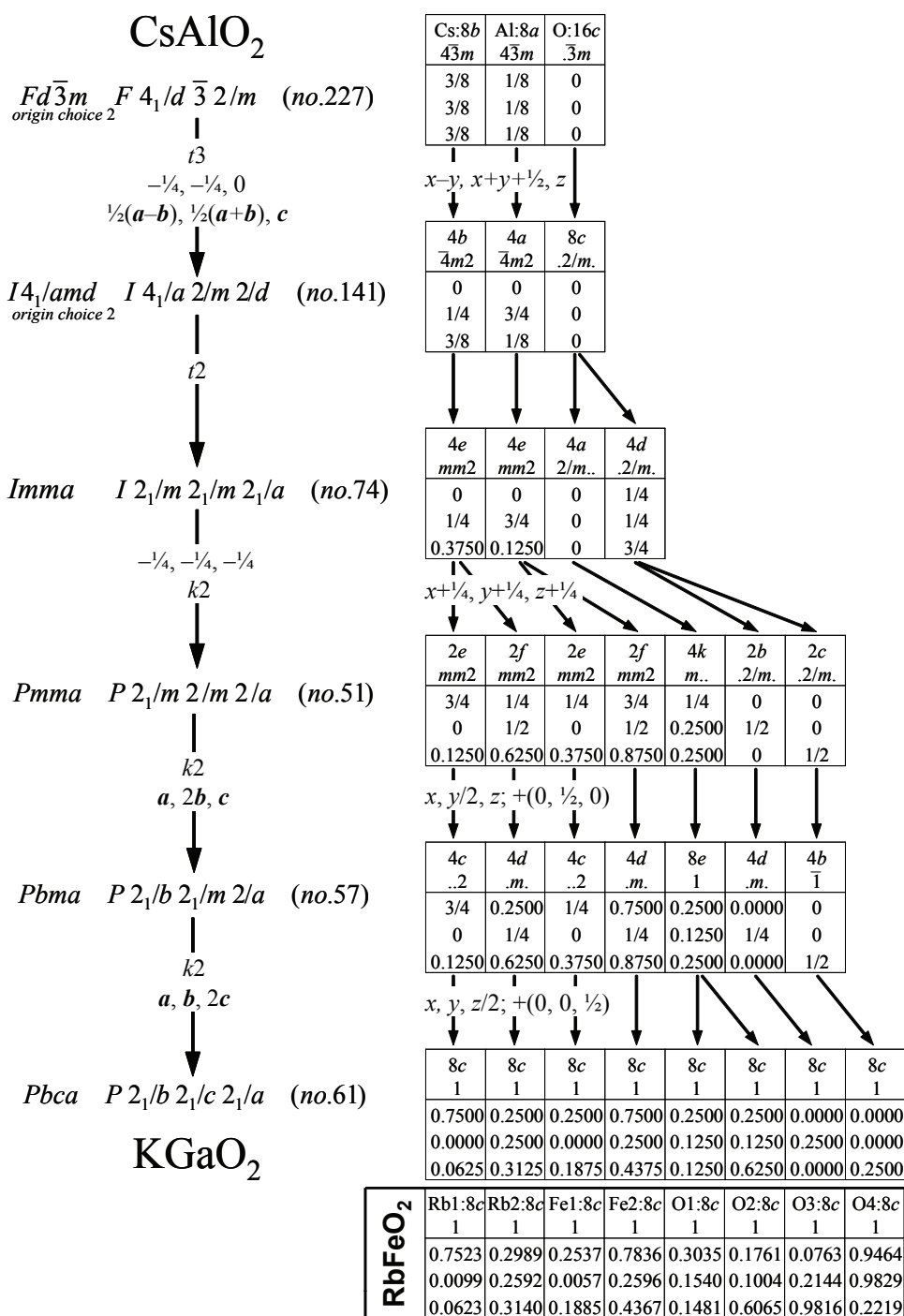


Fig. 4.6. Group-subgroup relation between CsAlO₂ and KGaO₂, including the coordinates of RbFeO₂ and how they arise from those of the aristotype, CsAlO₂. Given boxes contain: element, Wyckoff symbol, site symmetry, atomic coordinates x, y, z .

4. The $AFeO_2$ ($A = K, Rb$ and Cs) family

group-subgroup relation (*Bärnighausen-Stammbaum* [59]), including the possible site transformations. This structural feature is probably the reason for the twinning of the crystals under investigation.

In principle the ${}^3_{\infty}[FeO_{4/2}]^-$ framework in the investigated crystal of $RbFeO_2$ and $CsFeO_2$ corresponds to ${}^3_{\infty}[SiO_{4/2}]$ in β -cristobalite. The O—Fe—O bond angles in case of $RbFeO_2$ examined crystal ranges from $(108.0(1)^\circ \leq \angle O—Fe—O \leq 113.0(2)^\circ)$, indicating slightly distorted tetrahedra (Table 4.4). The bending angles on the oxygen atoms are $140.2(2)^\circ \leq \angle Fe—O—Fe \leq 149.8(2)^\circ$, and they differ distinctly from the ideal value (180°) reported for β -cristobalite. Whereas in case of $CsFeO_2$ investigated single crystal (at 298 K) the bending angle on oxygen atoms (O—Fe—O bond angles) varied from $152.2(5)^\circ$ to $161.6(4)^\circ$ whereby the Fe-O-Fe connections are much more “straight” than in $RbFeO_2$ and in $KFeO_2$, well in conformity with the bigger size of cesium atom. (Table 4.7) Whereas on heating the ‘single crystal’ of $CsFeO_2$ at around 400K reveals the disappearance to tiny reflections corresponding to orthorhombic distortion, confirming the structural phase transition from $KGaO_2$ type of structure to the $CsAlO_2$ structure, with the bending angle Fe—O—Fe of actually 157° to seemingly approach 180° , due to librational disorder. The Figure 4.4 (b) gives a lucid view of structural phase transition as observed in reticular pseudo-merohedral twinned crystal of $CsFeO_2$ seen via single crystal X-ray diffractometry. A comparison between the atomic coordinates of $RbFeO_2$ and $CsFeO_2$ (refined from single crystal X-ray diffractometry) and the idealized values indicate that the major structural changes, in comparison to the $CsAlO_2$ structure, is caused by a shift of the oxygen atoms, and to a lesser extent on heavy alkali atom and

4. The $AFeO_2$ ($A = K, Rb$ and Cs) family

iron respectively [60]. The relatively large displacement parameters determined for the oxygen atoms, at room temperature [27] support the statement.

The twinning consequently is infact a result of the synthesis procedure at high temperatures and subsequent cooling to room temperature (transformation twin). A comparable twinning phenomenon is also observed for the structurally related high/low phase transition of cristobalite (SiO_2). Below 500 K the cubic high-temperature modification (β -cristobalite) transforms into the tetragonal low-temperature modification (α -cristobalite) with three or six different twin domains present [3, 4]. The twinning phenomena reported here also is related to the so-called *Albite twinning* [61] in the sodium feldspar ($NaAlSi_3O_8$) caused by a displacive phase transition (collapse of the framework when the cation in the cavity site is too small) from high Albite (monoclinic) into low Albite (triclinic). This is in contrast to the *Pericline twinning* in K-bearing alkali feldspar caused by an order-disorder phase transition at the Al/Si site [62].

4.3.2. Thermal analysis and magnetic susceptibility characterization

The thermodynamics of the high temperature phase transition was investigated using DSC and the specific heat measurement on polycrystalline sample of $KFeO_2$, $RbFeO_2$ and $CsFeO_2$, showing transitions to occur at ~ 988 K in case of $KFeO_2$, ~ 721 K for $RbFeO_2$, and ~ 346 K for $CsFeO_2$, respectively. For each measurement, values of the transition enthalpy ($\Delta H_{\text{transition}}$) were determined from integrated peak areas, and the onset temperature (T_{onset}) from the intersection of tangent with an interpolated baseline (*c.f* Table 4.9).

4. The $AFeO_2$ ($A = K, Rb$ and Cs) family

Table 4.9: $\Delta H_{\text{transition}}$ and T_{onset} values obtained via specific heat measurement of polycrystalline sample of $AFeO_2$ samples ($A=K, Rb$ and Cs)

Sample ID	$\Delta H_{\text{transition}} / \text{KJ/mol}$	$T_{\text{onset}} / ^\circ \text{C}$	Peak / $^\circ \text{C}$
KFeO₂	0.11	$X_1 = 696.67$	a) = 703
	—	$X_2 = 704.12$	b) = 727*
RbFeO₂	0.41	$X_1 = 437.41$	c) = 439
CsFeO₂	0.27	$X_1 = 66.95$	d) = 71
	—	$X_2 = 72.42$	e) = 74

As is evident from table above in case of $KFeO_2$ the peak at 703°C and at 727°C (*extrapolated value) can be assigned explicitly to structural and magnetic ordering / transition respectively. Whereas due to limitation to measure the sample above 730°C in Perkin Elmer machine [*Pyris-1*] we could not observe any kink in commensurate to the magnetic ordering temperature in $RbFeO_2$ and $CsFeO_2$ respectively. However as displayed in Fig. 4.7, the peaks (c, e) at 439°C (712 K) and 74°C (347K) depicts the onset of structural phase transition temperature in rubidium and cesium oxoferrates respectively. However, the small shoulder in case of $CsFeO_2$ at 71°C , is still mysterious and similar behaviour is observed in case of high temperature neutron scattering experiments, where the data is fitted only for $T > 350\text{ K}$ (*c.f* section-4.3.4.1) and in case of temperature dependent magnetic susceptibility measurement, the structural phase transition at $\sim 350\text{ K}$ manifests itself by a peculiarity at this temperature (Fig. 4.8). Which is a subject of further investigation?

4. The $AFeO_2$ ($A = K, Rb$ and Cs) family

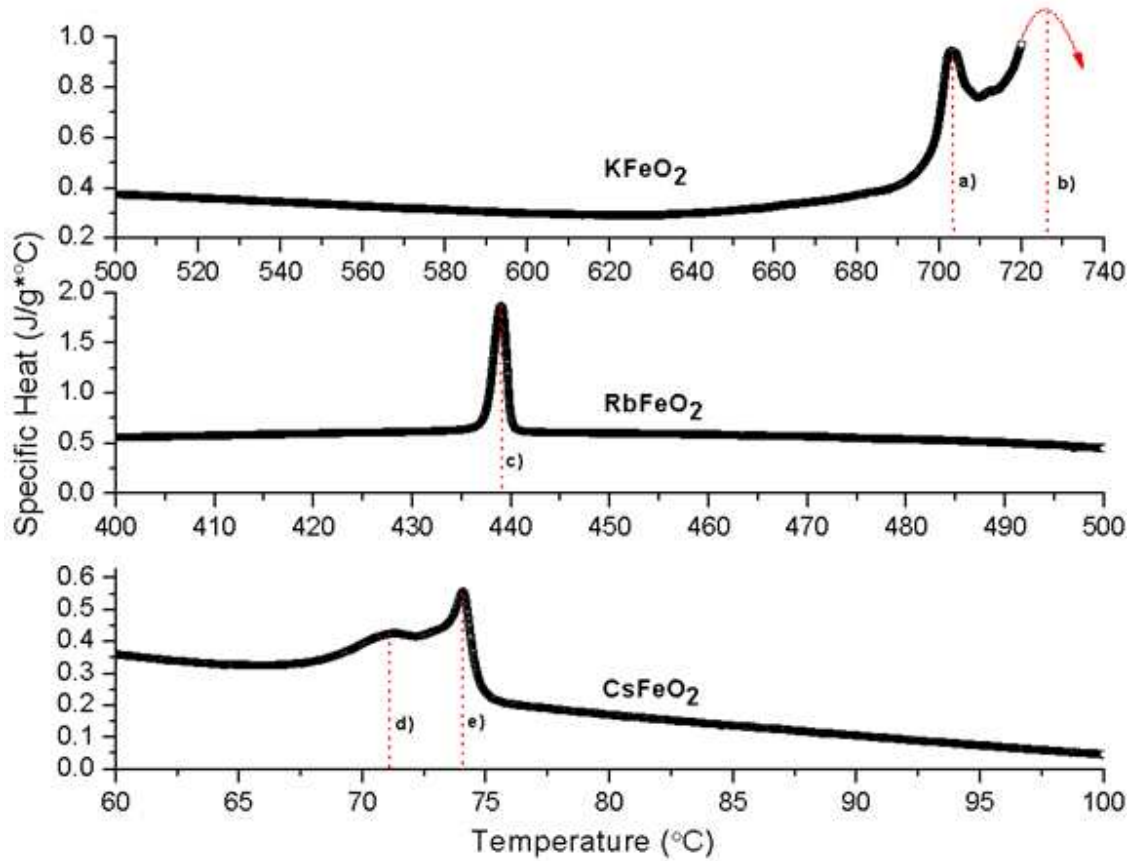


Fig. 4.7. Plot of Specific heat (C_p) versus temperature for $AFeO_2$ polycrystalline samples. The red dashed line a), b), c), d) and e) depicts the peak evolution in respective alkali oxoferrates

The plot of inverse magnetic susceptibility as a function of temperature displayed in Fig. 4.8 for $RbFeO_2$ and $CsFeO_2$ shows the kink at almost exactly their respective structural phase transition temperature. Due to lack of facility to carry out magnetic susceptibility measurement at temperature above 800 K in house (at MPI-FKF), we proceeded to neutron facility at PSI Switzerland and successfully managed not only to see the respective magnetic ordering temperature in all the respective alkali oxoferrates

4. The $A\text{FeO}_2$ ($A = \text{K}, \text{Rb}$ and Cs) family

[*c.f.* section 4.3.4.], but also the respective structural phase transition both by neutron and synchrotron radiations [*c.f.* section 4.3.3]

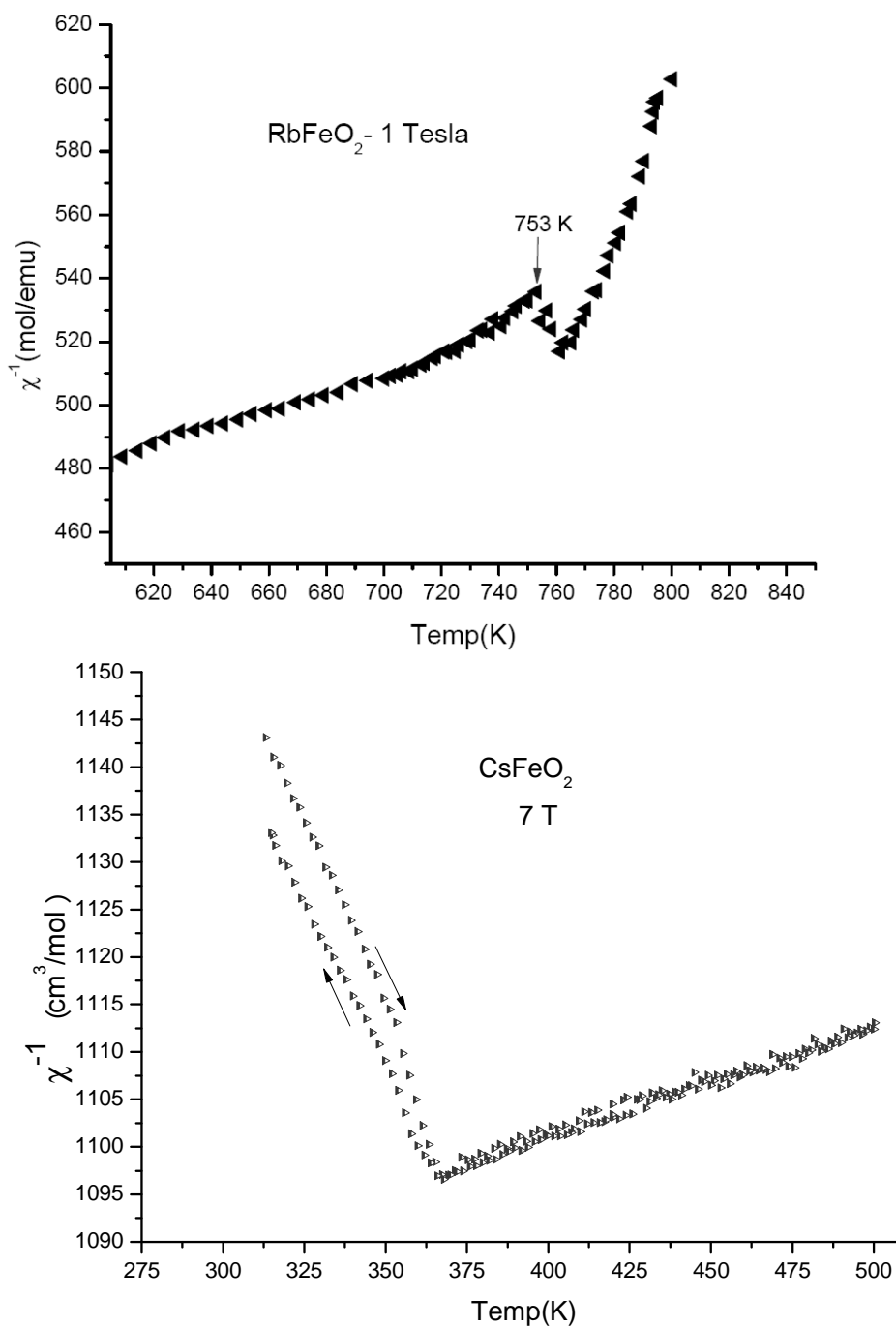


Fig. 4.8. Plot of inverse of magnetic susceptibility ($\chi + \chi_0$ uncorrected) vs temperature for RbFeO_2 and CsFeO_2 depicting an anomaly at around 753 K and 360 K respectively.

4. The $A\text{FeO}_2$ ($A = \text{K}, \text{Rb}$ and Cs) family

4.3.3. High-resolution synchrotron powder diffraction.

In agreement with the previously available results [25], the KFeO_2 crystal structure at room temperature has been found to possess the orthorhombic unit cell with lattice constants $a = 5.600 \text{ \AA}$, $b = 11.26 \text{ \AA}$, $c = 15.94 \text{ \AA}$ (thus $a \approx \frac{1}{2}b \approx c/\sqrt{8}$), and the space symmetry $Pbca$. We find that at room temperature both RbFeO_2 and CsFeO_2 are isostructural to KFeO_2 . The fundamental feature of the structure is a three dimensional network of corner-sharing $[\text{FeO}_{4/2}]^-$ tetrahedra, with alkali atoms occupying its interstices, forming a 3D network of two interpenetrating diamond-like structures (NaTl structure type) build up by respective alkali atom and iron, exclusively.

4. The $A\text{FeO}_2$ ($A = \text{K}, \text{Rb}$ and Cs) family

The crystal structure parameters of all three compounds have been refined for all temperatures by the Rietveld method using the data of the single crystal structure refinements as starting parameters. The Rietveld fit of synchrotron powder diffraction data of both the low temperature and high temperature modifications of the respective sample is shown in Figure 4.9 and 4.10, 4.11 respectively. Experimental details, crystallographic data, and atomic coordinates (refined from powder synchrotron data) at different temperatures for $A\text{FeO}_2$ ($A = \text{K}, \text{Rb}, \text{Cs}$) are given in Table 4.10 and Table 4.11 respectively. The atomic parameters as determined by Rietveld refinement were in good agreement to those found for the single crystals.

Table 4.10: Crystallographic data for $A\text{FeO}_2$ ($A = \text{K}, \text{Rb}, \text{Cs}$) at different temperatures (obtained from powder synchrotron data).

Compound	KFeO_2		RbFeO_2		CsFeO_2	
Temperature /K	303	1015	303	783	303	400
Formula weight	126.94		173.32		220.76	
Crystal system	orthorhombic	cubic	orthorhombic	cubic	orthorhombic	cubic
Space group, Z	$Pbca$, 16	$Fd\bar{3}m$, 8	$Pbca$, 16	$Fd\bar{3}m$, 8	$Pbca$, 16	$Fd\bar{3}m$, 8
Lattice constants /Å	$a=5.59483(1)$ $b=11.24908(3)$ $c=15.93549(4)$	$a=8.07754(2)$	$a=5.71547(1)$ $b=11.50563(4)$ $c=16.34578(5)$	$a=8.227186(6)$	$a=5.915303(8)$ $b=11.88481(2)$ $c=16.77518(2)$	$a=8.411704(3)$
Volume /Å ³	1002.926(4)	527.032(2)	1074.899(6)	556.870(1)	1179.333(3)	595.185(1)
ρ (calc.) /g·cm ⁻³	3.362	3.200	4.283	4.133	4.972	4.926
Diffractometer	Powder diffraction station of the Materials Science Beamline at the SLS, equipped with the microstrip detector.					
Radiation type	Synchrotron, 0.497015 Å					
θ range /°	<u>3.0</u> – <u>54.0</u>	<u>3.0</u> – <u>37.0</u>	<u>3.0</u> – <u>37.3</u>	<u>3.0</u> – <u>37.3</u>	<u>3.0</u> – <u>53.38</u>	<u>3.0</u> – <u>53.38</u>
Data points	13567	9051	9131	9131	13411	13411
No. of reflections	3195	41	1203	45	3646	114
No. of parameters	75	79	65	43	74	48
R_p, R_{wp}, χ^2	2.927, 3.853, 1.12	3.263, 4.720, 1.75	2.04, 2.65, 1.84	2.03, 2.66, 1.74	2.63, 3.34, 1.31	2.743, 3.50, 1.46
Deposition no.	CSD- 421185	CSD-421186	CSD-421187	CSD-421188	CSD-421189	CSD-421190

4. The $AFeO_2$ ($A = K, Rb$ and Cs) family

Table 4.11: Atomic coordinates and equivalent isotropic displacement parameters $U_{eq}/\text{\AA}^2$ for $AFeO_2$ ($A = K, Rb, Cs$) at different temperatures (refined from powder synchrotron data).

Compound, T	Atom	Site	x	y	z	U_{eq}
KFeO ₂ , 298 K	K1	8c	0.754(1)	0.0104(5)	0.0652(5)	0.0141(7)
	K2	8c	0.3041(7)	0.2611(5)	0.3157(5)	$U(K1)$
	Fe1	8c	0.2527(7)	0.0100(4)	0.1897(4)	0.0179(7)
	Fe2	8c	0.7858(6)	0.2644(3)	0.4368(4)	$U(Fe1)$
	O1	8c	0.298(2)	0.1578(12)	0.1529(7)	0.011(1)
	O2	8c	0.173(2)	0.0943(13)	0.6018(8)	$U(O1)$
	O3	8c	0.082(2)	0.2042(12)	0.9809(7)	$U(O1)$
	O4	8c	0.937(2)	0.9811(12)	0.2152(8)	$U(O1)$
KFeO ₂ , 1015 K	K	8b	3/8	3/8	3/8	0.101(1)
	Fe	8a	1/8	1/8	1/8	0.0432(5)
	O	16c	0	0	0	0.231(3)
RbFeO ₂ , 298 K	Rb1	8c	0.754(2)	0.0095(4)	0.0621(5)	0.0245(9)
	Rb2	8c	0.3003(6)	0.2595(5)	0.3133(5)	$U(Rb1)$
	Fe1	8c	0.258(1)	0.0076(6)	0.1901(6)	0.0047(9)
	Fe2	8c	0.7852(8)	0.2598(6)	0.4370(6)	$U(Fe1)$
	O1	8c	0.278(3)	0.1521(19)	0.1496(11)	0.010(3)
	O2	8c	0.173(3)	0.096(2)	0.6114(14)	$U(O1)$
	O3	8c	0.073(3)	0.212(2)	0.9869(10)	$U(O1)$
	O4	8c	0.959(3)	0.9796(19)	0.2230(12)	$U(O1)$
RbFeO ₂ , 783 K	Rb	8b	3/8	3/8	3/8	0.0701(10)
	Fe	8a	1/8	1/8	1/8	0.0653(6)
	O	16c	0	0	0	0.150(3)
CsFeO ₂ , 298 K	Cs1	8c	0.7503(4)	0.0034(1)	0.0624(2)	0.0236(1)
	Cs2	8c	0.2837(1)	0.2532(2)	0.3123(2)	$U(Cs1)$
	Fe1	8c	0.2540(7)	0.0031(4)	0.1872(4)	0.0098(2)
	Fe2	8c	0.7744(2)	0.2531(4)	0.4381(4)	$U(Fe1)$
	O1	8c	0.286(1)	0.140(1)	0.1391(8)	0.0096(9)
	O2	8c	0.194(1)	0.116(1)	0.6200(9)	$U(O1)$
	O3	8c	0.055(1)	0.2250(9)	0.9857(4)	$U(O1)$
	O4	8c	0.974(2)	0.985(1)	0.2334(7)	$U(O1)$
CsFeO ₂ , 400 K	Cs	8b	3/8	3/8	3/8	0.0368(1)
	Fe	8a	1/8	1/8	1/8	0.0163(1)
	O	16c	0	0	0	0.0660(8)

4. The $A\text{FeO}_2$ ($A = \text{K}, \text{Rb}$ and Cs) family

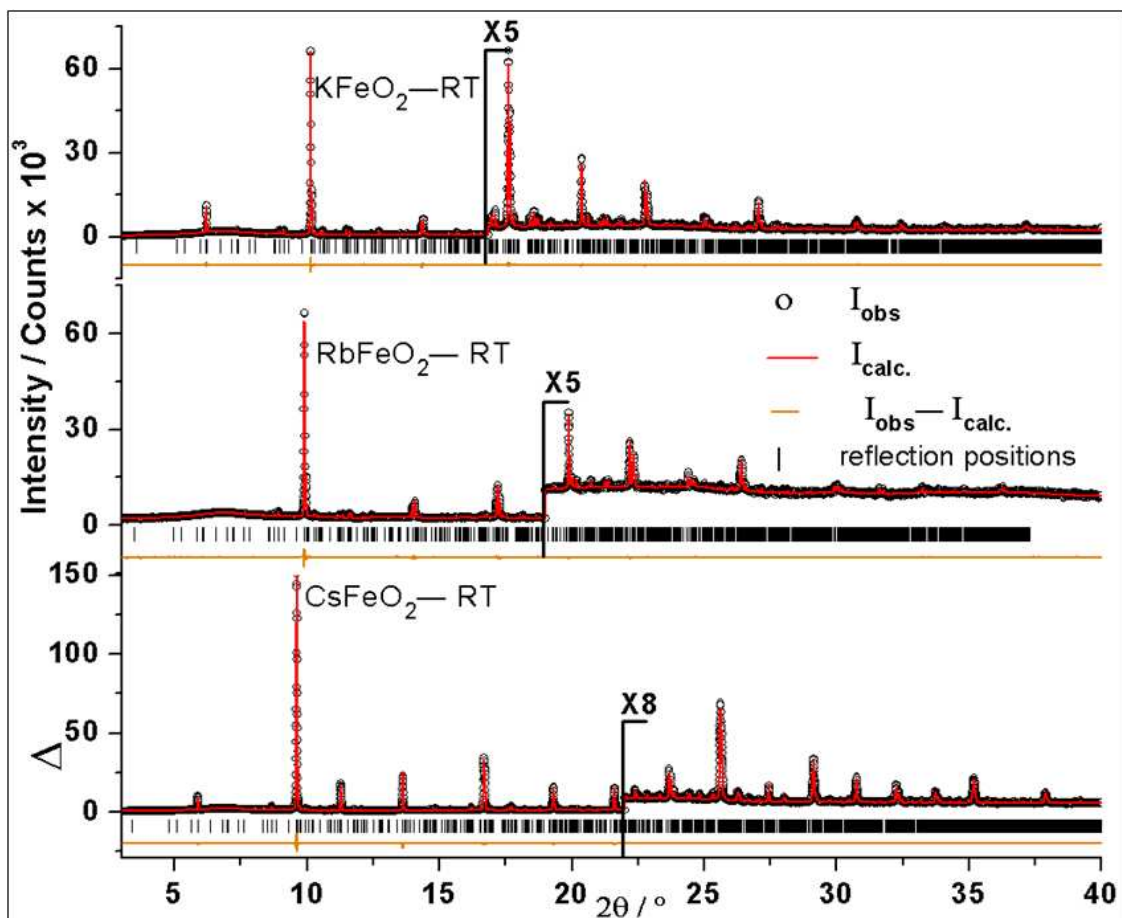


Fig. 4.9. Synchrotron Powder pattern of KFeO_2 , RbFeO_2 , and CsFeO_2 measured at ‘Room Temperature’ at Synchrotron powder diffraction station of the Materials Sciences (MS-Powder) beamline at the Swiss Light Source [SLS] Switzerland. Note that the higher angle part is enlarged by a factor of 5, 5 and 8 for K , Rb and Cs [FeO_2] respectively for lucid view.

4. The $A\text{FeO}_2$ ($A = \text{K}, \text{Rb}$ and Cs) family

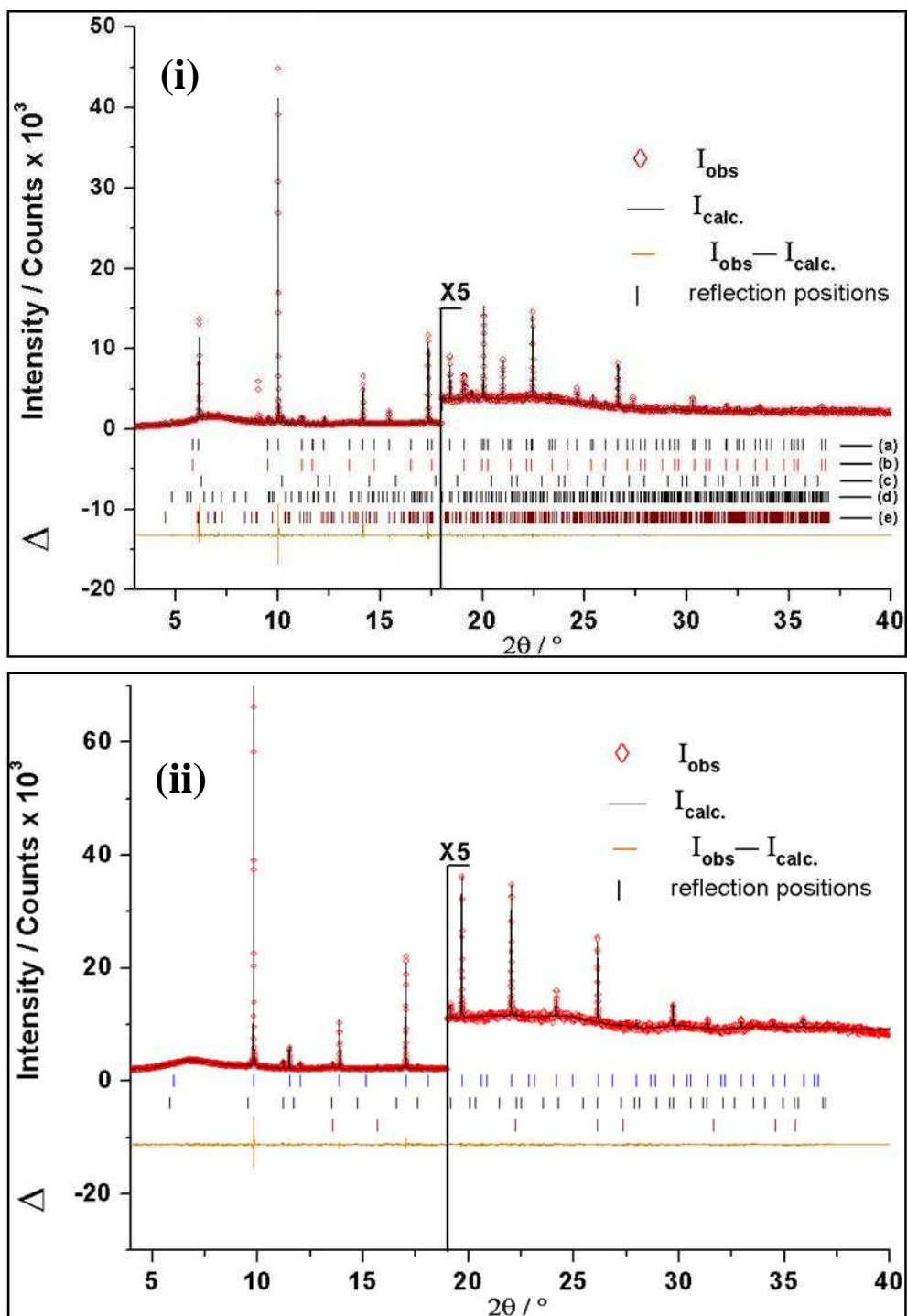


Fig. 4.10. Synchrotron Powder pattern of i) KFeO_2 and ii) RbFeO_2 measured at higher temperature [at $T > T_{\text{str}}$] at Synchrotron powder diffraction station of Swiss Light Source [SLS] Switzerland. Note that the higher angle part is enlarged by a factor of 5 for better visibility.

4. The $A\text{FeO}_2$ ($A = \text{K}, \text{Rb}$ and Cs) family

The synchrotron data collection for CsFeO_2 was done in the range of $T = 298\text{-}409$ K with steps of 1 K, and no decomposition of sample is observed both on heating and cooling back the sample to room temperature (Fig. 4.11).

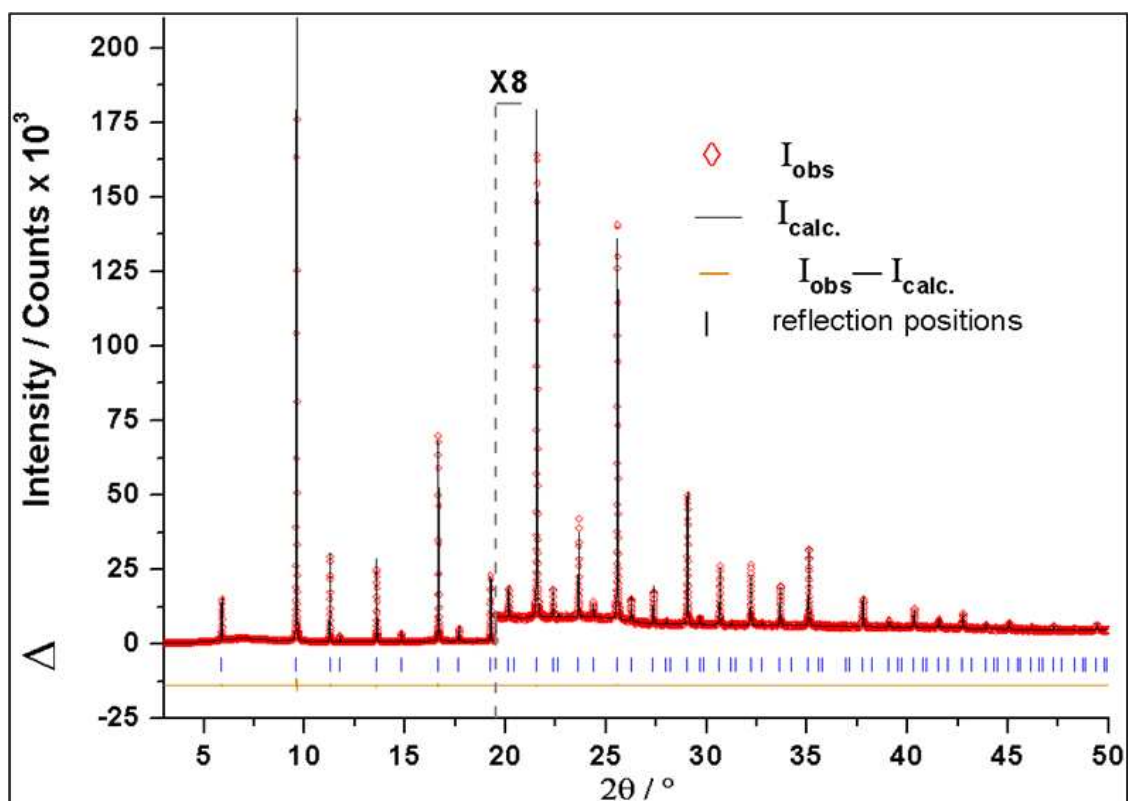


Fig. 4.11. Scattered X-ray intensity for polycrystalline sample of CsFeO_2 at $T = 409$ K (103°C) as a function of diffraction angle 2θ ($\lambda = 0.497$ Å), showing the observed pattern (red diamonds), calculated profile (black line), difference plot (orange line) and reflection markers (blue vertical bars). Note that the higher angle part is enlarged by a factor of 8 for better visibility.

For RbFeO_2 a partial decomposition, as indicated by the appearance of Fe_3O_4 at temperatures starting from ~ 680 K, was observed. At the highest temperature assessed for

4. The $AFeO_2$ ($A = K, Rb$ and Cs) family

$RbFeO_2$, the weight proportion of this impurity amounted up to $\sim 4\%$ (based on the results of two-phase Rietveld refinements). Upon cooling it remained at exactly this value (Fig. 4.10(ii) and 4.12).

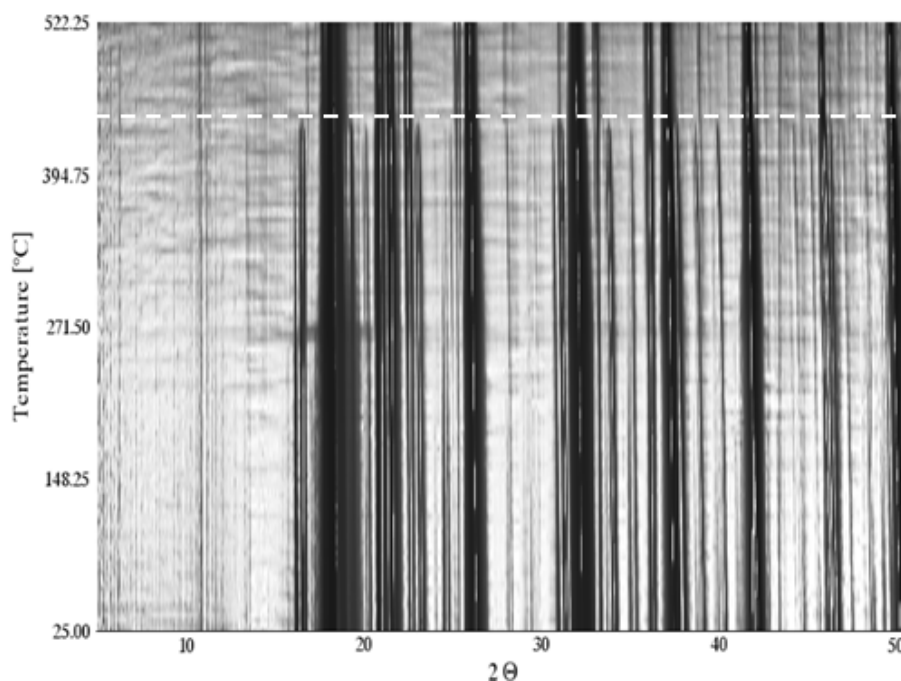


Fig. 4.12. The bar diagram (Guinier Aufnahme) for $RbFeO_2$ showing clearly the onset of structural phase transition at around 737 K (460 °C) as depicted by white dashed line

When heating $KFeO_2$, an even more severe decomposition was observed in the X-ray diffraction patterns parallel to the evolution of the crystal structure. The phases emerging at high temperatures included: Fe_3O_4 (starting from ~ 720 K) [49] and some potassium poor oxoferrates. These were identified as rhombohedral $K_{\sim 0.15}Fe_{10}O_{\sim 15.6}$ [50] (starting from ~ 900 K), K-deficient cubic phase with a probable composition $K_{\sim 0.67}FeO_2$ and an orthorhombic phase with an approximate composition $K_7Fe_5O_{16}$ [51], (both starting from ~ 940 K) (Fig. 4.10(i) and 4.13).

4. The $A\text{FeO}_2$ ($A = \text{K}, \text{Rb}$ and Cs) family

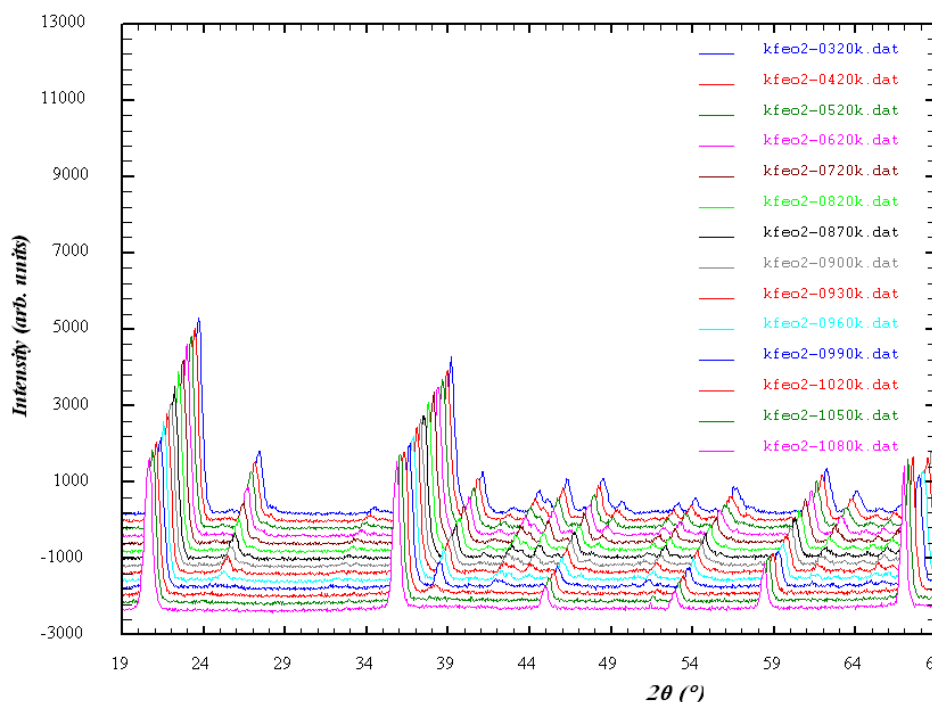


Fig. 4.13. **a , b**) Scattered X-ray intensity for polycrystalline sample of KFeO_2 between $T = 320 \text{ K}$ (47°C) and 1080 K (837°C) as a function of diffraction angle 2θ ($\lambda = 0.497 \text{ \AA}$), showing the observed pattern with disappearance of tiny splitting reflections due to orthorhombic distortions.

The Fe—O distances as derived from synchrotron data, in analogy with already available single crystal data, are very similar in all three structures and amount on average to 1.86 \AA . However, when going from KFeO_2 to RbFeO_2 and to CsFeO_2 , the unit cell volumes are increasing with the size of the alkali metal cation: from $\sim 1003 \text{ \AA}^3$ to $\sim 1075 \text{ \AA}^3$ to $\sim 1179 \text{ \AA}^3$. This gain of the volume in order to accommodate the alkali metal cations of corresponding bigger sizes is reflected by differences in the Fe—O—Fe bond angles: they grow at room temperature on average from 137° to 143° and 157° for KFeO_2 , RbFeO_2 and CsFeO_2 , respectively.

Table 4.7 compares bond angles Fe—O—Fe ($^\circ$) in the orthorhombic low temperature phases of $A\text{FeO}_2$ ($A = \text{K}, \text{Rb}, \text{Cs}$), describing the twisting of the FeO_4 tetrahedra, refined from both synchrotron and single crystal X-ray diffractometry. Thus, in the compound with the largest A cation (in CsFeO_2), the Fe—O—Fe connections are much more

4. The $A\text{FeO}_2$ ($A = \text{K}, \text{Rb}$ and Cs) family

“straight” than in RbFeO_2 and in KFeO_2 , where they are the most bent. Following as a result, the distances between nearest iron atoms are the smallest in KFeO_2 (3.45 Å on average), intermediate in RbFeO_2 (3.53 Å on average) and the largest in CsFeO_2 (3.63 Å on average).

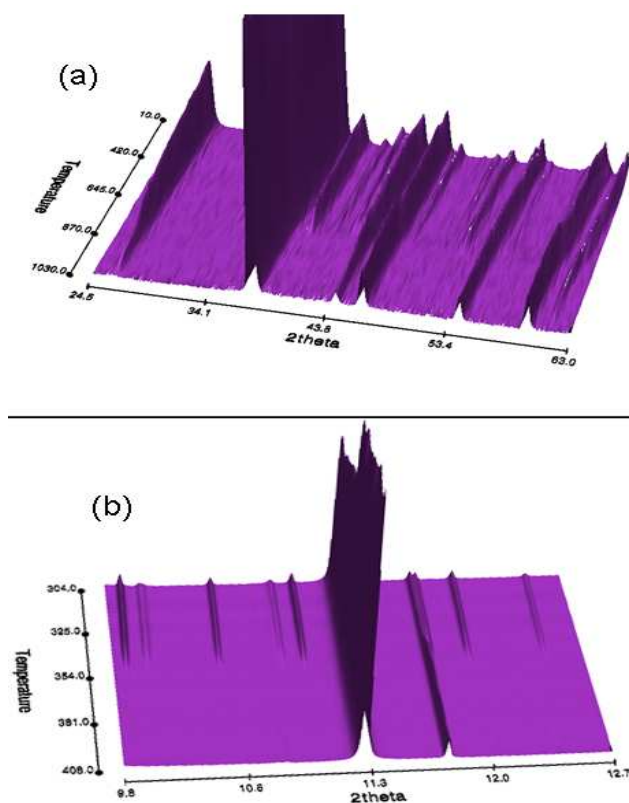


Fig. 4.14. A multidimensional view of structural phase transition as depicted by synchrotron X-ray powder diffraction patterns of a) RbFeO_2 and b) CsFeO_2 taken for illustration in respective Fragments.

The high temperature modifications of all three compounds (emerging at different temperatures (*c.f.* Fig. 4.14 for better view) have been found to also be isostructural to each other. All the diffraction patterns of the high-temperature modifications of KFeO_2 , RbFeO_2 and CsFeO_2 have been indexed on a cubic F -centered unit cell with a lattice constant a_{cub} related to those of the corresponding orthorhombic low-temperature modifications as: $a_{\text{cub}} \approx a_{\text{orth}} \cdot \sqrt{2} \approx b_{\text{orth}} / \sqrt{2} \approx \frac{1}{2} c_{\text{orth}}$. With the aid of high resolution synchrotron data, the precise monitoring of the structural parameters in the proximity of

4. The $AFeO_2$ ($A = K, Rb$ and Cs) family

the phase transitions, alongwith the really tiny splitting of the diffraction lines due to the orthorhombic distortions can be seen. At elevated temperatures a reversible structural phase transformation to a cubic structure space group $Fd\bar{3}m$) was observed. For $KFeO_2$, $RbFeO_2$ and $CsFeO_2$ this phase transformation takes place at 1003 K, 737 K and 350 K respectively, as confirmed by differential scanning calorimetry and synchrotron X-ray diffraction concomitantly. Upon heating through the transitions the major structural changes are driven by the onset or enhancement of librational motion of the FeO_4 tetrahedra. Due to this phenomenon the Fe—O—Fe bonds appear to step-wise getting straight, seemingly approaching 180° within the time and space averaged structure. The structures have been determined to possess the $CsAlO_2$ type of structure, with the main structural parameters (refined from synchrotron powder data) being tabulated in the Table 4.10 and 4.11.

The structural phase transitions in all the three compounds are of the first order according to the results of DSC and measurements and Rietveld refinement of synchrotron X-ray data, the low-temperature orthorhombic and the high-temperature cubic phases are coexisting in certain temperature ranges, with abrupt changes in the lattice parameters and the unit cell volume can be seen clearly in Fig. 4.15.

4. The $AFeO_2$ ($A = K, Rb$ and Cs) family

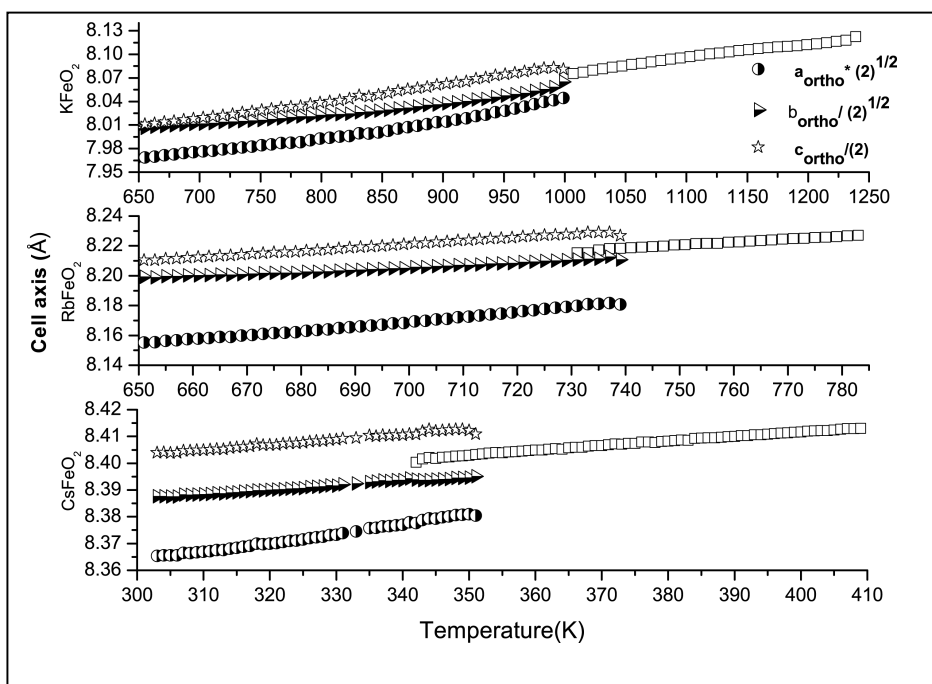


Fig. 4.15. Temperature dependence of unit cell parameters of $AFeO_2$ ($A = K, Rb, Cs$) as refined from the synchrotron data.

The temperature range of coexistence of the low- and high-temperature modifications of $CsFeO_2$ is ~ 12 K wide. A qualitatively similar situation has been observed in $RbFeO_2$, with the estimated width of the temperature range where the two phases are coexisting of ~ 8 K. The steps in temperature in the heating experiment of $KFeO_2$ were too coarse (8 K) to give an estimate for the same temperature range of the phase coexistence for $KFeO_2$, but the discontinuity of the lattice constants and unit cell volume at the transition from orthorhombic to cubic phase is qualitatively similar to the other two compounds. The transition temperatures estimated precisely (determined as those where the phases are in the 50:50 proportions) are thus ~ 1003 K, ~ 737 K and ~ 350 K for $AFeO_2$, where $A = K, Rb, Cs$.

4. The $AFeO_2$ ($A = K, Rb$ and Cs) family

4.3.4. Neutron scattering experiments.

Crystal structures of the low-temperature and high-temperature modifications

The temperature evolutions of crystal and magnetic structures of $KFeO_2$, $RbFeO_2$ and $CsFeO_2$ have also been also precisely investigated by neutron powder diffraction. Since contrast for seeing oxygen is much better through neutron [neutron scattering length of 5.80 femtometer] than X-ray [$Z=8$], thereby facilitating to study the oxygen site disorder at the structural phase transition.

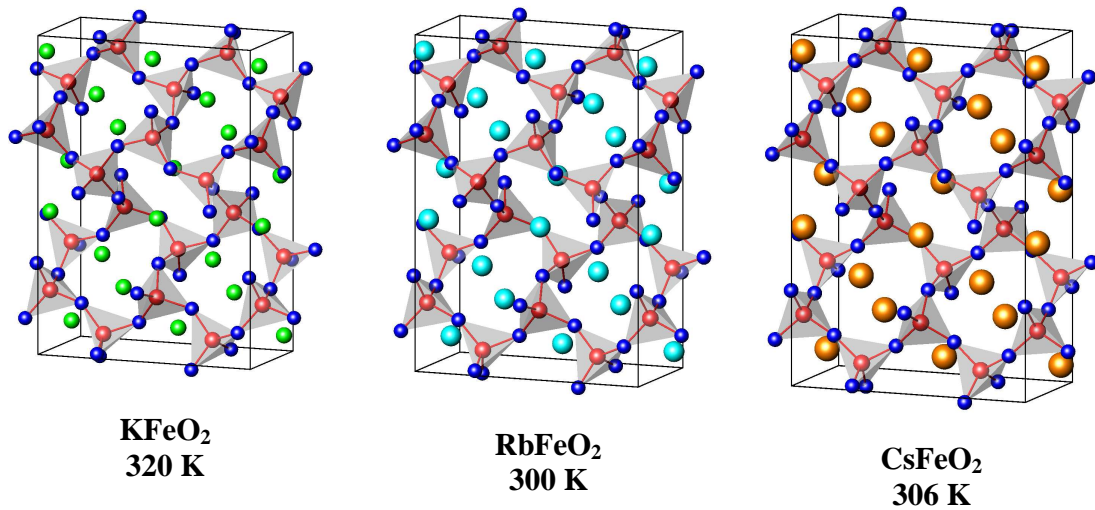


Fig. 4.16. Crystal structures of $KFeO_2$, $RbFeO_2$ and $CsFeO_2$ near room temperature (neutron diffraction).

In their room temperature modifications (Fig. 4.16) and also at lower temperatures down to $T = 10$ K, all the three ferrates are isostructural to orthorhombic $KGaO_2$ [33, 34] (space symmetry $Pbca$). Whereas the high temperature modifications of all three compounds ($KFeO_2$, $RbFeO_2$ and $CsFeO_2$) emerging at different temperatures have been found to be also isostructural to each other, indexed on a cubic F-centered unit cell with a lattice constant a_{cub} related to those of the corresponding orthorhombic low-temperature modifications as: $a_{cub} \approx a_{orth} * \sqrt{2} \approx \frac{b_{orth}}{\sqrt{2}} \approx \frac{c_{orth}}{2}$. The crystal structure parameters of all

4. The $AFeO_2$ ($A = K, Rb$ and Cs) family

three compounds refined from the neutron powder diffraction data at room temperature are listed in Table 4.12. While, in Fig. 4.16, we represent the room temperature crystal structures of the title $AFeO_2$ compounds as determined via neutron diffraction experiments.

Table 4.12: Crystal structure parameters at about room temperature for $KFeO_2$ (320 K), $RbFeO_2$ (300 K) and $CsFeO_2$ (306 K) refined from neutron powder diffraction data. Space group Pbc_a ($Z=16$). All atoms are located in the general (8c) sites.

Parameter		A=K ($KFeO_2$)	A=Rb ($RbFeO_2$)	A=Cs ($CsFeO_2$)
$a, \text{Å}$		5.6002 (1)	5.7197 (1)	5.9167 (1)
$b, \text{Å}$		11.2602 (2)	11.5141 (2)	11.8860 (2)
$c, \text{Å}$		15.9414 (2)	16.3457 (2)	16.7792 (3)
$V, \text{Å}^3$		1005.25 (3)	1076.49 (3)	1180.01(3)
A1 (K, Rb, Cs)	x	0.745 (2)	0.749 (1)	0.747 (2)
	y	0.5095 (10)	0.5105 (5)	0.5023 (10)
	z	0.4357 (11)	0.4371 (5)	0.4374 (10)
A2 (K, Rb, Cs)	x	0.3039 (14)	0.3009 (7)	0.2888 (11)
	y	0.2370 (11)	0.2390 (4)	0.2452 (9)
	z	0.684 (1)	0.6866 (4)	0.6870 (9)
A1, A2	$B, \text{Å}^2$	1.76 (10)	1.65 (4)	1.89 (6)
Fe1	x	0.7537 (7)	0.7554 (5)	0.7513 (9)
	y	0.0084 (4)	0.0056 (3)	0.0022 (5)
	z	0.1884 (4)	0.1900 (3)	0.1884 (6)
Fe2	x	0.7842 (5)	0.7842 (4)	0.7726 (5)
	y	0.2352 (3)	0.2396 (3)	0.2459 (5)
	z	0.5648 (4)	0.5631 (3)	0.5636 (5)
Fe1, Fe2	$B, \text{Å}^2$	0.85 (33)	0.55 (3)	0.89 (3)
O1	x	0.4325 (14)	0.4431 (10)	0.4628 (17)
	y	0.9805 (7)	0.9825 (5)	0.9907 (8)
	z	0.2179 (5)	0.2208 (4)	0.2317 (7)
O2	x	0.8411 (14)	0.8285 (11)	0.7924 (17)
	y	0.9082 (8)	0.9022 (5)	0.8880 (10)
	z	0.1008 (5)	0.1058 (4)	0.1146 (6)
O3	x	0.7985 (14)	0.8028 (12)	0.7832 (16)
	y	0.1649 (7)	0.1551 (5)	0.1389 (12)
	z	0.1573 (5)	0.1484 (4)	0.1377 (6)
O4	x	0.5774 (15)	0.5766 (10)	0.5569 (13)
	y	0.2934 (7)	0.2836 (6)	0.2711 (8)
	z	0.4804 (4)	0.4805 (3)	0.4841 (5)
O1, O2, O3, O4	$B, \text{Å}^2$	1.92 (6)	1.30 (5)	1.87 (5)

In extension to our previous synchrotron study [*c.f.* section 4.3.3] which was based on solely the X-ray diffraction data, in the current neutron study we were able to extract more precise information on the details of the high-temperature modifications of the title

4. The $A\text{FeO}_2$ ($A = K, Rb$ and Cs) family

compounds. In particular, based only on the synchrotron X-ray diffraction data, we were treating the displacements of oxygen atoms in the high-temperature modifications of the $A\text{FeO}_2$ compounds with the anisotropic thermal parameters. Having now the neutron data at hand, we are able to get a deeper insight into the mechanism of the structural phase transition into a cubic phase in the studied compounds. Previously we were assuming [c.f. section 4.3.3], that upon heating the samples, the bridging oxygen atoms forming the bent Fe-O-Fe junctions are getting disordered in the plane perpendicular to the Fe-Fe direct linkage, such that the Fe-O-Fe bonds are getting seemingly straight, producing the average Fe-O-Fe angle of 180° [Fig. 4.17 (a, b)]. In reality, however, it is just long-range three-dimensional order of the precise mutual orientations of the still effectively bent Fe-O-Fe linkages which is getting lost in the transition. Thus, because of this dynamical disorder of the long-range correlations in the mutual directions of the Fe-O-Fe linkages, oxygen is (speaking in terms of crystallographic description) getting disordered on a ring perpendicular to the Fe-Fe bond, as illustrated in Fig. 4.17, panel (c).

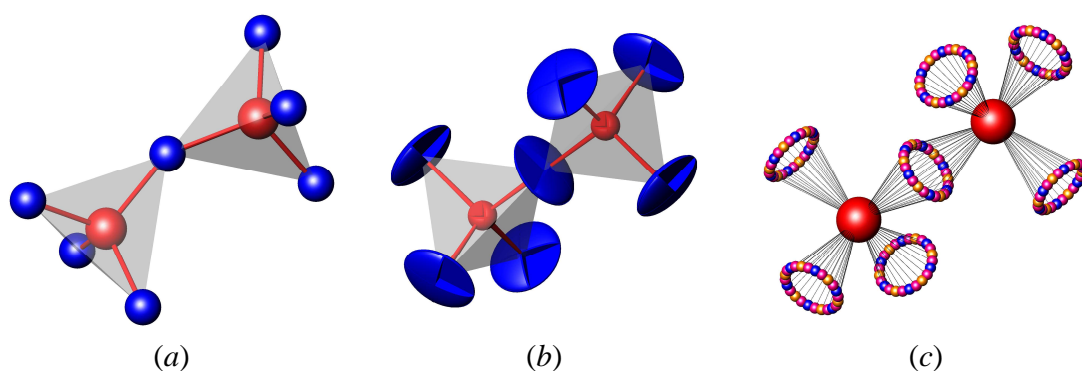


Fig. 4.17. Illustration of the crystal structure peculiarities of RbFeO_2 associated with the structural transition:
(a): Fe1-O-Fe2 junction at $T=300$ K, in the orthorhombic ordered phase
(b): Fe-O-Fe junction in the high temperature phase ($T=820$ K); approach with the anisotropic thermal parameters for the oxygen atoms used in our work [c.f. section 4.3.3],
(c): same, the newly proposed approach based on split oxygen sites.

4. The $AFeO_2$ ($A = K, Rb$ and Cs) family

In order to most properly model this structural peculiarity of the high-temperature phases of the $AFeO_2$ ($A=K, Rb, Cs$) compounds, we assumed the bridging oxygen atoms to be disordered on a circle with a radius R perpendicular to the Fe-Fe junction. Thus, instead of occupying the $16c$ (0,0,0) position, each oxygen is split into 24 equally occupied and equally spaced along the circle “atoms” occupying three sites: O1 in the $96h$ ($-x_1, 0, x_1$), O2 in the $96g$ ($-x_2, -x_2, 2x_2$) and O3 in the $192i$ ($-x_3, -y_3, x_3+y_3$). In order to keep the ring really uniform, the coordinates for these sites are forced in our refinements to be related to the radius R of the ring and the cubic lattice constant a_{cub} as follows:

$$\begin{aligned} x_1 &= \frac{1}{\sqrt{2}} \cdot \frac{R}{a_{cub}}; \\ x_2 &= \frac{1}{\sqrt{6}} \cdot \frac{R}{a_{cub}}; \\ x_3 &= \frac{1}{\sqrt{3}} \cdot \frac{R}{a_{cub}}; \quad y_3 = \sqrt{\frac{2-\sqrt{3}}{6}} \cdot \frac{R}{a_{cub}} \end{aligned} \quad (3)$$

The occupation factors for the O1, O2 and O3 sites are exactly 1/24. This way, the angular span between the neighbouring individual O_i ($i=1, 2, 3$) atoms along the ring is exactly 15° . This approach allows to realistically model the true temperature dependences of the interatomic distances and angles in the studied compounds. Notably, taking this measure does not require the number of the refined structural parameters to increase. Instead of the two components of the anisotropic thermal parameter tensor ($\beta_{11} = \beta_{22} = \beta_{33}$ and $\beta_{12} = \beta_{13} = \beta_{23}$) of the oxygen atom located in (0,0,0) [*c.f.* section 4.3.3], we are now refining another two parameters: R (by properly constraining the values of x_1, x_2, x_3 and y_3 : see equations (1)) and the isotropic thermal parameters $B_{iso}(O)$ constrained to be identical for the atoms O1, O2 and O3. The agreement factors of the refinement are indeed getting significantly better with such a new model, for example for the case of the

4. The $AFeO_2$ ($A = K, Rb$ and Cs) family

RbFeO₂ data collected at T = 820 K, the χ^2 improves from 2.01 to 1.77, the Bragg R-factor for the crystallographic RbFeO₂ phase – from 5.51 % to 4.14 %, and the magnetic R-factor for the RbFeO₂ antiferromagnetic phase from 11.0 % to 7.8 %. The refined values of the structural parameters in the cubic phases of all three compounds are presented in table 4.13 for selected representative temperatures (different for each compound).

Table 4.13: Crystal structure parameters for the high-temperature polymorphs of KFeO₂ (at T ≈ 1050 K), RbFeO₂ (at T ≈ 820 K) and CsFeO₂ (at T ≈ 400 K) refined from neutron powder diffraction data. Space group $Fd\bar{3}m$ (Z=8). Atoms A (K, Rb, Cs) at 8b sites (3/8,3/8,3/8), Fe at 8a sites (1/8,1/8,1/8), O1 at 96h (-x₁,0,x₁), O2 at 96g (-x₂,-x₂,2x₂) and O3 at 192i (-x₃,-y₃,x₃+y₃) sites. The x₁, x₂, x₃ and y₃ positional parameters are correlated to essentially one parameter – the radius of the ring R according to the expressions (1). The fractional occupation factors for the O1, O2 and O3 are all equal to 1/24.

Parameter		A = K (KFeO ₂), T = 1050 K	A = Rb (RbFeO ₂), T = 820 K	A = Cs (CsFeO ₂), T = 400 K
a , Å		8.09171 (9)	8.24263 (6)	8.41103 (4)
A (K, Rb, Cs)	B (Å ²)	7.57 (15)	5.40 (7)	2.84 (5)
Fe	B, (Å ²)	3.64 (5)	2.47 (3)	1.27 (3)
O(1,2,3)	R, (Å)	0.638 (3)	0.533 (3)	0.385 (3)
O(1,2,3)	B, (Å ²)	4.40 (15)	2.35 (11)	1.33 (9)
Fe-O distance,	(Å)	1.865 (2)	1.8624 (14)	1.8611 (14)
Fe-O-Fe angle,	(deg)	139.95 (9)	146.76 (6)	156.17 (6)

4. The $A\text{FeO}_2$ ($A = \text{K}, \text{Rb}$ and Cs) family

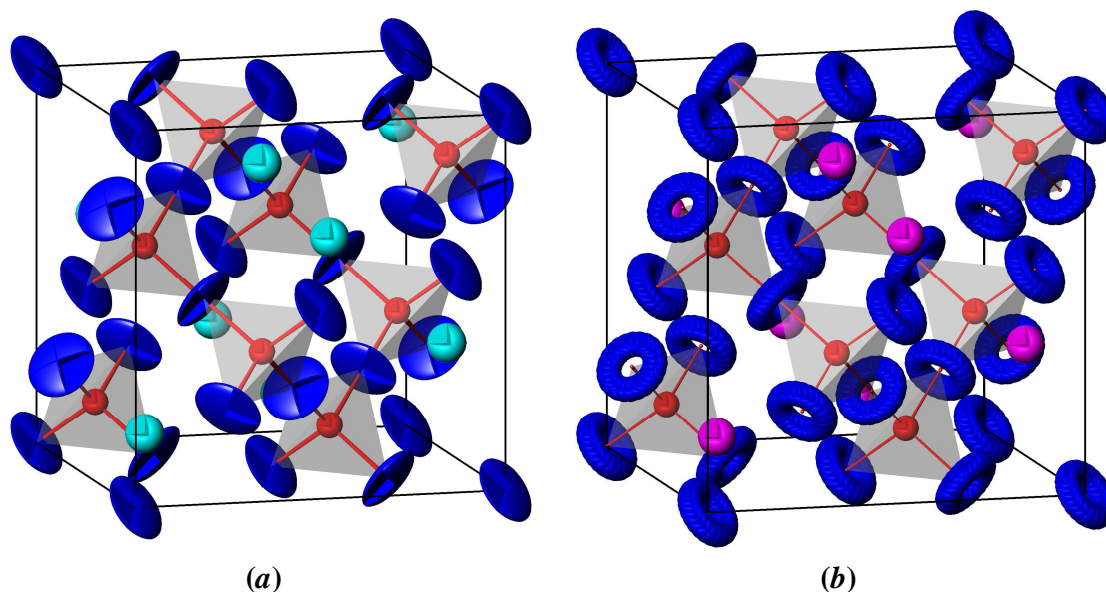


Fig. 4.18. Crystal structures of the high-temperature modifications of KFeO_2 , RbFeO_2 and CsFeO_2 . (a): From the model with the anisotropic thermal parameters for oxygen atoms as in [c.f. section 4.3.3], (b): approach based on split atom model with oxygen atoms being disordered on a ring. The sizes of the atoms are proportional to the refined thermal parameters of the atoms in RbFeO_2 at $T = 820 \text{ K}$.

In the Fig. 4.18, the illustration of the crystal structures of the high-temperature crystallographic phases of the $A\text{FeO}_2$ ($A = \text{K}, \text{Rb}, \text{Cs}$) compounds is given, with the strongly anisotropic character of the atomic thermal vibrations of the oxygen atoms (a) [c.f. section 4.3.3], and in the split atom model of the present neutron investigation (b). In the panel (b) of the Fig. 4.18, the FeO_4 tetrahedra are displayed with the Fe-O linkages based on the “time-average” positions of the corresponding oxygen atoms, though in reality, the oxygen atomic density is of course evenly distributed on the corresponding rings perpendicular to the Fe-Fe directions. Thus upon heating, as soon as the temperature-induced increase in the atomic displacement parameters (ADP’s) of oxygen atoms is becoming large enough, the oxygen atoms “jump” in a quantum-like manner from a given position with a well-defined orientation of the Fe-O-Fe bond angle into a state illustrated in the Fig. 4.18 (b), where these angles are of course preserved, but their orientations vary dynamically in a collective manner.

4. The $AFeO_2$ ($A = K, Rb$ and Cs) family

The structural phase transitions in all three compounds are of the first order, which has been convincingly illustrated by the unit cell volume discontinuities at the structural phase transitions [order of $\sim 3 \cdot 10^{-3}$], by the presence of certain temperature ranges of coexistence of the low- and high-temperature modifications, and by the temperature hysteresis of the transitions well seen in the DSC measurements [*c.f.* section 4.3.2]. In agreement with these previous findings, here we also observe the unit cell volume discontinuities at the phase transitions, as illustrated in the Fig. 4.19 (a). The temperature steps during the neutron data collection were however too coarse to be able to track in details the coexistence of the two phases in given temperature intervals.

4. The $A\text{FeO}_2$ ($A = \text{K}, \text{Rb}$ and Cs) family

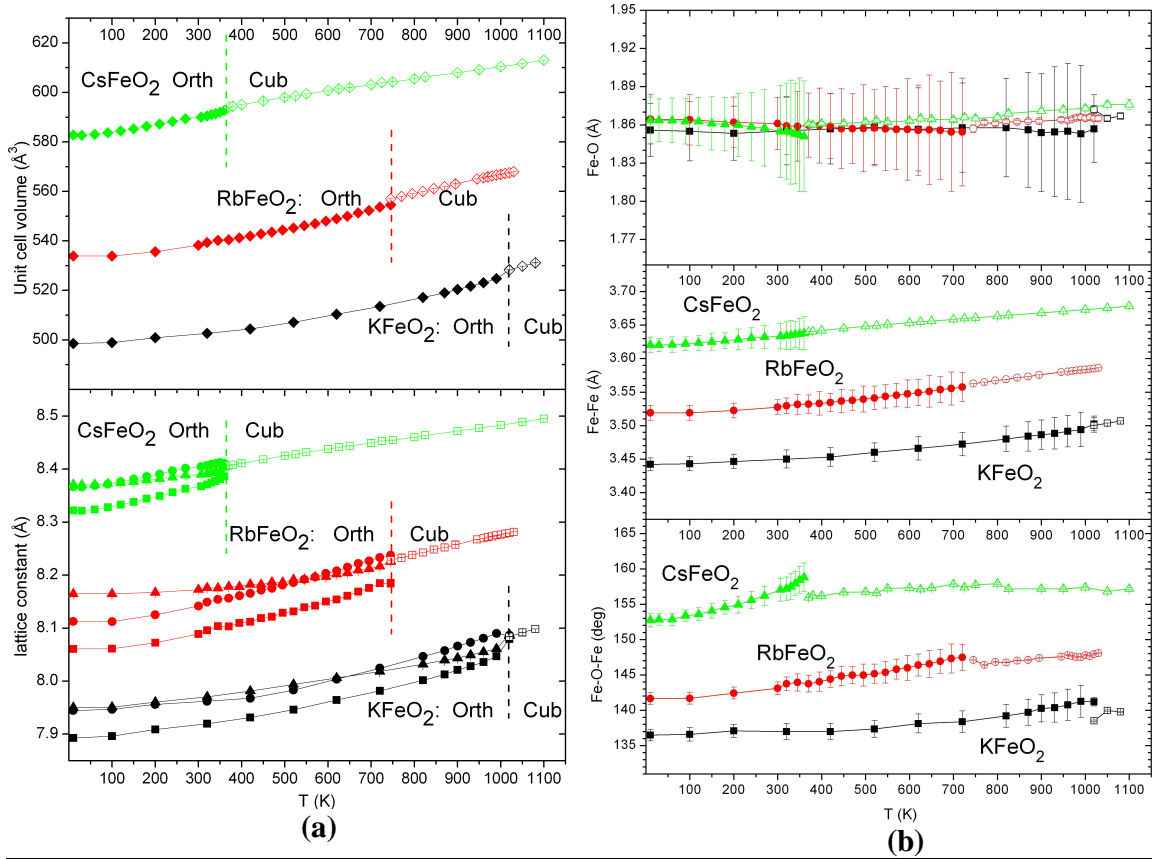


Fig. 4.19. **a)** Temperature dependences of the refined unit cell parameters ($\blacksquare - a_{\text{orth}} * \sqrt{2}$, $\bullet - b_{\text{orth}}/\sqrt{2}$, $\blacktriangle - c_{\text{orth}}/2$ for the orthorhombic phases, $\square - a_{\text{cub}}$ for the cubic phases) and of the unit cell volumes ($\blacklozenge - V_{\text{orth}}/2$, $\blacklozenge - V_{\text{cub}}$) of the orthorhombic low-temperature and cubic high-temperature crystallographic modifications of the $A\text{FeO}_2$ ($A = \text{K}, \text{Rb}, \text{Cs}$) compounds. The transition temperatures are also indicated.

b) Temperature dependences of the interatomic Fe-O (top), Fe-Fe (middle) distances and of the Fe-O-Fe bond angle (bottom) in the $A\text{FeO}_2$ compounds (\blacksquare and $\square -$ for KFeO_2 , \bullet and $\circ -$ for RbFeO_2 , \blacktriangle and $\triangle -$ for CsFeO_2). Filled and opened symbols represent the results for the low-temperature orthorhombic and for the high-temperature cubic phases respectively.

The newly-evolved structural model [split model] for the high-temperature modifications of the $A\text{FeO}_2$ ($A = \text{K}, \text{Rb}, \text{Cs}$) compounds allows also for a more realistic quantification of the internal structural changes with temperature.

4. The $A\text{FeO}_2$ ($A = \text{K}, \text{Rb}$ and Cs) family

From the Fig. 4.19 (b), it is seen that the Fe-O bond distances are practically temperature-independent in the whole temperature range up to ~ 1100 K and also are essentially identical in all three compounds.

They amount on average 1.86 \AA , and display a very slight discontinuity of $\sim 0.01 \text{ \AA}$ at the structural transition temperatures. In contrast, the Fe-O-Fe bond angles are strongly increasing with temperature (much faster in the orthorhombic phase, followed by visible negative discontinuities at the structural transitions and slower increases in the cubic phase), which leads in turn to the significant increases of the Fe-Fe distances with temperature: by as much as $0.06\text{--}0.07 \text{ \AA}$ on heating from low temperatures to ≥ 1000 K.

Both these Fe-Fe bond lengths and the Fe-O-Fe bond angles are determining the strengths of the magnetic exchange couplings between the Fe^{3+} ions: the more “straight” the Fe-O-Fe junction and the “shorter” the Fe-Fe Interatomic separation are, the stronger is the exchange. As we will see in paragraph below, these two effects “compensate” each other in such a way that effectively, the magnetic exchange energies and the magnetic transition temperatures in all three compounds are very similar to each other.

4.3.4.1. Magnetic structures and Magnetic transformations.

In the neutron diffraction patterns of all three $A\text{FeO}_2$ ($A=\text{K}, \text{Rb}, \text{Cs}$) compounds recorded at different temperatures, in addition to the structural phase transitions discussed above we also observe ‘magnetic ones’. These are related to the long-range magnetic ordering of the spins of the Fe^{3+} ions. An illustration of the observation of these two transitions is given in the Fig. 4.20 (a, b) for KFeO_2 and RbFeO_2 respectively and (c, d) for CsFeO_2 .

The signatures of both the structural phase transition (disappearance of some of the orthorhombic structure diffraction lines) at ~ 370 K and of the magnetic transition at

4. The $A\text{FeO}_2$ ($A = \text{K}, \text{Rb}$ and Cs) family

~ 1055 K are well noticeable in case of CsFeO_2 . The diffraction peaks at $\sim 26.5^\circ$, $\sim 44^\circ$, $\sim 61^\circ$ etc. are of magnetic origin. Qualitatively similar observations have been made for the KFeO_2 and RbFeO_2 compounds as well.

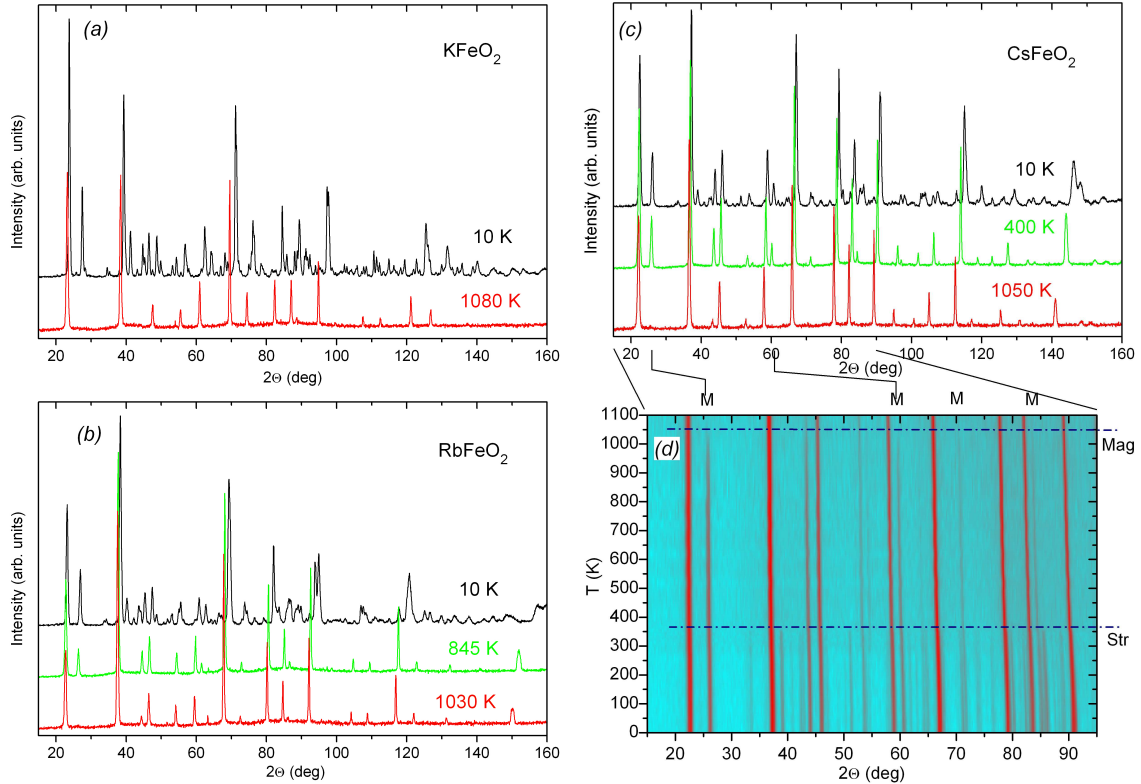


Fig. 4.20. **(a)**: Neutron powder diffraction (NPD) patterns of the KFeO_2 compound recorded for the orthorhombic and magnetic LT phase at $T=10$ K and for the cubic and paramagnetic HT phase at 1080 K; **(b)**: NPD patterns of the RbFeO_2 compound recorded for the orthorhombic and magnetic LT phase at $T = 10$ K, for the cubic and still magnetic HT phase at 845 K; and for the cubic and paramagnetic HT phase at 1030 K; **(c)**: NPD patterns of the CsFeO_2 compound recorded for the orthorhombic and magnetic LT phase at $T=10$ K, for the cubic and still magnetic HT phase at 400 K; and for the cubic and paramagnetic HT phase at 1050 K; **(d)**: Color intensity map of the temperature evolution of the diffraction patterns of CsFeO_2 (fragments of 36 diffraction patterns recorded between 10 and 1100 K in a 2Θ range from 15° to 95°). The horizontal dash-dotted lines indicate the temperatures of the structural (Str.) and magnetic (Mag.) phase transitions. The most evident magnetic diffraction peaks positions are marked with M.

4. The $A\text{FeO}_2$ ($A = \text{K}, \text{Rb}$ and Cs) family

The set of the magnetic diffraction lines in all three $A\text{FeO}_2$ ($A=\text{K}, \text{Rb}, \text{Cs}$) compounds is indexed in the parent orthorhombic primitive unit cell, thus the propagation vector of magnetic structure is $\kappa=(0,0,0)$. The symmetry analysis of the possible magnetic structures with this propagation vector for the positions of Fe ions in the unit cell of $A\text{FeO}_2$ ($A=\text{K}, \text{Rb}, \text{Cs}$) with a space group $Pbca$ has been carried out with the Program SARAh-2k [54] assuming that for both magnetic Fe^{3+} sites the ordering occurs with one and the same irreducible representation (IR). A total of eight IR's, for which the decomposition for both Fe sites has nonzero coefficients, are entering the decomposition of the magnetic representation for either of the sites Fe1 and Fe2. All resulting possibilities have been checked by Rietveld refinement, and it has been found that for all three compounds, there is exactly one IR providing the ideal fit. These magnetic structures are corresponding to antiferromagnetic ordering of the magnetic moments at the Fe sites such that the Fe-Fe couplings are antiferromagnetic in all four possible Fe-Fe linkages. Interestingly enough, the direction of the magnetic Fe^{3+} moments have been found to be parallel to the crystallographic b axis for KFeO_2 , and to the crystallographic c axis for RbFeO_2 and CsFeO_2 . This assignment of the moment directions is rather strict, since choosing the direction of the magnetic moments along the other crystallographic axis (choosing another IR) results in noticeable poisoning of the refinement, manifesting itself in the significant worsening of the refinement agreement factors. For example in case of the 10 K dataset of CsFeO_2 , choosing the direction of the magnetic moments along the crystallographic axes a or b instead of c leads to an increase of the magnetic R-factor for the magnetic phase from 2.43 to 3.52 and 3.23, and of the global weighted χ^2 from 1.45 to 1.75 and 1.61 correspondingly. Similar judgments are also valid for RbFeO_2

4. The $A\text{FeO}_2$ ($A = \text{K}, \text{Rb}$ and Cs) family

and KFeO_2 with the corresponding moment directions. The magnetic Fe^{3+} moment direction in KFeO_2 contradicts the earlier finding of [25], where the crystallographic axis a direction was proposed as the most probable for KFeO_2 . The determination of the magnetic Fe^{3+} moment directions for CsFeO_2 and for RbFeO_2 has been done here for the first time. Interestingly enough, if one considers the directions of magnetic moments in the orthorhombic low-temperature modifications of the studied compounds, the case of KFeO_2 is physically different from those of both RbFeO_2 and CsFeO_2 . In the former case (KFeO_2), the magnetic Fe moments are aligned parallel to the direction of one of the Fe-O-Fe zig-zag chains and thus parallel to one of the plane diagonals of the parent (high-temperature) cubic unit cell, while in both RbFeO_2 and CsFeO_2 , they are perpendicular to this direction (inclined at different angles to the directions of *all* the Fe-O-Fe zig-zag chains), thus formally being aligned along one of the unit cell basic vectors of the parent high-temperature cubic cell. In the high-temperature cubic phases, the magnetic structures stay essentially the same, with the only difference that all directions (a , b , c) become equal, so we arbitrarily direct the moments in all three compounds along the crystallographic axis a (though, for KFeO_2 , in order to preserve the consistency with the magnetic moments directions in the low-temperature orthorhombic phase, one would rather direct them along any plane diagonal of the cube, e.g. along the $\mathbf{a}+\mathbf{b}$ direction; we cannot however distinguish these peculiar details in our powder experiment, so all three compounds were just supposed to have the magnetic moments directions along the a lattice direction in the high-temperature cubic form).

4. The $AFeO_2$ ($A = K, Rb$ and Cs) family

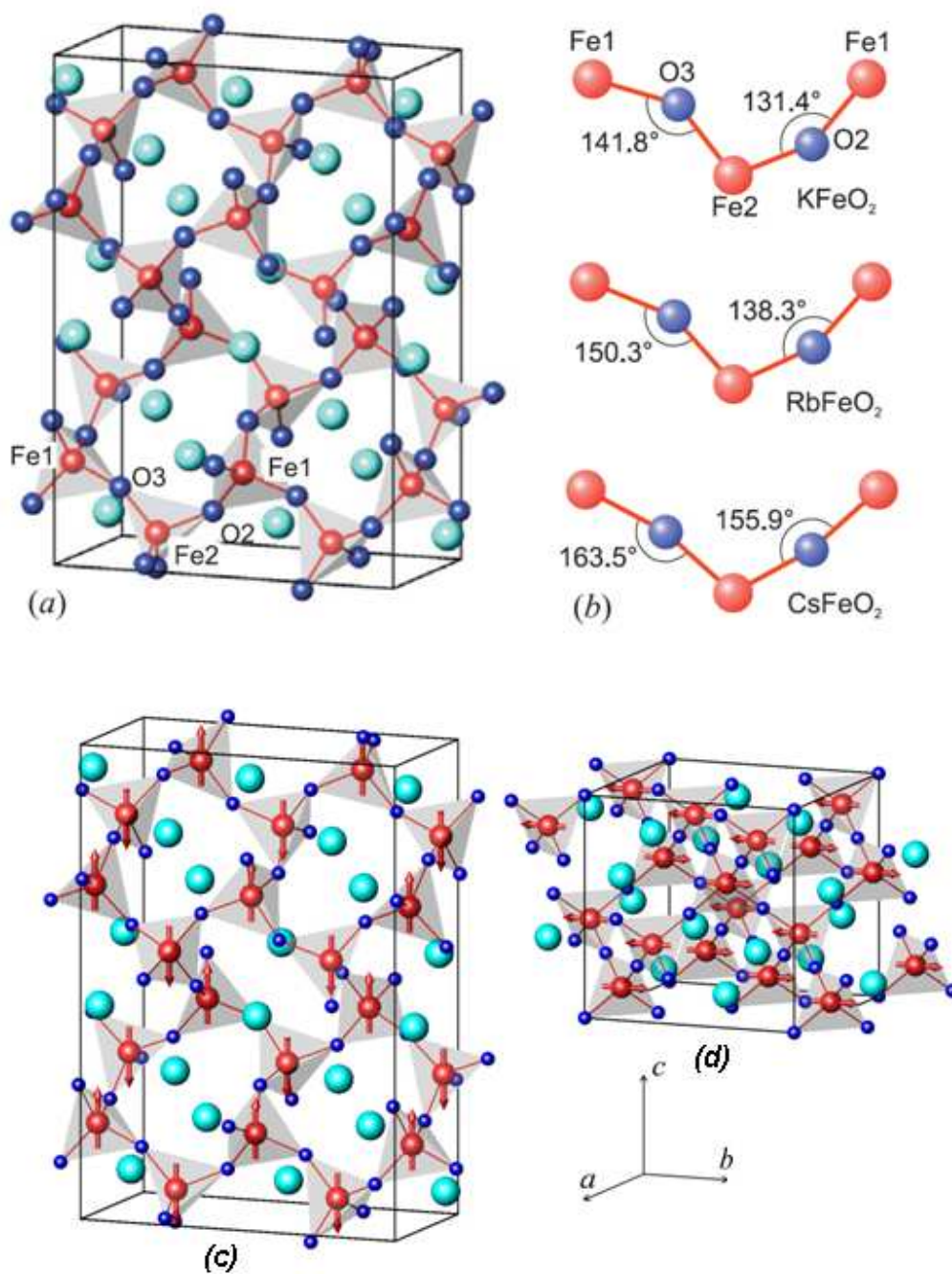


Fig. 4.21. **a**) Schematic view of crystal structure of $AFeO_2$ ($A=K, Rb$, and Cs) in the low-temperature orthorhombic phase e.g. $RbFeO_2$ **b**) Illustration of the systematic increase of Fe-O-Fe angles with increasing size of A-cation. **c**) image of the magnetic structure of $RbFeO_2$ at $T=300$ K (in the low-temperature orthorhombic phase) and **d**) at $T=820$ K (high-temperature cubic phase).

4. The $A\text{FeO}_2$ ($A = \text{K}, \text{Rb}$ and Cs) family

The illustration of the magnetic structures of the low- and high-temperature modifications of the title $A\text{FeO}_2$ ($A=\text{K}, \text{Rb}, \text{Cs}$) compounds is given in the Fig. 4.21 (a, b, c, d) for the case of RbFeO_2 .

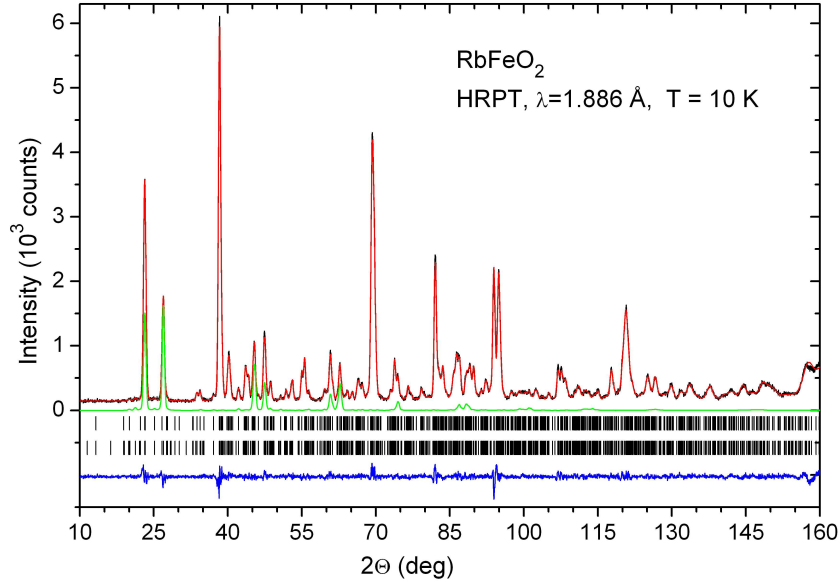


Fig. 4.22. Rietveld refinement fit of RbFeO_2 at $T = 10$ K (low-temperature orthorhombic phase). Experimental points, calculated profile and the difference curve are shown. The ticks below the graph indicate the calculated positions of the diffraction peaks: chemical structure (top) and magnetic phase (bottom). The contribution of solely the magnetic diffraction to the total diffraction intensity is shown in green.

The quality of the Rietveld refinements of crystal and magnetic structure parameters from neutron powder diffraction data is demonstrated in the Fig. 4.22 for the RbFeO_2 refinement at $T = 10$ K. The magnetic moment magnitudes refined from the neutron powder diffraction data are presented in the Fig. 4.23. The data in Fig. 4.23 were fitted to

the empirical equation: $M(T) = M_0 * \left[1 - \left(\frac{T}{T_N} \right)^\alpha \right]^\beta$, which qualitatively well fits the

data at all temperatures below T_N .

4. The $A\text{FeO}_2$ ($A = \text{K}, \text{Rb}$ and Cs) family

The data for CsFeO_2 were fitted only for $T > 350$ K, since the structural phase transition at ~ 350 K manifests itself by a peculiarity at this temperature. The fitted Néel temperatures for the three $A\text{FeO}_2$ compounds amount to 1001 (2) K, 1027 (1) K and 1055 (1) K for $A=\text{K}, \text{Rb}, \text{Cs}$ respectively. The estimated “critical exponent” parameters β are very close in all three compounds: 0.382 (15), 0.378 (6) and 0.378 (12) for $A=\text{K}, \text{Rb}, \text{Cs}$.

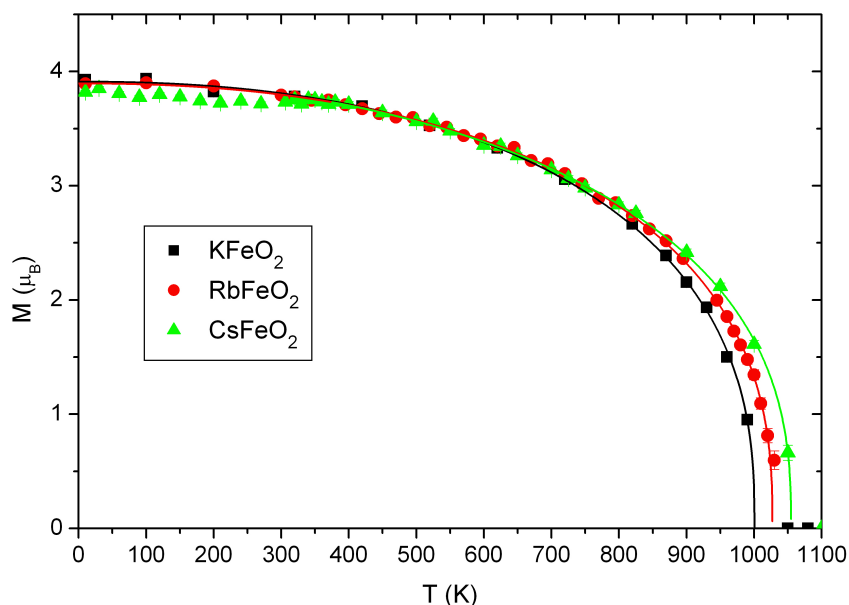


Fig. 4.23. Temperature dependences of the refined magnetic Fe^{3+} magnetic moments for $A\text{FeO}_2$ (squares for $A=\text{K}$, circles for $A=\text{Rb}$, triangles for $A=\text{Cs}$) compounds. Solid lines are fits to the formula explained in the text. The peculiarity in the CsFeO_2 data at $T \approx 350$ K is exactly coinciding with the structural phase transition.

4.4. Discussion and Conclusions.

All the three $A\text{FeO}_2$ ($A = \text{K}, \text{Rb}$ and Cs) compounds were synthesized with the help of the azide nitrate route [39, 40], whereupon the concomitant structures and structural and magnetic transitions were systematically investigated by single crystal X-ray diffraction, thermal analysis, high resolution synchrotron and neutron powder diffraction techniques.

4. The $AFeO_2$ ($A = K, Rb$ and Cs) family

The low-temperature and high-temperature modifications of all three compounds are isostructural to each other: the known $KGaO_2$ -type [33, 34] orthorhombic structure with $Pbca$ space group at low temperature and the cubic one with space group $Fd\bar{3}m$ at high temperature [c.f. section 4.3.3]. Likewise in case of $CsFeO_2$ because of feasibility to achieve the transition temperature of 358 K using Bruker AXS single crystal diffractometer, the same transition was counter verified using single crystal data [c.f. section 4.3.1]. Our findings differ distinctly from previously reported room temperature cubic ($Fd\bar{3}m$) structure of $CsFeO_2$ [27].

The lengths of the Fe-O bonds are very similar in all three compounds in both respective modifications, and are remaining almost constant at all temperatures, increasing on average only slightly – from ~ 1.86 Å at ~ 10 K to ~ 1.87 Å at ≥ 1000 K, in a good agreement with the sum of the ionic radii.

The Fe-O-Fe bond angles, however, vary significantly, which is due to the different sizes of the A cations – the more space is needed to accommodate the A-cation, the more “straight” (more close to 180°) is the Fe-O-Fe bond angle. Thus it increases continuously from β - $NaFeO_2$ (126°), $KFeO_2$ (135°), $RbFeO_2$ (144°) to $CsFeO_2$ (157°).

With increasing temperature, the Fe-O-Fe angles are steadily increasing, displaying observable discontinuities at the structural transition temperatures, which in turn leads to a discontinuous increase in the Fe-Fe separation with temperature. Upon heating through the structural transition points, the orientational long-range order of the Fe-O-Fe bindings is lost. The magnitudes of the Fe-O-Fe angles in these bindings are only slightly affected by the transitions, but their mutual orientations from one Fe-Fe junction to another most probably start varying dynamically in a collective manner, while they become no longer correlated on a long-range scale. The insights obtained are expected to facilitate the understanding of the magnetic superexchange mechanisms and their dependencies on the

4. The $A\text{FeO}_2$ ($A = \text{K}, \text{Rb}$ and Cs) family

Fe—O—Fe angles and distances varying with temperature, in particular on the dynamic disorder of the unclear structure.

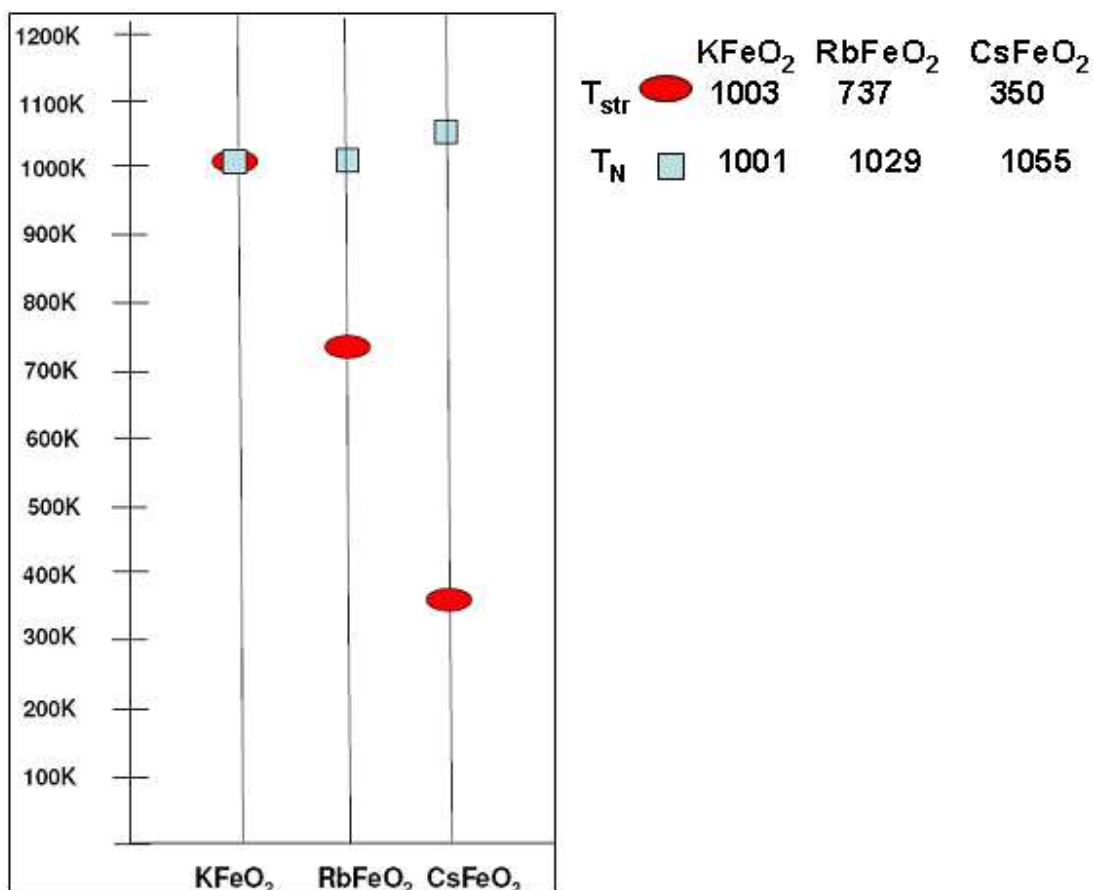


Fig. 4.24. Schematic plot depicting a lucid view of the various temperatures at which the structural phase transitions and magnetic ordering occurs for $A\text{FeO}_2$ ($A=\text{K}, \text{Rb}$ and Cs) polycrystalline samples.

While the temperatures of the structural phase transitions differ significantly in the three studied compounds (~ 1003 K, ~ 737 K and ~ 350 K for $A = \text{K}, \text{Rb}$ and Cs , [*c.f.* section 4.3.3]), the magnetic transition temperatures are very close to each other (~ 1001 , ~ 1027 and ~ 1055 K correspondingly [*c.f.* 4.3.4]) as displayed schematically in Fig. 4.24. The

4. The $A\text{FeO}_2$ ($A = \text{K}, \text{Rb}$ and Cs) family

magnetic structures of all three compounds were determined to be antiferromagnetic with low-temperature saturated value of the magnetic Fe^{3+} moments of $\sim 3.9 \mu_{\text{B}}$, and are characterized by the antiferromagnetic Fe-Fe interactions in all four directions for each Fe ion. The observed value of $\sim 3.9 \mu_{\text{B}}$ of the low-temperature saturated magnetic Fe^{3+} moments is below the physically maximal expected value of $5 \mu_{\text{B}}$ probably because of the combination of the strong covalency effects between the magnetic $3d$ orbitals of Fe and the $2p$ orbitals of oxygen leading to a reduction of the magnetic neutron scattering form factor of Fe, with transfer of magnetic moments to the oxygen ions, implying a net moment on the oxygen ions, see for example [63, 64] and of the defects in the magnetic structures. The direction of Fe^{3+} magnetic moments in KFeO_2 was found to be along the crystallographic b axis, in contrast to the previous finding of the Tomcowicz *et. al.* [25], and in RbFeO_2 and in CsFeO_2 – along the crystallographic c axis.

Ideally it could be nice to find out the reasons for the so close antiferromagnetic transition temperatures in these compounds, while the structural transitions happen to occur at dramatically different temperatures. In the past, different phenomenological parameters were proposed in order to systematize the statistics on the Néel temperatures in the magnetic iron-based oxides, and even to predict them. Yet, having obtained the current newer results on the $A\text{FeO}_2$ ($A=\text{K}, \text{Rb}, \text{Cs}$) compounds, we fail to justify any of these. For example, in [65] (Fig. 4.25-a), the T_{N} in RFeO_3 ($\text{R}=\text{rare earth}$) was found to be proportional to the average cosine of the Fe-O-Fe angles, ranging from ~ 630 to ~ 740 K for the $\cos(\text{Fe—O—Fe})$ changing from ~ 0.78 to ~ 0.92 . In our case [Fig. 4.25(b)], the observed values of the $|\cos(\langle \text{Fe-O-Fe} \rangle_{\text{orth}})| / |\cos(\text{Fe-O-Fe})_{\text{cub}}|$ obviously do not scale similarly to predict the almost identical temperatures of the antiferromagnetic phase

4. The $AFeO_2$ ($A = K, Rb$ and Cs) family

transitions. They amount to ~ 0.77 , ~ 0.84 and ~ 0.92 for $A=K, Rb$, and Cs respectively at the antiferromagnetic transition temperatures; yet not only are the Neel temperatures very close to each other, but also they all fall completely out of range predicted in [65] for the $RFeO_3$ compounds.

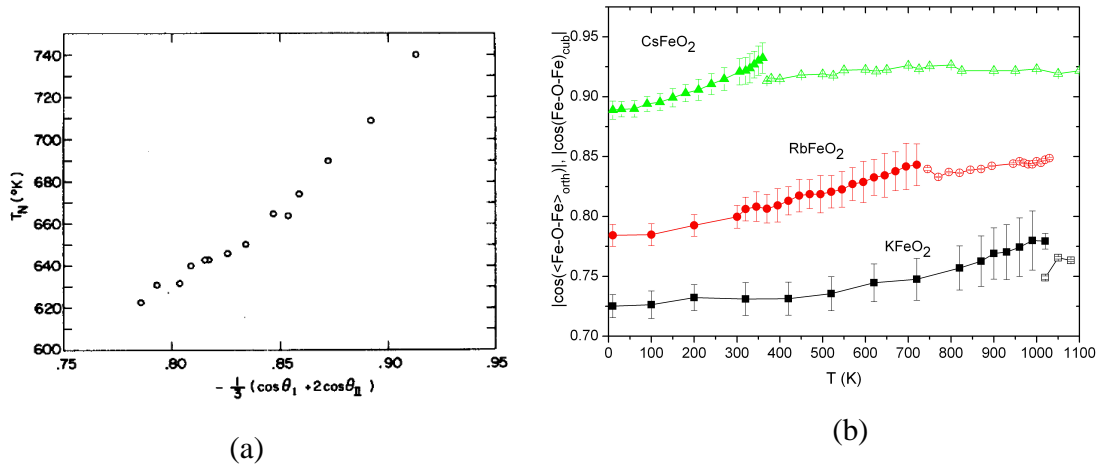


Fig. 4.25. (a): Figure scanned from Ref. [65] showing the systematic dependence of the T_N values for the $RFeO_3$ compounds on $\langle \cos(Fe-O-Fe) \rangle$, (b): the similar values derived from the neutron powder diffraction data on the $AFeO_2$ ($A=K, Rb, Cs$) compounds in our study [c.f. 4.3.4]

In [66], a value of T_c/n , where T_c is an antiferromagnetic transition temperature, and n is the effective coordination number of Fe in different simple and mixed iron oxides was found to be on average equal to 115K (ranging from 106 K to 132 K). In our study, again, this parameter (assuming the ideal 4-fold coordination for Fe) would have to amount to ~ 250 , ~ 257 and 264 K for $A=K, Rb$ and Cs correspondingly, thus falling far out of the predicted in [66] values.

Apart from the mentioned above empirical quantities, also other possibilities have been explored. For example in [67], for the case of the $RMnO_3$ manganites (R = rare earth), a puzzling $T_N \sim \langle \cos^2\phi \rangle$ proportionality has been established - which again is not consistent with our case as well.

4. The $AFeO_2$ ($A = K, Rb$ and Cs) family

Finally, in [68], the empirical proportionality of the exchange energy and of the magnetic

transition temperatures to the $\frac{|\cos(M-O-M)|}{d_{M-O}^{3.5}}$ ratio, where M-O is the metal-oxygen

bond length, and M-O-M is the valence M-O-M angle for the case of the σ -bonding between the d -orbitals of metal and the p -orbitals of oxygen is discussed. In our case, this

again would be incompatible if we take the M-O bond lengths, yet there might be some kind of a universal scaling obtained if we take the M-M bond lengths (Fe-Fe distances in

our case) instead. The temperature dependences of the values of $\frac{|\cos(Fe-O-Fe)|}{d_{Fe-Fe}^{3.5}}$ are

presented in the Fig. 4.26.

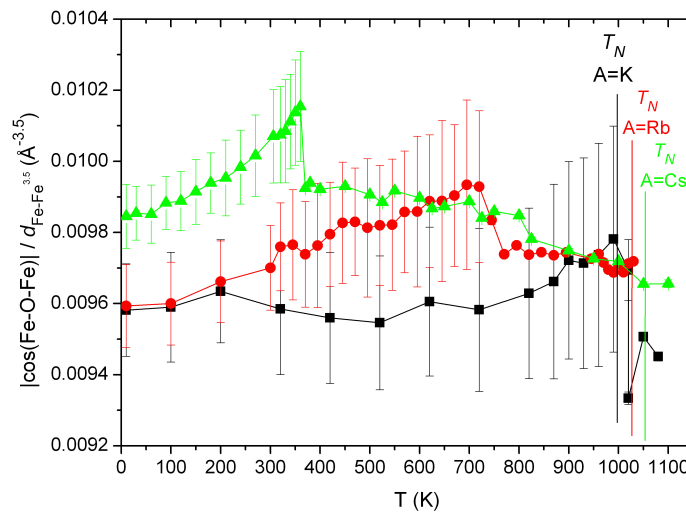


Fig. 4.26. Temperature dependences of the $\frac{|\cos(Fe-O-Fe)|}{d_{Fe-Fe}^{3.5}}$ value for the $AFeO_2$ ($A=K, Rb, Cs$) compounds.

In a very recent publication [69], the origin of the high Neel temperatures in $KFeO_2$ and $RbFeO_2$ has been addressed by employing first-principles band-structure calculations and Monte-Carlo simulation. The authors were able to show that it is exactly the extremely

4. The $A\text{FeO}_2$ ($A = \text{K}, \text{Rb}$ and Cs) family

short Fe–O bond lengths in the KFeO_2 and RbFeO_2 (significantly shorter than in various $A\text{FeO}_3$ oxides) which contribute to the much stronger covalency of these bonds, with exceptionally strong p–d hybridization producing the molecular bondlike states. Such highly localized states are claimed to be responsible for the unexpectedly strong superexchange interactions between the Fe ions and to lead to the exceptionally high values of T_N in the KFeO_2 and RbFeO_2 compounds. The predicted transition temperatures in [69] for KFeO_2 and RbFeO_2 amount to 804 K and 821 K respectively, whereas in present investigation, the experimentally observed Neel temperatures [60] have been found to be even higher — ~ 1001 K and — ~ 1027 K respectively, and the one observed in CsFeO_2 (~ 1055 K) is herewith the highest ever observed in Fe oxides.

However, concerning the obvious failure of previous concepts in rationalizing T_N , one must keep in mind that the systems under consideration here are rather unique because of the counteracting factors of influence (Fe-O-Fe angle and Fe-Fe distance) and also because the systems are dynamically disordered. This latter influence is hard to assess, thereby it requires an independent probe for the structural and magnetic transformation with a different time resolution, namely Moessbauer spectroscopy [*c.f. sec. 4.5*].

4.5. Mössbauer Spectroscopy on RbFeO_2 and CsFeO_2

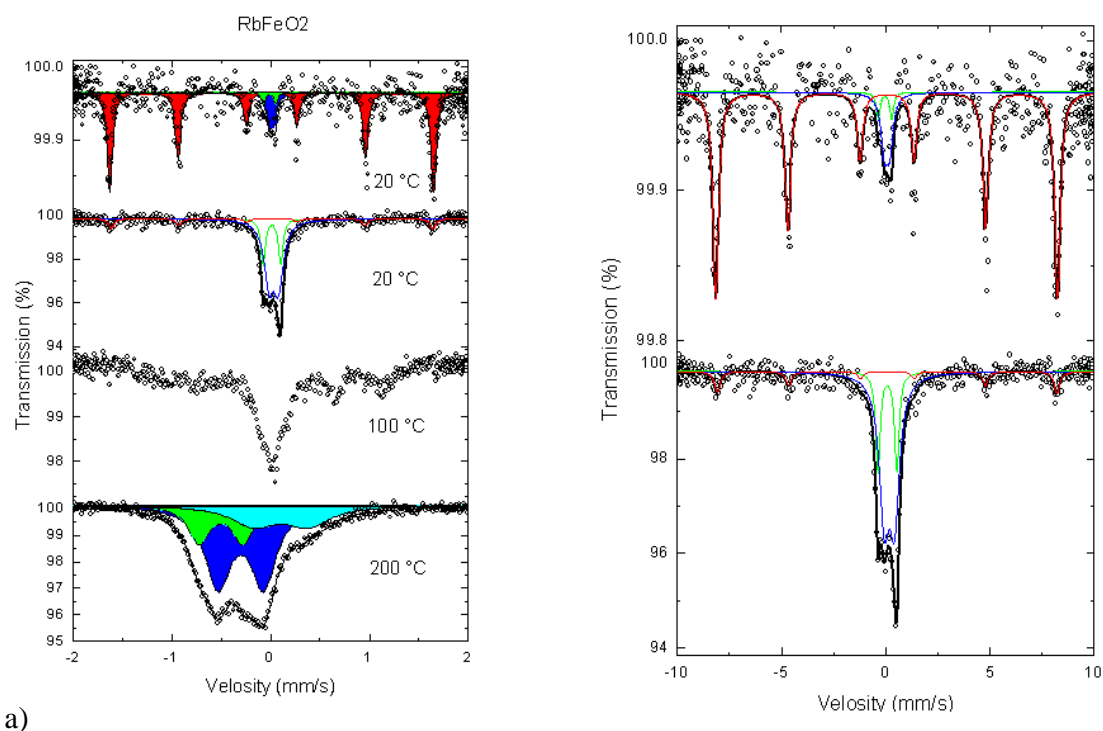
A short report on the Mössbauer Spectroscopy on KFeO_2 in a wide temperature range (80-993 K) confirms the Neel temperature for KFeO_2 to be 983 ± 10 K [70]. In much analogy we extended the Moessbauer investigation to the whole family of $A\text{FeO}_2$ [$A=\text{K}, \text{Rb}$ and Cs] compounds and come up with the following.

4. The $A\text{FeO}_2$ ($A = \text{K}, \text{Rb}$ and Cs) family

4.5.1 Mössbauer Spectroscopy on RbFeO_2

Fig. 4.27 a) shows the temperature dependent spectra that we obtained upon heating RbFeO_2 from room temperature to 200°C in streaming argon gas.

Unfortunately, we have to admit that the compound has transformed during opening of ampoule. This transformation is clearly shown in Fig. 4.27 (b), which compares the Mössbauer spectra ‘before’ and ‘after’ opening of ampoule. The initial spectrum taken at room temperature shows a sextet (shaded red) due to pure RbFeO_2 alongwith two tiny doublets (shaded blue and green) at the centre due to impurity contribution. And upon heating till 200°C the spectra do not show any magnetic splitting (sextet) anymore, validating the decomposition of air and moisture sensitive sample.



a)

Fig. 4.27. Mössbauer spectra of RbFeO_2 : **a)** at several temperatures, in streaming argon gas (except for spectrum at top, see text). **b)** Mössbauer spectra of RbFeO_2 taken at room temperature in closed ampoule (top) and after opening (bottom) in argon atmosphere.

4. The $AFeO_2$ ($A = K, Rb$ and Cs) family

The intensity of magnetically split subspectrum measured in quartz ampoule has a value about IS (sextet) = 84% and after opening the quartz ampoule in flowing argon the intensity of sextet drops to about 11%.

4.5.2. Mössbauer Spectroscopy on $CsFeO_2$

Fig. 4.28 below shows the Mossbauer spectrum of $CsFeO_2$ measured between room temperature and upon heating till 850°C in argon atmosphere. With increase in temperature ($> 500^\circ\text{C}$) the signal to noise ratio (S-N) gets worsen. The initial spectrum taken at room temperature Fig. 4.28 (a) depicts two subspectra that can be recognized – a sextet and a double at the centre. The sextet can solely be assigned to the $CsFeO_2$ pure powder. The hyperfine parameters resulting from the fit are listed in Table 4.14.

Table 4.14: Isomer-shift (IS) relative to $\alpha\text{-Fe}$ (mm/s), half width Γ of the lines with Lorentzian shape (mm/s), quadrupole splitting QS (mm/s), internal magnetic field (H) and area A (%).

	<i>IS</i>	<i>QS</i>	<i>H</i>	<i>$\Gamma/2$</i>	<i>Area</i>
	(mm/s)	(mm/s)	(T)	(mm/s)	(%)
Doublet 1	-0.29(17)	1.27(28)	--	0.59(24)	8.1 (1.9)
Sextet 1	0.2044(44)	0	51.615(36)	0.187(10)	62.7 (4.0)
Sextet 2	0.207(38)	0	47.93(45)	0.452(90)	29.2 (7.2)

4. The $A\text{FeO}_2$ ($A = \text{K}, \text{Rb}$ and Cs) family

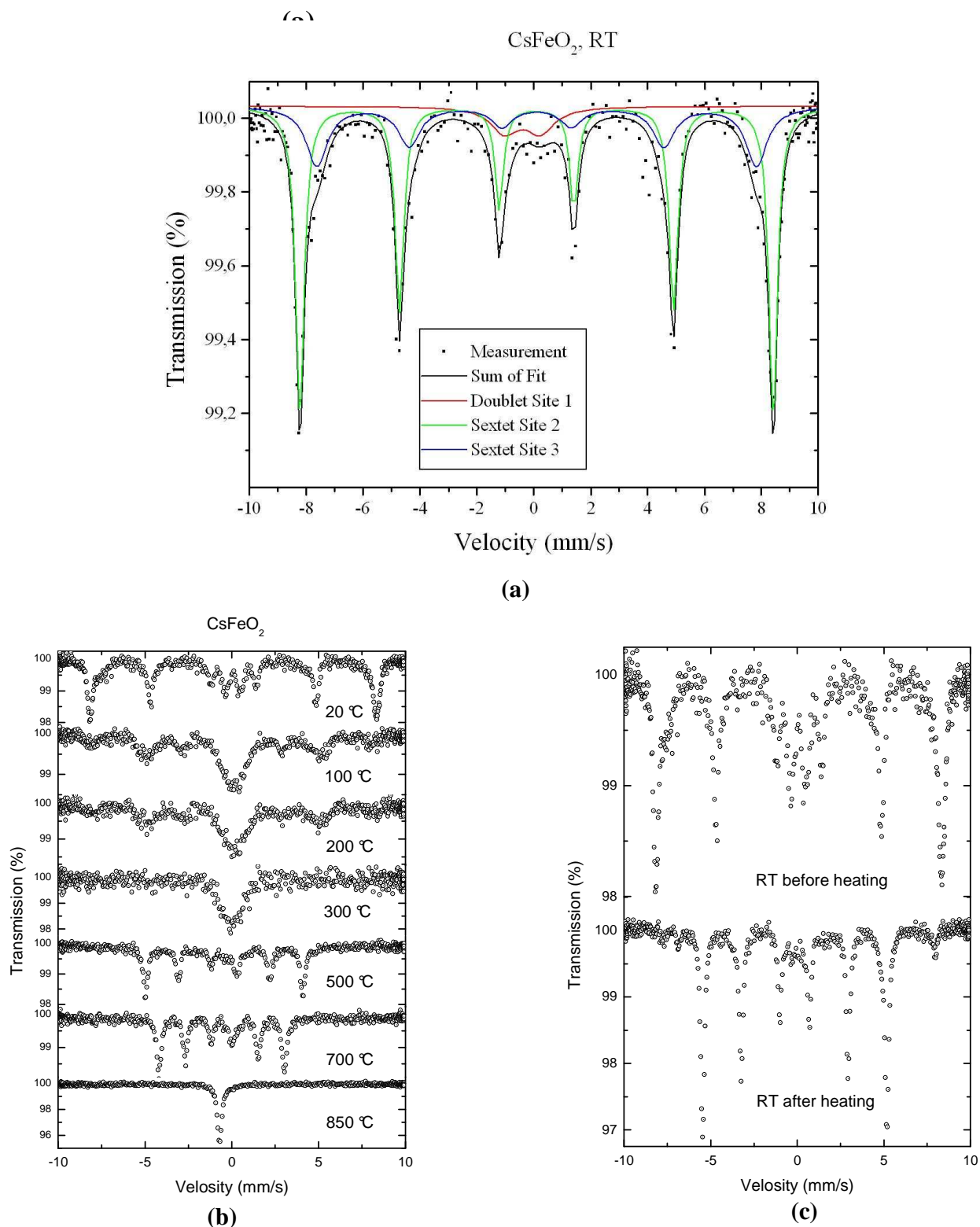


Fig. 4.28. Mössbauer spectrum of CsFeO_2 in streaming argon gas: **a)** Room temperature (5 days measuring time) **b)** high temperature (37 days measuring time) **c)** comparison of Moessbauer spectra before and after heating the sample (RT). **Courtesy:** M. Myndyk, Dr. Sven-Ulf Weber K.D. Becker Institut für Physikalische und Theoretische Chemie, TU Braunschweig.

4. The $AFeO_2$ ($A = K, Rb$ and Cs) family

The oxidation state and the coordination of iron can be determined comparing the resulting isomer shift values with Fig. 4.29.

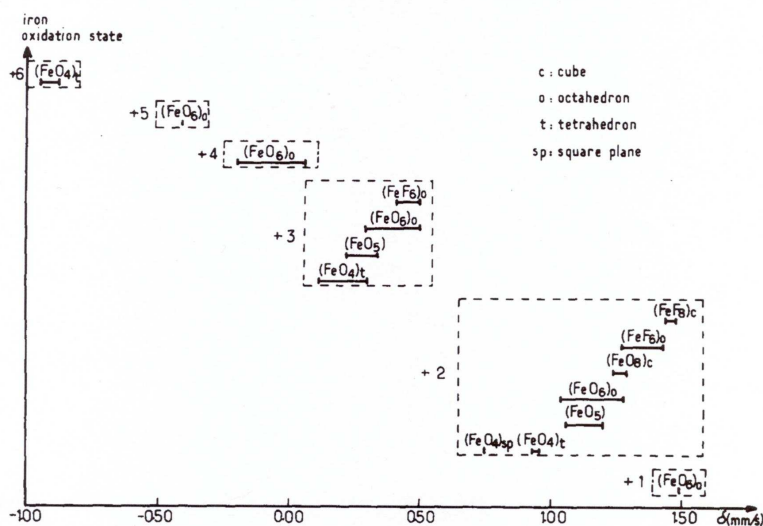


Fig. 4.29. Isomer shifts of different Fe-X polyhedra at room temperature. [71]

According to this comparison, Sextet 1 and 2 can be assigned to magnetic ordered, tetrahedrally coordinated Fe^{3+} , while doublet 1 can be assigned to paramagnetic ordered, octahedrally coordinated Fe^{4+} . It must be admitted, however, that the existence of the doublet - due to the low signal to noise of the spectrum - is not fully reliable.

As displayed in Fig. 4.28 (b), the trend that can be observed from the spectra from room temperature up to $300^{\circ}C$ is the disappearance of the magnetic subspectrum. In parallel, a broad singlet line appears at the centre. Then at $500^{\circ}C$ and above, the spectra show a magnetic splitting again. Which later, at $800^{\circ}C$ results in collapsing of magnetic hyperfine splitting with a bit narrow half width of spectrum without any quadrupole splitting.

4. The $A\text{FeO}_2$ ($A = \text{K}, \text{Rb}$ and Cs) family

Fig. 4.30 shows the temperature dependence of internal magnetic field. Between room temperature and 400°C there is a 15 % decrease in the local magnetic field from 51,1 T to 42,8 T. The slope of the curve is in well agreement with the Brillouin function for $S=5/2$ system and in agreement with the high temperature neutron scattering experiments performed for KFeO_2 by Ichida *et. al* [70]. However, there could be two explanations; either the compound gets magnetic again with rising temperature, or the material at 500°C has already been transformed. From the magnetic splitting observed back at room after the high-temperature measurements it can be concluded that the spectrum at and above 500°C is due to metallic iron. However the kink shown in magnetic susceptibility measurement and anomaly in case of neutron scattering experiments at around 350 K, demands further investigation of issue.

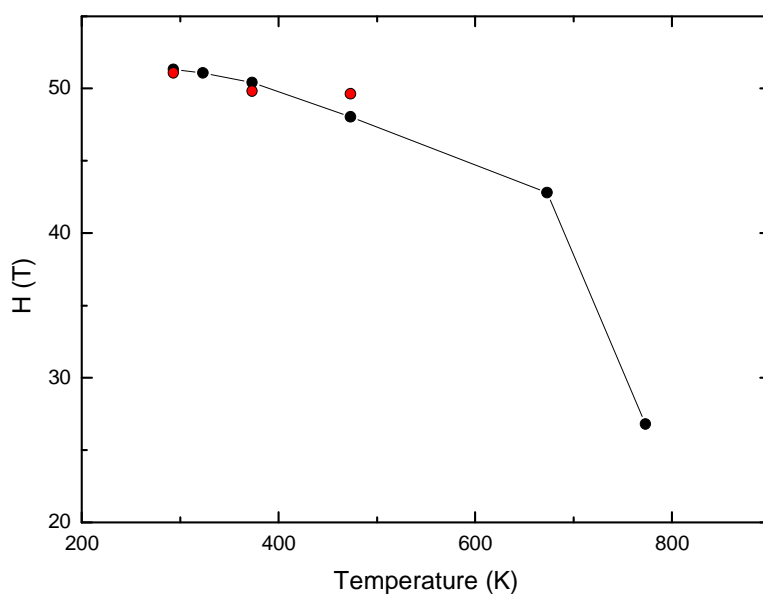


Fig. 4.30. Temperature dependence of local magnetic field of ^{57}Fe in CsFeO_2 .

Black Symbols: Moessbauer study; Red dots: Neutron study

4. The $AFeO_2$ ($A = K, Rb$ and Cs) family

Briefly, although it appears impracticable to perform high-temperature Mössbauer measurements on $CsFeO_2$ under the given conditions due to the interaction of the material with the flowing argon/hydrogen atmosphere and aggressive reaction of sample with wall of quartz tube (Fig. 4.31).

The use of Vanadium foil of thickness 5 micron is a step forward but still some modification in sample holder needs to be done for successful high temperature Moessbauer investigation.

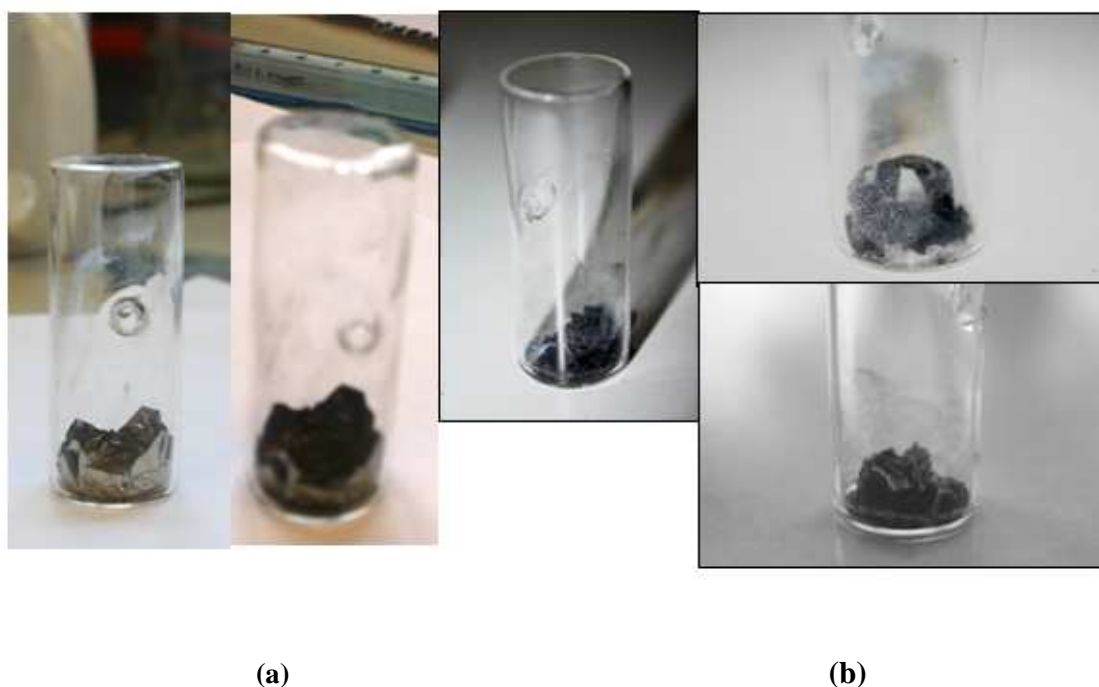


Fig. 4.31. Sample Holder (*self made*) for Moessbauer Spectroscopy. a) before measurement, b) after end of measurement of 37days.

In conclusion, as discussed in detail [*c.f section-4.3.4*], the extremely high value of T_N (e.g. $CsFeO_2 = T_N 1050 K$) could not be harmonized with various models and concepts already available in literature. Unlike the $\alpha \rightarrow \beta$ cristobalite transformation which took

4. The $A\text{FeO}_2$ ($A = \text{K}, \text{Rb}$ and Cs) family

almost a century to resolve, here in present study, our system is in itself unique because of the counteracting factors of influence (Fe-O-Fe angle and Fe-Fe distance), and unlike silicon here we have magnetic centre (Fe), and above all the systems are dynamically disordered. This latter influence is hard to assess, and is still a subject of further investigation both theoretically and experimentally.

4.6. Parametric Rietveld refinement (direct access to the order parameters)

The ferroelastic phase transition of CsFeO_2 (*the deviation of the framework crystal structure of CsFeO_2 relative to the high-symmetry parent structure*) has been studied in the temperature range from 303 K to 409 K by sequential (individual) and parametric Rietveld refinement. Both symmetry mode (SM) and rigid-body (RB) refinements were performed. For both types of parametric Rietveld refinements (SM, RB), the lattice parameters varied only slightly. In contrast to sequential Rietveld refinement of individual dataset independently, whereby for a set of 100 powder diffraction patterns collected at different temperatures each requiring refinement of 20 parameters, one requires 100 independent refinement using 2000 parameters in total [72]. However using the '*Parametric Rietveld refinement method approach*', any parameter can be described by a *single overall function (value)* describing its evolution throughout the data collection, and can be simultaneously refined from a large ensemble of diffraction data.

Software packages like (e.g. ISODISPLACE [73, 74] and AMPLIMODES [75]), were employed to automatically reparameterize a low-symmetry structure in terms of symmetry-adapted order parameters of a higher symmetry structure and then later the results were saved as a system of linear equations in TOPAS .str format [74].

4. The $A\text{FeO}_2$ ($A = \text{K}, \text{Rb}$ and Cs) family

The parametric model produced diffraction patterns that agreed well with corresponding experimental patterns at each temperature, demonstrated the effectiveness of the parametric approach and the inclusion of an adequate structural-parameter set.

Below the phase transition, all strain order parameters and lattice parameters exhibit the anticipated *power law trends*, while above the transition, the lattice parameters can be adequately fitted using a linear function within the investigated temperature range.

In our investigation the semiautomated parametric refinement of structural order parameters (*e.g. lattice strain, displacive, occupancy*) that arise at the cubic-orthorhombic structural phase transition of CsFeO_2 is described. This parametric refinement against diffraction patterns collected over a wide range of temperatures yielded power-law exponents and coefficients describing the evolution of the atomic displacements and the ferroelastic lattice-strains that contribute to the distortion.

Two different parameterizations of the distortion, the symmetry-adapted distortion mode description and the internal rigid-body (*i.e. z-matrix*) description, proved to be closely related due to the natural tendency of symmetry modes to produce polyhedral tilts like those observed in CsFeO_2 .

A suitable rigid building unit that describes both the low and high-temperature CsFeO_2 structures consists of two regular corner-sharing FeO_4 tetrahedra that are tilted with respect to each other as shown in Fig. 4.32.

Taking symmetry equivalent positions into account, the resulting rigid body consists of four oxygen and two iron atoms with two tilting angles and the average Fe-O distance as internal degrees of freedom. The two tilt angles are (1) the Fe1-O1-Fe2 (tilt-1) bond angle and (2) the O4-Fe2-O1-Fe1 torsion angle (tilt-2) between the two tetrahedra. For

4. The $AFeO_2$ ($A = K, Rb$ and Cs) family

the Rietveld refinement, the rigid body was set up in form of a z-matrix that naturally describes the position of each atom in terms of its distance, angle and torsion angle relative to previously defined atoms [76]. The bridging O1 oxygen atom of the two tetrahedra was used as the centre of the rigid body.

The orientation and position of the rigid body relative to the internal coordinate system of the crystal was held constant over the entire temperature range of investigation and only the three internal degrees of freedom were subjected to refinement. As the two Cs atoms in the voids of the framework are independent of the rigid body, their crystallographically relevant atomic coordinates were refined separately.

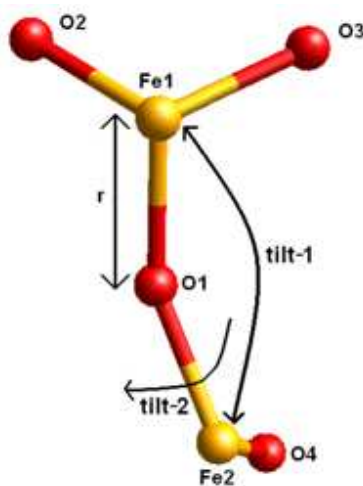


Fig. 4.32. Rigid body consisting of the crystallographically independent atoms of the structure building double tetrahedron in $CsFeO_2$ exhibiting three internal parameters: r , **tilt-1** and **tilt-2**.

With both models, the automated parametric refinement greatly increased the speed of the refinement and post-refinement analysis. We have seen that the parametric Rietveld refinement of symmetry modes and internal rigid body parameters as a function of external variables proved to be a powerful tool for investigating structural phase transitions.

4.7. References

- [1] T. F. W. Barth, Amer. J. Sci. **24**, 97-110 (1932).
- [2] W. Nieuwenkamp, Z. Kristallogr. **92**, 82-88 (1935).
- [3] W. A. Dollase, Z. Kristallogr. **121**, 369-377 (1965).
- [4] D. R. Peacor, Z. Kristallogr. **138**, 274-298 (1973).
- [5] R. W. G. Wyckoff, Amer. J. Sci. **9**, 448-459 (1925).
- [6] T. F. W. Barth, Amer. J. Sci. **23**, 350-356 (1932).
- [7] W. Nieuwenkamp, Z. Kristallogr. **96**, 454-458 (1937).
- [8] A. J. Leadbetter, T.W. Smith, and A. F. Wright, Nature Phys. Sci. **244**, 125-126 (1973).
- [9] A. F. Wright and A. J. Leadbetter, Philos. Mag. **31**, 1391-1401 (1975).
- [10] M. O'Keefe and B. G. Hyde, Acta Cryst. B, **32**, 2923-2936 (1976).
- [11] W. W. Schmahl, I. P. Swainson, M. T. Dove and A. Graeme-Barber, Z. Kristallogr. **201**, 125-145 (1992).
- [12] I. P. Swainson, M. T. Dove and D. C. Palmer, Phys. Chem. Miner. **30**, 353-365 (2003).
- [13] D. R. Spearing, I. Farnan and J. F. Stebbins, Phys. Chem. Miner. **19**, 307-321 (1992).
- [14] B. L. Phillips, J. G. Thompson, Y. Xiao and R. J. Kirkpatrick, Phys. Chem. Miner. **20**, 341-352 (1993).
- [15] Akira Takada, P. Richet, C. R. A. Catlow, G. D. Price, J. Non-Cryst. Solids, **354**, 181-187 (2008).
- [16] G. L. Hua, T. R. Welberry, R. L. Withers and J. G. Thompson, J. Appl. Crystallogr. **21**, 458-465 (1988).
- [17] L. Gracia, J. Contreras-Garcia, A. Beltran, J. M. Recio, High Pressure Research, **29**, 93-96 (2009).
- [18] Shamus L. G. Husheer, John G. Thompson and Alexandra Melnitchenko, J. Solid State Chem. **147**, 624-630 (1999).
- [19] F. Liu, S. H. Garofalini, R. D. King-Smith and D. Vanderbilt, Phys. Rev. Lett. **70** 2750 (1993).
- [20] I. P. Swainson and M. T. Dove, Phys. Rev. Lett. **71**, 3610 (1993).

4. The $AFeO_2$ ($A = K, Rb$ and Cs) family

- [21] D. Taylor, *Mineral. Mag.* **48**, 65-79 (1984).
- [22] D. M. Hatch and S. Ghose, *Phys. Chem. Min.* **17**, 554-562 (1991).
- [23] M. Tabuchi, K. Ado, H. Kobayashi, I. Matsubara, H. Kageyama, M. Wakita, S. Tsutsui, S. Nasu, Y. Takeda, C. Masquelier, A. Hirano and R. Kanno, *J. Solid State Chem.* **141**, 554-561 (1998).
- [24] F. Bertaut and P. Blum, *C. R. Acad. Sci.* **239**, 429-431 (1954).
- [25] Z. Tomkowicz and A. Szytuła, *J. Phys. Chem. Solids* **38**, 1117-1123 (1977).
- [26] R. Hoppe, *Angew. Chem.* **77**, 551. *Angew. Chem. Int. Ed. Engl.* **4**, 534-535 (1965).
- [27] G. Frisch, and C. Röhr, *Z. Naturforsch.* **59b**, 771-781 (2004).
- [28] R. W. Cahn, *Adv. Phys.* **3**, 363-445 (1954).
- [29] J. V. Smith and W. L. Brown, *Feldspar Minerals, 1. Crystal structures, physical, chemical, and microtexture properties (sec. Ed.)*. Springer Verlag, Berlin, Germany (1988).
- [30] I. E. Grey, Roderick J. Hill and Alan W. Hewat, *Z. Kristallogr.* **193**, 51-69 (1990).
- [31] J. C. Anderson and M. Schieber, *J. Phys. Chem. Solids*, **25**, 961-968 (1964).
- [32] R. Famery, P. Bassoul and F. Queyroux, *J. Solid State Chem.*, **61**, 293-300 (1986).
- [33] R. Hoppe, *Angew. Chem.* **77** (1965) 551; *Angew. Chem. Int. Ed. Engl.* **4**, 534-535 (1965).
- [34] E. Vielhaber and R. Hoppe, *Z. Anorg. Allg. Chem.* **369**, 14-32 (1969).
- [35] C. W. F. T. Pistorius, G. F. de Vries, *Z. Anorg. Allg. Chem.* **395**, 119-121 (1973).
- [36] J. Nuss, N. Z. Ali, M. Jansen, *Acta Crystallogr.* **B63**, 719-725 (2007).
- [37] G. Frisch, C. Röhr, *Z. Naturforsch.* **59b**, 771-781 (2004).
- [38] T. F. W. Barth, *J. Chem. Phys.* **3**, 323-325 (1935).
- [39] D. Trinschek, M. Jansen, *Angew. Chem.* **111** 234-235 (1999); *Angew. Chem. Int. Ed. Engl.* **38**, 133-135 (1999).
- [40] M. Sofin, E.-M. Peters and M. Jansen, *Z. Anorg. Allg. Chem.* **628**, 2697-2700 (2002).
- [41] H. D. Fair and R. F. Walker, *Energetic Materials*, vol. 1. (pp 30-38) Physics and chemistry of inorganic azides, Plenum press, New York and London (1977).

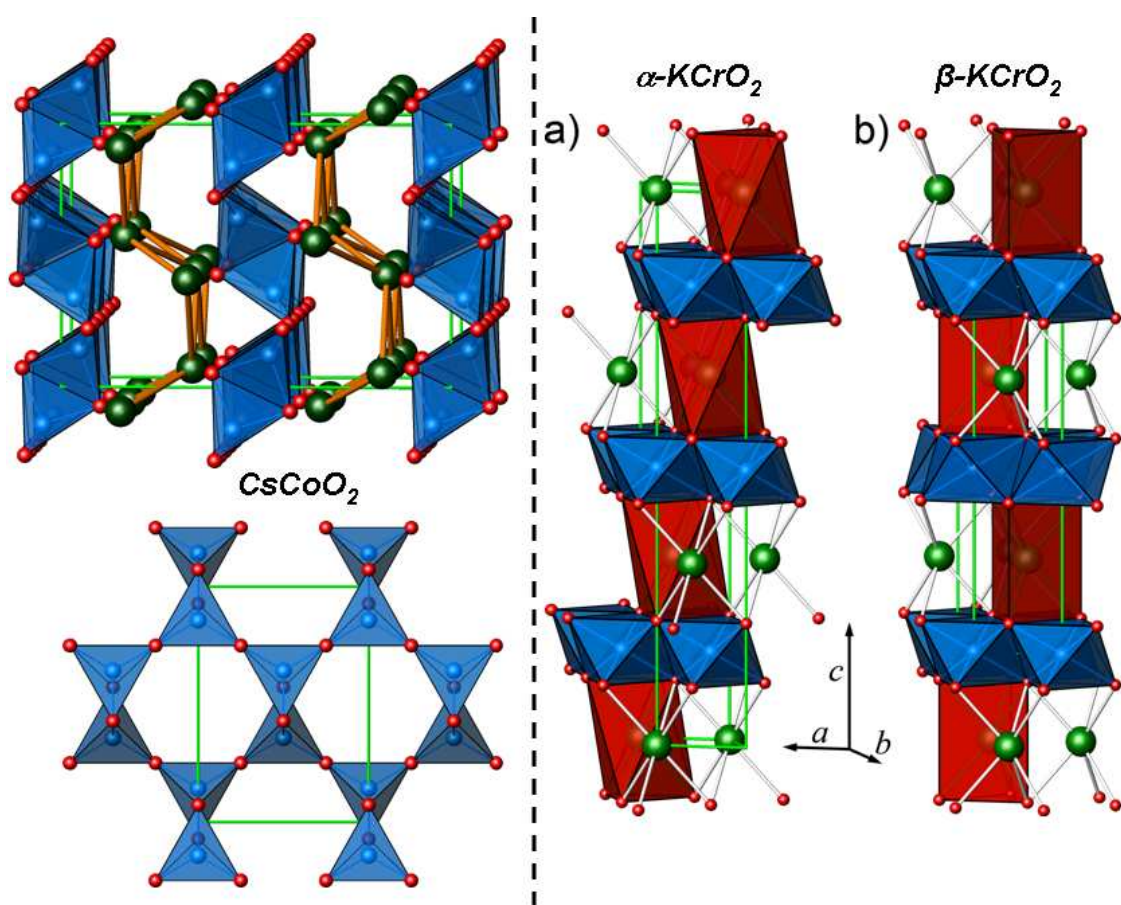
4. The $AFeO_2$ ($A = K, Rb$ and Cs) family

- [42] *Bruker Suite*, version 2008/3, Bruker AXS Inc., Madison, WI, USA (2008).
- [43] J. Nuss, M. Jansen, *Acta Crystallogr.* **B63**, 843-849 (2007).
- [44] G. M. Sheldrick, *TWINABS—Bruker AXS scaling for twinned crystals*, version 2008/4, University of Göttingen, Germany (2008).
- [45] G. M. Sheldrick, *SADABS—Bruker AXS area detector scaling and absorption*, Version 2008/1, University of Göttingen, Germany (2008).
- [46] G. M. Sheldrick, *Acta Crystallogr.* **A64**, 112–122 (2008).
- [47] G. Langlet, *C. R. Hebd. Seances Acad. Sci.*, **259**, 3769-3770 (1964).
- [48] <http://sls.web.psi.ch/view.php/beamlines/ms/pd/index.html>
- [49] M. E. Fleet, *Acta Crystallogr. B*, **37**, 917-920 (1981).
- [50] S. Nariki, S. Ito, K. Kozawa, T. Uchida and N. Yoneda, *Solid State Ionics*, 40-41, 95-98 (1990).
- [51] Akira Niwata and Kazuyuki Itoh, *J. Phy. Soc. Jpn.* **64**, 4733-4738 (1995).
- [52] J. Rodríguez-Carvajal, *Physica B*, **192**, 55-69 (1993).
- [53] Fischer P *et al* *Physica B* **276** 146-148 (2000).
<http://sinq.web.psi.ch/sinq/instr/hrpt/index.html>
- [54] Wills A S *Physica B* **276** 680 (2000). Program available from www.ccp14.ac.uk.
- [55] H. Lueken, *Magnetochemie*, Teubner, Leipzig, (1999).
- [56] Hahn, Th. & Klapper, H.. *International Tables for Crystallography*, edited by Authier, Vol. D, ch. 3.3, pp. 393–448. Dordrecht: The Netherlands: Kluwer Academic Publishers (2003).
- [57] H. Wondratschek, U. Müller (Editors), *International Tables for Crystallography*, Vol. A1. Dordrecht, The Netherlands: Kluwer Academic Publishers (2004).
- [58] U. Müller, *Z. Anorg. Allg. Chem.* **630**, 1519-1537 (2004).
- [59] H. Bärnighausen, *MATCH, Commun. Math. Chem.* **9**, 139-175 (1980).
- [60] D. Sheptyakov, N. Z. Ali, M. Jansen, *Journal of Physics: Condensed Matter* **22**, 426001 (2010).
- [61] J. R. Goldschmidt and D. M. Jenkins, *Am. Mineral.* **70**, 911-923 (1985).
- [62] H. Xu, D. R. Veblen and G. Luo, *Acta. Cryst.* **A51**, 53-60 (1995).
- [63] E. Byrom, A. J. Freeman and D. E. Ellis, *AIP Conf. Proc.* **24** 209-210 (1974).
- [64] B. C. Tofield and B. E.F. Fender, *J. Phys. Chem. Solids*, **31** 2741-2749 (1970).

4. The $AFeO_2$ ($A = K, Rb$ and Cs) family

- [65] D. Treves, M. Eibschütz and P. Coppens, *Phys. Lett.* **18**, 216-217 (1965).
- [66] M. A. Gilleo, *Phys. Rev.* **109** 777-781 (1958).
- [67] Zhou J -S and Goodenough J B, *Phys Rev. B* **68**, 054403 (2003).
- [68] W. A. Harrison, "Electronic Structure and the Properties of Solids", San Francisco: Freeman, (1980).
- [69] M. Kim, B. H. Kim, H. C. Choi and B. I. Min, *Phys. Rev. B* **81** 212405 (2010).
- [70] T. Ichida, T. Shinjo, Y. Bando and T. Takada, *J. Phys. Soc. Japan* **29** 1109-10, (1970).
- [71] F. Menil, *J Phys Chem Solids* 46(7):763-789 (1985).
- [72] G. W. Stinton and J. S. O. Evans, *Parametric Rietveld refinement*, *J. appl. Crystallography* **40**, 87-95 (2007).
- [73] B.J. Campbell, H.T. Stokes, D.E. Tanner and D.M. Hatch: *J. Appl. Cryst.* **39**, 607 (2006).
- [74] B.J. Campbell, J S.O. Evans, F.Perselli, H.T.Stokes, *IUCr Computing Commission Newsletter* **8**, 81-95 (2007)
- [75] D. Orobengoa, C. Capillas, M.I. Aroyo and J.M. Perez- Mato: *J. Appl. Cryst.* **A42**, 820 (2009).
- [76] A.R. Leach: *Molecular Modelling: Principles and Applications* (Prentice-Hall, 1996).

Chapter. 5: New two dimensional layered magnetic oxides



Chapter 5

New two dimensional layered magnetic oxides

5-A: Synthesis, crystal structure and magnetic properties of CsCoO_2 , a new two dimensional layered structure.

5.1 Introduction

The importance of magnetic transition metal oxides has shown a spectacular increase in the last few decades. Transition metal oxides with two dimensional layered structures became the subject of interest for scientific community after the discovery of superconductivity ($T_c = 5\text{K}$) in $\text{Na}_x\text{CoO}_2 \cdot y\text{H}_2\text{O}$. Takada *et. al.* reported in Nature [1] that sodium cobalt oxide is oxidized to reduce its sodium content and further intercalated with water to further separate the cobalt oxide layers, resulting in a novel 2-D superconductor. The superconducting phase is confined to the narrow interval $\frac{1}{4} < x < \frac{1}{3}$ [2]. The essential role of water molecules in stabilizing the superconducting state is the ability of water molecules to screen strongly fluctuating electrostatic potential of the Na ions from the charge carriers in the CoO_2 layers [3—5]

In addition to high-temperature superconductivity, they also exhibit multitude of exotic phenomenon like, thermoelectricity, multiferroicity, metalinsulator transition, colossal

5. Two dimensional layered magnetic oxides

magnetoresistance (CMR) effect, cathode materials in solid oxide fuel cells, spin (up/down) and charge degrees of freedom, which shifts the attention of the scientific community entangled to find reason of superconductivity in cuprates related compound.

Generally, oxides have been regarded as unsuitable for thermoelectric (TE) applications because of their poor electrical conductivity. However a layered transition-metal oxide NaCo_2O_4 first identified by Jansen and Hoppe [6], became the focus of interest after 23 years of its discovery when I-Terasaki *et. al.* in 1997 reported high TE performances in NaCo_2O_4 and reported it as a potential thermoelectric material [7]. High temperature stability, oxidation durability, nontoxicity, low cost and high performances make the layered cobalt oxides the best choice in power generators applications. The layered cobalt oxides families belong to P-type TE materials and possess high TE performances due to having the conductive edge-shared CoO_2 layer and disorder states. Some researchers reported electronic structures and transport properties of NaCo_2O_4 , and brought forward that high TE performances of NaCo_2O_4 come from the strong correlated CoO_2 layer [8]. Optimizing electronic structure by adjusting crystal structure is a way to improving TE performances, which provides theoretical sustainment for the choice of material. Layered structures will be superior to other structures keeping in view the the theory of a phonon glass and an electron crystal [9].

The effect of different cations substitutions on TE performances is also extensively investigated [10—11]. Ag substitution among Na-site substitutions shows a remarkable enhancement of the power factor [12]. Cations substitutions mainly change the carrier

5. Two dimensional layered magnetic oxides

concentration, and then affect the electrical conductivity and Seebeck coefficient. Furthermore, a key facet of cobalt oxides that distinguish them clearly from its counterpart is the spin state degree of freedom of the Co^{3+} —ions: it can be low spin (LS, $S=0$), high spin (HS, $S=2$) and even intermediate spin (IS, $S=1$) [13]. For the exemplary LaCoO_3 compound, for illustration, various early studies accredited the low temperature spin state change to be of LS-HS nature, while studies in the last decade put a lot of effort to propose a LS-IS scenario instead. Various spectroscopic studies unearthed spectacular results in recent past about the spin state of Co^{3+} ions in different local coordination [13]. However, in contrast to octahedral coordination of transition metal, a less common coordination geometry observed is the tetrahedron where the weaker crystal field splitting of energy levels [$10Dq(\text{Td}) = 4/9 * 10Dq(\text{Oh})$] favours the high spin complexes. In the present investigation the crystal and magnetic structure of recently identified new two dimensional layered cobaltate, CsCoO_2 will be discussed with Co^{3+} in a unique tetrahedral coordination.

5.2 Experimental Details

Material synthesis. CsCoO_2 has been prepared along the azide/nitrate route [14, 15] as a reddish black microcrystalline powder. Starting materials for the preparation of the CsCoO_2 were CsN_3 , CsNO_3 (Sigma-Aldrich, 99%) and Co_3O_4 . Cobalt oxide (Co_3O_4) was prepared by heating $\text{Co}(\text{C}_2\text{O}_4) \cdot 2\text{H}_2\text{O}$ (Johnson Matthey, 99%) in a flow of oxygen at 623K for 20 h. Whereas the CsN_3 was synthesized from aqueous HN_3 and cesium carbonate [16].

5. Two dimensional layered magnetic oxides

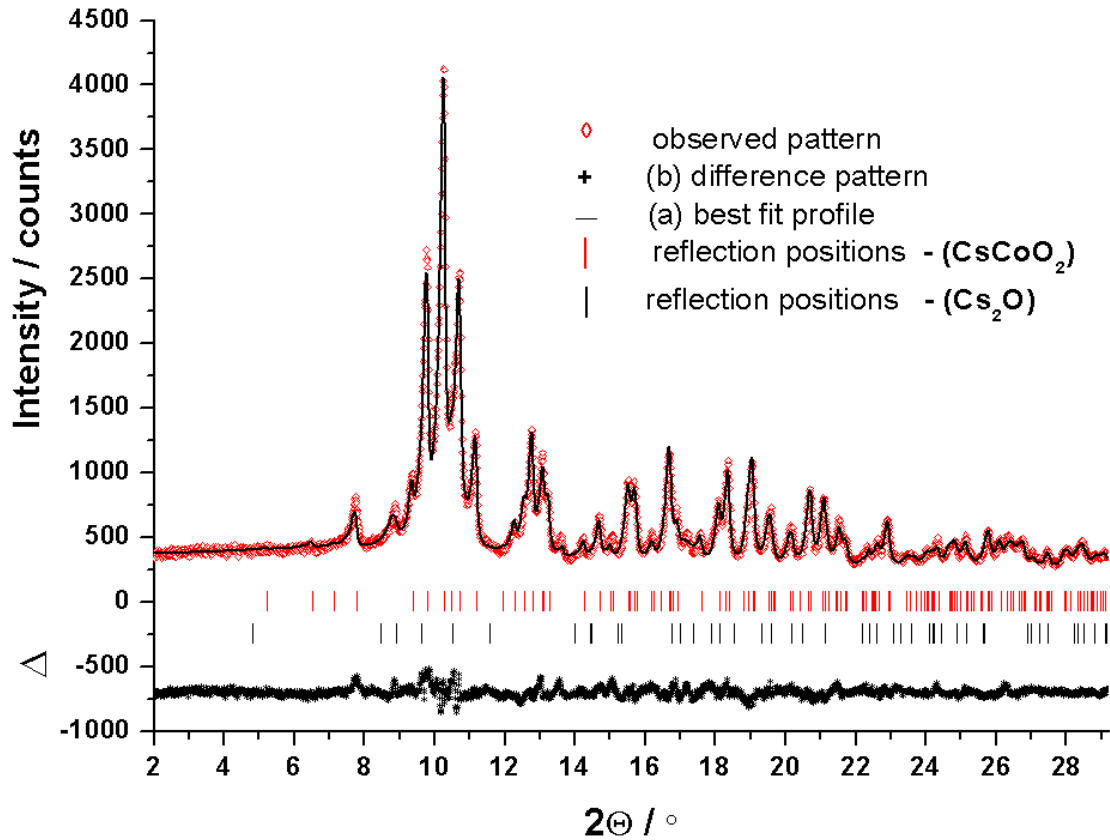


Fig. 5.1. Scattered X-ray intensity for polycrystalline sample of CsCoO_2 at $T = 298$ K as a function of diffraction angle 2θ ($\lambda = 0.559407$ Å), showing the observed pattern (diamonds), calculated profile (line a), difference plot (line b) and reflection markers (vertical bars).

The starting materials were mixed in the ratio required according to (1) and ground in a ball mill, pressed in pellets ($\varnothing 13$ mm) under 10^5 N, dried under vacuum (10^{-3} mBar) at 423K overnight and placed under argon in a tightly closed steel vessel [15], provided with a silver inlay. In a flow of dry argon the following temperature profile was applied: 298→533 K (100 K/h); 533→653 K (5 K/h); 653→833 K (20 K/h); and subsequent annealing for 60 hours at 833 K.

5. Two dimensional layered magnetic oxides



Hazards: The heating profile as stated above must be followed strictly; otherwise the containers may blow up!

The obtained reddish black CsCoO_2 powders, being extremely sensitive to humid air, were sealed in glass ampoules under argon atmosphere and all following manipulations with these substances were performed in inert atmospheres of purified argon.

Structure determination. Reddish black single crystals of CsCoO_2 of approximate size were obtained after 400 hour annealing of the sample at 873 K, in silver crucibles, enclosed in glass ampoules under dried Ar. Better quality crystal of approximate size [0.18 x 0.12 x 0.08 mm³] were singled out and picked for X-ray single crystal diffractometry. Single crystal diffraction data were collected on a three circle diffractometer (Bruker AXS, Karlsruhe, Germany) equipped with a SMART-CCD (APEX I), at 293 K. The collection and reduction of data were carried out with the Bruker Suite software package [17]. Intensities were corrected for absorption effects applying a multi-scan method [18]. The structure was solved by direct methods and refined by fullmatrix least-squares fitting with the SHELXTL software package [19].

The X-ray investigation on powder samples was performed on an STOE StadiP diffractometer with $\text{AgK}\alpha_1$ radiation ($\lambda=0.559407 \text{ \AA}$) at room temperature using a position-sensitive detector and a curved germanium monochromator. The powder diffraction data were collected for duration of 20 hours in the 2Θ range of 4–30° sealed in

5. Two dimensional layered magnetic oxides

0.3 mm quartz capillary (Hilgenberg) kept rotating during data collection for better particle statistics. The collected powder data for CsCoO₂ are given in Fig. 5.1.

The differential scanning calorimetry (DSC) measurements were carried out on a polycrystalline sample of CsCoO₂. The Perkin Elmer (*Pyris 1*) instrument operating in a power compensation mode, was employed with inert atmosphere of He gas (He 4.6, purity 99,996 vol. %). Background contributions were subtracted using external sapphire calibrations. The sample was heated at a rate of 10 K min⁻¹ in a sealed Aluminium crucible upto 600 K. Multiple heating and cooling cycles were performed to ascertain the authenticity of the results.

Electrical Resistivity

Temperature dependent resistivity (conductivity) has been obtained for a pressed pellet of CsCoO₂ powder using van der Pauw method [20, 21]. The polycrystalline sample of CsCoO₂ was pressed into a 6 mm diameter by 1 mm thick pellet. The pellet was then connected to four probes methodology for the resistivity measurement. A current of 10 mA (Keithley 2400 current source) was applied, and the voltage was measured with a Hewlett Packard 34420 nanovoltmeter in temperature range 5K to 281 K at ~5 K interval.

Temperature dependence of the specific heat (C_p) of a polycrystalline sample of CsCoO₂ was measured between 2 and 200 K using a commercial PPMS (Physical Property Measurement System, Quantum Design, 6325 Lusk Boulevard, San Diego, CA.) employing the relaxation method [22, 23]. To thermally fix the sample tablet (Ø = 5 mm and thickness 1mm) to the sapphire sample platform, a minute amount of Apiezon N vacuum grease was used. The heat capacity of the sample holder platform and grease was individually determined in a separate run and subtracted from the total measured heat capacities.

5. Two dimensional layered magnetic oxides

The magnetic susceptibility $\chi(T)$ of polycrystalline powder samples of CsCoO₂ have been measured in the temperature range from 2 K to 300 K in magnetic fields up to 7 T using a SQUID-Magnetometer (MPMS 5.5, Quantum Design). The sample was contained in warily dried SUPRASIL ampoule ($\varnothing = 3$ mm) that was long enough to extend over the coils of the magnetometer. The raw data obtained is finally corrected for temperature independent term (χ_o) [$\chi_o = \chi_{\text{dia}} + \chi_{\text{vv}}$] which accounts for core electrons diamagnetic contribution (χ_{dia}) and van vleck paramagnetic contribution (χ_{vv}) for the Co³⁺ ion. The diamagnetic susceptibility of the core electrons in closed shell can be estimated by incremental method of the all the ions as tabulated, e.g, by Lueken [24], resulting in a total diamagnetic contribution of $\chi_{\text{dia}} = -65.25 \times 10^{-6} \text{ cm}^3/\text{mol}$ per formula unit. Whilst the Van Vleck paramagnetic contribution per Co³⁺: cation amount to [100x $10^{-06} \text{ cm}^3/\text{mol}$] [25].

5.3. Results and discussion

5.3.1. Single crystal X-ray diffraction

5.3.1.1 *Description of crystal structure*

CsCoO₂ can be easily prepared by the azide/nitrate route as a blackish red polycrystalline powder. Experimental details on crystallographic data and data collection are given in Table 5.1. Table 5.2 shows the atomic parameters, coordinates and equivalent isotropic displacement parameters, and Table 5.3 tabulates the anisotropic displacement parameters from the single crystal data. Bond lengths(Å) and angles(°) for CsCoO₂ alongwith the Maple calculations [26, 27, 28] effective coordination numbers and mean fictive ionic radii for CsCoO₂ are given in Table 5.4 and 5.5 respectively.

5. Two dimensional layered magnetic oxides

Table 5.1. Crystal data and structure refinement for CsCoO₂.

Empirical formula	Co Cs O ₂
Formula weight	223.84
Temperature	296(2) K
Wavelength	0.71073 Å
Crystal system	orthorhombic
Space group	Cmca
Unit cell dimensions	a = 5.9904(4) Å α = 90°. b = 12.2558(8) Å β = 90°. c = 8.2736(6) Å γ = 90°.
Volume	607.42(7) Å ³
Z	8
Density (calculated)	4.895 Mg/m ³
Absorption coefficient	17.194 mm ⁻¹
F(000)	784
Crystal size	0.18 x 0.12 x 0.08 mm ³
Theta range for data collection	3.32 to 36.74°.
Index ranges	-9 ≤ h ≤ 9, -20 ≤ k ≤ 20, -13 ≤ l ≤ 13
Reflections collected	5431
Independent reflections	806 [R(int) = 0.0214]
Completeness to theta = 36.74°	99.0 %
Max. and min. transmission	0.3400 and 0.1478
Refinement method	Full-matrix least-squares on F ²
Data / restraints / parameters	806 / 0 / 24
Goodness-of-fit on F ²	1.115
Final R indices [I > 2σ(I)]	R1 = 0.0163, wR2 = 0.0372
R indices (all data)	R1 = 0.0196, wR2 = 0.0387
Largest diff. peak and hole	1.653 and -0.833 e.Å ⁻³

5. Two dimensional layered magnetic oxides

Table 5.2. Atomic coordinates and equivalent isotropic displacement parameters (\AA^2)

for CsCoO₂. U(eq) is defined as one third of the trace of the orthogonalized U^{ij} tensor.

	x	y	z	U(eq)
Cs(1)	0	0.335445(14)	0.07317(2)	0.01997(5)
Co(2)	0	0.04734(3)	0.14257(4)	0.01333(7)
O(1)	0	0.10007(16)	-0.0723(2)	0.0177(3)
O(2)	0.25	0.0875(2)	0.25	0.0246(4)

Table 5.3. Anisotropic displacement parameters (\AA^2) for CsCoO₂.

	U ¹¹	U ²²	U ³³	U ²³	U ¹³	U ¹²
Cs(1)	0.01818(8)	0.02139(8)	0.02033(8)	-0.00282(5)	0	0
Co(2)	0.01119(12)	0.01574(13)	0.01305(13)	0.00193(10)	0	0
O(1)	0.0239(8)	0.0152(7)	0.0141(7)	0.0024(6)	0	0
O(2)	0.0139(8)	0.0376(12)	0.0221(9)	0	-0.0059(6)	0

The anisotropic displacement factor exponent takes the form: $-2\pi^2 [h^2 a^{*2} U^{11} + \dots + 2 h k a^* b^* U^{12}]$

Table 5.4. Bond lengths [\AA] and angles [$^\circ$] for CsCoO₂

Co(2)-O(2)#6	1.8096(7)	O(2)#6-Co(2)-O(2)	111.70(6)
Co(2)-O(2)	1.8096(7)	O(2)#6-Co(2)-O(1)	111.64(5)
Co(2)-O(1)	1.8915(18)	O(2)-Co(2)-O(1)	111.64(5)
Co(2)-O(1)#8	1.898(2)	O(2)#6-Co(2)-O(1)#8	114.15(7)
O(1)-Co(2)#8	1.898(2)	O(2)-Co(2)-O(1)#8	114.15(7)
O(2)-Co(2)#12	1.8096(7)	O(1)-Co(2)-O(1)#8	92.14(8)
Co(2)-Co(2)#8	2.6290(7)		
Co(2)-O(1)-Co(2)#8	87.86(8)	O(2)#6-Co(2)-Co(2)#8	124.10(3)
Co(2)#12-O(2)-Co(2)	148.47(15)	O(2)-Co(2)-Co(2)#8	124.10(3)
		O(1)-Co(2)-Co(2)#8	46.17(6)
		O(1)#8-Co(2)-Co(2)#8	45.97(6)

Symmetry transformations used to generate equivalent atoms:

#1 -x,-y+1/2,z+1/2	#2 -x+1/2,-y+1/2,-z	#3 -x-1/2,-y+1/2,-z	#7 x-1/2,y+1/2,z	#8 -x,-y,-z	#9 x,y-1/2,-z+1/2
#4 -x,-y+1/2,z-1/2	#5 x,y+1/2,-z+1/2	#6 x-1/2,y,-z+1/2	#10 x-1/2,y-1/2,z	#11 x+1/2,y-1/2,z	#12 x+1/2,y,-z+1/2

5. Two dimensional layered magnetic oxides

Table 5.5

Interatomic distances (in Å), coordination numbers (CN), effective coordination numbers (ECoN) and mean fictive ionic radii (MEFIR) for CsCoO₂.

Atom	O1	O2	CN	ECoN	MEFIR
Cs1	3.038	3.207	10	7.67	172.21
	3.098	3.690			
	3.126	3.731			
Co2	1.809	1.891	4	3.93	41.79
CN	6	8			
ECoN	5.95	5.77			
MEFIR	143.56	148.33			
Atom		binary	ternary	$\sum\Delta^a$	a) ternary-binary: MAPLE(CsCoO ₂)—0.5 MAPLE(Cs ₂ O)—0.5 MAPLE Co ₂ O ₃ b) from Cs ₂ O
Cs	1x	98.99 ^{b)}	102.80	3.81	
Co	1x	1217.92 ^{c)}	1173.7	-44.2	c) from Co ₂ O ₃
O1	1x	454.1 ^{d)}	537.5	83.4	d) = 0.5 MAPLE (O in Cs ₂ O) + 0.5
O2	1x	592.1 ^{c)}	566.8	-25.3	MAPLE(O in Co ₂ O ₃)
Σ		2363.11	2380.8	$\Delta=17.7(0.7\%)$	

5. Two dimensional layered magnetic oxides

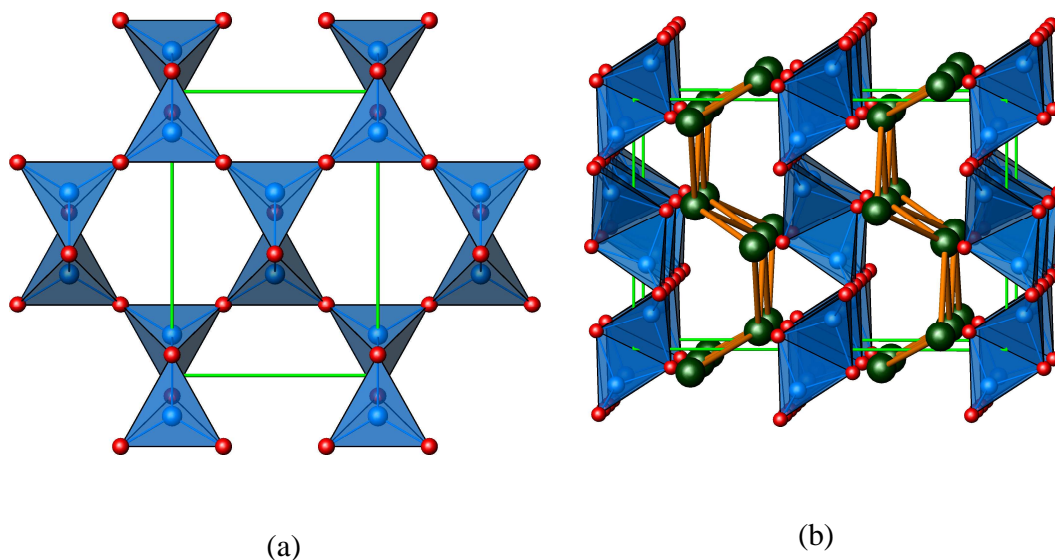


Fig. 5.2 a) A network of CsCoO_2 (view along b -direction) with unit cell drawn in green. b) Crystal structure of CsCoO_2 viewed along a -direction comprises of pairs of CoO_4 tetrahedra (blue) edge-linked to form bow-tie-shaped Co_2O_6 dimer units and these units condense by vertex sharing to form two dimensional layered structure of CsCoO_2 with Cs atoms (green) incorporated in between.

The crystal structure of the new Cesium cobaltate CsCoO_2 was determined from single-crystal data collected at 298 K and is displayed in Fig. 5.2(a, b). CsCoO_2 crystallizes in the orthorhombic space group — $Cmca$ (no. 64) with lattice parameters precisely determined to be, $a = 5.9904(4) \text{ \AA}$, $b = 12.2558(8) \text{ \AA}$, $c = 8.2736(6) \text{ \AA}$, with $R_1 = 1.96\%$ (all data) showing the excellent quality of the single crystal. The prominent features of the structure are pairs of CoO_4 tetrahedra edge-linked to form bow-tie-shaped Co_2O_6 dimer (butterfly-motif) units and these units condense by vertex sharing of the four remaining unshared vertexes to form two dimensional layered structure spreading along

5. Two dimensional layered magnetic oxides

(001) axis whereby the sheets are separated by Cesium ions, resulting in a first and unique structure of its kind in the field of ternary oxide chemistry [29].

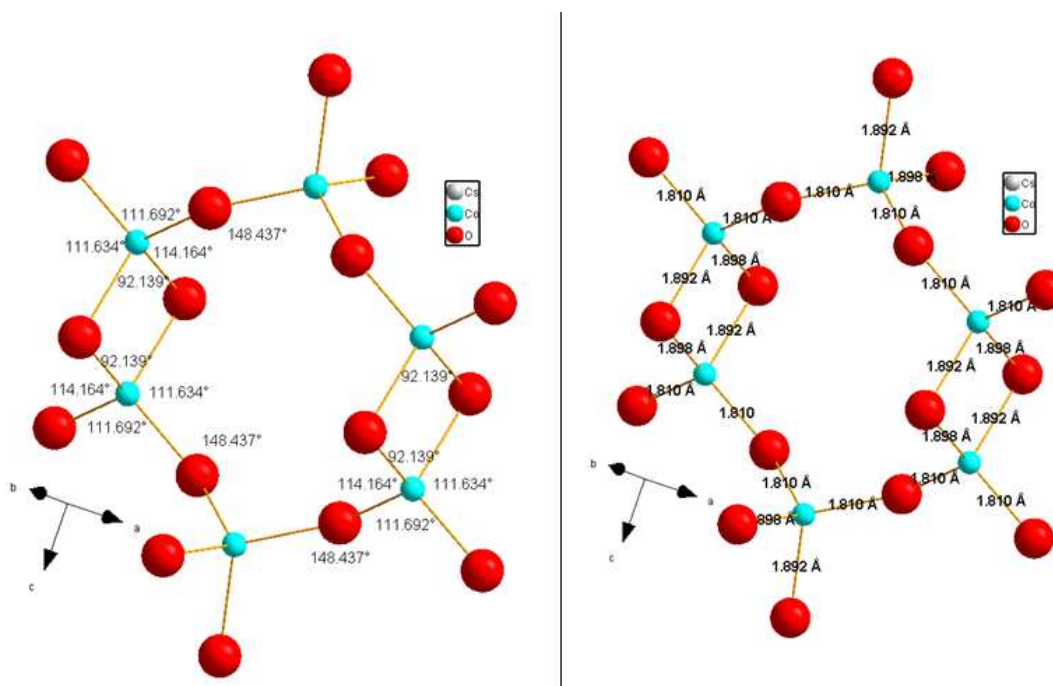


Fig. 5.3 a) The pictorial view of selected bond angles in CsCoO_2

Fig. 5.3 b) The pictorial view of selected bond distances in CsCoO_2

The pictorial view of selected bond angles and distances in CsCoO_2 is displayed in Fig. 5.3 a, b. X-ray single crystal structure analysis revealed tetrahedral coordination of cobalt (Co^{III}) cations, although rare, but not without precedent.[30—34]

The Co–O bond lengths (Table 5.4) agree, on average, well with the data reported in the literature [32, 33] and with the sum of ionic radii [34]. The Co-O1 distances of 1.898, 1.892Å (common edge) are substantially longer than the two Co-O2 distances of 1.81Å (bridging). Furthermore The $\text{O}_2\text{-Co-O}_2$ angle of 111.70(6)° [Table 5.4] is close to ideal

5. Two dimensional layered magnetic oxides

tetrahedral angle (109.5°), whereas the O1-Co-O1 angle associated with the shared edge is greatly reduced to $92.14(8^\circ)$. Detailed inspection of the Co–O distances and respective angles reveals a bit distortion in the structure, as consequences of repulsion between Co atoms separated by the shared tetrahedral edge than to one with shared corner. However, this can be easily understood in terms of the different functionalities of the oxygen atoms involved. As a rule, edges shared by two polyhedra are contracted, while the centering cations repel each other. With these qualitative rules in mind, the centering Co^{III} cations of one Co_2O_6 dimer repel each other, which results in elongated Co–O bonds (1.898, 1.892 Å for Co–O1) compared to the bridging ligands and the contraction of the corresponding angle, $87.86(8^\circ)$ for Co–O1–Co, appear in accordance with the rule. Accordingly, the bond lengths to the bridging oxygen atoms are shorter (1.810 Å for Co–O2) and the corresponding angle is much above the ideal tetrahedral value of 109° (here 111° for O₂–Co–O₂). The cesium atoms are coordinated by five oxygen atoms in the form of strongly distorted pentagonal pyramids with Cs–O distances vary from 3.0379(18) to 3.731(2), which is in the expected range [35].

5.3.2. Structural phase transitions in CsCoO_2

We have investigated the thermodynamics of the high temperature phase transition in CsCoO_2 compound initially using DSC (differential scanning calorimetric technique) as seen in Figure 5.4, showing sharp reversible peak at $T \approx 495$ K in both heating and cooling cycles indicative of the high-temperature phase transition from α - CsCoO_2 (orthorhombic, space group- $Cmca$) to β - CsCoO_2 (cubic, space group- $Fd\bar{3}m$) polymorph.

5. Two dimensional layered magnetic oxides

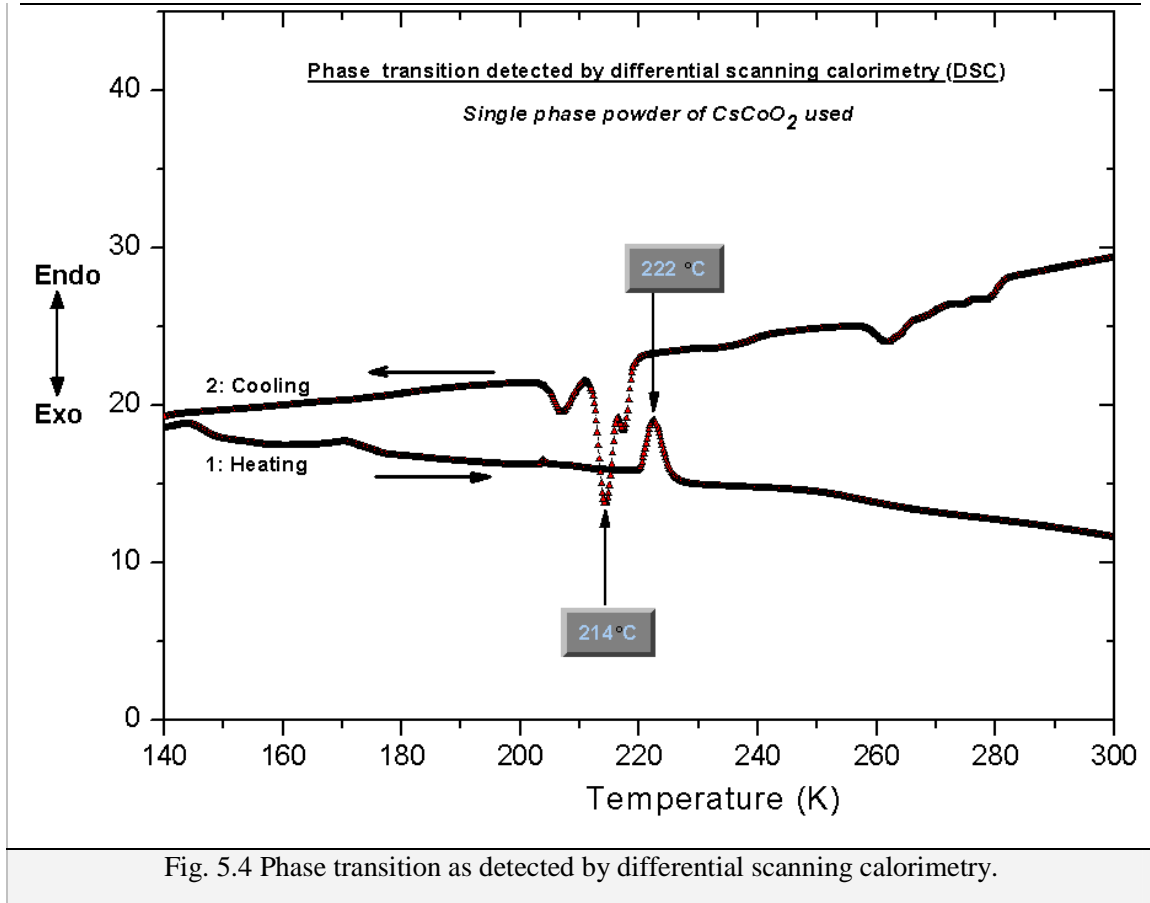


Fig. 5.4 Phase transition as detected by differential scanning calorimetry.

Afterwards in depth X-ray investigation on powder samples of cesium oxocobaltate was performed using a D8-Advance laboratory diffractometer (Bruker AXS, Karlsruhe, Germany) with $\text{Mo-K}\alpha_1$ radiation ($\lambda = 0.709300 \text{ \AA}$) both at room temperature and high temperature. For heating measurements a water-cooled capillary heater stage (mri Physikalische Geräte GmbH) with a temperature stability $<1 \text{ K}$ was used. Diffraction patterns were collected from 5.0° – 50.0° in 2θ with a total measurement time of 20 h. Structural refinements have been performed with the TOPAS program [36] (version 3, Bruker AXS).

5. Two dimensional layered magnetic oxides

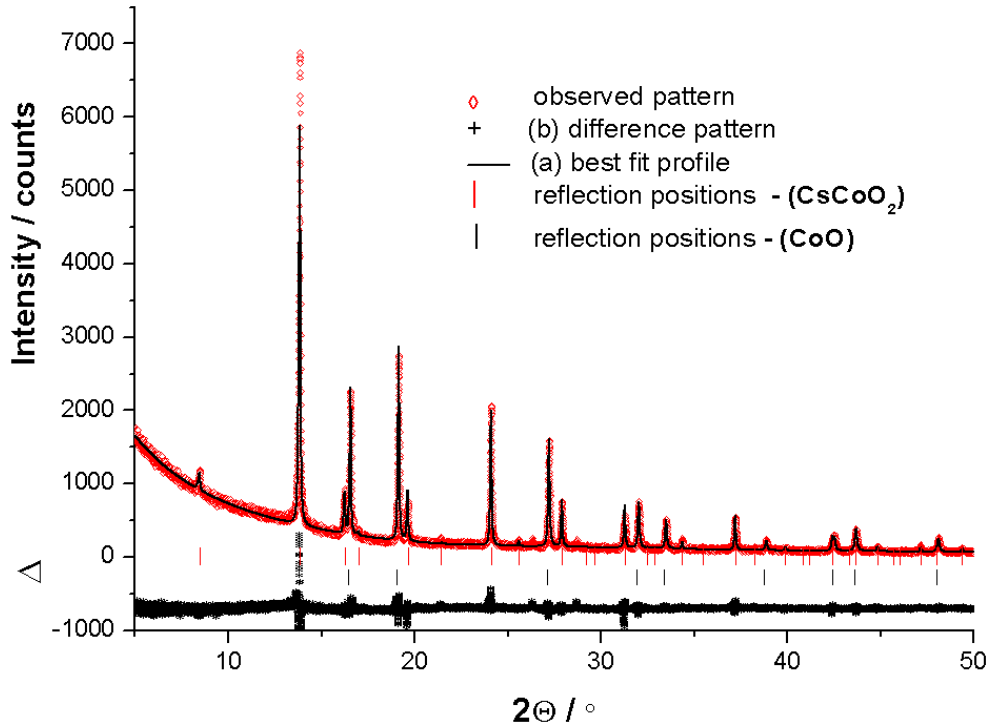


Fig. 5.5 Scattered X-ray intensity for HT- CsCoO_2 as a function of diffraction angle 2θ ($\lambda = 0.709300 \text{ \AA}$), showing the observed pattern (diamonds), calculated profile (red-line), difference plot (black crosses) and respective reflection markers (vertical bars).

For stabilizing the high temperature modification, the high-pressure experiments were run in a belt press apparatus equipped with graphite resistance heater at 6 GPa with the temperature of 923K. After annealing time of 9 hours at 923K the sample was temperature-quenched, while pressure was released at a slow rate, in order to avoid blow-outs and anvil damage. Post-experiment, the samples were opened in the glove box.

5. Two dimensional layered magnetic oxides

The polycrystalline powder of CsCoO₂ contains traces of cobalt (II) oxide as an impurity. The impurity contents remain almost same before and after the experiments as controlled by the multi-component Rietveld refinement procedures.

Later the thermal behaviour of the quenched phase (β - CsCoO₂) has been investigated by DSC. Thermal curves, reported in Fig. 5.4, display a reversible thermal (exo-endothermic) peak at 222 °C (495 K) and 215 °C (488 K) respectively. We call it high temperature stabilized high pressure phase because it's infact a high temperature modification of CsCoO₂ as confirmed by the occurrence of sharp reversible peak in the DSC investigation for both the normal room temperature(α -modification) and high temperature β -modification at exactly the same temperature. Due to the fact that the high pressure phases are mostly metastable at room temperature, the DSC investigation should show only one irreversible peak, which was not the case. The successive high temperature X-ray diffractometry experiments were carried out on this new modification using a 0.3mm quartz capillary (Hilgenberg GmbH) which is continuously rotated during measurement inside the oven assembly. During the measurement, the capillaries with the powder samples was slowly heated from room temperature to 573 K and diffraction patterns were collected at an interval of 50K each. At around 573 K back transformation to the ambient pressure (ambient temperature) α -phase was detected, well in agreement with the DSC measurements.

5. Two dimensional layered magnetic oxides

In conclusion, the new high-temperature cubic polymorphs of CsCoO₂ crystallizes orthorhombic in space group $Fd\bar{3}m$ ($Z = 8$) with lattice constant of $a_{\text{cubic}} = 8.318(2) \text{ \AA}$. The crystal structure parameter for the new cubic modification [Cs at $8b$ sites ($3/8, 3/8, 3/8$), Co at $8a$ sites ($1/8, 1/8, 1/8$), O at $96h$ ($0, 0, 0$) sites] are refined by the multi-component Rietveld refinement method using the program TOPAS 4.1[36], employing the data of the CsAlO₂ type of structure as starting parameters. The Rietveld fit of CsCO₂-HT (β) sample is shown in Fig. 5.5. High resolution synchrotron measurement at high temperature are planned to investigate the tiny splitting of the peaks in the proximity of phase transition.

5.3.3 The result of a temperature-dependent resistivity

The result of a temperature-dependent conductivity (both on heating and cooling back the sample) in the temperature range from 5 K to 293 K in a zero magnetic fields on polycrystalline sample of CsCoO₂ is displayed in Fig. 5.6. The specific electrical conductivity remains independent of temperature at $\text{temp} < 100 \text{ K}$. However at temperature above 100K it increases linearly with increase in temperature from 0.0183 S/cm at 100K to 0.0295 S/cm at 293 K, where the measurement stops. The low temperature insulating behaviour and anomaly at around 100K is a matter of further investigation. On contrary to experimental proofs, initial Density functional theory (DFT) calculations with GGA/PBE functional at 0K shows that CsCoO₂ is an antiferromagnetic metal. However, upon incorporating the on-site coulomb repulsion within the GGA+U

5. Two dimensional layered magnetic oxides

limit depicts band gap opening (insulating behaviour) at $U_{\text{eff}} \approx 4\text{eV}$. Further investigation of the electronic and magnetic structural transitions in the frame work of DFT and Hubbard (U) model is under investigation to proof the candidature of CsCoO_2 as a strongly correlated material. In depth investigation using synchrotron and neutron experiments would probably help to understand the mechanism particularly at around 100K.

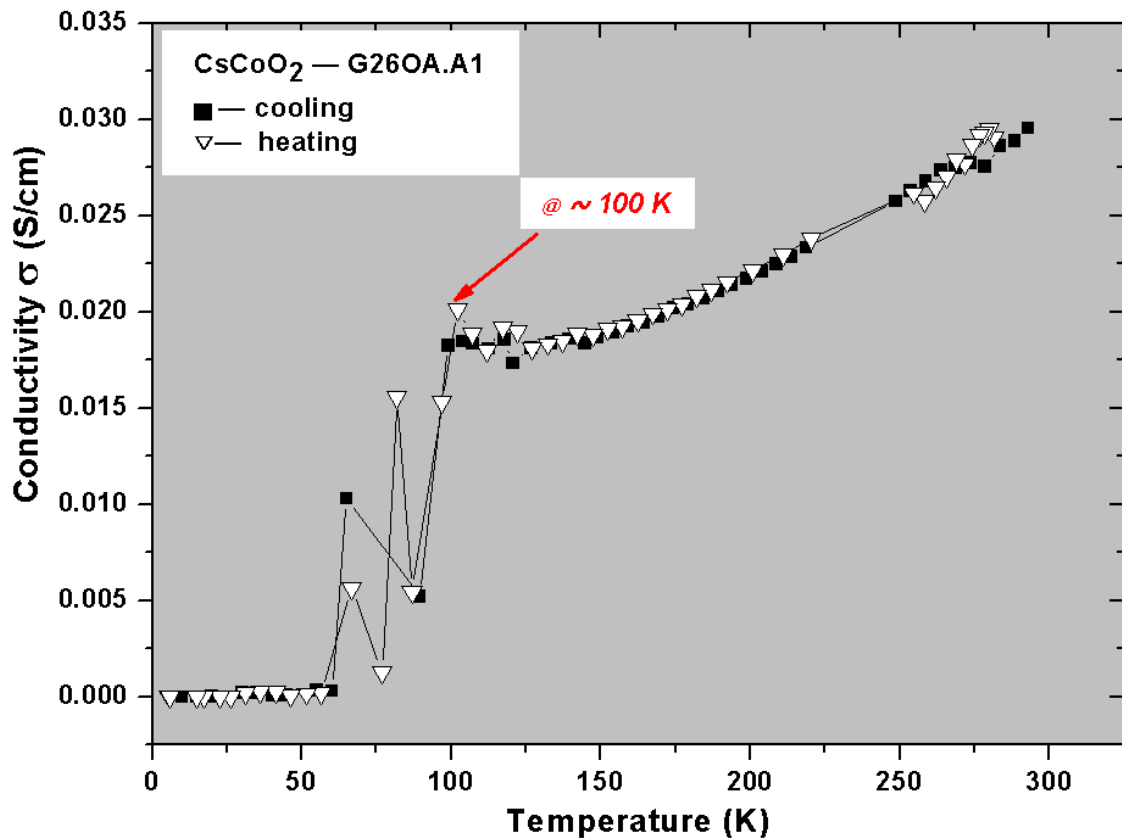


Fig. 5.6. Temperature dependence of Electrical conductivity (Siemens/cm) upon heating [∇] and cooling back [\blacksquare] for polycrystalline sample of CsCoO_2

5. Two dimensional layered magnetic oxides

5.3.4 Thermal analysis and magnetic characterization

In order to construct a model for the spin interactions in CsCoO₂, the magnetic properties of CsCoO₂ have been measured in the temperature range from 2 K to 350 K in magnetic fields up to 7 T as displayed in Fig. 5.7. The magnetic susceptibility data at 7 Tesla is fitted by Curie Weiss law in the high temperature range of 155K to 300K, giving a Curie constant of $C = 2.921 \text{ cm}^3 \text{ K mol}^{-1}$ per Co (III) and $\theta = -383\text{K}$, $g = 1.97$ [$\mu_{\text{eff}}/\mu_B = g[S(S+1)]^{1/2}$] corresponding to Co³⁺ (d^{06}) ions being in a high spin state ($S=2$), indicating a predominant intercluster antiferromagnetic interaction between Co³⁺ ions. μ_{eff} calculated from the Curie constant is $4.83 \mu_B$ which is in good agreement with the spin only value of $4.89 \mu_B$ expected for a high spin Co³⁺ (d^6) system. However, at even lower temperature and lower magnetic field (0.01 Tesla) there occurs a sharp inflexion point at 7 K, which is further endorsed by λ -type anomaly observed in the $C_p/T(T)$ curve (from the heat capacity measurements), as shown in Fig. 5.8. Which we assign to the onset ferromagnetic coupling between Co^{III} ions within the Co₂O₆ cluster.

5. Two dimensional layered magnetic oxides

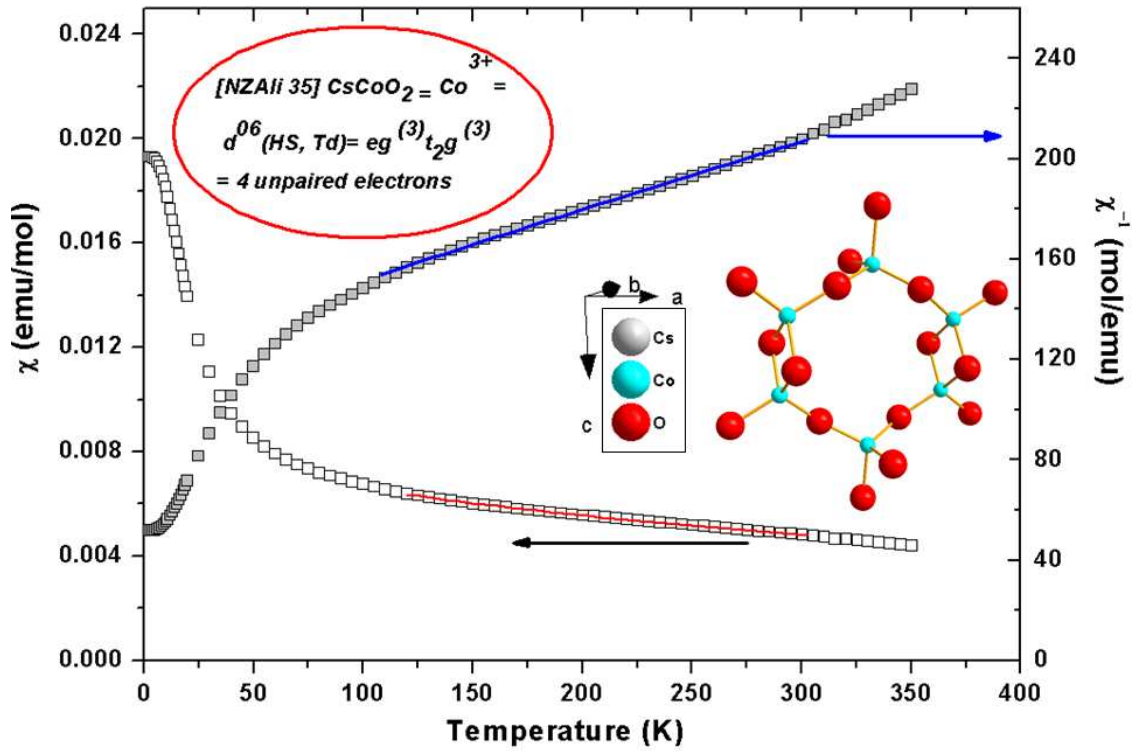


Fig. 5.7. Temperature dependent Magnetic Susceptibility (χ -□open black square) and inverse magnetic susceptibility (χ^{-1} -■ filled grey square) plot of $CsCoO_2$ at 7 T with a respective Curie Weiss fit.

5. Two dimensional layered magnetic oxides

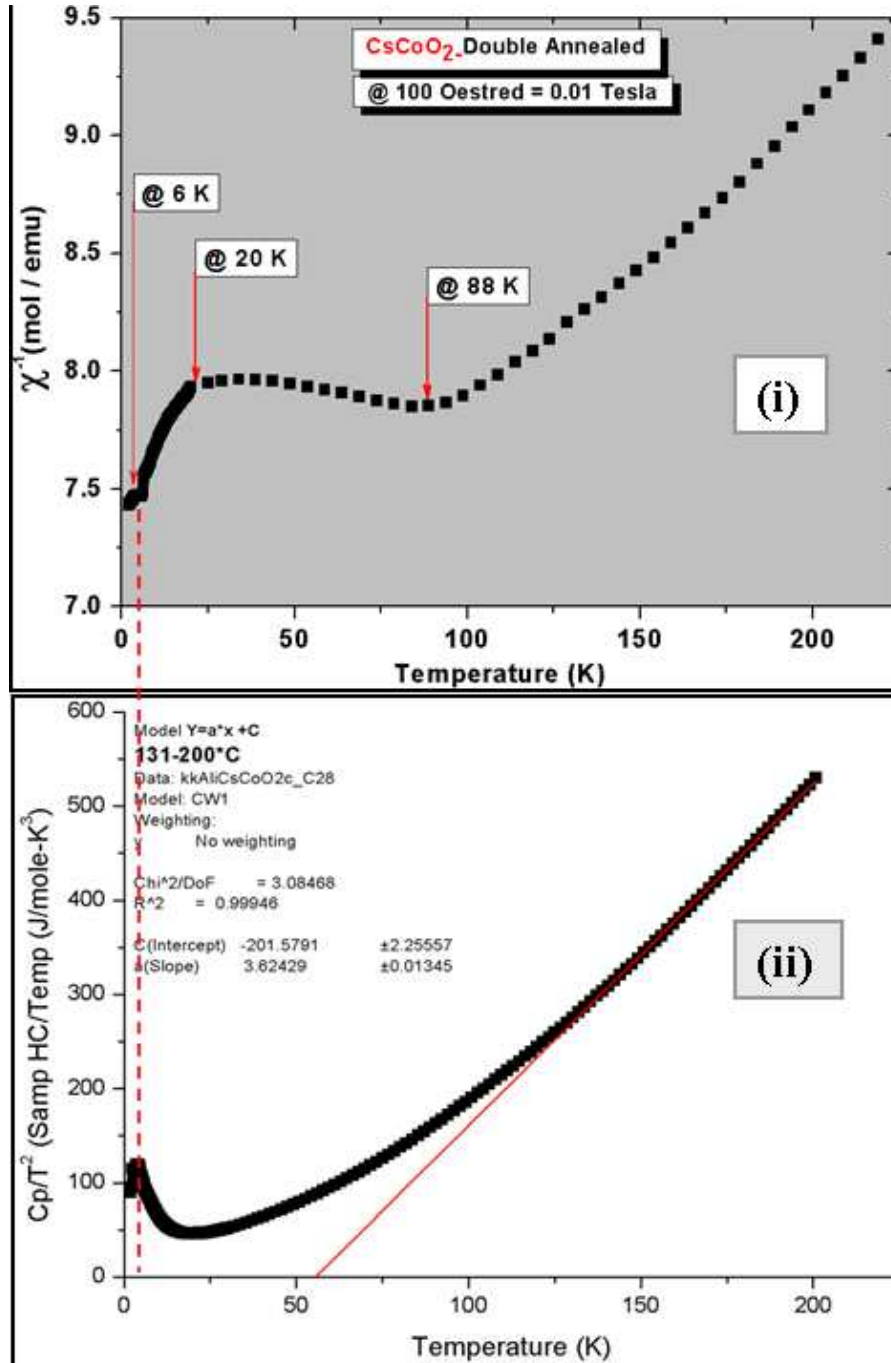


Fig. 5.8 i) Temperature dependent susceptibility (χ^{-1} -■ filled black square) plot of CsCoO_2 at 0.01 T
 ii) Specific heat (C_p/T^2) at zero field as a function of T of polycrystalline sample of CsCoO_2 .

5. Two dimensional layered magnetic oxides

5.4 Conclusion

In a nut shell, we hereby report a first and unique structure of its kind in the field of ternary oxide chemistry, CsCoO₂ synthesized via the azide/nitrate route. The structure solution has been performed by single crystal the X-ray analysis. The main feature of crystal structure is the pairs of CoO₄ tetrahedra edge-linked to form bow-tie-shaped Co₂O₆ dimer (butterfly-motiv) which share vertexes to form layered structure. In order to construct a model for the spin interactions in CsCoO₂, the magnetic properties of CsCoO₂ have been measured. The magnetic susceptibility data is fitted by Curie Weiss law in the high temperature range of 155K to 300K, giving a Curie constant of $C = 2.921 \text{ cm}^3 \text{ K mol}^{-1}$ per Co (III) corresponding to Co³⁺ (d^6) ions being in a high spin state ($S=2$), indicating a predominant intercluster antiferromagnetic interaction between Co³⁺ ions. μ_{eff} calculated from the Curie constant is $4.83 \mu_B$ which is in good agreement with the spin only value of $4.89 \mu_B$ expected for a high spin Co³⁺ (d^6) system. However, at even lower temperature there occurs a sharp inflexion point at 7 K, which is in good agreement with the magnetic ordering transition temperature determined from the heat capacity measurements, which we presume is from the ferromagnetic coupling between Co^{III} ions within the Co₂O₆ cluster. The plot of temperature dependent (DC) electrical conductivity depicts that the sample is insulator at lower temperature showing an anomaly at 100K. The thermodynamics of phase transitions was also systematically investigated by high resolution X-ray powder diffraction (Bruker Mo D8-Diffractometer) and DSC technique, showing transitions to occur at ~495 K from low temperature α -CsCoO₂

5. Two dimensional layered magnetic oxides

(*Cmca*) to high temperature cubic polymorphs of CsCoO₂ crystallizes in space group $Fd\bar{3}m$ ($Z = 8$) with lattice constant of $a_{\text{cubic}} = 8.318(2) \text{ \AA}$.

The room temperature structure of CsCoO₂ is isostructural to the BaSiN₂ [39] reported by Simon J. Clarke et. al. In contrast to Simon J. Clarke *et. al* statement, explaining the reason for unlikelihood of the BaSiN₂ analogue in oxide chemistry, stating (in verbatim) “*These (structures) are not found in the analogous oxides because this would entail too much repulsion of the tetrahedral atom across the shared edge*”. By successful synthesis of the isostructural compound (CsCoO₂) in oxide chemistry we’ve proven the power of azide nitrate route that this route is particularly suitable for all those families of structures that are not thermodynamically stable in normal conditions.

5-B: Synthesis, crystal structure and magnetic properties of β -KCrO₂

5.5. Introduction

The two dimensional layered magnetic oxides with triangular lattice, also recognized as (TLHAF) triangular lattice Heisenberg antiferromagnet are extensively studied compounds whereby exotic magnetic phenomena have been observed [40].

The unusual ground states alongwith its propensity to weak perturbations makes these geometrically frustrated system, in particular alkali-oxochromates the widely studied compounds [40]. Among them, ACrO₂ [A=Li, Na and K] constitute an extensively studied family of compounds that crystallize in the α -NaFeO₂ layer structure (space group R-3m), wherein the alkali (A⁺) ion occupy the antiprismatic arrangement embedded between the layers of edge shared [CrO₆]⁹⁻ octahedral. However for compounds of the family AMO₂ with larger A cations an alternative structure (β -RbScO₂ type of structures) has been observed. Here the A⁺ cation generates a trigonal prismatic surrounding [41, 42]. Very few examples of the latter structure type of compounds are known with lighter A⁺ cation entrenched between the slabs in trigonal prismatic configuration [43, 44].

Various theoretical models have been proposed to construct a model for the spin interactions in 2-D triangular lattice Heisenberg antiferromagnet and to estimate the intralayer exchange integral J using the series expansion coefficients computed by Rushbrooke and Wood. Similarly, to derive the Curie temperature of a 2-D Heisenberg ferromagnet with good accuracy the Stanley and Kaplan formula was frequently used [45]. In these respective 2-D oxochromates, the increase in the

5. Two dimensional layered magnetic oxides

interlayer Cr-Cr distances with increasing the size of alkali cation (A^+), compared to intralayer distances, results in significant reduction of the ordering temperature [46, 48].

In the $ACrO_2$ family, the magnetic structure is built by stacking well-separated, triangular planes of Cr^{3+} with spin $S = 3/2$ in an ABCABC sequence. In this study, we present results on a new high temperature, polymorph of the $ACrO_2$ family ($A = Li, Na, K$), namely β - $KCrO_2$ which is built by stacking well-separated, triangular planes of Cr^{3+} ($S = 3/2$) with oxygen ion stacking sequence of ABBAAB with unusual trigonal prismatic coordination of K^+ cation.

5.6. Experimental

β - $KCrO_2$ was prepared via the azide/nitrate route [49, 50]. Starting materials for the preparation of the potassium chromate were KN_3 , KNO_3 (Aldrich, 99%) and Cr_2O_3 . Chromium oxide was prepared by heating $(NH_4)_2Cr_2O_7$ (Aldrich, 99.5%) in a flow of oxygen at 923 K for 24 h. whereas the KN_3 was synthesized from aqueous HN_3 and cesium carbonate [51].

The starting materials were mixed in the ratio required according to (1) and ground in a ball mill, pressed in pellets ($\varnothing 13$ mm) under 10^5 N, dried under vacuum (10^{-3} mbar) at 423 K for 12 h and placed under argon in a tightly closed steel vessel provided with a silver inlay [50]. In a flow of dry argon, the following temperature profile was applied: 25 \rightarrow 533 K (100 K/h); 533 \rightarrow 653K (5K/h), 653 \rightarrow 853K (20 K/h) with subsequent annealing for 50 h at 853 K and later quenching to room temperature.



Hazard: The sample container may blow up if heated too rapidly!!

5. Two dimensional layered magnetic oxides

The obtained dark green KCrO_2 powder, being extremely sensitive to humid air, was sealed in glass ampoules under streaming argon atmosphere and all following manipulations with the substances were performed in inert atmospheres of purified argon.

The atom ratio of the heavy elements was confirmed with a scanning electron microscope (XL 30 TMP, Philips, Holland, tungsten electrode, 25 kV), equipped with an integrated EDAX–EDX system (S–UTW–Si(Li)–detector).

The X-ray investigation on powder samples was performed using a D8-Advance laboratory diffractometer (Bruker AXS, Karlsruhe, Germany) with $\text{Mo-K}\alpha_1$ radiation ($\lambda = 0.709300 \text{ \AA}$) both at room temperature and high temperature using a Vântag-1 position-sensitive detector (6° opening angle) and a curved germanium monochromator. The powder diffraction data were collected in the 2Θ range of $4\text{--}40^\circ$ sealed in 0.3 mm quartz capillary (Hilgenberg) kept rotating during data collection for better particle statistics. For heating a water-cooled capillary heater stage (mri Physikalische Geräte GmbH) with a temperature stability $<1 \text{ K}$ was used.

Single crystals of $\beta\text{-KCrO}_2$ have been grown by subsequent annealing of the pressed reaction product at 773K for 200 h in silver crucibles, which were sealed in glass ampoules under dried Ar. Whereas the single crystals of $\beta\text{-KCrO}_2$ were singled out and picked in a dry box under an argon atmosphere ($\text{O}_2, \text{H}_2\text{O} < 0.1 \text{ ppm.}$, M. Braun GmbH, Garching, Germany) and finally mounted in a sealed glass capillaries. Furthermore, the atom ratio of potassium and chromium was confirmed by EDX analysis, and found to be $\text{K:Cr} = 1:1$.

Diffraction intensities were collected with a SMART APEX I three-cycle diffractometer (Bruker AXS, Karlsruhe, Germany) equipped with a SMART-CCD (APEX), with $\text{Mo-K}\alpha$ radiation ($\lambda = 0.71073 \text{ \AA}$) at room temperature (298 K). The

5. Two dimensional layered magnetic oxides

collection and reduction of data were carried out with the Bruker Suite software package [52]. Intensities were corrected for absorption effects applying a multi-scan method [53]. The structural data was refined by full-matrix least-squares fitting with the *SHELXTL* software package [54], within the space groups *P*-31c (163), whereby the atomic coordinates of β -RbScO₂ [55] type of structure were used as starting models for this new high temperature modifications of potassium chromate. Experimental details on crystallographic data and data collection are given in Table 5.6. Table 5.7 shows the atomic parameters and equivalent isotropic displacement parameters, and Table 5.8 tabulates the anisotropic displacement parameters from the single crystal data.

5. Two dimensional layered magnetic oxides

Table 5.6. Crystal data and structure refinement for β -KCrO₂.

Identification code	β -KCrO ₂
Empirical formula	β -Cr K O ₂
Formula weight	123.10
Temperature	298(2) K
Wavelength	0.71073 Å
Crystal system	Trigonal
Space group	P -3 1 c (163)
Unit cell dimensions	a = 3.0427(4) Å $\alpha = 90^\circ$. b = 3.0427(4) Å $\beta = 90^\circ$. c = 11.924(2) Å $\gamma = 120^\circ$.
Volume	95.60(3) Å ³
Z	2
Density (calculated)	4.276 Mg/m ³
Absorption coefficient	7.730 mm ⁻¹
F(000)	118
Crystal size	0.20 x 0.10 x 0.10 mm ³
Theta range for data collection	3.42 to 34.89°.
Index ranges	-4 ≤ h ≤ 4, -4 ≤ k ≤ 4, -
	19 ≤ l ≤ 18
Reflections collected	1248
Independent reflections	143 [R(int) = 0.0360]
Completeness to theta = 34.89°	93.2 %
Max. and min. transmission	0.5120 and 0.3070
Refinement method	Full-matrix least-squares on F ²
Data / restraints / parameters	143 / 0 / 8
Goodness-of-fit on F ²	1.287
Final R indices [I > 2σ(I)]	R1 = 0.0253, wR2 = 0.0655
R indices (all data)	R1 = 0.0265, wR2 = 0.0663
Largest diff. peak and hole	0.575 and -0.575 e.Å ⁻³

5. Two dimensional layered magnetic oxides

Table 5.7. Atomic coordinates and equivalent isotropic displacement parameters (\AA^2) for β -KCrO₂. U(eq) is defined as one third of the trace of the orthogonalized U^{ij} tensor.

	x	y	z	U(eq)
Cr	0	0	0	0.079(2)
K	1/3	2/3	1/4	0.0123(2)
O	1/3	2/3	0.5858(2)	0.0088(4)

Table 5.8. Anisotropic displacement parameters (\AA^2) for β -KCrO₂. The anisotropic displacement factor exponent takes the form: $-2\pi^2[h^2 a^{*2}U^{11} + \dots + 2 h k a^* b^* U^{12}]$

	U ₁₁ =U ₂₂	U ³³	U ₂₃ =U ₁₃	U ¹²
Cr	0.0081(3)	0.0080(3)	0	U ₁₁ /2
K	0.0131(3)	0.0107(4)	0	U ₁₁ /2
O	0.0092(6)	0.008(9)	0	U ₁₁ /2

Thermal analysis: The differential scanning calorimetry (DSC) measurements were carried out with a DSC device (DSC 404 C, Netzsch GmbH, Selb, Germany). The samples were heated at a rate of 10 Kmin⁻¹ in an Aluminium crucible under dry argon.

Temperature dependence of the specific heat (C_p) of a polycrystalline sample of KCrO₂ was measured between 2 and 300 K using a commercial PPMS (Physical Property Measurement System, Quantum Design, 6325 Lusk Boulevard, San Diego, CA.) employing the relaxation method [56, 57]. To thermally fix the sample tablet (\emptyset = 5 mm and thickness 1mm) to the sapphire sample platform, a minute amount of Apiezon-N vacuum grease was used. The heat capacity of the sample holder platform

5. Two dimensional layered magnetic oxides

and grease was individually determined in a separate run and subtracted from the total measured heat capacities.

Magnetic measurements: Magnetic susceptibility $\chi(T)$ of powder sample of title compound with mass of 28.1 mg was recorded in the temperature range from 2 to 350 K in external magnetic fields ranging from 0.01 to 7 T using a SQUID-Magnetometer (MPMS 5.5, Quantum Design). The sample was contained in warily dried SUPRASIL ampoule that was long enough to extend over the coils of the magnetometer. The core electron diamagnetic correction has been applied using tabulated values [58]. Whilst the van vleck paramagnetic contribution (χ_{VV}) for the Cr^{3+} ion is also performed [59, 60].

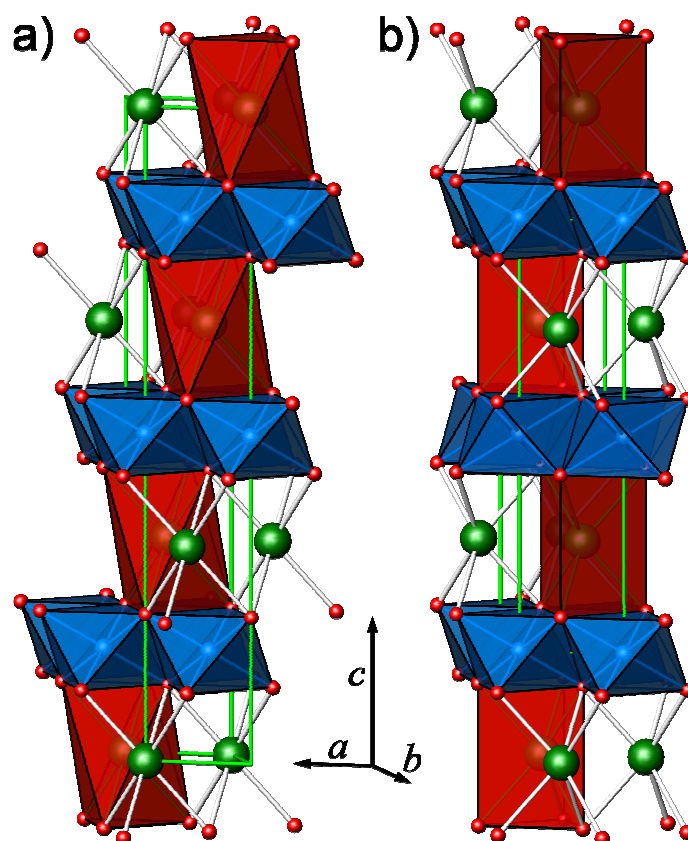


Fig. 5.9: Polyhedral view of the crystal structure of **a)** α -KCrO₂ (left) [*c.f.* ref 41] and **b)** β -KCrO₂ (right) [this study]. The K atoms are shown as green spheres forming red trigonal antiprism (left) and trigonal prism (right), the coordinating O atoms ~ as red, and the Cr atoms~ as blue spheres.

5.7. Results and discussion

5.7.1 Description of crystal structure

The polyhedral view of the crystal structure of β -KCrO₂ is shown in Fig. 5.9 (right). The new β -KCrO₂ crystallizes in β -RbScO₂ type of structure, in the space group $P-31c$ (163) with $a = 3.0427(4)$ Å, $c = 11.924(2)$ Å, ($c/a = 3.918$ Å, $Z = 2$) [*c.f.* table 5.6]. The unique feature of the structure is the CdCl₂ analogue layers of edge-shared [CrO₆] octahedra spreading perpendicular to [001] planes with K⁺ atoms incorporated between the layers in a trigonal-prismatic arrangement.

The Cr³⁺ occupy the octahedral interstices with $d(\text{Cr-O}) = 203.26(11)$ pm whereas K⁺ ions reside in a trigonal prismatic surrounding of oxide anion with

5. Two dimensional layered magnetic oxides

$d(\text{K}^+-\text{O}^{2-}) = 263.09(16)$ pm with Cr—O—Cr angle of $96.91(7)^\circ$, whereas the O—Cr—O angle ranges from 83.08° to 96.92° .

The oxygen ion stacking sequence ABBAAB in $\beta\text{-KCrO}_2$ results from the change of antiprismatic coordination mode of K^+ within the cubic-closest packing of O^{2-} anions (stacking sequence: ABCABC) in $\alpha\text{-NaFeO}_2$ ($\alpha\text{-KCrO}_2$) to prismatic one in $\beta\text{-KCrO}_2$ (current investigation) as a twisting effect to gain more space for K^+ cation at higher temperature due to the bond length fluctuation effect [61]. In much the same way, the ratio of the ionic radii ratio of $r_i(\text{Cr}^{3+}) / r_i(\text{K}^+)$ is (0.615 / 1.38) for CN = 6 is very uncommon and normally not favoured [62]. However to stabilize such an unusual coordination environment around potassium only quenching the sample from higher temperatures has proven to be a feasible approach. The selected interatomic distances and angles for $\beta\text{-KCrO}_2$ are listed in Table 5.9.

Table 5.9. Selected interatomic distances (Å) and bond angles ($^\circ$) for $\beta\text{-KCrO}_2$

K—O (6x)	2.6309(16)
Cr—O (6x)	2.0326 Å (0.0011)
O—Cr—O	96.92(7) x 6
	83.08(7) x 6
	180.00(10) x 3
Cr—O—Cr	96.91(7) x 3
O—K—O	70.66(5) x 6
	140.99(2) x 6
	96.22(6) x 3

The O—O intralayer distance within the coordination polyhedral spreading parallel to (001) plane is $d_{\text{O-O}} = 3.0427$ Å (6x), whereas interlayers distances connected via K^+ trigonal prisms $d_{\text{O-O}} = 3.9170$ Å. The large separation between Cr planes in contrast to Li and Na analogues is due to the bigger size of alkali K^+ comparatively.

5. Two dimensional layered magnetic oxides

5.7.2 MAPLE calculations ^[63, 64, 65] were performed for β -KCrO₂ as a means of checking the plausibility of this new structure. The calculated value (2389.09 kcal mol⁻¹) for β -KCrO₂ and the sums of the calculated partial Madelung energies derived from respective binary oxides (2383.26 kcal mol⁻¹) agree well with deviation of 0.24%, which is well within the permissible limit thereby reflecting the excellent quality of the structure refinements.

Comparative MAPLE calculations for α -KCrO₂ (2386.2 kcal mol⁻¹) also show energy differences of this magnitude [41], which suggests that the energetics of this crystal are in order. A closer view of the coordination sphere of Cr and K in β -KCrO₂ shows a distance of (d_{Cr-O}) 203.29 pm and 263 pm (d_{K-O}) between the 6 nearest oxygen atoms with the 7th oxygen atom lie at a distance of 366 pm and 400 pm respectively, without any coordinative contribution. With almost identical K-O bond lengths, O-O distances in KO₆ trigonal prism (3.0427Å) are longer than in antiprism (Octahedra) [2.97447 Å]. The results of these calculations are summarized in Table 5.10.

5. Two dimensional layered magnetic oxides

Table 5.10. MAPLE comparison [kcal/mole] of α -KCrO₂ and β -KCrO₂.

β -KCrO ₂ (<i>P-31c</i>)				^[41] α -KCrO ₂ (<i>R-3m</i>) / Maple comparison		
Atom	binary	ternary	$\sum\Delta^a$	binary	ternary	$\sum\Delta^a$
K	104.73 ^{b)}	122.2075	17.48	104.9 ^{b)}	122.8	+17.9
Cr	1206.65 ^{c)}	1180.6	-26.05	1205.7 ^{c)}	1177.2	-28.5
O1	487.05 ^{d)}	543.1418	56.09	195.0 ^{d)}	543.2	+348.2
O2	584.83 ^{c)}	543.1418	-41.69	876.6 ^{c)}	543.2	-333.4
Σ	2383.26	2389.09	$\Delta=5.83$ (0.24%)	2382.2	2386.2	$\Delta=+4.2$ (0.17%)

a) ternary-binary: MAPLE (KCrO₂)-0.5 MAPLE(K₂O)-0.5 MAPLE Cr₂O₃

b) from K₂O c) from Cr₂O₃ d) = 0.5 MAPLE (O in K₂O) + 0.5 MAPLE(O in Cr₂O₃)

5.8. Structural phase transitions

In 1989 Hoppe et. al [41] reported that the α -KCrO₂ modification of potassium oxochromates crystallizes in α -RbScO₂ type of structure. In another study they also reported the occurrence of another phase β -RbScO₂ at and above 300 K [42].

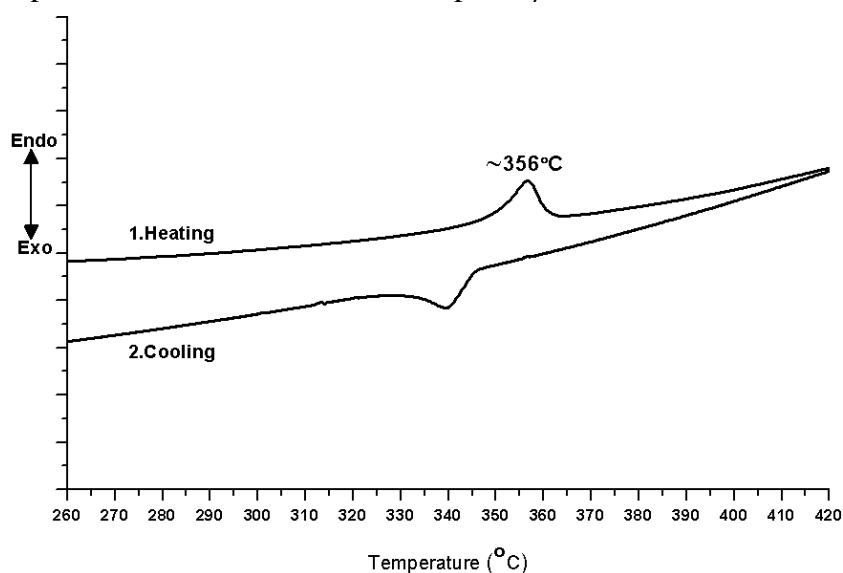


Fig. 5.10. Phase transitions detected by differential scanning calorimetry (DSC).

In much analogy we investigated the phase diagram alongwith the thermodynamics of the high temperature phase transition in KCrO₂ compound using DSC as seen in

5. Two dimensional layered magnetic oxides

Figure 5.10, showing sharp reversible peak at $T \approx 629$ K in both heating and cooling cycles indicative of the high-temperature phase transition from α -KCrO₂ to β -KCrO₂.

Afterwards in depth X-ray investigation on powder samples of potassium oxochromates, confirm in reasonable agreement with the DSC measurements, the disappearance of some of the diffraction lines corresponding to α -KCrO₂ alongwith appearance of resulting high temperature phase that could be indexed as trigonal (space group $P\bar{3}1c$) in good agreement with the single crystal measurement. The effect of this structural phase transition on the diffraction patterns is also illustrated in the Figure 5.11(i).

The different diffraction patterns labelled as a, b, c and d, represents the various stages at which the samples was measured. Plot a) represents the as prepared quenched sample, whereas samples b, c and d were measured sporadically after two three and four weeks of annealing time respectively. With increasing the duration of annealing the amount (%) of alpha phase started dominating as evidenced by the quantitative multi-component Rietveld analysis. The structures of the samples were refined by the Rietveld method using the data of the single structure refinements as starting parameters. Also the atomic parameters as determined by Rietveld refinement were very close to those found for the single crystals. The fit of sample (c) is shown in Fig. 5.11(ii).

5. Two dimensional layered magnetic oxides

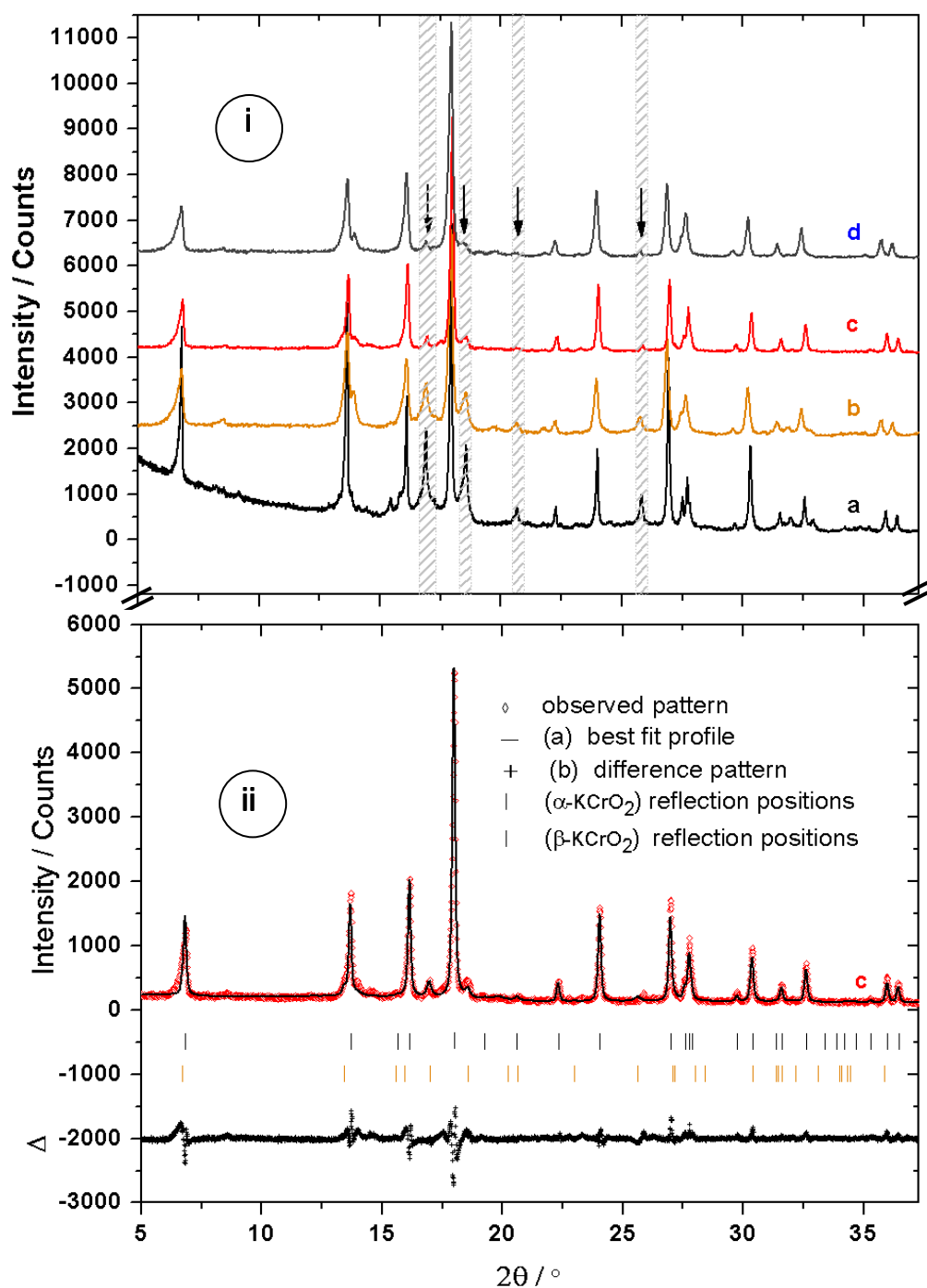


Fig. 5.11. The effect of the structural phase transition on the X-ray diffraction patterns sporadically collected and measured on Brucker Mo D8-Diffractometer ($\lambda = 0.709300 \text{ \AA}$). The shaded region in upper part **i**) clearly depicts the disappearance of some peaks belongs to $\beta\text{-KCrO}_2$. The lower graph **ii**) shows the quantitative Rietveld refinement fit of sample (c) using the data from the single structure refinements as starting parameters.

In a similar fashion the successive high-temperature X-ray powder diffraction measurements for KCrO_2 using 0.3 mm quartz capillary in a narrow 2θ window were also performed at (a) $T = 373 \text{ K}$, (b) $T = 473 \text{ K}$ (c) $T = 573 \text{ K}$ (d) $T = 673 \text{ K}$ (e)

$T = 713$ K (f) $T = 773$ K with steps of ~ 100 K for KCrO_2 . The onset of phase transition at $T > 673$ K is observed as can be seen in the Fig. 5.12.

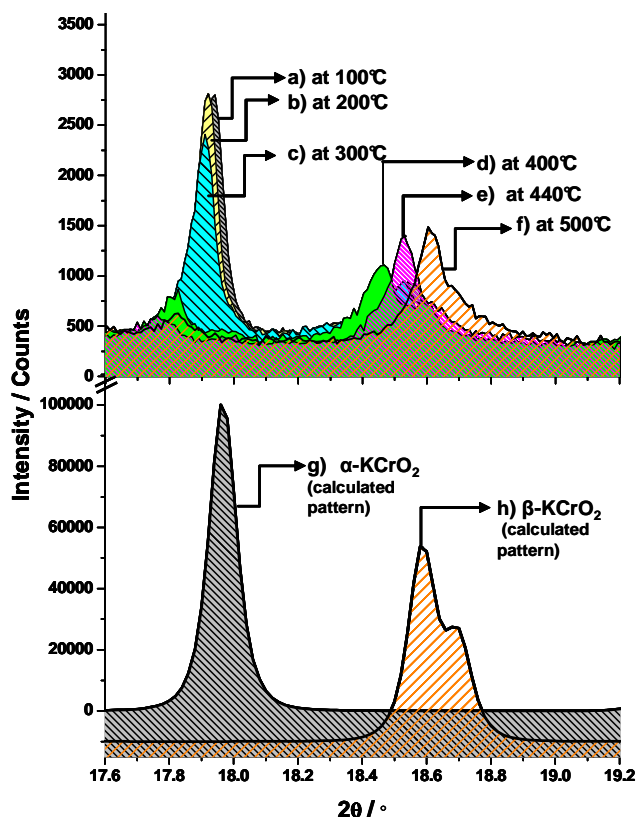


Fig. 5.12. Phase transitions as detected by continuous HT XRD experiments in quartz capillary (on Bruker Mo D8-Diffractometer).

5.9. A comparison of $\alpha\text{-KCrO}_2$ to $\beta\text{-KCrO}_2$

A comparison of lattice parameters of room temperature phase ($\alpha\text{-KCrO}_2$) with that of high temperature phase ($\beta\text{-KCrO}_2$) reveals a 1.5 times contraction in c-axis [$c\text{-axis}_{(\text{beta})} = 2/3 c\text{-axis}_{(\text{alpha})}$], considerable expansion in interlayer distance c/Z alongwith expansion in molar volume. The above assessment depicts that the high temperature phase is less dense compared to the room temperature one.

However the coordination of potassium that changes from prism to anti prism reveals that in both surroundings the K-O distances remain similar, but the O-O distances in KO_6 prisms being shorter than in KO_6 antiprisms (Octahedra.), generate more O-O

5. Two dimensional layered magnetic oxides

repulsion and ending up in larger MO_6 interlayer distances for prismatic structure in comparison to antiprismatic analogues. However in case of β - RbScO_2 structure, in contrast to potassium chromates, repulsion is much weaker due to larger interlayer distances, owing to larger cationic radii, thereby favouring the trigonal prismatic configuration of alkali cations.

In another study, calculations of electrostatic energy has revealed that the prismatic configuration for alkali cation is less favourable than the antiprismatic / octahedral coordination [61, 66, 67]. The stability effect in case of alpha and beta RbScO_2 is, however, less pronounced due to overall larger cations.

The rare coordination of potassium in trigonal prismatic can also be explained in terms of contribution of entropy to the free energy. Since at high temperature, due to strong bond fluctuations (dynamics) the prismatic structure with wider bottleneck conformation provides more freedom for alkali motion and result in larger entropy [66]. The high temperature modification is stabilized only because of the factors such as repulsion between the mobile potassium cations and higher entropy.

However, the probability of sheet gliding in transforming from alpha to beta phase is expected to be kinetically slow. The decisive factor in stabilizing the respective phase lies in the rate of cooling sample back to room temperature. After annealing, slowly cooling the sample back to room temperature will predominate the alpha phase, whilst the quenching the sample favours the desired beta phase of KCrO_2 .

5.10. Magnetic properties

The magnetic behaviour of two dimensional oxochromates of the family ACrO_2 [A=Na, Li and K] has been extensively investigated by C. Delmas *et. al.* using

5. Two dimensional layered magnetic oxides

neutron, Moessbauer and magnetic susceptibility measurements [68, 69 and 70]. In one of the recent review, it was also proposed that KCrO_2 would be a nice candidate to study two dimensional 2D antiferromagnetic character because of large separation between Cr planes in contrast to Li and Na analogues [40].

The plot in Fig. 5.13 displays the temperature dependent magnetic susceptibility of a polycrystalline sample of the title compound. As shown in Fig. 5.13 the inverse magnetic susceptibility grows almost linearly with increasing temperature and is independent of the applied magnetic field above T_N at various applied magnetic fields. And data can be fit applying Curie-Weiss law [$\chi_{\text{mol}} = C / (T-\theta) + \chi_o$] with Curie –weiss temperature θ and Curie constant C, whereas temperature independent term, $\chi_o = \chi_{\text{dia}} + \chi_{\text{VV}}$ accounts for

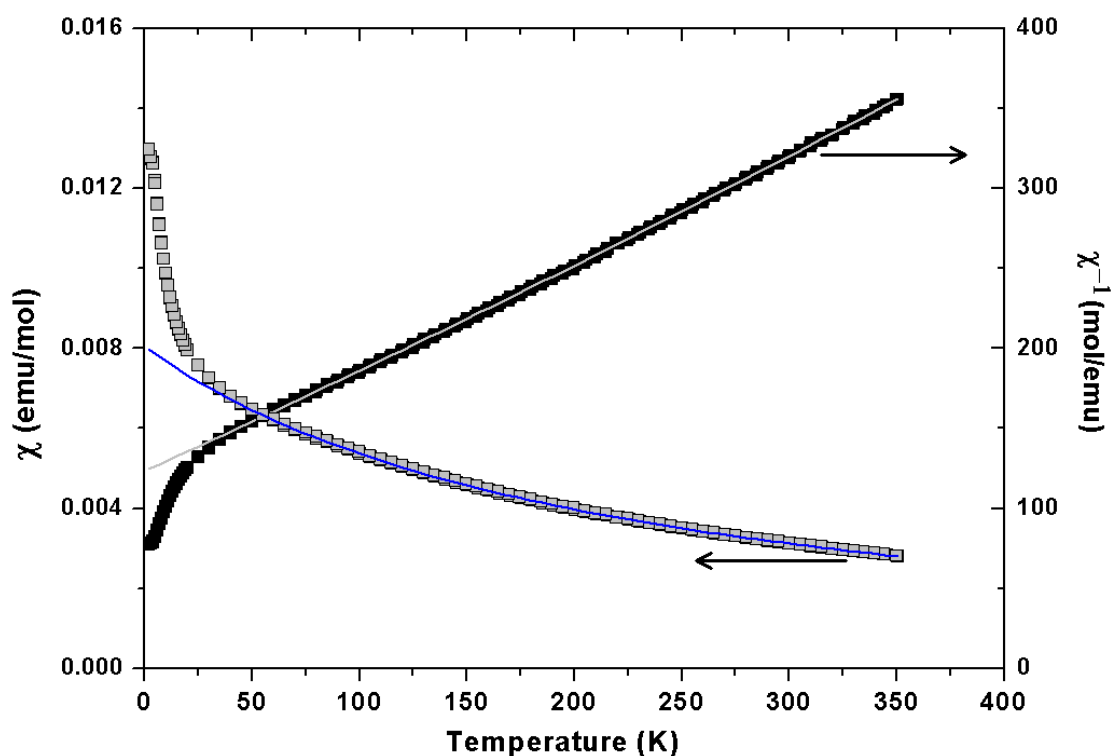


Fig. 5.13. Temperature dependence of the magnetic susceptibility (χ and $1/\chi$ vs T) for $\beta\text{-KCrO}_2$. The solid line represents the fit of the data to the Curie–Weiss law. The inset in the top-left corner presents the $1/\chi$ vs T plot to show the magnetic field independence of the powder sample with temperature.

5. Two dimensional layered magnetic oxides

core electrons diamagnetic contribution (χ_{dia}) and van vleck paramagnetic contribution (χ_{VV}) for the Cr^{3+} ion. The diamagnetic susceptibility of the core electrons in closed shell can be estimated by incremental method of the all the ions as tabulated, e.g, by [58] (Cr^{3+} : $-11 \times 10^{-6} \text{ cm}^3/\text{mol}$; K^+ : $-13 \times 10^{-6} \text{ cm}^3/\text{mol}$; 2O^{2-} : $-24 \times 10^{-6} \text{ cm}^3/\text{mol}$) resulting in a total diamagnetic contribution of $\chi_{\text{dia}} = -48 \times 10^{-6} \text{ cm}^3/\text{mol}$ per formula unit. Whilst the Van Vleck paramagnetic contribution per Cr^{3+} cation amount to $[75 \times 10^{-6} \text{ cm}^3/\text{mol}]$ [59, 60]. For Cr^{3+} (d^3 system) with $S=3/2$ one expects a μ_{eff} in the range of $3.70\text{-}3.90 \mu_B$ [58]. The curie Weiss fit of experimental data at temperature above $\sim 75 \text{ K}$ with $\chi_0 = \chi_{\text{dia}} + \chi_{\text{VV}} \approx +27 \times 10^{-6} \text{ cm}^3 / \text{mol}$ (per Cr^{3+}), the negative Curie-Weiss temperature of $-208 \text{ K}(\theta)$ is achieved indicating predominant antiferromagnetic spin-exchange interaction, with an effective magnetic moment (μ_{eff}) of the order of $3.82 \mu_B$ corresponding to a Lande' g-factor of 1.97. However, in conformity with the neutron diffraction studies results of *Claus delmas et al*, the reciprocal susceptibility plot of title compound doesnot exhibit any minimum down to 2 K [70], but however there is a sharp decrease from the linear behaviour at 26 K in conformity with the earlier results [71] .

The Weiss constant (θ) was determined to be -216 K , a value 8 times larger than the ordering temperature $T_N \approx 26\text{K}$. A ratio $|\theta| / T_N$ around ~ 10 is usually considered an indication for a frustrated magnetic system, and this ratio is therefore frequently denoted as frustration index [73]. Whether this magnetic frustration; occurs because of competing, antagonistic couplings of parts of the magnetic moments having an

5. Two dimensional layered magnetic oxides

unfavorable mutual alignment, or it arises from the specific geometric arrangement of antiferromagnetically interacting ions, in a triangular array or in the so-called kagomé lattice [74], is still debatable. However, to have a better perspective about the origin of the frustration, the angular-dependent magnetic properties; i.e., the magnetic response parallel and perpendicular to the crystallographic c -axis of single crystal has to be examined, which was not possible in present study due to small size of single crystals. Similarly the abrupt change in the susceptibility at temp $< 26\text{K}$ can be attributed to spurious paramagnetic impurities [72] and/or lattice defects or may be the intrinsic phenomenon in the KCrO_2 compound, which is a subject of further investigation using neutron scattering and in particular positive muon-spin rotation and relaxation ($\mu^+\text{SR}$) experiment using a powder sample at the temperatures below 26 K.

5.11 The specific heat of KCrO_2

The specific heat for KCrO_2 was recorded in the temperature range of 2—300K. In the low temperature region one can see a λ -type anomaly at 23 k in the C_p (T) curve, as shown in Fig. 5.14(a), which we assign to the onset of long-range AFM ordering. The onset of AFM ordering as observed by $\chi(T)$ plot is well in accordance with the anomaly observed in specific heat plot. Consequently, the absolute values of C_p are uncertain and a substantial lattice contribution cannot be ruled out [75]. To probe the nature of the specific heat anomaly at T_N in more detail, we also plotted C_p/T versus T as shown in upper inset of Fig. 5.14(b), and C_p/T^2 versus T (see the lower inset of Fig. 5.14(c) [76] both show a lucid picture with the Neel temperature precisely determined to be 23 K. However closer inspection of the data with a plot of C_p/T^2 vs T^2 [Fig. 5.14(d)] unearth another kink at 12 K, which can be assigned to the

ferromagnetic interaction within the layers. So it became clear that the magnetic structure consists of ferromagnetic layers perpendicular to the c axis which are antiferromagnetically coupled to adjacent layers [77].

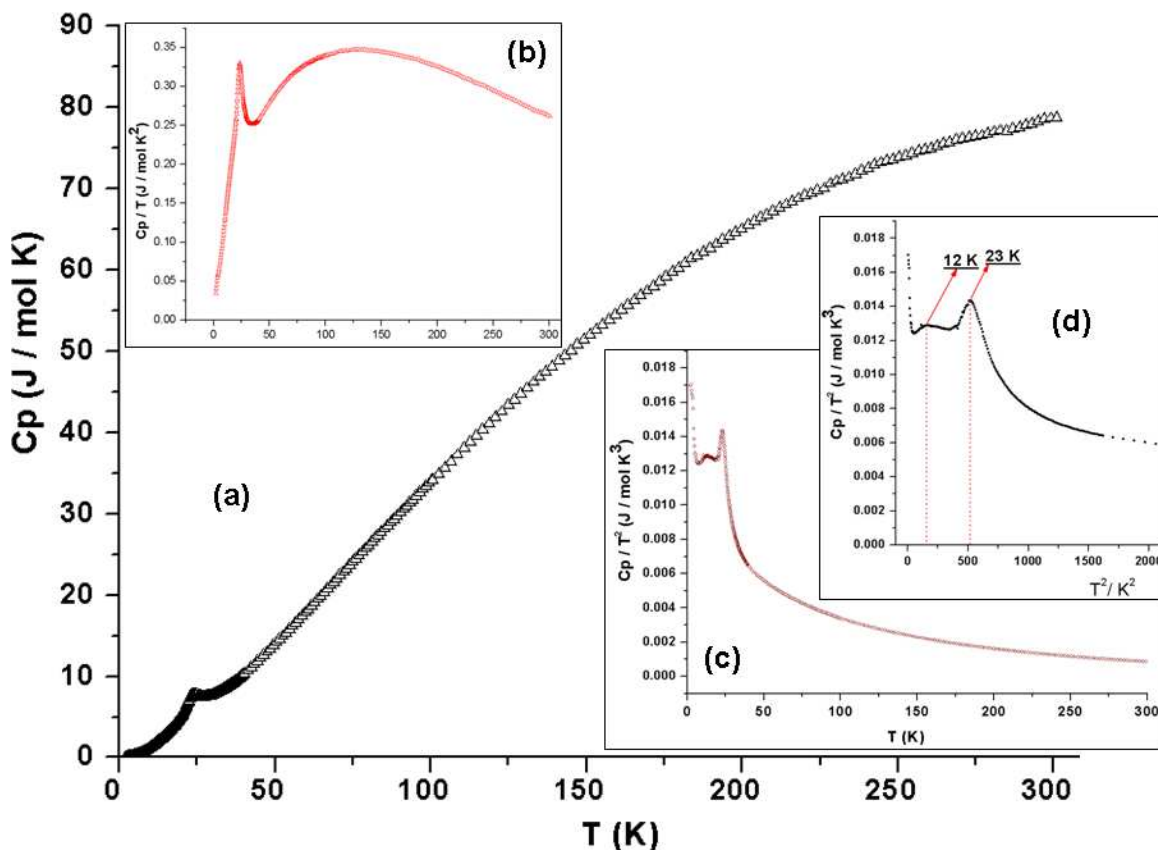


Fig. 5.14. a) Specific heat (C_p) at zero field as a function of T of polycrystalline sample of $KCrO_2$. The inset at the top b) C_p/T and inset c) bottom shows C_p/T^2 both as a function of T whereas inset d) plot C_p/T^2 vs T^2 with lucid view around the respective magnetic ordering temperatures.

5.12. Conclusion

The β - $KCrO_2$ was synthesized with the help of the azide nitrate route [45, 46], revealing the distinctive structure comprises layers of edge-shared CrO_6 octahedra spreading perpendicular to c -axis with K atoms incorporated between the layers in a unique trigonal-prismatic arrangement. The magnetic susceptibility measurement (χ^{-1} vs T) reveals a sharp decrease from the linear behaviour at 26 K in conformity

5. Two dimensional layered magnetic oxides

with the earlier results [71]. However, in contrast to previous finding, we have clearly grasped in the specific heat measurements, λ -type anomaly at 23 K, endorsing the onset of long-range AFM ordering. The thermodynamics of phase transitions was systematically investigated by high resolution X-ray powder diffraction (Bruker Mo D8-Diffractometer) and DSC technique, showing transitions to occur at ~ 629 K from low temperature α -KCrO₂ (R-3m) to high temperature β -KCrO₂ (P-31c) with twisting of K⁺ cation from anti trigonal prism to trigonal prismatic structure. At higher temperature due to strong repulsion between highly mobile K⁺ ions and also due to entropy contribution the beta modification is stabilized over alpha analogue. The insights obtained are expected to facilitate the understanding of the transition mechanism involved, whether it's a sheet gliding or sheet reconstruction.

In order to further stabilize the high temperature β -KCrO₂ phase and to understand the mechanism involved, the high pressure methodology using belt press is in pipeline and will be discussed separately.

5.13 References

- [1] K. Takada et al., Nature **422**, 53 (2003).
- [2] R. E. Schaak, T. Klimczuk, M. L. Foo, and R. J. Cava, Nature **424**, 527 (2003).
- [3] R. Jin, B. C. Sales, P. Khalifah, and D. Mandrus, Phys. Rev. Lett. **91**, 217001 (2003)
- [4] F. C. Chou et al., Phys. Rev. Lett. **92**, 157004 (2004).
- [5] T. Fujimoto et al., Phys. Rev. Lett. **92**, 047004 (2004).
- [6] M. Jansen and R. Hoppe, Z. Anorg. Allg. Chem. **408**, 104 (1974).
- [7] I. Terasaki, Y. Sasago: Phys. Rev. B. **56**, 12685 (1997).
- [8] D.J. Singh: Phys. Rev. B. **61**, 13397, (2000).
- [9] K. Takahata, Y. Iguchi, D. Tanaka: Phys. Rev. B **61**, 12551 (2000).
- [10] T. Kawata, Y. Iguchi, T. Itoh: Phys. Rev. B. **60**, 10584 (1999).

5. Two dimensional layered magnetic oxides

- [11] R. Kitawaki, I. Terasaki: *J. Phy: Condens. Matter* **14**, 12495 (2002).
- [12] H. Yakabe, K. Fujita, K. Nakamura: 17th Inter. Conf. Thermoelectrics, pp .551, (1998)
- [13]
http://www.nsrcc.org.tw/NsrccWebSystem/UPLOADS%5CCHINESE%5CPUBLISH_YEARLY%5C2003~2004/03.pdf
- [14] D. Trinschek, and M. Jansen, *Angew. Chem. Int. Edn.* **38**, 133 (1999).
- [15] M. Sofin, E.-M Peters, and M. Jansen, *Z. Anorg. Allg. Chem.* **628**, 2697 (2002).
- [16] H. D. Fair and R. F. Walker, *Energetic Materials*, vol. 1. (pp 30-38) Physics and chemistry of inorganic azides, Plenum press, New York and London (1977).
- [17] Bruker Suite, Version 2008/3, Bruker AXS Inc., Madison, USA (2008).
- [18] G. M. Sheldrick, SADABS, Bruker AXS area detector scaling and absorption, Version 2008/1, University of Göttingen, Germany (2008).
- [19] G. M. Sheldrick, *Acta Crystallogr. A* **64**, 112 (2008).
- [20] L. J. Van der Pauw, *Philips Res. Rep.*, **13**, 1 (1958).
- [21] J. P. Suchet, *Electrical Conduction in Solid Materials*, Pergamon Press, Oxford, (1975).
- [22] R. Bachmann, F. J. DiSalvo Jr., T. H. Geballe, R. L. Greene, R. E. Howard, C. N. King, H. C. Kirsch, K. N. Lee, R. E. Schwall, H. U. Thomas, and R. B. Zubeck, *Rev. Sci. Instrum.* **43**, 205 (1972).
- [23] J. S. Hwang, K. J. Lin, and C. Tien, *Rev. Sci. Instrum.* **68**, 94, (1997).
- [24] H. Lueken, *Magnetochemie*, Teubner, Leipzig, (1999).
- [25] M. Blangero, R. Decourt, D. Carlier, G. Ceder, M. Pollet, J-P. Doumerc, J. Darriet, C. Delmas., *Inorganic Chemistry* **44**, 9299 (2005).
- [26] Hoppe R., *Angew. Chem. Int. Ed. Engl.* **5**, 95 (1966).
- [27] Hoppe R., *Angew. Chem. Int. Ed. Engl.* **9**, 25 (1970).

5. Two dimensional layered magnetic oxides

- [28] Huebenthal R., "MAPLE, Program for the Calculation of the Madelung Part of Lattice Energy," University of Giessen, Germany (1993).
- [29] R. D. Shannon, *Acta Crystallogr. Sect. A*, **32**, 751 (1976).
- [30] M. Jansen, R. Hoppe, *Z. Anorg. Allg. Chem.* **417**, 31 (1975).
- [31] C. Delmas, C. Fouassier, P. Hagenmuller, *J. Solid State Chem.* **13**, 165 (1975).
- [32] W. Burow, R. Hoppe, *Naturwissenschaften*, **67**, 192 (1980).
- [33] J. Birx, R. Hoppe, *Z. Anorg. Allg. Chem.* **597**, 19 (1991).
- [34] L. C. Baker, T. P. McCutcheon, *J. Am. Chem. Soc.* **78**, 4503 (1956).
- [35] M. Jansen, R. Hoppe, *Z. Anorg. Allg. Chem.* **75**, 408 (1974).
- [36] A. A. Coelho, *J. Appl. Crystallogr.* **36**, 86 (2003).
- [37] M. E. Fisher, *Philos. Mag.* **7**, 1731 (1962).
- [38] A. Möller, U. Löw, T. Taetz, M. Kriener, G. André, F. Damay, O. Heyer, M. Braden, and J. A. Mydosh, *Phys. Rev. B* **78**, 024420 (2008).
- [39] Zoltán A. Gaál, Phillip M. Mallinson, Heston J. Orchard, and Simon J. Clarke, *Inorg. Chem.*, **43**, 3998-4006 (2004).
- [40] Olariu A., Mendels P., Bert F., Alexander L. K., Mahajan A. V., Hillier A. D. and Amato A., *Physical Review B* **79**, 224401 (2009).
- [41] W. Scheld and R. Hoppe, *Z. Anorg. Allg. Chem.*, **568**, 151 (1989).
- [42] B. Deng and James A. Ibers, *Acta Cryst.* **E61**, i15-i17 (2005).
- [43] J. M. Babo and T. Schleid, *Z. Anorg. Allg. Chem.* **635**, 1 (2009).
- [44] R. Hoppe and H. Sabrowsky, *Z. Anorg. Allg. Chem.*, **339**, 144 (1965).
- [45] H. E. Stanley and T. A. Kaplan, *PRL*, **17**(17) 913 (1966).
- [46] C. Delmas, G. Le Flem, C. Fouassier and P. Hagenmuller, *J. Phys. Chem. Solids* **39**, 55 (1978).

5. Two dimensional layered magnetic oxides

- [47] S. Angelov and J. P. Doumerc, Solid State Comm., **77**(3) 213 (1991).
- [48] G. Le Flem, Ph. Courbin and C. Delmas, Magnetic properties of 2D oxides, Z. Anorg. Allg. Chem., **476**, 69 (1981).
- [49] D. Trinschek and M. Jansen, Angew. Chem. **111**, 234 (1999); Angew. Chem. Int. Ed. Engl. **38**, 133 (1999).
- [50] M. Sofin, E.-M. Peters and M. Jansen, Z. Anorg. Allg. Chem. **628**, 2697 (2002).
- [51] H. D. Fair and R. F. Walker, Energetic Materials, vol. 1. (pp 30-38) Physics and chemistry of inorganic azides, Plenum press, New York and London (1977).
- [52] Bruker Suite, version 2008/3, Bruker AXS Inc., Madison, WI, USA (2008).
- [53] Sheldrick G. M., *SADABS—Bruker AXS area detector scaling and absorption*, Version 2008/1, University of Göttingen, Germany (2008).
- [54] Sheldrick G. M., Acta Crystallogr. **A64**, 112 (2008).
- [55] Von H. Wiench, G. Brachtel and R. Hoppe, Z. Anorg. Allg. Chem., **436**, 169 (1977).
- [56] R. Bachmann, F. J. DiSalvo Jr., T. H. Geballe, R. L. Greene, R. E. Howard, C. N. King, H. C. Kirsch, K. N. Lee, R. E. Schwall, H. U. Thomas, and R. B. Zubeck, Rev. Sci. Instrum. **43**, 205 (1972).
- [57] J. S. Hwang, K. J. Lin, and C. Tien, Rev. Sci. Instrum. **68**, 94, (1997).
- [58] H. Lueken, Magnetochemie, Teubner, Stuttgart (1999).
- [59] T. A. Hewston and B. L. Chamberland, Magnetic and structural studies of Cr₂O₅ and Cr₃O₈, Journal of Magnetism and Magnetic Materials **43**, 89 (1984).
- [60] J. Benkowitsch and H. Winter, Physica Scripta. **31**, 222 (1985).

5. Two dimensional layered magnetic oxides

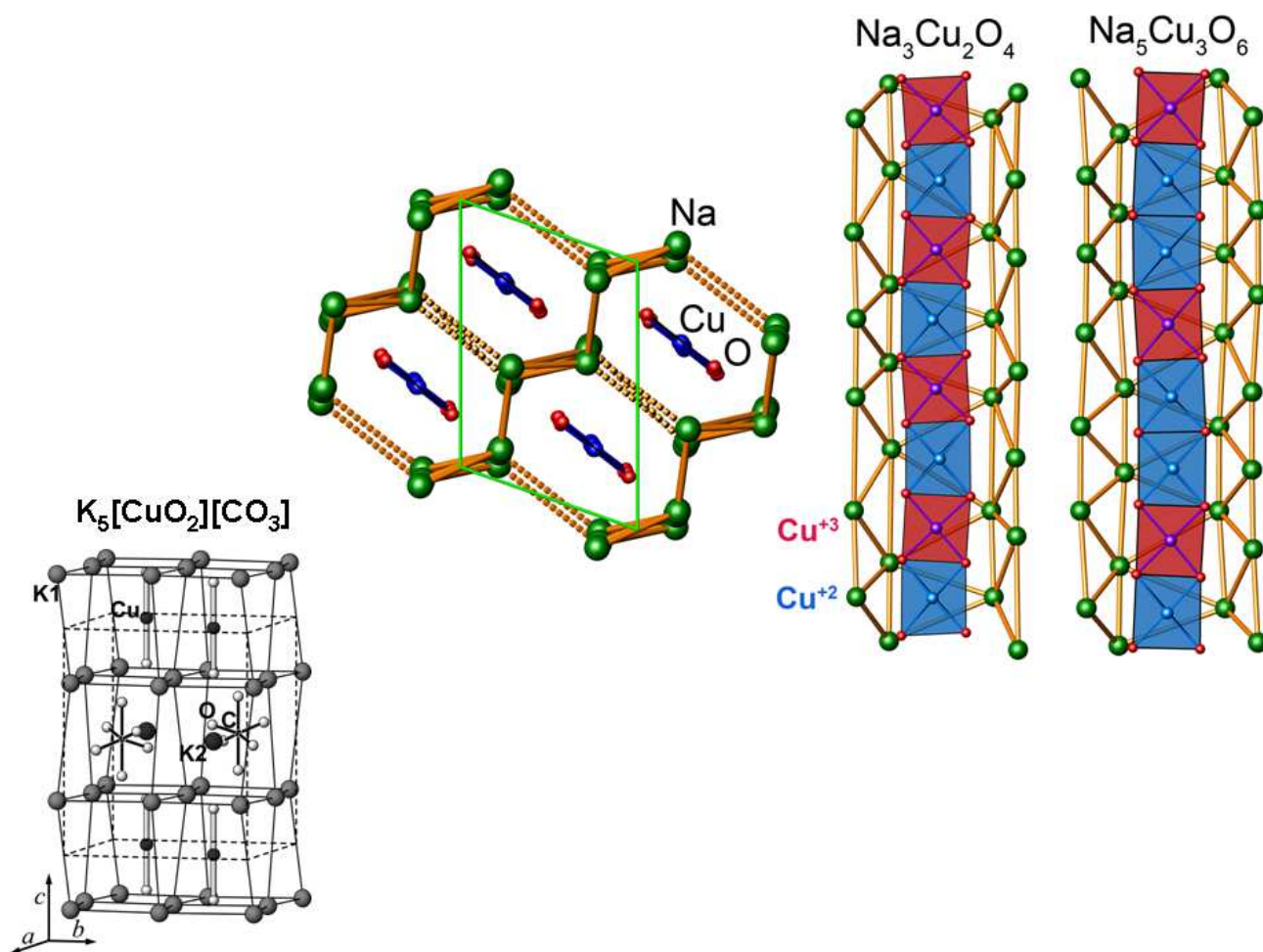
- [61] O. A. Smirnova, M. Avdeev, V. B. Nalbandyan, V. V. Kharton, F. M. B. Marques, *Mater. Res. Bull.* **41**, 1056 (2006).
- [62] R. D. Shannon *Acta Crystallogr. A* **32**, 751 (1976).
- [63] R. Hoppe, *Angew. Chem. Int. Ed. Engl.* **5**, 95 (1966).
- [64] R. Hoppe, *Angew. Chem. Int. Ed. Engl.* **9**, 25 (1970).
- [65] R. Huebenthal, "MAPLE, Program for the Calculation of the Madelung Part of Lattice Energy," University of Giessen, Germany (1993).
- [66] C. Delmas, J. J. Braconnier and P. Hagenmuller, *Mat. Res. Bull.*, **17**, 117 (1982).
- [67] C. Delmas, C. Fouassier and P. Hagenmuller, *Mater. Res. Bull.* **11**, 1483 (1976).
- [68] C. Delmas, G. Le Flem, C. Fouassier and P. Hagenmuller, *J. Phys. Chem. Solids* **39**, 55 (1978).
- [69] C. Delmas, F. Menil, G. Le Flem, C. Fouassier and P. Hagenmuller, *J. Phys. Chem. Solids* **39**, 51 (1978).
- [70] J. L. Soubeyroux, D. Fruchart, C. Delmas and G. Le Flem, *J. Magnetism Magnetic Mater.* **14**, 159 (1979).
- [71] J. L. Soubeyroux, D. Fruchart, J. C. Marmeggi, W. J. Fitzgerald, C. Delmas and G. Le Flem, *Phy. Stat. sol. (a)* **67**, 633 (1981).
- [72] T. R. McGuire, J. E. Scott and F. H. Grannis, AFM in a Cr_2O_3 Crystal, *Physics Review*, **102**(4), 1000 (1956).
- [73] P. Ramirez, *Annu. Rev. Mater. Sci.* **24**, 453 (1994).
- [74] J. E. Greedan, *Oxides with the trirutile and pyrochlore structures, Landolt-Bornstein III27g*, Springer-Verlag, Berlin, pp. 87± 123, (1992).
- [75] L. J. de Jongh and A. R. Miedema, *Advances in Physics* **50**(8), 947, (2001).

5. Two dimensional layered magnetic oxides

[76] A. Möller, U. Löw, T. Taetz, M. Kriener, G. André, F. Damay, O. Heyer, M. Braden, and J. A. Mydosh, *Phys. Rev. B* **78**, 024420 (2008).

[77] F. M. R. Engelsman and B. Van Laar, *Journal of solid state chemistry* **6**, 384-386 (1973).

Chapter 6: Charge and spin ordering phenomenon in one dimensional alkali oxocuprates



Chapter 6

One-Dimensional Alkali-oxocuprates

6.1. Synthesis, structure and magnetic properties of the new Wigner crystallized chain cuprate $\text{Na}_5\text{Cu}_3\text{O}_6$

6.1.1. Introduction

Multinary oxides constitute a remarkably versatile and prolific class of materials. They have continued to play a major role in the fields of high temperature superconductivity (HTSC) [1] and colossal magneto resistivity (CMR) [2], or, more recently, multiferroics and spintronics [3]. Although, during the past decades, a lot of effort has gone into unraveling the phenomena of HTSC in cuprates [4] and of CMR in manganates, no fully consistent and conclusive microscopic explanation has become available yet. In the first place, this unpleasant state is due to the high complexity of the problems resulting among others from strong electron correlation, and coupled charge, spin and orbital ordering in collective systems. Furthermore, virtually all oxide materials showing HTSC or CMR include severe structural disorder, even decay into multiphase systems (phase separation, stripe formation) [5-7], a fact that has impeded theoretical analyses commonly relying upon translational invariance, and blurred experimental observations by inhomogeneous signal broadening effects. Thus, it would be highly desirable to employ fully periodic and chemically well defined materials as model systems for studying charge spin and orbital ordering, either coupled or independent.

With the "azide/nitrate route" we have developed a rather efficient approach for the solid state synthesis of intrinsically doped multinary transition metal oxides [8, 9]. As a particular strength of this procedure, the oxygen content, and thus the valence state of the transition metal, can be precisely fixed by the alkali azide/nitrate ratio weighed in. At various illustrative examples, the "azide/nitrate route" has been proven to be rather versatile in providing highly defined materials showing interesting structural and physical properties. Among these, in particular, a new family of quasi one-dimensional intrinsically doped sodium cuprates(II/III) [10-14] has been found to be excellently suited for investigating the wealth of

6. One-Dimensional Alkali-oxocuprates

physical properties related. Among them is the unique phenomenon of separation of spin and charge excitations, which constitutes potential for applications in non-linear photoelectric devices. Furthermore, the close structural and electronic relationship of these materials to the high-temperature superconductors (HTSC), and the known instabilities of the HTSC towards low-dimensional phenomena forms a background, which provides a strong motivation for close scrutiny of these materials [15-17].

The sodium cuprates (II/III) realized thus far, $\text{Na}_3\text{Cu}_2\text{O}_4$ and $\text{Na}_8\text{Cu}_5\text{O}_{10}$ [10], are intrinsically doped Mott insulators. In both compounds the one dimensional ${}^1\infty\text{CuO}_2^{n-}$ spin chains based on edge-sharing CuO_4 units with Cu—O—Cu bonds close to 90° are the dominating structural units. In contrast to many two-dimensional cuprates, these materials do not become superconducting upon doping. Instead, a charge-ordered state develops, in which spin-bearing divalent copper ions and non-magnetic Zhang-Rice singlets (holes/ Cu^{+3}) [18] alternate with specific periodicities matching the hole filling factors of $1/2$ and $2/5$, respectively [10].

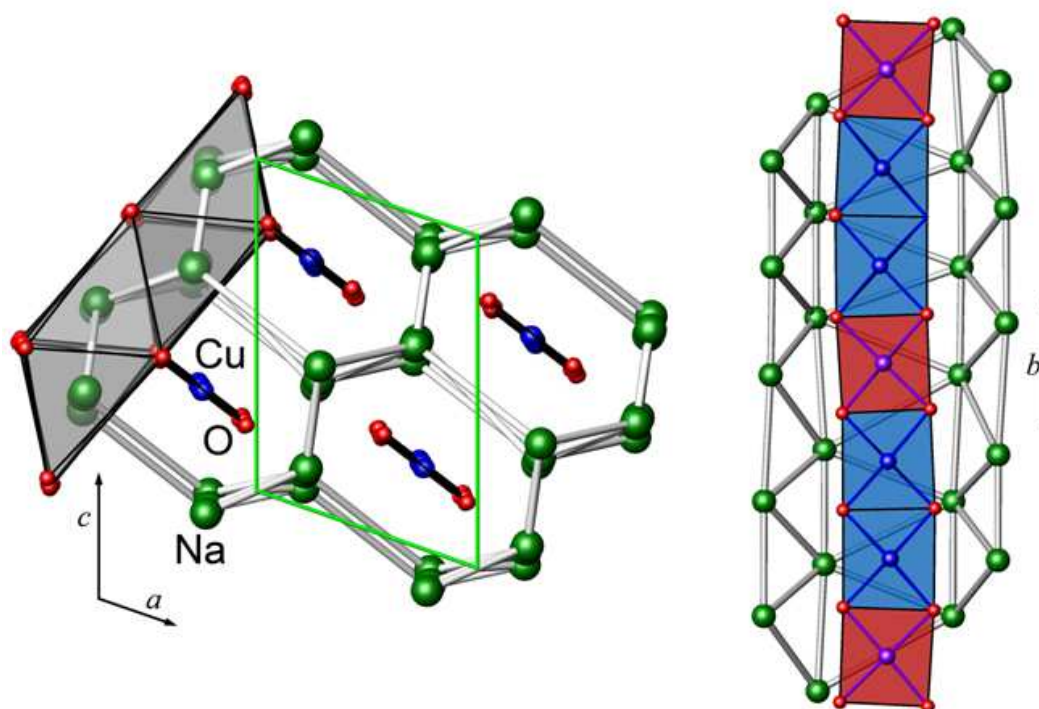


Fig. 6.1. Crystal structure with unit cell (green sticks) of $\text{Na}_5\text{Cu}_3\text{O}_6$: (left) showing the periodicities of Na and CuO_2 units with Na ions forming a honeycomb pattern (emphasized by white sticks) with the voids occupied by cuprate ribbons; (right) CuO_2 chains in $\text{Na}_5\text{Cu}_3\text{O}_6$: Cu^{3+} —red squares, Cu^{2+} —blue squares.

6. One-Dimensional Alkali-oxocuprates

The two orthogonal oxygen p -orbitals overlap with the d -orbitals of the copper ions, thereby strongly reducing the next nearest neighbour hopping integrals, and the corresponding superexchange becomes very weak. This explains, among others, why even these doped edge-sharing 1D cuprates $[\text{Na}_{1+x}\text{CuO}_2]$ are insulators.

Interestingly, these linear cuprates represent the first unambiguous manifestations of Wigner lattices [19, 20], which highlight the importance of long-range coulomb interaction in strongly correlated systems and provide a one-dimensional test ground for the study of charge stripe formation. They are perfect examples of one dimensional spin $\frac{1}{2}$ Heisenberg chains with long-range exchange interactions which depend on the charge ordering pattern and the distance between the spins.

Chain cuprates with edge-sharing geometry show a number of intriguing magnetic properties. Due to the almost 90° angle of Cu—O—Cu bonds, the hopping t_1 between nearest neighbor Cu sites results mainly from direct Cu—Cu exchange while the next-nearest neighbor hopping t_2 originates mainly from the Cu—O—O—Cu path. Therefore the magnitude of the effective next-nearest neighbor exchange interaction J_2 is expected to be similar or even larger than that of the nearest-neighbor exchange J_1 . Furthermore, J_1 tends to be ferromagnetic and J_2 antiferromagnetic leading at least locally to a non-collinear spin structure. This non-collinearity is believed to be at the heart of the recently observed multiferroic behavior of the undoped edge-sharing chain cuprates LiCuVO_4 and LiCu_2O_2 [21-24] and has triggered a number of theoretical studies of the one-dimensional Heisenberg model with nearest and next-nearest neighbor interactions [25-28]. However, the question what are realistic values for the exchange constants J_1 and J_2 is far from settled. For LiCuVO_4 , for example, recent neutron scattering data have been interpreted in terms of two weakly coupled antiferromagnetic chains, i.e. $J_2 \gg |J_1|$ [29]. Others, however, have argued that both

6. One-Dimensional Alkali-oxocuprates

Table 6.1. X-ray and crystallographic data for Na₅Cu₃O₆

Empirical formula	Cu ₃ Na ₅ O ₆
Formula weight	401.57
Temperature	293(2) K
Wavelength	0.71073 Å
Crystal system	monoclinic
Space group, Z	<i>P</i> 2 ₁ / <i>n</i> (no. 14), 4
Unit cell dimensions	<i>a</i> = 5.7055(17) Å <i>b</i> = 16.795(5) Å <i>c</i> = 8.113(3) Å <i>β</i> = 109.326(4)°
Volume	733.6(4) Å ³
Density (calculated)	3.636 Mg/m ³
Crystal shape, colour	Rods, black
Absorption coefficient	8.896 mm ⁻¹
F(000)	760
Crystal size	0.30 x 0.20 x 0.20 mm ³
Theta range for data collection	2.43 to 34.84°
Index ranges	-9 ≤ <i>h</i> ≤ 9, -26 ≤ <i>k</i> ≤ 26, -12 ≤ <i>l</i> ≤ 12
Reflections collected	11152
Independent reflections	3045, <i>R</i> _{int} = 0.0427
Transmission <i>t</i> _{max} , <i>t</i> _{min}	0.2692, 0.1755
Parameters	137
Goodness-of-fit on F ²	1.089
Final R indices [<i>I</i> > 2σ(<i>I</i>)]	<i>R</i> 1 = 0.0654, <i>wR</i> 2 = 0.1558
R indices (all data)	<i>R</i> 1 = 0.0769, <i>wR</i> 2 = 0.1634
Extinction coefficient	0.0047(4)
Δ <i>e</i> _{max} , Δ <i>e</i> _{min}	2.028, -2.073 eÅ ⁻³
Absorption correction	SADABS [33]
Diffractometer	Smart APEX I CCD, Bruker AXS
CSD number:	422413

interactions are of comparable magnitude [30], a view which is also supported by optical data [31] and an analysis of the susceptibility data [28].

6. One-Dimensional Alkali-oxocuprates

Table 6.2. Atomic coordinates and equivalent isotropic displacement parameters (\AA^2) for $\text{Na}_5\text{Cu}_3\text{O}_6$

	x	y	z	U_{eq}
Cu1	0.23663(10)	0.04412(3)	0.76471(7)	0.01173(16)
Cu2	0.23799(10)	-0.12180(3)	0.75447(7)	0.01287(16)
Cu3	0.24767(10)	0.21046(3)	0.75715(7)	0.01185(16)
Na1	-0.2284(4)	0.04657(13)	0.8780(3)	0.0185(4)
Na2	-0.2272(4)	-0.13312(12)	0.8807(3)	0.0155(4)
Na3	-0.2833(5)	-0.2695(2)	0.5997(4)	0.0427(9)
Na4	-0.2866(5)	-0.0537(3)	0.5591(3)	0.0490(10)
Na5A	0.2138(10)	0.3582(4)	1.0574(6)	0.0253(9)
Na5B	0.7186(10)	0.1862(4)	0.6055(8)	0.0297(11)
O1	0.4223(7)	-0.03841(19)	0.6959(5)	0.0164(6)
O2	0.0545(7)	0.13220(18)	0.8177(4)	0.0119(5)
O3	0.4351(7)	0.12706(18)	0.7106(6)	0.0172(7)
O4	0.0450(7)	-0.04160(19)	0.8131(5)	0.0155(6)
O5	0.0656(7)	0.2958(3)	0.7951(6)	0.0240(8)
O6	0.0572(7)	-0.2112(2)	0.8003(5)	0.0218(7)

U_{eq} is defined as one third of the trace of the orthogonalized U_{ij} tensor.

Here, we report on $\text{Na}_5\text{Cu}_3\text{O}_6$, a new member of the family of mixed valent chain cuprates with a hole filling factor of $1/3$. From the effective one-dimensional spin $1/2$ Heisenberg model used to analyze the magnetic properties of $\text{Na}_3\text{Cu}_2\text{O}_4$ and $\text{Na}_8\text{Cu}_5\text{O}_{10}$ the magnetic structure of $\text{Na}_5\text{Cu}_3\text{O}_6$ is expected to be particularly simple: the spin-bearing divalent copper ions on next-nearest lattice sites within the chain should form dimers which are only weakly coupled among each other. Surprisingly, this is not the case. We discuss the reasons for the unexpected magnetic properties and present a quantitative theoretical analysis of the susceptibility data.

6.1.2. Experimental Details

6.1.2.1. Material synthesis. $\text{Na}_5\text{Cu}_3\text{O}_6$ ($\text{Na}_{1.667}\text{CuO}_2$) has been prepared along the "azide/nitrate route" according to equation (1), as a single phase microcrystalline powder [8, 9]. The starting materials, NaNO_3 (Merck, 99.99%), NaN_3 (Sigma-Aldrich, 99.99%), and

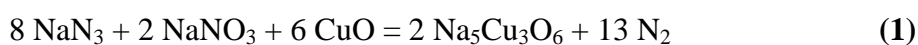
6. One-Dimensional Alkali-oxocuprates

CuO (prepared by heating $\text{Cu}(\text{C}_2\text{O}_4) \cdot 1/2 \text{H}_2\text{O}$ in a flow of dry oxygen at 593 K, for 20 h) were mixed in the ratio required according to Eq. (1), further milled in a planet ball mill, pressed in

Table 6.3. Anisotropic thermal displacement parameters (in \AA^2) for $\text{Na}_5\text{Cu}_3\text{O}_6$

	U_{11}	U_{22}	U_{33}	U_{23}	U_{13}	U_{12}
Cu1	0.0106(3)	0.0131(3)	0.0116(3)	0.00112(16)	0.00382(19)	-0.00073(16)
Cu2	0.0094(3)	0.0109(3)	0.0172(3)	-0.00194(17)	0.0030(2)	0.00003(16)
Cu3	0.0111(3)	0.0097(3)	0.0142(3)	0.00178(17)	0.00345(19)	-0.00067(16)
Na1	0.0168(9)	0.0200(10)	0.0195(9)	-0.0031(7)	0.0073(8)	-0.0016(7)
Na2	0.0096(8)	0.0216(9)	0.0136(8)	-0.0016(6)	0.0018(6)	-0.0012(6)
Na3	0.0203(12)	0.0567(19)	0.0556(18)	-0.0438(16)	0.0184(12)	-0.0166(12)
Na4	0.0232(13)	0.110(3)	0.0133(11)	0.0001(14)	0.0053(9)	0.0225(15)
Na5A	0.027(2)	0.031(3)	0.019(2)	-0.0007(18)	0.0090(18)	0.006(2)
Na5B	0.024(2)	0.029(3)	0.041(3)	0.018(2)	0.017(2)	0.007(2)
O1	0.0179(16)	0.0101(13)	0.0253(17)	0.0052(11)	0.0126(13)	0.0031(11)
O2	0.0137(14)	0.0119(13)	0.0127(13)	0.0001(10)	0.0077(11)	-0.0003(10)
O3	0.0154(16)	0.0074(13)	0.034(2)	-0.0027(11)	0.0151(14)	-0.0006(10)
O4	0.0117(14)	0.0106(13)	0.0225(16)	0.0009(11)	0.0035(12)	-0.0013(10)
O5	0.0111(15)	0.033(2)	0.029(2)	0.0177(16)	0.0082(14)	0.0045(13)
O6	0.0142(15)	0.0283(19)	0.0249(18)	-0.0112(14)	0.0092(14)	0.0016(13)

pellets under 10^5 N , dried under vacuum (10^{-3} mbar) at 423 K for 12 h, and placed under argon in a closed steel container [9] provided with a silver inlay. In a flow of dry argon the following temperature profile was applied: 298→533 K (100 K/h); 533→673 K (5 K/h); 673→923 K (600 K/h); 923→943 K (200 K/h) and subsequent annealing for 50 h at 943 K.



Hazards: The reaction container must not be welded and not to be heated too rapidly, otherwise the containers may blow up!

6. One-Dimensional Alkali-oxocuprates

Table 6.4. Interatomic distances (in Å), CN, ECoN and MEFIR^[24] (in Å) for Na₅Cu₃O₆

Atom	O1	O2	O3	O4	O5	O6	CN	ECoN	MEFIR
Cu1	1.936(3)	1.936(3)	1.935(3)	1.926(3)			4	4.0	0.53
Cu2	1.903(3)			1.896(4)	1.904(4)	1.926(4)	4	4.0	0.50
Cu3		1.881(3)	1.874(3)		1.855(4)	1.880(4)	4	4.0	0.46
Na1	2.499(4)	2.332(4)	2.373(4)	2.335(4) 2.377(4)			5	4.9	0.95
Na2	2.606(4)	2.315(4)		2.374(4)	2.316(4)	2.340(4)	5	4.7	0.93
Na3		2.501(5)	2.703(5)		2.332(5)	2.300(5) 2.318(5)	5	4.4	0.93
Na4	2.297(5) 2.493(5)		2.408(5)	2.299(5)			4	3.8	0.92
Na5a	2.604(7)	2.355(6)	2.333(6)		2.270(7)		4	3.6	0.90
Na5b		2.295(6)	2.290(6)		2.397(8) 2.767(8)	2.614(7)	5	4.1	0.93
CN	7	7	7	6	7	6			
ECoN	6.3	6.8	6.5	6.0	6.3	5.6			
MEFIR	1.46	1.42	1.43	1.41	1.42	1.42			

The obtained black powders, being very sensitive to humid air, were sealed in glass ampoules under argon atmosphere and all following manipulations with these substances were performed in inert atmospheres of purified argon.

6. 1.2.2. Structure determination. Single crystals in the form of black needles can easily be singled out immediately after the reaction. However for better crystal quality the sample was post annealed at 873 K for 400 hours. Single crystal diffraction data were collected on a three circle diffractometer (Bruker AXS, Karlsruhe, Germany) equipped with a SMART-CCD (APEX I), at 293 K. The collection and reduction of data were carried out with the Bruker Suite software package [32]. Intensities were corrected for absorption effects applying a multi-scan method [33].

The structure was solved by direct methods and refined by fullmatrix least-squares fitting with the SHELXTL software package [34]. Experimental details on crystallographic data and data collection are given in Table 6.1. Table 6.2 shows the atomic parameters and equivalent isotropic displacement parameters, and Table 6.3 tabulates the anisotropic displacement

6. One-Dimensional Alkali-oxocuprates

Table 6.5. Selected bond angles (°) in Na₅Cu₃O₆

atoms	angles (°)	atoms	angles (°)
O(3)-Cu(1)-O(1)	91.92(15)	O(5)-Cu(3)-O(6)	84.81(18)
O(3)-Cu(1)-O(2)	84.09(15)	O(3)-Cu(3)-O(6)	92.83(17)
O(4)-Cu(1)-O(1)	85.67(15)	O(5)-Cu(3)-O(2)	95.06(16)
O(4)-Cu(1)-O(2)	98.28(15)	O(3)-Cu(3)-O(2)	87.31(15)
O(4)-Cu(1)-O(3)	177.52(15)	O(5)-Cu(3)-O(3)	177.26(16)
O(1)-Cu(1)-O(2)	175.11(14)	O(6)-Cu(3)-O(2)	179.26(17)
O(4)-Cu(2)-O(1)	87.43(15)	Cu(2)-O(1)-Cu(1)	93.13(16)
O(1)-Cu(2)-O(5)	93.96(17)	Cu(3)-O(2)-Cu(1)	94.13(15)
O(4)-Cu(2)-O(6)	96.44(16)	Cu(3)-O(3)-Cu(1)	94.42(16)
O(5)-Cu(2)-O(6)	82.24(17)	Cu(2)-O(4)-Cu(1)	93.66(17)
O(4)-Cu(2)-O(5)	177.64(18)	Cu(3)-O(5)-Cu(2)	97.22(18)
O(1)-Cu(2)-O(6)	175.54(15)	Cu(3)-O(6)-Cu(2)	95.68(17)
Cu(1)-Cu(3)-Cu(2)	179.15(3)		
Cu(2)-Cu(1)-Cu(3)	176.29(3)		
Cu(1)-Cu(2)-Cu(3)	178.42(3)		

parameters from the single crystal data. Further details may be obtained from Fachinformationszentrum Karlsruhe, on quoting the CSD number written in Table 6.1.

6.1.2.3. *The X-ray investigation on powder samples* was performed using a D8-Advance diffractometer (Bruker AXS, Karlsruhe, Germany) with Cu-K α_1 radiation ($\lambda = 1.54178 \text{ \AA}$) at room temperature using a position-sensitive detector and a curved germanium monochromator.

6.1.2.4. *The differential scanning calorimetry (DSC)* measurements were carried out with a DSC device (DSC 404 C, Netzsch GmbH, Selb, Germany). The sample was heated at a rate of 30 K min^{-1} in a corundum crucible under dry argon.

6. One-Dimensional Alkali-oxocuprates

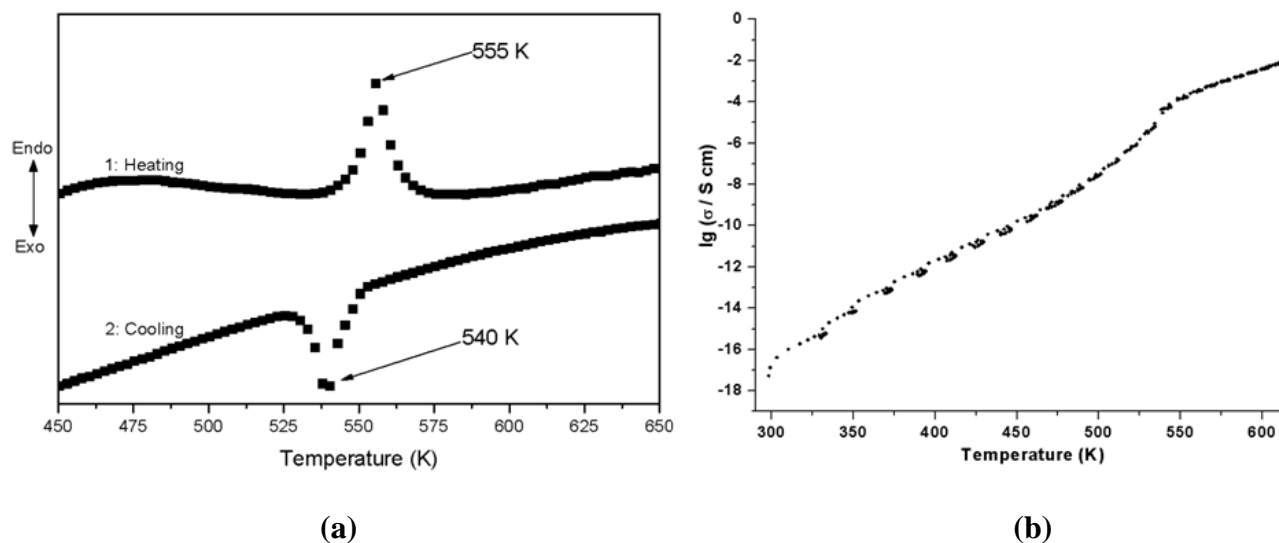


Fig. 6.2 (a). Thermal behaviour of Na₅Cu₃O₆ as detected by differential scanning calorimetry (DSC) (b). High temperature conductivity of polycrystalline sample of Na₅Cu₃O₆

6.1.2.5. Temperature dependence of the specific heat (C_p) of a polycrystalline sample of Na₅Cu₃O₆ was measured between 2 and 250 K using a commercial PPMS (Physical Property Measurement System, Quantum Design, 6325 Lusk Boulevard, San Diego, CA.) employing the relaxation method [35, 36]. To thermally fix the sample tablet ($\varnothing = 5$ mm and thickness 1mm) to the sapphire sample platform, a minute amount of Apiezon N vacuum grease was used. The heat capacity of the sample holder platform and grease was individually determined in a separate run and subtracted from the total measured heat capacities.

6.1.2.6. The magnetic susceptibility $\chi(T)$ of polycrystalline powder samples of Na₅Cu₃O₆ have been measured in the temperature range from 2 K to 680 K in magnetic fields up to 7 T using a SQUID-Magnetometer (MPMS 5.5, Quantum Design). For measurements above 350 K the sample was contained in warily dried SUPRASIL ampoule ($\varnothing = 3$ mm) that was long enough to extend over the coils of the magnetometer inside the oven. In order to nullify the contribution, whatsoever, from spurious ferro- and paramagnetic impurities the Honda Owen correction [37, 38] was made to the whole raw data obtained at 1, 3 and 7 Tesla, at magnetic field approaching infinity [$H^{-1} = 0$]. Later the data is further corrected for core electron diamagnetic [-129×10^{-6} emu/mol] [39, 40] and van Vleck contributions [$(+43 \times 10^{-6} \times 2)$ (emu/mol)] [41] to get the original spin susceptibility χ_{spin} .

6.1.2.7. *Computational methods.*

The numerical calculation were performed using a TMRG (Transfer matrix renormalization group) algorithm which a powerful numerical tool for exact calculation of thermodynamic quantities and help in fit of experimental susceptibility data to the susceptibility for a Heisenberg model particularly at lower temperature. Compared with QMC methods it has further the advantage of never suffering under the fermion sign problem restricting the QMC method often to relatively high temperatures.

6.1.3. RESULTS AND DISCUSSION

6.1.3.1. *Crystal Structure and Structure Comparison*

The crystal structure of $\text{Na}_5\text{Cu}_3\text{O}_6$ ($\text{Na}_{1.667}\text{CuO}_2$), a new member of the one dimensional commensurate composite crystal family $\text{Na}_{1+x}\text{CuO}_2$ [10, 42], has been solved through single crystal X-ray diffractometry (c.f. Table 6.1). Accordingly, the main structural characteristic is a one-dimensional polyanionic ${}^1_{\infty}\text{CuO}_2^{n-}$ chain, in which Cu is coordinated by oxygen in a square planar arrangement and these CuO_4 -squares knit together in linear chains, sharing edges in trans-position, with mean intrachain Cu—Cu distances of 2.80 Å (Fig. 6.1, right).

Neighboring $\text{CuO}_{4/2}$ chains are stacked parallel to each other like in $M\text{CuO}_2$ cuprates formed by the bigger alkali metals ($M = \text{K}$ [43], Rb and Cs [44]). The linear chains in the title compound are shifted relative to each other by $b/2$ [Fig. 6.3(b)], in contrast to the latter ones. The interchain Cu—Cu distances amount to 4.36 Å, on average. The sodium ions fill the space in-between the $\text{CuO}_{4/2}$ chains, in the form of layers of slightly elongated edge sharing NaO_6 polyhedra, with Na ions forming a tubular honeycomb-like arrangement (Fig. 6.1, left) with the channels occupied by cuprate ribbons.

6. One-Dimensional Alkali-oxocuprates

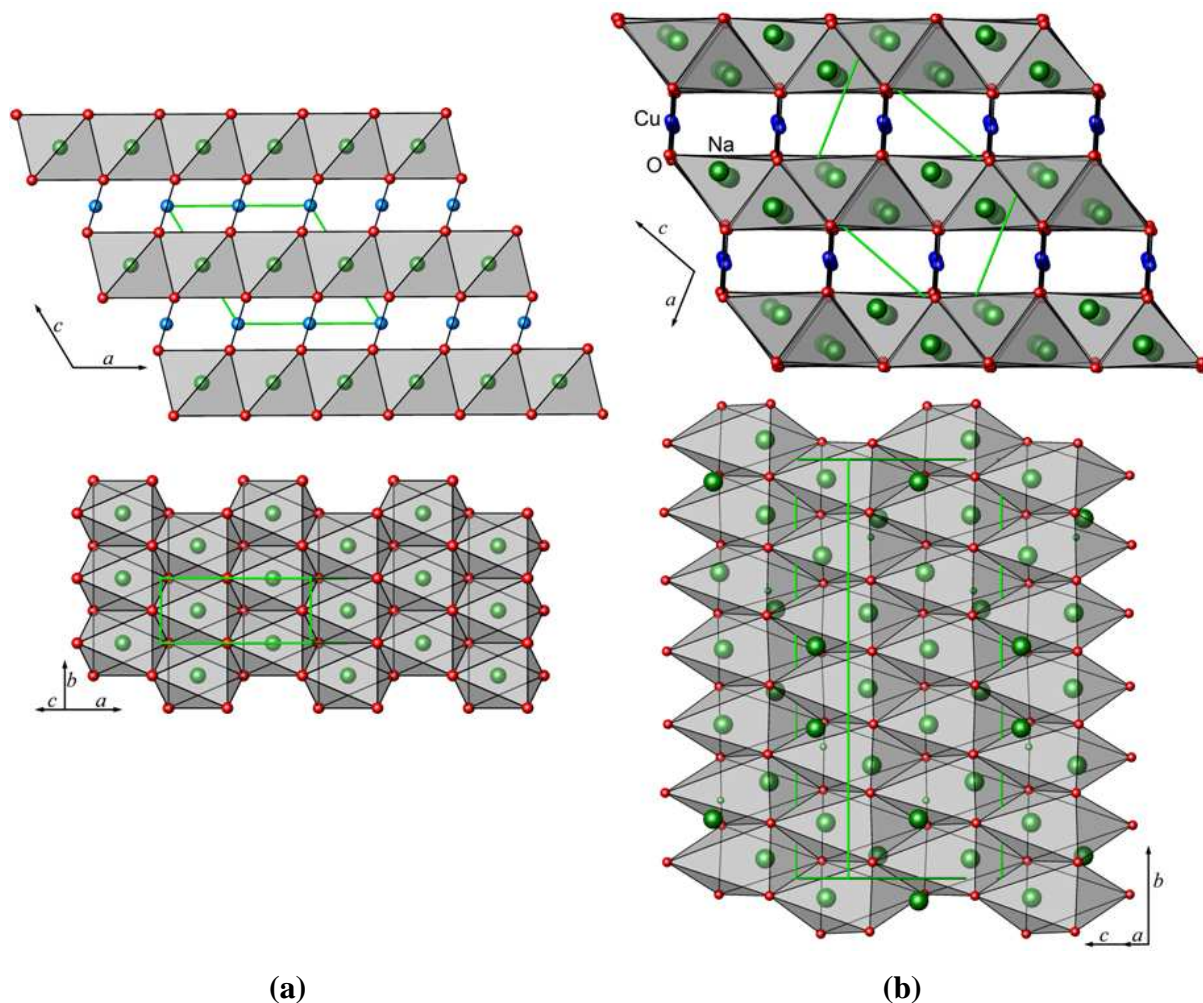


Fig. 6.3. Comparison of crystal structures of a) NaCuO_2 ^[44] with b) $\text{Na}_5\text{Cu}_3\text{O}_6$

The crystal structures of all members of chain cuprates belonging to the general family $\text{Na}_{1+x}\text{CuO}_2$ [10, 42, 45], differ in the Na/CuO_2 ratios, thus in the $\text{Cu}^{2+}/\text{Cu}^{3+}$ ratios. These two features determine the periodicity/modulation along b (chain direction). The resulting repetition unit for $\text{Na}_5\text{Cu}_3\text{O}_6$ is $\text{Cu}^{2+}-\text{Cu}^{3+}-\text{Cu}^{2+}-\text{Cu}^{2+}-\text{Cu}^{3+}-\text{Cu}^{2+}$. The Cu^{3+} and Cu^{2+} oxidation states can be clearly assigned according to the $\text{Cu}-\text{O}$ bond distances, which are in the range of 1.855(4) - 1.881(3) for Cu^{3+} and 1.896(3) - 1.936(3) Å for Cu^{2+} (Table 6.4). The way of linking the primary structural units, as well as the variations of the copper to oxygen distances inevitably leads to deviations of the $\text{O}-\text{Cu}-\text{O}$ angles from the ideal 90° and

6. One-Dimensional Alkali-oxocuprates

furthermore cause a slight undulation of the linear chains ($\angle\text{Cu—Cu—Cu} \approx 177.5^\circ$) (Table 6.5).

In contrast to NaCuO_2 where all Na^+ ions are in the centers of the oxygen octahedral [Fig. 6.3(a)], in title compound the sodium atoms are in turn off centered, thereby giving freedom to accommodate more sodium atoms [Fig. 6.3(b)]. This displacement in turn leads to two different oxygen environments for the Na atoms with Na–O bond length ranging from 2.270 to 2.767 Å.(c.f Table 6.4). The sodium atoms are shifted from the centers of the oxygen polyhedra in order to maximize the Na—Na distances. This leads in some cases to unusual thermal displacement parameters. This is true particularly for the position of Na5, which is better described applying a split position (Na5A and NA5B, Table 6.2). Nevertheless, the interatomic distances, coordination numbers (CN) in comparison with the effective coordination numbers (ECoN) and mean fictive ionic radii (MEFIR) [46] for $\text{Na}_5\text{Cu}_3\text{O}_6$, confirm coordination numbers 4 and 5 for all sodium atoms (Table 6.4).

Alternatively the structure of the title compound can also be interpreted within the 3+1D superspace approach [47-49], when considering the structure as a composite one. $\text{Na}_5\text{Cu}_3\text{O}_6$ has the same small basic unit cell as $\text{Na}_3\text{Cu}_2\text{O}_4$ or $\text{Na}_8\text{Cu}_5\text{O}_{10}$ [$1/4 \times b(\text{Na}_3\text{Cu}_2\text{O}_4) \approx 1/5 \times b(\text{Na}_8\text{Cu}_5\text{O}_{10}) \approx 1/6 \times b(\text{Na}_5\text{Cu}_3\text{O}_6)$], the same superspace group, but a different modulation vector along the chain direction ($q = 5/6 \times b^*$).

6. One-Dimensional Alkali-oxocuprates

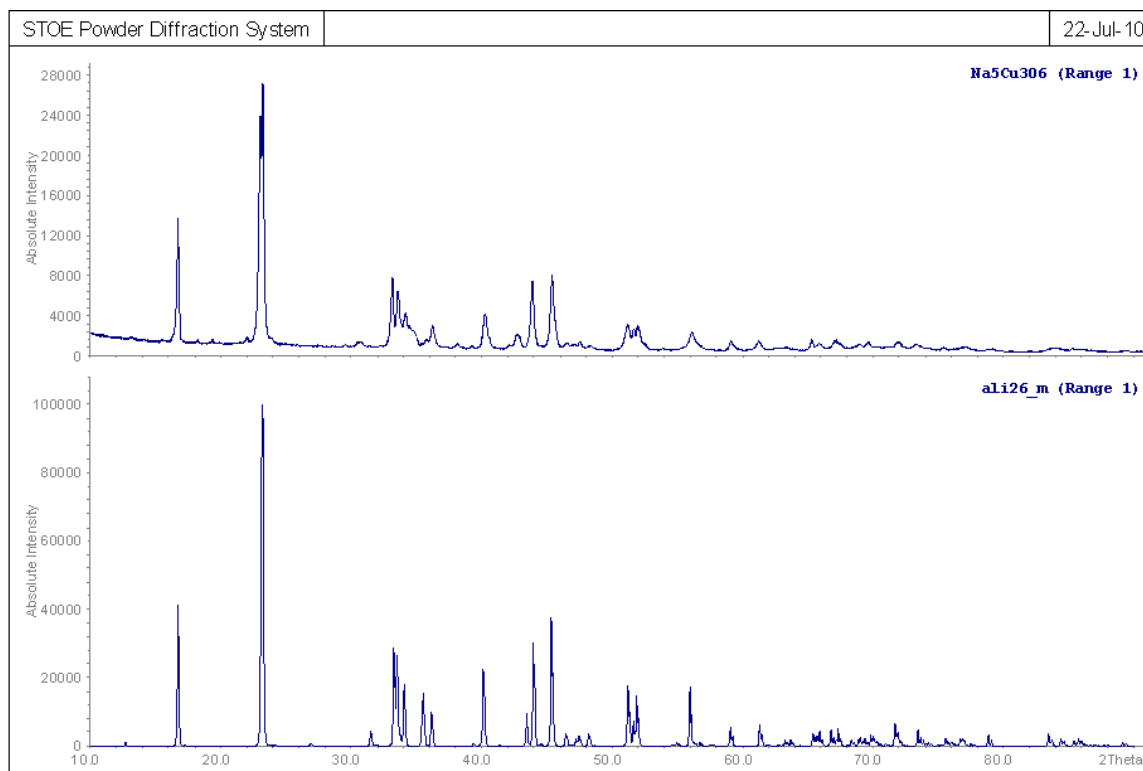


Fig. 6.4. Scattered X-ray intensity for polycrystalline sample of Na₅Cu₃O₆ at $T = 298$ K as a function of diffraction angle 2θ ($\lambda = 1.54059$ Å), showing measured (upper inset) and calculated based on single crystal data (lower inset).

6.1.3.2. Thermal analysis and magnetic characterization

As monitored by differential scanning calorimetry there is a sharp reversible thermal signal at $T = 555$ K for Na₅Cu₃O₆, which can be assigned to the WL (wigner lattice) melting [20] (Fig. 6.2). The sample begins to decompose at about 1058 K, leaving mixtures of NaCuO [50], NaCu₂O₂ [51], and Cu₂O [52] as the only solid residues. The phase purity of sample was monitored by X-ray powder analysis as can be seen in Fig. 6.4. DC and AC conductivity measurement were also performed depicting a clear transition from Arrhenius behaviour below T_m (Wigner lattice melting) to an almost temperature independent conductivity regime above T_m (Fig. 6.2 (b)).

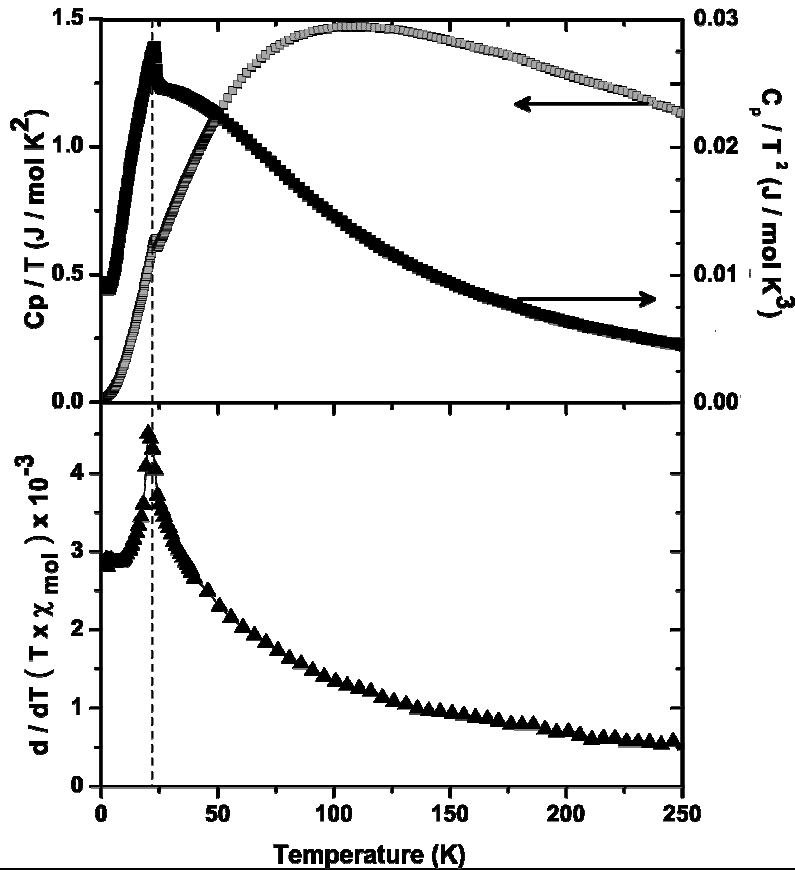
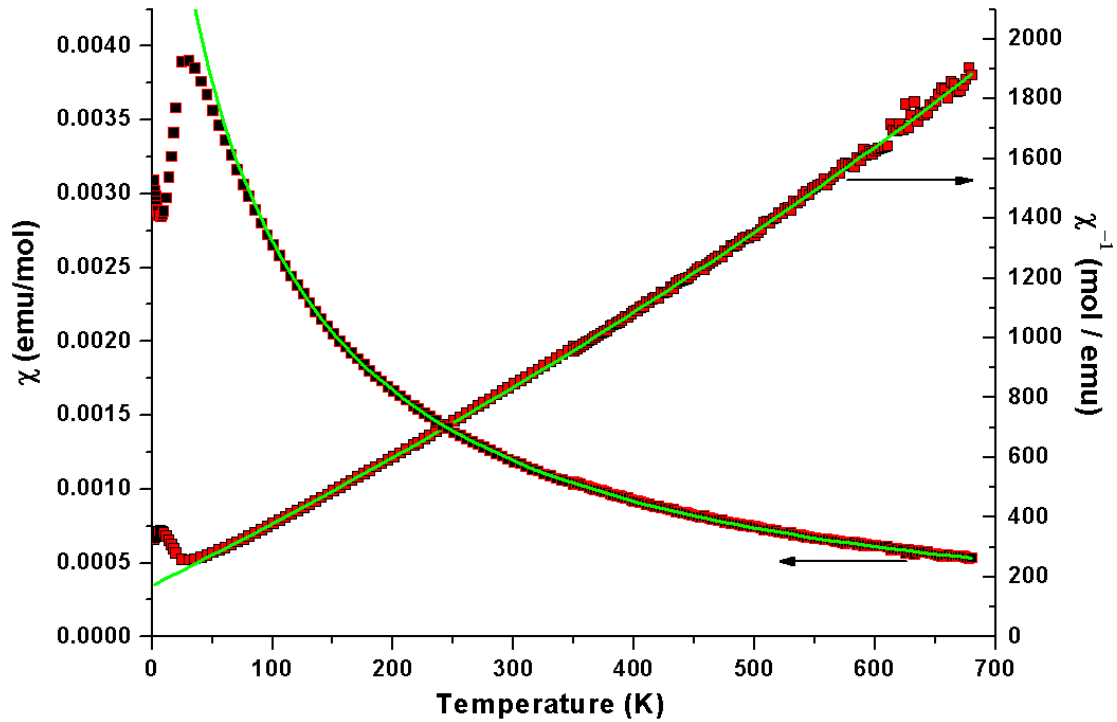


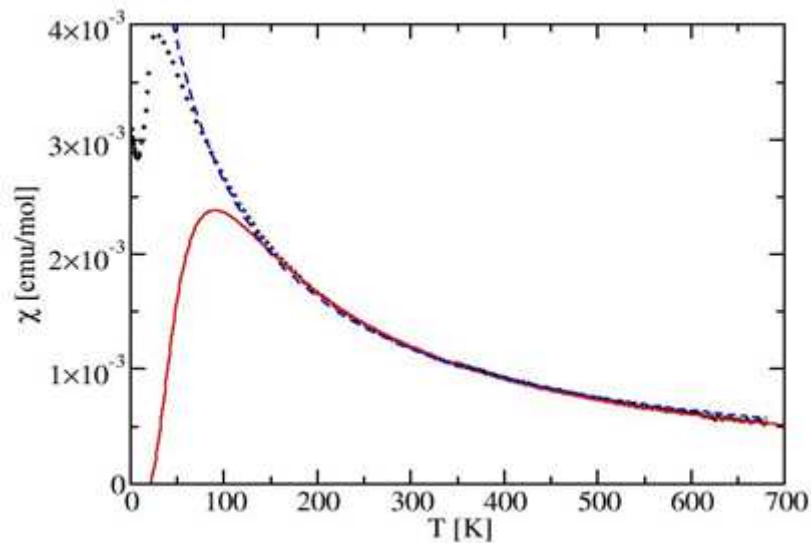
Fig. 6.5. Specific heat (C_p) at zero field as a function of T of polycrystalline sample of $\text{Na}_5\text{Cu}_3\text{O}_6$. The inset above also shows C_p/T^2 as a function of T around T_N , and the lower inset shows $d/dT(\chi_{\text{mol}} \times T)$ (Fisher's heat capacity).

The specific heat for $\text{Na}_5\text{Cu}_3\text{O}_6$ was recorded in the temperature range of 2 - 250K. In the low temperature region one can see a λ -type anomaly at 23 k in the $C_p/T(T)$ curve, as shown in Fig. 6.5, which we assign to the onset of long-range AFM ordering. The ratio of $T(\chi_{\text{max}})/T(C_{\text{max}})$ is closer to the $S = 1/2$ Heisenberg model than to the Ising value [53]. Consequently, the absolute values of C_p are uncertain and a substantial lattice contribution cannot be ruled out. To probe the nature of the specific heat anomaly at T_N in more detail, we also plotted temperature derivative of the quantity $\chi_{\text{mol}} \times T$ ("Fisher's heat capacity", cf. ref. [54]) as shown in upper inset of Fig. 6.5, and C_p/T^2 versus T (see the lower inset of Fig. 6.5) [55] both show a lucid picture with the Neel temperature precisely determined to be 22 K.

6. One-Dimensional Alkali-oxocuprates



(a)



(b)

Fig. 6.6(a). Temperature dependence of the magnetic susceptibility (χ and $1/\chi$ vs T) for polycrystalline sample of $\text{Na}_5\text{Cu}_3\text{O}_6$. The solid green line represents the fit of the data to the Curie–Weiss law in the temperature range of 135 to 680 K.

Fig. 6.6(b). Measured susceptibility (symbols) compared to a Curie law fit (dashed line) for $100 \text{ K} < T < 700 \text{ K}$ with $C = 0.42 \text{ K emu/mol}$ and $\theta = -60.2 \text{ K}$ and to an independent dimer model (solid line) with exchange constant $J_2 = 145 \text{ K}$ and $\chi_0 = -9 \times 10^{-5} \text{ emu/mol}$.

The magnetic susceptibility data is fitted by Curie Weiss law (*c.f.* Fig. 6.6(a)) in the temperature range of 135 to 680 K, giving a Curie constant of $C = 0.45 \text{ cm}^3 \text{ K mol}^{-1}$ per Cu(II) and $\theta = -62 \text{ K}$, corresponding to $S = 1/2$, $g = 2.18$, which indicates a predominant antiferromagnetic interaction between adjacent Cu^{2+} ions. μ_{eff} calculated from the Curie constant is $1.89 \mu\text{B}$ which is in good agreement with the spin only value of $1.73 \mu\text{B}$ expected for a $\text{Cu}^{2+} (d^9)$ system [41]. The susceptibility increases as temperature decreases down to $\sim 24 \text{ K}$, where it has a rounded maximum. Below this temperature it shows a steep decrease with an inflexion point at $T_N = 23 \text{ K}$ which is, within the experimental error, in good agreement with the magnetic ordering transition temperature determined from the heat capacity measurements, $T_N = 23 \text{ K}$.

6.1.4. Theoretical investigation of the magnetic properties

In contrast to the corner-sharing geometry of copper-oxygen plaquettes as realized, for example, in the high- T_c cuprates, the edge-sharing geometry leads to strongly reduced hopping amplitudes. As a consequence, long-range Coulomb interactions within the chain

$$H_{\text{Coul}} = U \sum n_j n_j + \sum V_d n_j n_{j+d} \quad (2)$$

become important. For the doping concentration $x = 1/3$ as realized in $\text{Na}_5\text{Cu}_3\text{O}_6$ this leads to a charge localization with a unit cell comprising two Cu^{2+} and one Cu^{3+} ion as depicted in Fig. 6.1. However, the charge order is not frozen and the system will still undergo virtual excitations in order to take partial advantage of the kinetic energy.

$$H_{\text{kin}} = \sum t_d (c_{i+d}^{\text{dagger}} c_i + h.c.) \quad (3)$$

6. One-Dimensional Alkali-oxocuprates

These virtual transitions with hopping amplitudes t_d lead to effective magnetic exchange interactions J_d in a Heisenberg model with long-range interactions

$$H_{HB} = \frac{1}{2} \sum J_d S_i S_{i+d} \quad (4)$$

The exchange constants contributing are determined by the charge ordering pattern. The relevant couplings for $\text{Na}_5\text{Cu}_3\text{O}_6$ are shown schematically in Fig. 6.7.

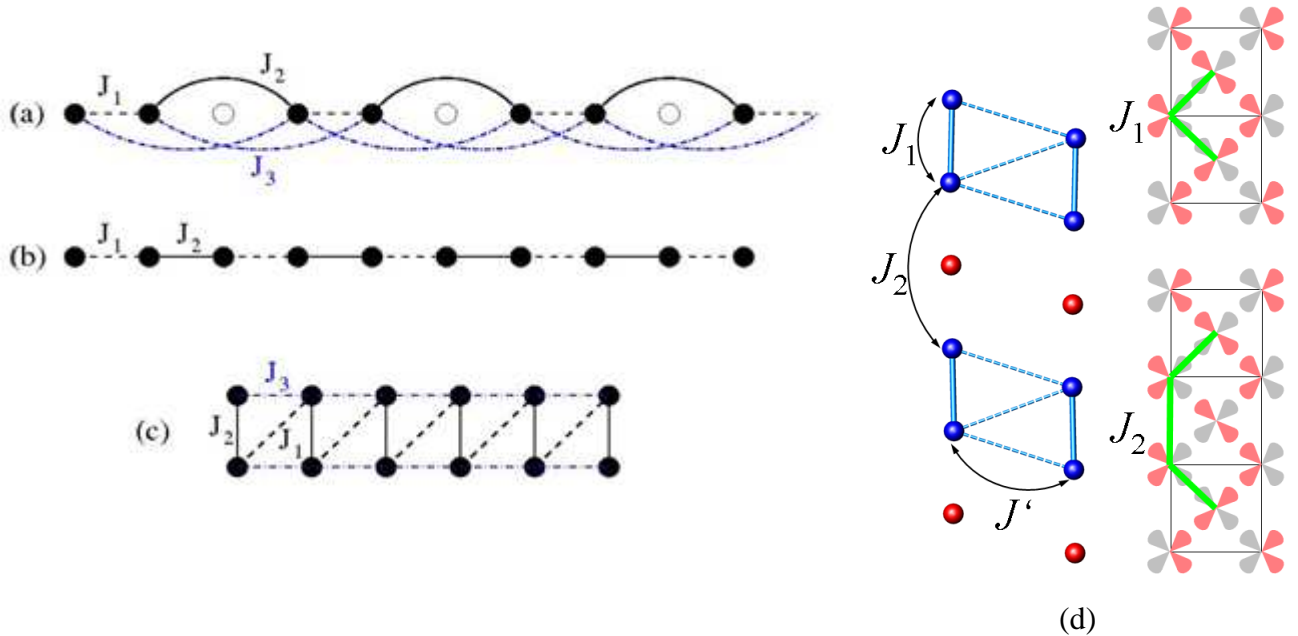


Fig 6.7. (a) Chain with Cu^{2+} (filled circles) and Cu^{3+} ions and magnetic exchange couplings J_1, J_2, J_3 . (b) Simplified magnetic structure showing only magnetic Cu^{2+} ions and couplings J_1, J_2 . In this approximation the model is an alternating ferro-antiferromagnetic Heisenberg chain. (c) Taking also J_3 into account the magnetic model is a Heisenberg ladder. (d) Nearest neighbour ferromagnetic interaction (J_1), $\sim 90^\circ$ Cu-O-Cu angle (mainly direct d-d overlap). Next nearest neighbour Cu-O-O-Cu ($J_2 \gg J_1$) dominant overlap of oxygen p-orbitals with the d-orbitals of Cu ions.

For $\text{Na}_3\text{Cu}_2\text{O}_4$ or $\text{Na}_8\text{Cu}_5\text{O}_{10}$ it was found that J_2 is antiferromagnetic and dominant [20]. Starting with the simplified magnetic structure as shown in Fig. 6.7 (b, d) therefore suggests that the system consists of weakly coupled dimers. If this is the case, we can estimate J_2 by

6. One-Dimensional Alkali-oxocuprates

fitting the measured susceptibility at high temperatures to an independent dimer model. The result of an independent dimer fit is shown in Fig. 6.6(b).

While the independent dimer model with $J_2 = 145$ K does fit the data well for high temperatures down to $T \sim 150$ K, it cannot describe the data at low temperatures due to the singlet-triplet gap of the dimer, $\Delta_D = J_2 = 145$ K. This large gap cannot be overcome by the other exchange couplings nor by the coupling between the chains J' which is expected to be of the order of the Neel temperature, $J' \sim T_N \sim 30$ K. In this regard it is also important to note that the simple magnetic model shown in Fig. 6.7(b) smoothly connects for increasing ferromagnetic coupling J_1 a dimer model (for $|J_1| \ll J_2$) with an effective antiferromagnetic $S = 1$ Heisenberg chain (for $|J_1| \gg J_2$). In the latter limit the model has a Haldane gap $\Delta_H \sim 0.4 J_2$, i.e., in both limits the model shows a large gap and therefore cannot describe the experimental data.

The Curie fit shown in Fig. 6.6(b), on the other hand, clearly demonstrates that the dominant exchange interaction is antiferromagnetic. To understand this puzzle, we have to analyze the model $H = H_{\text{Coul}} + H_{\text{kin}}$ in detail. Naively, the exchange couplings J_d are determined by charge fluctuations involving a doubly occupied site in the virtual state and consequently $J_d \sim 4t_d^2/U$. Since t_2 is expected to be the dominant hopping amplitude due to the edge-sharing geometry, this approximation leads us to the dimer model shown in Fig. 6.7(b). However, there are also kinetic exchange contributions which might dramatically alter the exchange couplings J_d and might even turn antiferromagnetic exchange constants ferromagnetic as we will demonstrate in the following.

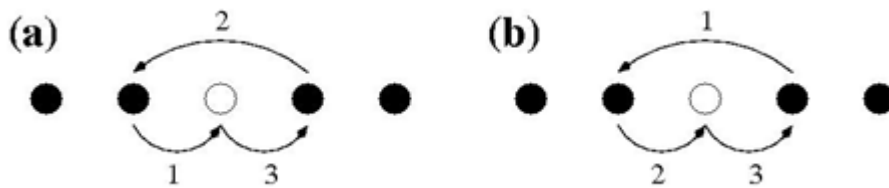


Fig. 6.8. (a) kinetic exchange term giving a contribution $\sim t_1^2 t_2 / D^2$ to J_2 . (b) mixed exchange process yielding a contribution $J_2 \sim t_1^2 t_2 / (UD)$.

In Fig. 6.8 a kinetic exchange is shown which yields a contribution $J_2^{\text{kin}} \sim 8t_1^2 t_2 / D^2$ where D is the energy cost in transferring an electron from an adjacent Cu^{2+} site onto the Cu^{3+} site.

6. One-Dimensional Alkali-oxocuprates

The relative importance of the kinetic exchange for the charge ordered cuprates therefore depends on the energy scale D for charge fluctuations. Starting from the charge ordered state, this energy scale can easily be calculated. Taking Coulomb terms up to a distance of 4 lattice sites into account we find $D_{\text{Na5}} = 2V_2 - 4V_3 + V_4$ for $\text{Na}_5\text{Cu}_3\text{O}_6$. Under the assumption that $V_d = V/d$ we can sum up the whole series of Coulomb energies and find $D_{\text{Na5}} = V (\ln 9 - 2) \approx 0.2 V$. For $\text{Na}_3\text{Cu}_2\text{O}_4$ with doping concentration $x = 1/2$, on the other hand, we find including terms up to 4th order $D_{\text{Na3}} = 2V_1 - 4V_2 + 4V_3 - 4V_4$. Again we can sum up the whole series assuming a one over distance decay of the Coulomb interaction and find $D_{\text{Na3}} = V (4\ln 2 - 2) \approx 0.8 V$. The energy scale for charge fluctuations is therefore much smaller for $\text{Na}_5\text{Cu}_3\text{O}_6$ than it is for $\text{Na}_3\text{Cu}_2\text{O}_4$. Since D enters quadratically in J_2^{kin} , this has a dramatic effect. We also want to remark that due to screening effects the Coulomb interaction may decay faster than one over distance. Nevertheless, a qualitative difference will remain: while the charge order in $\text{Na}_3\text{Cu}_2\text{O}_4$ is stabilized by V_1 , the next-nearest neighbor interaction V_2 is necessary for stability in the case of $\text{Na}_5\text{Cu}_3\text{O}_6$. Depending on the screening function, we estimate that $D_{\text{Na5}} = 0.2 - 0.6 V$ and $D_{\text{Na3}} = 0.8 - 1.3 V$.

The various exchange processes in $\text{Na}_5\text{Cu}_3\text{O}_6$ lead to

$$J_1 = 4 \frac{t_1^2}{U} + 8 \frac{t_1^2 t_2}{D^2} + 16 \frac{t_1 t_2}{UD} + 16 \frac{t_1^2 t_2^2}{D^4}; \quad (5a)$$

$$J_2 = 4 \frac{t_2^2}{U} + 4 \frac{t_1^2 t_2}{D^2} + 8 \frac{t_1^2 t_2}{UD}; \quad (5b)$$

$$J_3 = 4 \frac{t_3^2}{U} + 4 \frac{t_1 t_2 t_3}{D^2} + 8 \frac{t_1 t_2 t_3}{UD} \quad (5c)$$

For J_1 we have also included the 4th order process involving charge fluctuations at two different Cu^{3+} sites. In addition, we expect a ferromagnetic contribution to J_1 due to Hund's coupling to the oxygen sites. The role played by the kinetic exchange terms is now determined by the *sign of the hopping amplitudes* t_2, t_3 .

The optical data in [31] for LiCuVO_4 suggest that the next-nearest hopping amplitude is negative, $t_2 \sim -0.1 \text{ eV}$. The other parameters have been estimated as $U \sim 3.75 \text{ eV}$, $V \sim 1.6 \text{ eV}$, and $t_1 \sim 0.08 \text{ eV}$. Neither the sign nor the magnitude of t_3 are known. In Fig. 6.9 we show the exchange constants as given in Eq. (5) as a function of D assuming $t_3 \sim -0.05 \text{ eV}$.

6. One-Dimensional Alkali-oxocuprates

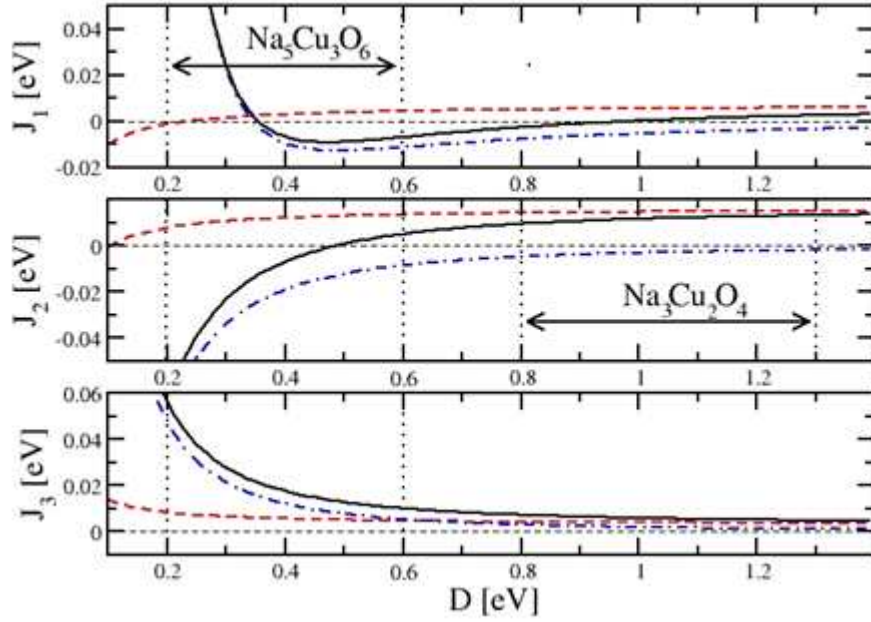
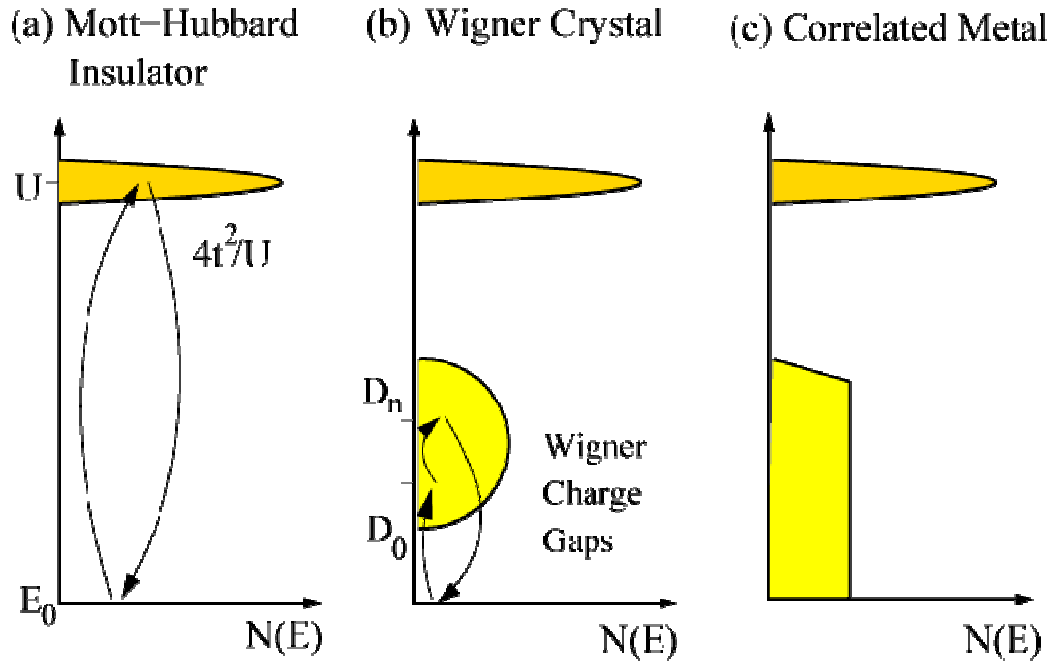


Fig. 6.9. Exchange constants, Eq. (5), as a function of the energy scale for charge fluctuations D for hopping parameters and Coulomb interaction strengths as given in the text. Shown are the total exchange constants (solid lines), the superexchange contributions involving U (dashed lines), and the kinetic exchange terms (dot-dashed lines).

The figure 6.9 clearly shows that kinetic exchange terms, while negligible for $\text{Na}_3\text{Cu}_2\text{O}_4$, play an important role for $\text{Na}_5\text{Cu}_3\text{O}_6$ leading to a much smaller or even ferromagnetic coupling J_2 . As example, we take $D = 0.45$ eV as reasonable for $\text{Na}_5\text{Cu}_3\text{O}_6$ and obtain $J_1 \sim -100$ K, $J_2 \sim 0$ K, $J_3 \sim 180$ K. This means that J_3 is the dominant antiferromagnetic interaction in sharp contrast to $\text{Na}_3\text{Cu}_2\text{O}_4$ where with $D = 0.9$ eV we obtain $J_2 \sim 130$ K. Note that in the latter case the exchange paths J_1 and J_3 do not exist due to the charge ordering pattern. A value of $J_2 \sim 130$ K for $\text{Na}_3\text{Cu}_2\text{O}_4$ is in good agreement with the previous theoretical analysis in Ref. [20].

The exchange constants we have found for $\text{Na}_5\text{Cu}_3\text{O}_6$ mean that the magnetic structure of a single chain can be understood as a two-leg ladder with antiferromagnetic couplings along the legs and ferromagnetic coupling along the rungs as shown in Fig. 6.7(c). Such a system will also show an excitation gap, however, in this case the gap is only of order $\Delta \sim 0.2 |J_1| \sim 20$ K [56] and can easily be overcome by interchain couplings.



(a) In a Mott-Hubbard insulator excitations from the ground state at E_0 to double occupied configurations in the upper Hubbard band with energy U lead to conventional antiferromagnetic superexchange interaction $\sim 4t^2/U$.
 (b) The charge excitations D_n of a Wigner crystal are in general small compared to U . Higher order processes of such charge excitations can contribute to superexchange with antiferro- or ferromagnetic interactions and thereby compete with the conventional superexchange.
 (c) When the Wigner lattice melts, e.g. at high temperature, charge gaps disappear and the system changes into a correlated metal.

In contrast to a conventional Mott-Hubbard insulator, in a Wigner crystal there are also virtual excitations across the Wigner charge gap, as displayed in **Fig. 7(b)**, that must be taken into account [23]. Careful analysis shows that these excitations also contribute to magnetism and can dramatically alter the exchange couplings J_d as we will demonstrate in the following.

To calculate the susceptibility for the Heisenberg model as depicted in **Fig. 6.7(c)**, we have used a density-matrix renormalization group algorithm applied to transfer matrices. This algorithm allows it to perform the thermodynamic limit exactly. The density-matrix renormalization group is used to extend the transfer matrices in imaginary time direction (corresponding to a successive lowering of the temperature) while keeping the number of states in a truncated Hilbert space fixed. For details the reader is referred to Refs. [57-61]. In Fig. 6.10 we show that the exchange parameters as obtained by the considerations above indeed allow for an even quantitatively satisfying fit of the experimental data.

The small deviations might be related to the non-negligible interchain as well as longer-ranged intrachain couplings.

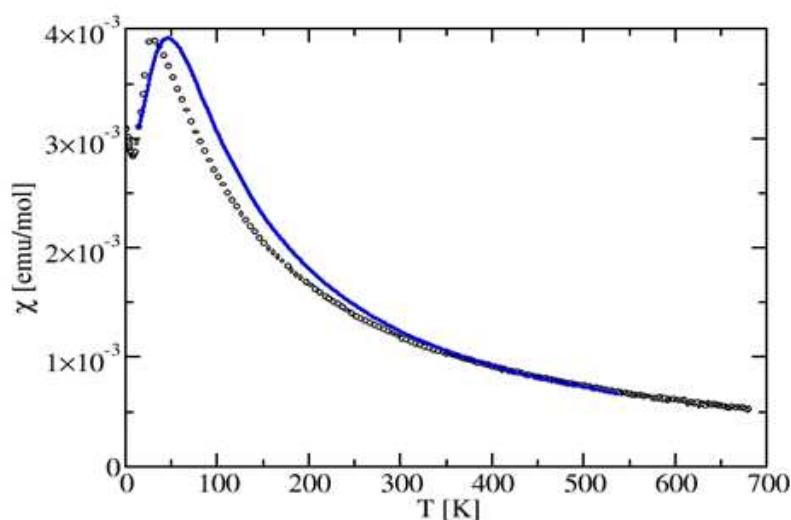


Fig. 6.10. Experimental data for the susceptibility (symbols) compared to the susceptibility for a Heisenberg model with $J_1 = -86$ K, $J_2 = 0$ K, $J_3 = 138$ K as calculated numerically using a TMRG algorithm.

6.1.5. Conclusion

In this article, the synthesis via the azide/nitrate route, structure determination from single-crystal data, as well as thermal and magnetic properties of new member of mixed-valent sodium cuprate (II,III) are presented. The structural and magnetic properties are discussed. In general, we show the experimental data of the 1D network of most demanding Heisenberg chain compounds which pose a considerable challenge to our theoretical understanding of the elementary excitations of the cuprates. The intention of this paper is to give an impression of the breadth over which pertinent information can be obtained, and thus due to space considerations some of the results are presented, but for the better understanding of the frustrated Heisenberg chain model in the current system the in depth theoretical investigation needs to be taken to unravel the hidden mysteries of various complex phenomena.

Chapter 6-B

6.2 Reinvestigation of physical properties of the Wigner crystallized chain cuprate $\text{Na}_3\text{Cu}_2\text{O}_4$

It was known from the past that the $\text{Na}_3\text{Cu}_2\text{O}_4$ undergoes long range antiferromagnetic ordering at 13K (T_N), however the author [62] also necessitates to carry out further investigation on the title compound. In much analogy we carry out again the synthesis of the title compound and studied physical properties thereof.

6.2.1 Experimental details:

6.2.1.1. Material synthesis. $\text{Na}_3\text{Cu}_2\text{O}_4$ ($\text{Na}_{1.50}\text{CuO}_2$) has been prepared along the "azide/nitrate route" [8, 9] under argon stream, as a single phase microcrystalline powder by following the methodology explained earlier [62]. The only difference in methodology was the new autoclave set up that we used for the preparation of the cuprates in present investigation. The advantage of this new autoclave set up is the special arrangement of silver tubes that don't allow the powder to flow out of the crucible after the aggressive temperature profile employed, thereby retaining the starting stoichiometry of the precursors and ends up in producing the pure powder of $\text{Na}_3\text{Cu}_2\text{O}_4$.

The obtained black powder with black needles, being very sensitive to humid air, was sealed in glass ampoules under dried argon atmosphere and all following manipulations with these substances were performed in inert atmospheres of purified argon. The single phase powder as monitored by X-ray powder analysis (Fig. 6.11) is used further for the analysis of physical properties.

6. One-Dimensional Alkali-oxocuprates

6.2.1.2. *The X-ray investigation on powder samples* was performed using a D8-Advance diffractometer (Bruker AXS, Karlsruhe, Germany) with Cu-K α_1 radiation ($\lambda = 1.54178 \text{ \AA}$) at room temperature using a position-sensitive detector and a curved germanium monochromator. The powder diffraction data (Fig. 6.11) were collected in the 2Θ range of $10\text{--}60^\circ$ sealed in 0.3 mm quartz capillary (Hilgenberg) kept rotating during data collection for better particle statistics.

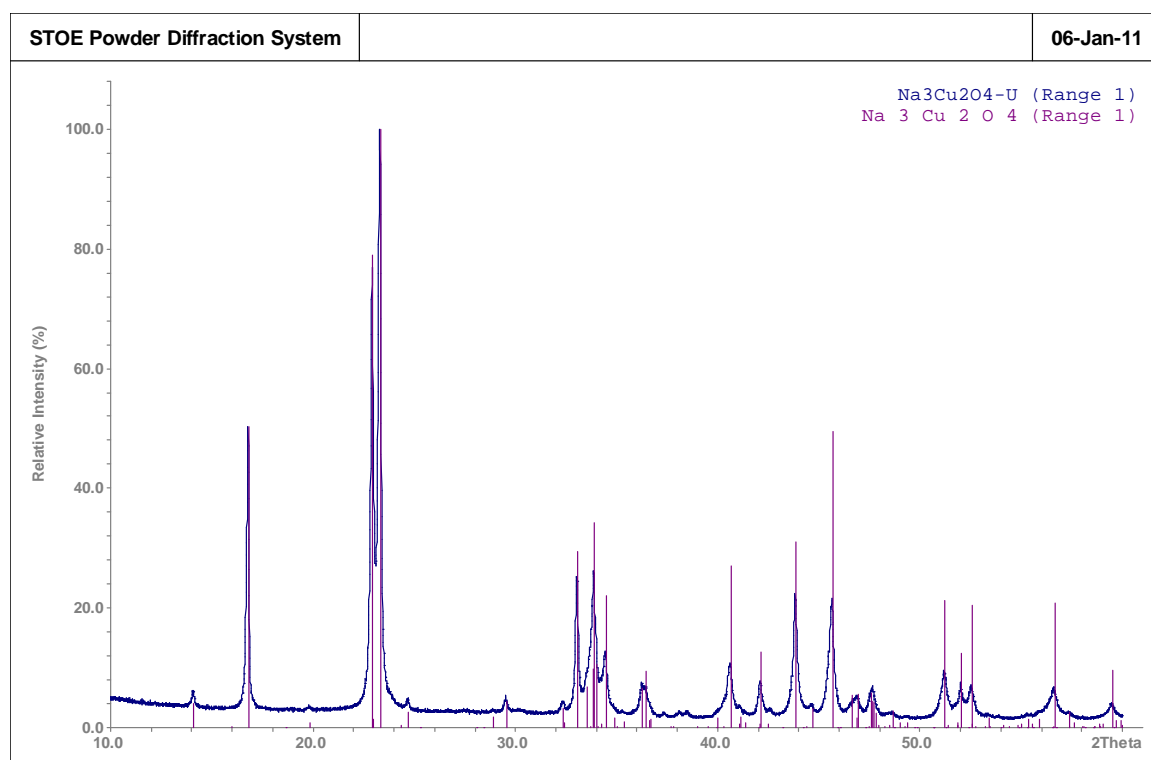


Fig. 6.11. Measured (blue) and calculated* (red lines) powder diffractogram of polycrystalline sample of Na₃Cu₂O₄.

* The peaks data (red lines) calculated using already available single crystal data using WinXPow STOE program [63].

6.2.1.3. Temperature dependence of the specific heat (C_p) of a polycrystalline sample of $\text{Na}_3\text{Cu}_2\text{O}_4$ was measured between 2 and 250 K using a commercial PPMS (Physical Property Measurement System, Quantum Design, 6325 Lusk Boulevard, San Diego, CA.) employing the same methodology explained earlier (*c.f.* section 6.1.2.5).

6.2.1.4. The magnetic susceptibility $\chi(T)$ of polycrystalline powder samples of $\text{Na}_3\text{Cu}_2\text{O}_4$ have been measured in the temperature range from 2 K to 350 K in magnetic fields up to 7 T using a SQUID-Magnetometer (MPMS 5.5, Quantum Design) Fig. 6.12(a). For measurements at various applied field the sample shows the field independent behaviour as displayed in Fig. 6.12(b). Since in addition to intrinsic spin susceptibility there is an orbital contribution to the total susceptibility, which can be further split into the diamagnetic and Van Vleck susceptibility. Consequently later the data is further corrected for core electron diamagnetic $[(-84.35 \times 10^{-6} \text{ emu/mol})]$ [39, 40] and van Vleck contributions $[(+25.5 \times 10^{-6} \times 1) \text{ (emu/mol)}]$ [64] to get the original spin susceptibility $\chi_{\text{spin}} [X_0 = (-84.35 \times 10^{-6}) + (25.5 \times 10^{-6}) = -58.85 \times 10^{-6} \text{ emu/mol}]$.

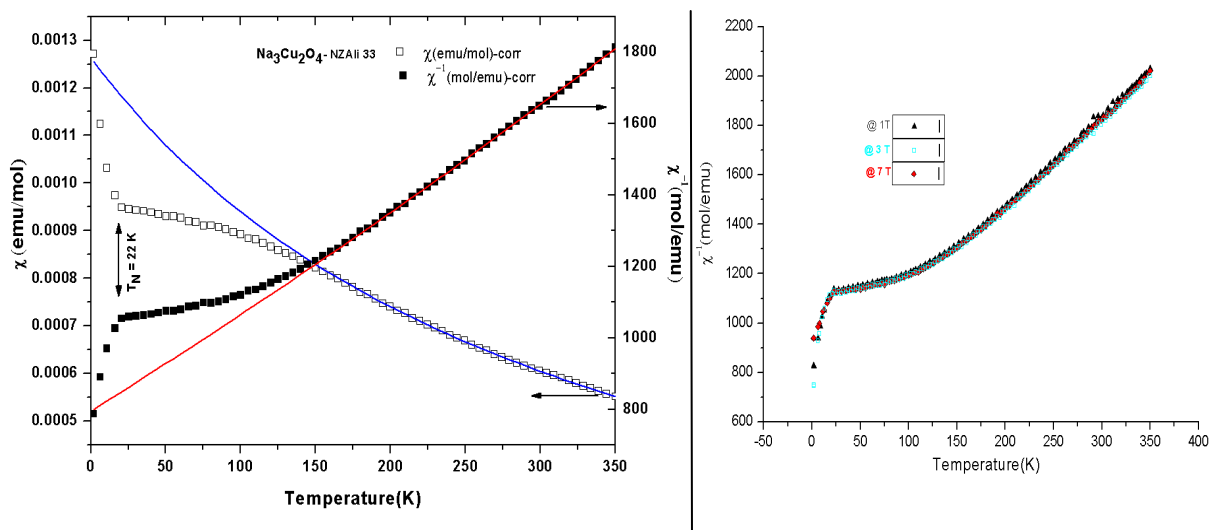


Fig. 6.12 (a) Temperature dependent Magnetic Susceptibility (χ -□open black square) and inverse magnetic susceptibility (χ^{-1} -■ filled black square) plot of $\text{Na}_3\text{Cu}_2\text{O}_4$ at 3 T with a respective Curie Weiss fit.

(b) Plot of inverse magnetic susceptibility versus temperature at 1, 3 and 7 T focusing the field (H) independency of pristine sample of $\text{Na}_3\text{Cu}_2\text{O}_4$.

6. One-Dimensional Alkali-oxocuprates

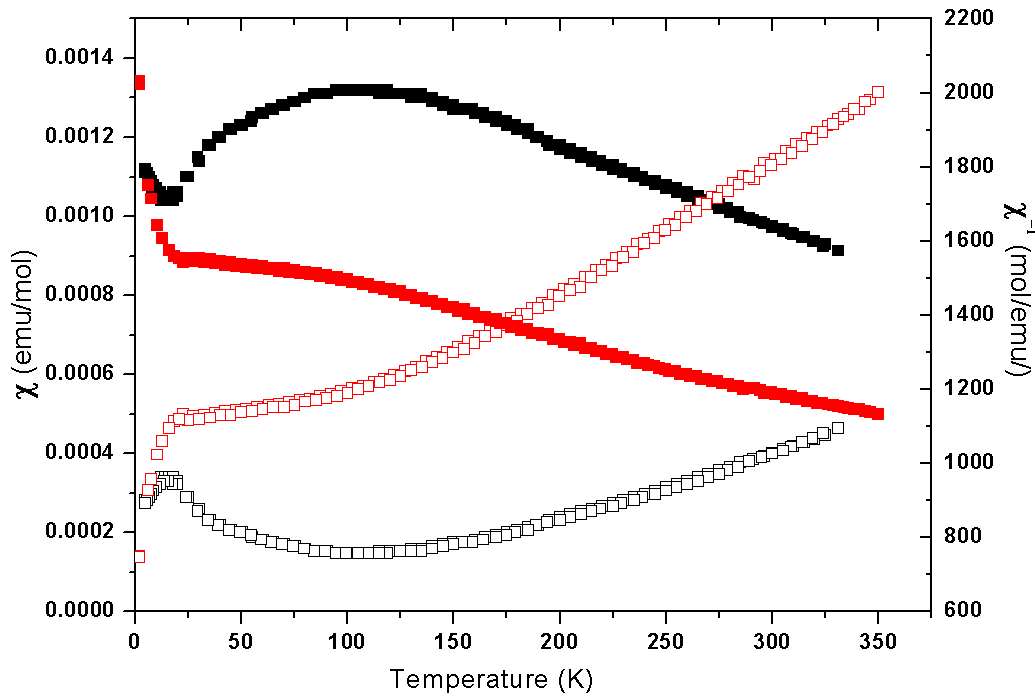


Fig. 6.13. Comparison of temperature dependent Magnetic Susceptibility (χ - \square open black square) and inverse magnetic susceptibility (χ^{-1} - \blacksquare filled black square) plot of $\text{Na}_3\text{Cu}_2\text{O}_4$ with old data ^[10] red squares.

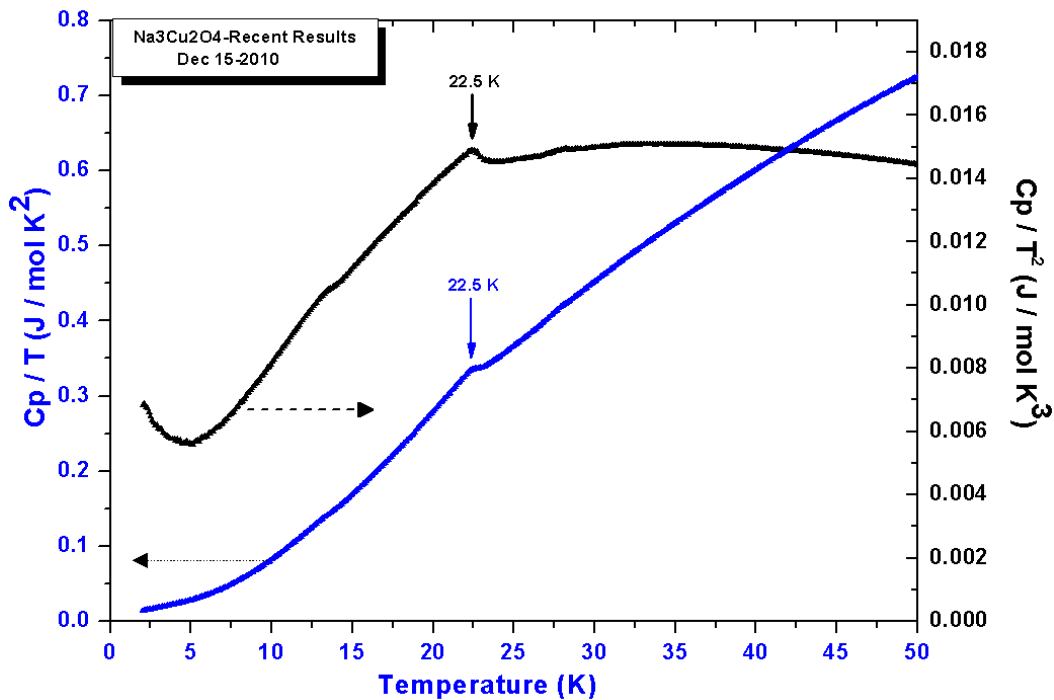


Fig. 6.14. Specific heat (C_p) at zero field as a function of T of polycrystalline sample of $\text{Na}_3\text{Cu}_2\text{O}_4$. The upper black line shows plot of C_p/T as a function of T and the blue line symbolizes a lucid plot of C_p/T^2 as a function of T around T_N (22.5K).

6.2.2 Results and discussion

The comparison between the measured (blue) and calculated (red lines- calculated using the single crystal data [10]) powder diffractogram of polycrystalline sample of $\text{Na}_3\text{Cu}_2\text{O}_4$ is displayed in Fig. (6.11), showing accurate fit of calculated peaks with measured reflections endorsing the excellent quality of the single crystal structure refinement done previously [62]. Also the atomic parameters as determined by Rietveld refinement were very close to those found for the single crystals diffraction data of $\text{Na}_3\text{Cu}_2\text{O}_4$ [c.f ref. 10].

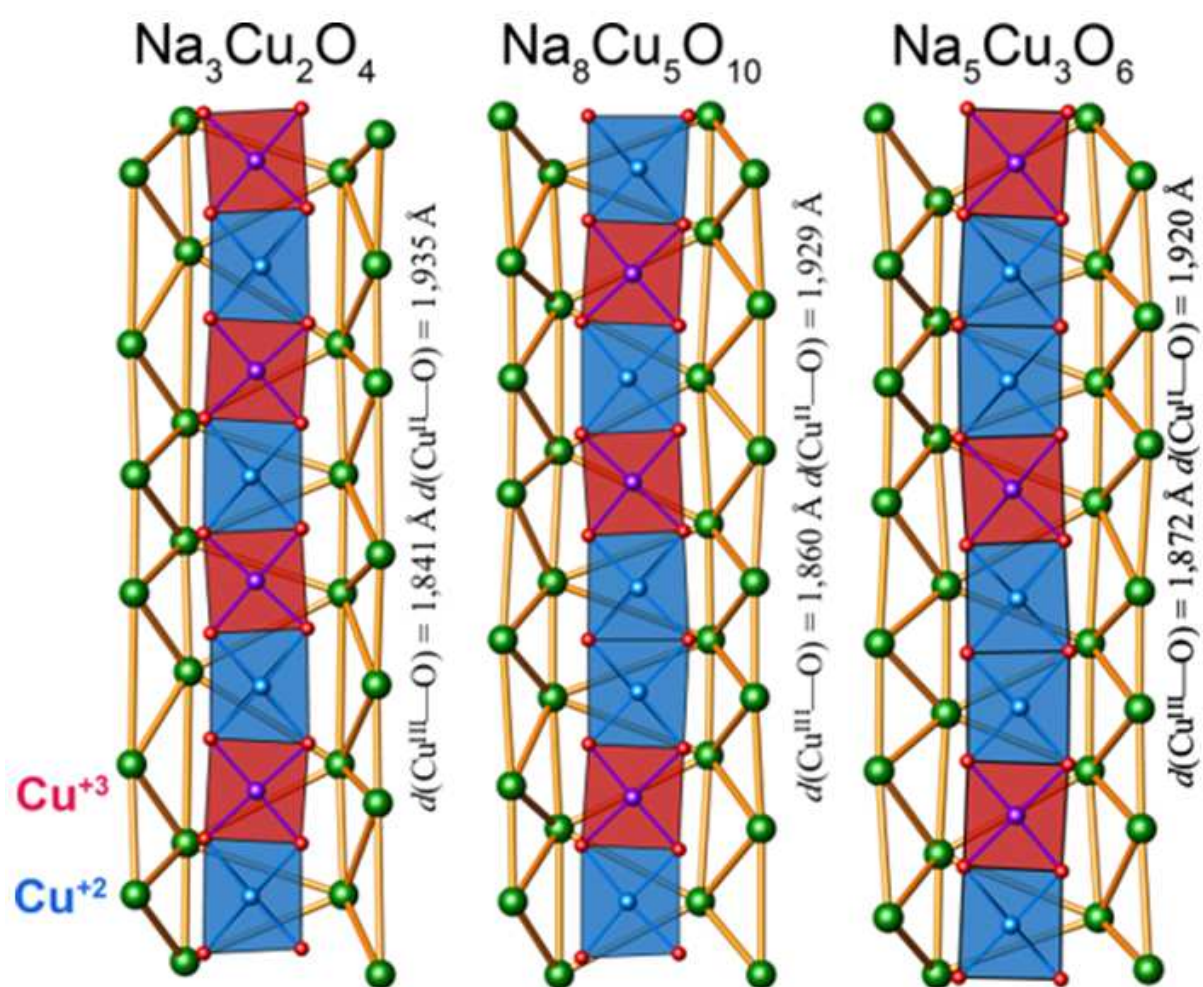


Fig. 6.15. Wigner charge order and associated Heisenberg spin structure showing periodicities of CuO_2 chains in $\text{Na}_5\text{Cu}_3\text{O}_6$ (right), $\text{Na}_8\text{Cu}_5\text{O}_{10}$ (middle) and $\text{Na}_3\text{Cu}_2\text{O}_4$ (left): Cu^{3+} (non-magnetic)—red squares, and Cu^{2+} (magnetic)—blue squares.

6. One-Dimensional Alkali-oxocuprates

The magnetic susceptibility data obtained recently is fitted by Curie Weiss law (Fig. 6.12(a)) in the temperature range of 172 to 350 K, giving a Curie constant of $C = 0.36 \text{ cm}^3 \text{ K mol}^{-1}$ per Cu(II) and $\theta = -268 \text{ K}$, $g = 1.94$ [$\mu_{\text{eff}}/\mu_B = g[S(S+1)]^{1/2}$] corresponding to $S = 1/2$ system, indicating a predominant antiferromagnetic interaction between adjacent Cu^{2+} ions. μ_{eff} calculated from the Curie constant is $1.68 \mu_B$ which is in good agreement with the spin only value of $1.73 \mu_B$ expected for a Cu^{2+} (d^9) system [41]. The susceptibility increases as temperature decreases down to $\sim 22 \text{ K}$, where it has a rounded maximum. Below this temperature it shows a steep decrease with an inflexion point at $T_N = 22 \text{ K}$ which is, within the experimental error, in good agreement with the magnetic ordering transition temperature determined from the heat capacity measurements, $T_N = 22.5 \text{ K}$. The comparison between the temperature dependent Magnetic Susceptibility (χ and χ^{-1} —black square) plot of $\text{Na}_3\text{Cu}_2\text{O}_4$ with old data [62] red squares shows the difference behaviour of plot particularly at lower temperature as is displayed in Fig. 6.13. To our perception the effect at 13 K that was considered as Neel temperature for $\text{Na}_3\text{Cu}_2\text{O}_4$ was indeed due to the impurity of NaCu_2O_2 ($T_N=13\text{K}$) or some other phenomenon which we were unable to observe, so neutron diffractometry is highly recommendable in this scenario to research the unsearched. Whereas the kink at 23K as seen clearly in the present investigation on the title compound is due to the inception of long antiferromagnetic ordering [T_N] of the title compound, in perfect analogy with the rest of member of $\text{Na}_{1+x}\text{CuO}_2$ thoroughly investigated. The specific heat for $\text{Na}_3\text{Cu}_2\text{O}_4$ was recently measured in the temperature range of $2 - 250\text{K}$. In the low temperature region one can see a λ -type anomaly at 23 k in the $C_p/T(T)$ curve, as shown by ‘blue filled squares’ in Fig. 6.14, which we assign to the onset of long-range AFM ordering. To probe the nature of the specific heat anomaly at T_N in more detail, we also plotted C_p/T^2 versus T (see the “black filled squares” in (Fig. 6.14) both show a lucid picture with the Neel temperature (T_N) precisely determined to be 22 K . In previous study [62] however, the C_p/T

6. One-Dimensional Alkali-oxocuprates

versus T plot depicted along with 13 K a weak thermal effect at 23 K, however no such effect at 23 K was observed before [62] while measuring the temperature dependent magnetic susceptibility. However as per author [62] suspicions, we reinvestigated the physical properties of the sample and conclude with confidence, keeping in view the magnetic susceptibility data endorsed with the low temperature specific heat plot as displayed in Fig. 6.14 that the Neel temperature of $\text{Na}_3\text{Cu}_2\text{O}_4$ is 22 K (T_N) in gut compliance with the rest of member of intrinsically doped sodium oxocuprates series [$\text{Na}_{1+x}\text{CuO}_2$], having unambiguous Wigner charge order and associated Heisenberg spin structure with specific periodicities of CuO_2 chains along b-axis as displayed in Fig. 6.15. However for further explanation of magnetic structures nuclear magnetic resonance (NMR) spectroscopy studies of $\text{Na}_3\text{Cu}_2\text{O}_4$ and $\text{Na}_5\text{Cu}_3\text{O}_6$ are underway.

The numerical calculation using a TMRG algorithm of experimental susceptibility data to the susceptibility for a Heisenberg model as explained in detail in section 6.1.4. for the case of $\text{Na}_5\text{Cu}_3\text{O}_6$, whereby it was shown that the charge order in this family of sodium oxocuprates is not frozen and the system undergoes virtual excitations in order to take partial advantage of the kinetic energy. These virtual transitions with hopping amplitudes t_d lead to effective magnetic exchange interactions J_d in a Heisenberg model with long-range interactions (Fig. 6.8). These kinetic exchange contributions (figure 6.9) while negligible for $\text{Na}_3\text{Cu}_2\text{O}_4$ compared to $\text{Na}_5\text{Cu}_3\text{O}_6$, however cannot be ignored and demands further theoretical analysis of the recently obtained magnetic susceptibility data with the new theoretical model (*c.f* section. 6.1.4).

Chapter 6-C

6.3. Crystal Structure and Raman Spectroscopic Study of $K_5[CuO_2][CO_3]$

6.3.1. Introduction:

The discovery of superconductivity in copper oxycarbonates by 'late' Schnering et al. [65], gears up a plethora of new compounds of this family in the last two decades [66-70]. The stimulus behind this is the higher critical temperature of these new high- T_c ~ superconductors than its non carbonated counterpart cuprates [71]. In most of these high T_c compounds, it was found out that the alkali and alkaline earth metal cations included in the parent cuprates display strong chemical affinity for small carbonate groups CO_3^{-2} which under certain conditions partially substitute the $[CuO_2]$ in the parent structures [72]. Nearly all the compounds with monovalent atoms crystallize in a unique tetragonal crystal structure with an alternate stacking of $[(Cu, M) O_2]$ layers, in which M / Cu ions are ordered forming an isolated $[MO_2]^{3-}$ dumb-bell unit, whereas the carbonate ion, CO_3^{-2} , exist as a nearly regular triangle of oxygen atoms centered around the carbon in disordered fashion [73-74]. Unfortunately, due to the fact that most of the copper oxycarbonates are reported to be unstable above their formation temperature, where they start to release carbon evolving CO_2 gas, it seems almost impossible to grow good-quality single crystals, at least under standard pressure conditions because of dynamical behaviour of CO_3 molecule alongwith an order-disorder type structural phase transition like in the case of $[Sr_2CuO_2(CO_3)]$ [75]. Most of the

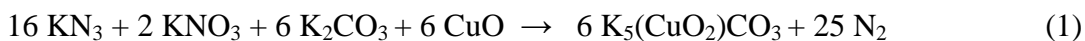
6. One-Dimensional Alkali-oxocuprates

studies were conducted by structure refinement using powder diffraction techniques [76-77]. However a few studies are reported where authors reported on the growth of copper oxycarbonate crystals at slightly high pressure [78], but unfortunately not enough single crystal structural data on these types of interesting crystals have been reported. In retrospect, including carbonate anions in perovskite related multinary oxides has proven a versatile measure to modify the stacking modes encountered [79]. This option has been widely exercised during attempts to improve the performance of cuprate based superconductors [71, 80-82]. The first member of these isolated linear $[\text{MO}_2]^{3-}$ complexes with $\text{M} = [\text{Fe}, \text{Co}, \text{Ni} \text{ and } \text{Cu}]$ was reported in 1985 by Hoppe *et. al.* [83-85]. However, also in the field of multinary alkali metal oxides mixed anionic sodium nickelate carbonate [86] and cobaltate carbonate [87] have been studied. Here we report on a new potassium cuprate carbonate, prepared along the azide nitrate route [8, 9].

6.3.2. Experimental Section

6.3.2.1 Synthesis

$\text{K}_5[\text{CuO}_2][\text{CO}_3]$ was prepared via the azide nitrate route [8, 9]. Mixtures of the starting precursors (CuO , KN_3 , KNO_3 and K_2CO_3), according to equation 1, were heated in a special regime.



The starting materials were ground thoroughly in an agate mortar, pressed into pellets ($\varnothing = 6$ mm) under 10^5 N, dried in vacuum (10^{-3} mbar) at 400 K overnight and later placed under argon into a closed steel vessel, provided with a silver inlay [9]. In a flow of dry argon the following temperature profile was applied: $298 \rightarrow 533$ K (100 K h^{-1}); $533 \rightarrow 653$ K (5 K h^{-1});

6. One-Dimensional Alkali-oxocuprates

653 \rightarrow 833 K (20 K h⁻¹) with subsequent annealing for 50 h. The powder obtained is very sensitive to humid air and must be handled in an inert atmosphere. Single crystals have been grown by subsequent annealing of the powder at 823 K for 500 hours in a tightly closed silver crucible, further sealed in a quartz ampoule under dry Argon. The phase purity of the precursors was monitored by X-ray powder analysis.

Hazard: The sample container may blow up if heated too rapidly!!

6.3.2.2 X-ray Analysis

For single-crystal X-ray diffraction experiments, a dark yellow single crystal was selected in a dry-box (MB 150B–G–II, M. Braun GmbH, München, Germany) and mounted in a sealed glass capillary. The diffraction data were collected at 298(2) K on a SMART-APEX-I CCD X-ray diffractometer (Bruker AXS, Karlsruhe, Germany) with graphite-monochromated MoK α radiation. The reflection intensities were integrated with the SAINT subprogram in the Bruker Suite software package [32], a multi-scan absorption correction was applied using SADABS [33]. The structures were solved by direct methods and refined by full-matrix least squares fitting with the SHELXTL software package [34]. Experimental details are given in Table 6.6, Atomic coordinates, site occupancies and displacement parameters are presented in Tables 6.7 and 6.8. Further details may be obtained from Fachinformationszentrum Karlsruhe [88].

6. One-Dimensional Alkali-oxocuprates

Table 6.6. Crystal data, data collection, and refinement details for $K_5[CuO_2][CO_3]$.

$K_5[CuO_2][CO_3]$	
Formula weight	351.05
Temperature /K	298(2)
Space group (no.), Z	$P4/nbm$ (125), 2
Lattice constants / \AA	$a = 7.4067(5)$ $c = 8.8764(8)$
$V / \text{\AA}^3$,	486.95(6)
$\rho_{\text{xray}} / \text{g cm}^{-3}$	2.394
Crystal size	$0.15 \times 0.10 \times 0.08$
Diffractometer	SMART APEX I, Bruker AXS
X-ray radiation, $\lambda / \text{\AA}$	0.71073
Absorption correction	multi-scan, SADABS [18]
2θ range / $^\circ$	$4.58 \leq 2\theta \leq 61.98$
Index range	$-10 \leq h \leq 10$, $-10 \leq k \leq 10$, $-12 \leq l \leq 12$
Reflection collected	5743
Data, R_{int}	433, 0.030
No. of parameters	29
Transmission: $t_{\text{max}}, t_{\text{min}}$	0.722, 0.561
$R_1[F^2 > 2\sigma(F^2)]$	0.053
$wR(F^2)$	0.145
Extinction coefficient	0.007(3)
Deposition no. [20]	CSD-422228

6. One-Dimensional Alkali-oxocuprates

Table 6.7. Atomic coordinates and equivalent isotropic displacement parameters $U_{\text{eq}} / \text{\AA}^2$ for $\text{K}_5[\text{CuO}_2][\text{CO}_3]$.

Atom	Site	x	y	z	U_{eq}	Occ.
Cu	$2a$	$\frac{1}{4}$	$\frac{1}{4}$	0	0.0252(4)	1
K1	$8m$	0.0286(3)	$-x$	0.2401(2)	0.0646(7)	1
K2	$2b$	$\frac{1}{4}$	$\frac{1}{4}$	$\frac{1}{2}$	0.0409(7)	1
O1	$4g$	$\frac{1}{4}$	$\frac{1}{4}$	0.2013(6)	0.028(1)	1
C	$2d$	$\frac{3}{4}$	$\frac{1}{4}$	$\frac{1}{2}$	0.038(3)	1
O2	$4h$	$\frac{3}{4}$	$\frac{1}{4}$	0.663(2)	0.093(7)	0.5
O3	$8m$	0.139(1)	$-x$	0.543(1)	0.059(3)	0.5

Table 6.8. Anisotropic displacement parameters $U_{ij} / \text{\AA}^2$ for $\text{K}_5[\text{CuO}_2][\text{CO}_3]$.

Atom	$U_{11} = U_{22}$	U_{33}	U_{12}	$U_{13} = -U_{23}$
Cu	0.0279(5)	0.0199(6)	0	0
K1	0.072(1)	0.0494(9)	-0.047(1)	0.0054(7)
K2	0.051(1)	0.0207(9)	0	0
O1	0.031(1)	0.021(2)	0	0
C	0.036(3)	0.043(6)	0	0
O2	0.11(1)	0.06(1)	0.04(1)	0
O3	0.062(4)	0.053(6)	0.010(6)	0.012(4)

6.3.2.3 Raman Spectroscopy and Chemical Analysis

Raman spectra of a single crystal were collected on Laser Raman spectrometer (LabRAM system, Horiba Jobin-Yvon) with a laser excitation source at 784 nm (20 mW diode laser) coupled with the optical filters and a multichannel CCD detector. The spectra were taken in the range of 400–1200 cm^{-1} with the single crystal zipped in the glass capillary, at room temperature (298K).

6. One-Dimensional Alkali-oxocuprates

The atom ratio of the heavy elements was confirmed with a scanning electron microscope (XL 30 TMP, Philips, Holland, tungsten electrode, 25 kV), equipped with an integrated EDAX–EDX system (S–UTW–Si(Li)–detector).

6.3.3. Results and Discussion

Dark yellow single crystals of $K_5[CuO_2][CO_3]$, which are sensitive to air and moisture, have been prepared by the azide nitrate route. The crystal data are given in **Table 6.6**, atomic coordinates and displacement parameters in **Tables 6.7** and **6.8**. The atom ratio of potassium and copper was additionally confirmed by EDX analysis, and found to be $K/Cu = 5/1$.

$K_5[CuO_2][CO_3]$ crystallizes tetragonal in the space group $P4/nbm$ (no. 125) with $a = 7.4067(5)$ and $c = 8.8764(8)$ Å. The specific feature of the crystal structure are linear $[Cu(I)O_2]^{3-}$ dumbbells (Cu—O bond length = $1.787(5)$ Å, O—Cu—O angle = 180°) and carbonate CO_3^{2-} anions. The latter are not connected to the transition element. The K1 atoms form a distorted, oblique-angled, cubic primitive grid with $1/4$ of the cubes filled with $[CuO_2]^{3-}$ dumbbells, $1/4$ with CO_3^{2-} , $1/4$ with K^{2+} , and $1/4$ is left empty (**Figure 6.16 (a)**). The structure represents an ordered variant of the $Na_5[NiO_2][CO_3]$ type of structure [**86**]. In the latter structure type (space group $P4/mmm$), which has also been found for $Na_5[CuO_2][CO_3]$ [**89**] and $Na_5[CoO_2][CO_3]$ [**87**], the oxygen atoms of the carbonate anion are completely disordered, and the sodium atoms are arranged in the shape of regular square prisms. In contrast, in the title compound, the carbonate group is found to be disordered in two distinguished orientations on the same crystallographic site, with the site symmetry $\bar{4}2m$, see **Figure 6.16 (b)** and **Table 6.7**.

6. One-Dimensional Alkali-oxocuprates

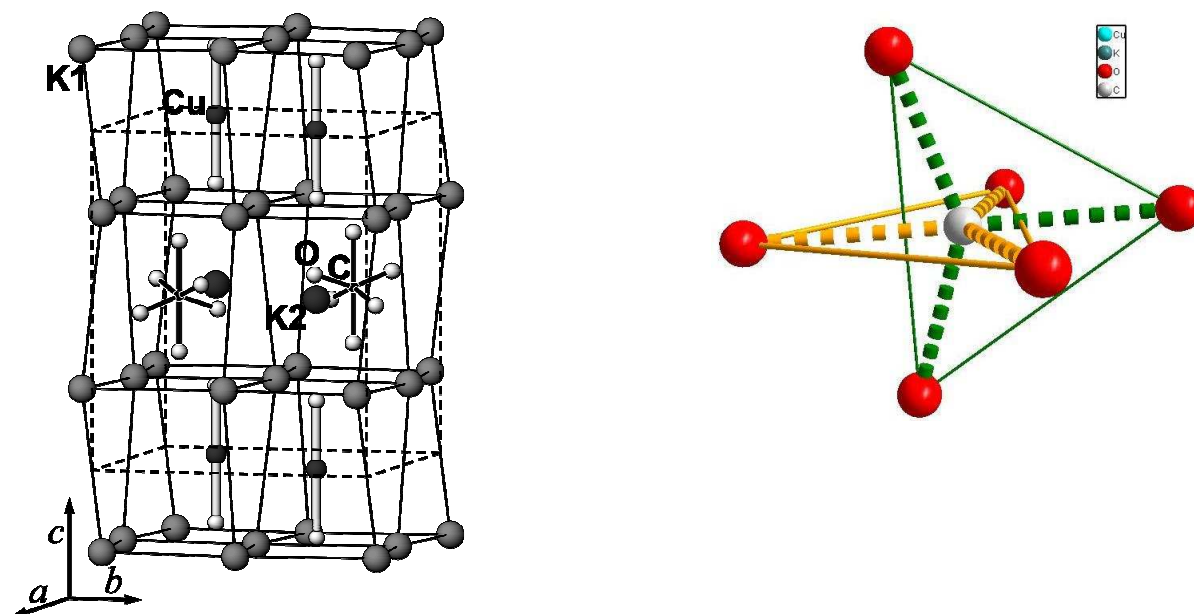


Fig. 6.16. a) Perspective representation of the crystal structure of $K_5[CuO_2][CO_3]$. The margins of the unit cell are shown in dotted lines. b) The disordered carbonate group found to be in two distinguished orientations on the same crystallographic site.

Due to the halved scattering power of the oxygen split positions, we regarded an independent confirmation of the presence of the carbonate anion desirable. The single crystal Raman spectrum (Figure 6.17) clearly exhibits the characteristic Raman signature of trigonal planar CO_3^{2-} anions at 1049 cm^{-1} that can be assigned to the totally symmetric mode $\nu_1 (A_1)$ [90-92]. Whilst the second prominent line at 604 cm^{-1} can reliably be assigned to the A_{1g} phonons of Cu and O1 respectively [93-95].

6. One-Dimensional Alkali-oxocuprates

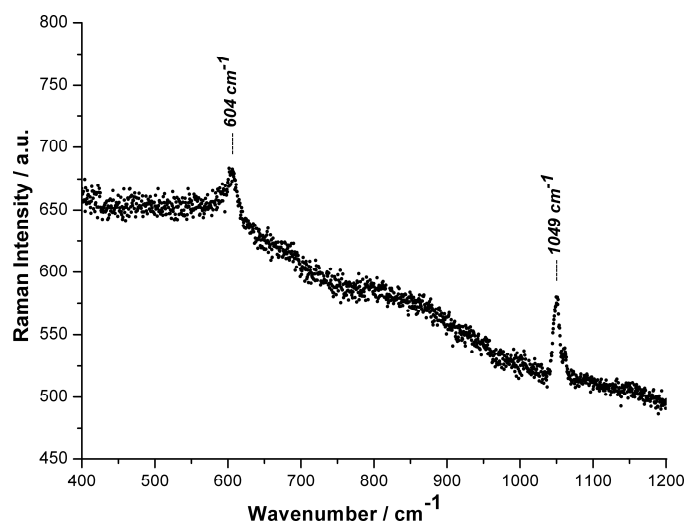


Fig. 6.17. Single crystal Raman spectrum of $K_5[CuO_2][CO_3]$.

6.4 References

- [1]: T. Mayer, M. Eremin, I. Eremin, and P. F. Meier, *J. Phys.: Condens. Matter* **19**, 116209, (2007).
- [2]: C. N. R. Rao, R. Mahesh, A. K. Raychaudhuri, and R. Mahendiran, *J. Phys. Chem. Solids* **59**(4), 487, (1998).
- [3]: C. Felser, G. H. Fecher, and B. Balke, *Angew. Chem. Int. Edn.* **46**, 668, (2007).
- [4]: H. Takagi, *Nature Materials* **6**, 179, (2007).
- [5]: V.V. Moshchalkov, L. Trappeniens, and J. Vanacken, *Physica C: Superconductivity* **887**, 341-348, (Part 2), (2000).
- [6]: J. M. Tranquada, B. J. Stemlieb, J. D. Axe, Y. Nakamura, and S. Uchida, *Nature (London)* **375**, 561 (1995).
- [7]: N. Kumar, and C. N. R. Rao, *ChemPhysChem.* **4**(5), 439, (2003).
- [8]: D. Trinschek, and M. Jansen, *Angew. Chem. Int. Edn.* **38**,133, (1999).
- [9]: M. Sofin, E.-M Peters, and M. Jansen, *Z. Anorg. Allg. Chem.* **628**, 2697, (2002).
- [10]: M. Sofin, E.-M. Peters, and M. Jansen, *J. Solid State Chem.* **178** (12), 3708, (2005).
- [11]: L. Capogna, M. Mayr, P. Horsch, M. Raichle, R. K. Kremer, M. Sofin, A. Maljuk, M. Jansen, and B. Keimer, *Phys. Rev. B* **71**, 140402(R) (2005).
- [12]: M. Mayr, and P. Horsch, *Phys. Rev. B* **73**, 195103, (2006).
- [13]: M. Raichle, M. Reehuis, G. Andre, L. Capogna, M. Sofin, M. Jansen, and B. Keimer, *Phys. Rev. Lett.* **101**, 047202 (2008).
- [14]: L. Capogna, M. Reehuis, A. Maljuk, R. K. Kremer, B. Ouladdiaf, M. Jansen, and B. Keimer, *Phys. Rev. B* **82**, 014407 (2010).
- [15]: C. Kim, A. Y. Matsuura, Z. Shen, N. Motoyama, H. Eisaki, S. Uchida, T. Tohyama, and S. Maekawa, *Phys. Rev. Lett.* **77**(19) 4054, (1996).
- [16]: M. Coey, *Nature* **430**, 155, (2004).

6. One-Dimensional Alkali-oxocuprates

- [17]: S. A. Kivelson, I. P. Bindloss, E. Fradkin, V. Oanesyan, J. M. Tranquada, A. Kapitulnik, and C. Howald, *Rev. Mod. Physics* **75**, 1201, (2003).
- [18]: F. C. Zhang, and T. M. Rice, *Phys. Rev. B* **37**, R3759, (1988).
- [19]: E. Wigner, *Phys. Rev.* **46**, 1002, (1934).
- [20]: P. Horsch, M. Sofin, M. Mayr, and M. Jansen, *Phys. Rev. Lett.* **94**, 076403, (2005).
- [21]: T. Masuda, A. Zheludev, A. Bush, M. Markina, and A. Vasiliev, *Phys. Rev. Lett.* **92**, 177201 (2004).
- [22]: S. Park, Y. J. Choi, C. L. Zhang, and S.-W. Cheong, *Phys. Rev. Lett.* **98**, 057601 (2007).
- [23]: S. Seki, Y. Yamasaki, M. Soda, M. Matsuura, K. Hirota, and Y. Tokura, *Phys. Rev. Lett.* **100**, 127201 (2008).
- [24]: F. Schrettle, S. Krohns, P. Lunkenheimer, J. Hemberger, N. Büttgen, H.-A. Krug von Nidda, A. V. Prokofiev, and A. Loidl, *Phys. Rev. B* **77**, 144101 (2008).
- [25]: T. Vekua, A. Honecker, H.-J. Mikeska, and F. Heidrich-Meisner, *Phys. Rev. B* **76**, 174420 (2007).
- [26]: J. Sudan, A. Lüscher, and A. M. Läuchli, *Phys. Rev. B* **80**, 140402 (R) (2009).
- [27]: F. Heidrich-Meisner, I. P. McCulloch, and A. K. Kolezhuk, *Phys. Rev. B* **80**, 144417 (2009).
- [28]: J. Sirker, *Phys. Rev. B* **81**, 014419 (2010).
- [29]: M. Enderle, B. Fåk, H.-J. Mikeska, R. K. Kremer, A. Prokofiev, and W. Assmus, *Phys. Rev. Lett.* **104**, 237207 (2010).
- [30]: S.-L. Drechsler, S. Nishimoto, R. Kuzian, J. Malek, W. E. A. Lorenz, J. Richter, J. van den Brink, M. Schmitt, and H. Rosner, arXiv:1006.5070
- [31]: Y. Matiks, P. Horsch, R. K. Kremer, B. Keimer, and A. V. Boris, *Phys. Rev. Lett.* **103**, 187401 (2009).
- [32]: Bruker Suite, Version 2008/3, Bruker AXS Inc., Madison, USA, (2008).
- [33]: G. M. Sheldrick, SADABS, Bruker AXS area detector scaling and absorption, Version 2008/1, University of Göttingen, Germany, (2008).
- [34]: G. M. Sheldrick, *Acta Crystallogr. A* **64**, 112, (2008).

6. One-Dimensional Alkali-oxocuprates

- [35]: R. Bachmann, F. J. DiSalvo Jr., T. H. Geballe, R. L. Greene, R. E. Howard, C. N. King, H. C. Kirsch, K. N. Lee, R. E. Schwall, H. U. Thomas, and R. B. Zubeck, *Rev. Sci. Instrum.* **43**, 205 (1972).
- [36]: J. S. Hwang, K. J. Lin, and C. Tien, *Rev. Sci. Instrum.* **68**, 94, (1997).
- [37]: K. Honda, *Ann. Phys.* **32**, 1027, (1910).
- [38]: M. Owen, *Ann. Phys.* **37**, 657, (1910).
- [39]: Landolt-Börnstein, *Zahlenwerte und Funktionen aus Naturwissenschaften und Technik; Neue Serie, Gr. II, Bd. 2*, Springer, Berlin, (1966).
- [40]: P. W. Selwood, *Magnetochemistry*, 2nd ed. Interscience, New York, p. 78, (1956).
- [41] H. Lueken, *Magnetochemie*, Teubner, Leipzig, (1999).
- [42] N. E. Brese, M. O' Keefe, R. B. von Dreele, and V. G. Young, *J. Solid State Chem.* **83**, 1, (1989).
- [43] G. A. Costa, and E. Kaiser, *Thermochimica Acta* **269**, 591, (1995).
- [44] K. Hestermann, and R. Hoppe, *Z. Anorg. Allg. Chem.* **367**, 249, (1969).
- [45] J. Pickardt, W. Paulus, M. Schmalz, and R. Schollhorn, *J. Solid State Chem.* **89**, 308, (1990).
- [46] R. Hoppe, *Z. Kristallogr.* **150**, 23, (1979).
- [47] S. van Smaalen, R. E. Dinnebier, M. Sofin, and M. Jansen, *Acta Crystallogr.* **B63**, 17, (2007).
- [48] S. van Smaalen, *Z. Kristallogr.* **219**, 681, (2004).
- [49] J. Nuss, S. Pfeiffer, S. van Smaalen, and M. Jansen, *Acta Crystallogr.* **B66**, 27, (2010).
- [50] R. Hoppe, H. Hestermann, and F. Schenck, *Z. Anorg. Allg. Chem.* **367**, 275, (1969).
- [51] G. Tams, and Hk. Müller-Buschbaum, *J. Alloy. Compd.* **189**, 241, (1992).
- [52] A. Kirfel, and K.D.Eichhorn, *Acta Crystallogr.* **A46**, 271, (1990).
- [53] L. J. de Jongh and A. R. Miedema, *Advances in Physics* **50**(8), 947, (2001).
- [54] M. E. Fisher, *Philos. Mag.* **7**, 1731 (1962).
- [55] A. Möller, U. Löw, T. Taetz, M. Kriener, G. André, F. Damay, O. Heyer, M. Braden, and J. A. Mydosh, *Phys. Rev. B* **78**, 024420 (2008).

6. One-Dimensional Alkali-oxocuprates

- [56] S. Larochelle, and M. Greven, *Phys. Rev. B.* **69**, 092408 (2004).
- [57] R. Bursill, T. Xiang, and G. Gehring, *J. Phys. Condens. Matter* **8**, L583 (1996).
- [58] X. Wang, and T. Xiang, *Phys. Rev. B* **56**, 5061 (1997).
- [59] N. Shibata, *J. Phys. Soc. Jpn.* **66**, 2221 (1997).
- [60] J. Sirker and A. Klümper, *Phys. Rev. B* **66**, 245102 (2002).
- [61] J. Sirker and A. Klümper, *Europhys. Lett.* **60**, 262 (2002).
- [62] M. Sofin, Ph. D. thesis, page.27, Department of Chemistry, Universitaet Stuttgart (2003).
- [63] Program WINXPOW 1.10, Stoe & Cie GmbH, Darmstadt (1999).
- [64] Sebastian Eggert, *Phys. Rev. B* **53**, 5116-5118 (1996).
- [65] H.G. von Schnering, M. Hartweg, L. Walz, T. Popp, T. Becker, and M. Schwarz,
Jahresbericht des MPI fuer Festkoerperforschung Stuttgart 94 (1988).
- [66] J. Akimitsu, H. Nakata and M. Uehara, *Journal of Superconductivity*, **7**,19-22 (1994).
- [67] Y. Miyazaki, H. Yamane, N. Kobayashi, T. Hirai, H. Nakata, K. Tomimoto and J. Akimitsu. *Physica C* **202**, 162 (1992).
- [68] M. Huvé, C. Michel, A. Maignan, M. Hervieu, C. Martin and B. Raveau. *Physica C* 205, 219 (1993).
- [69] D. Pelloquin, M. Caldes, A. Maignan, C. Michel, M. Hervieu and B. Raveau. *Physica C* 208, 121 (1993).
- [70] A. Maignan, M. Huvé, C. Michel, M. Hervieu, C. Martin and B. Raveau. *Physica C*, **208**, 149 (1993).
- [71] K. Kinoshita, T. Yamada, *Nature*, **357**, 313-315 (1992).
- [72] A. Baszczuk, A. Zygmunt and M. Wolczyk, *Journal of Alloys and Compounds*, **346**, 68-79 (2002).
- [73] G. Calestani, F.C. Maticotta, A. Migliori, P. Nozar, L. Righi, K.A. Thomas, *Physica C*, **261**, 38-55 (1996).
- [74] B. Raveau, C. Michel, B. Michel, B. Mercey, J.F. Hamet and M. Hervieu *J. Alloys Comp.* **229**, 134 (1995).

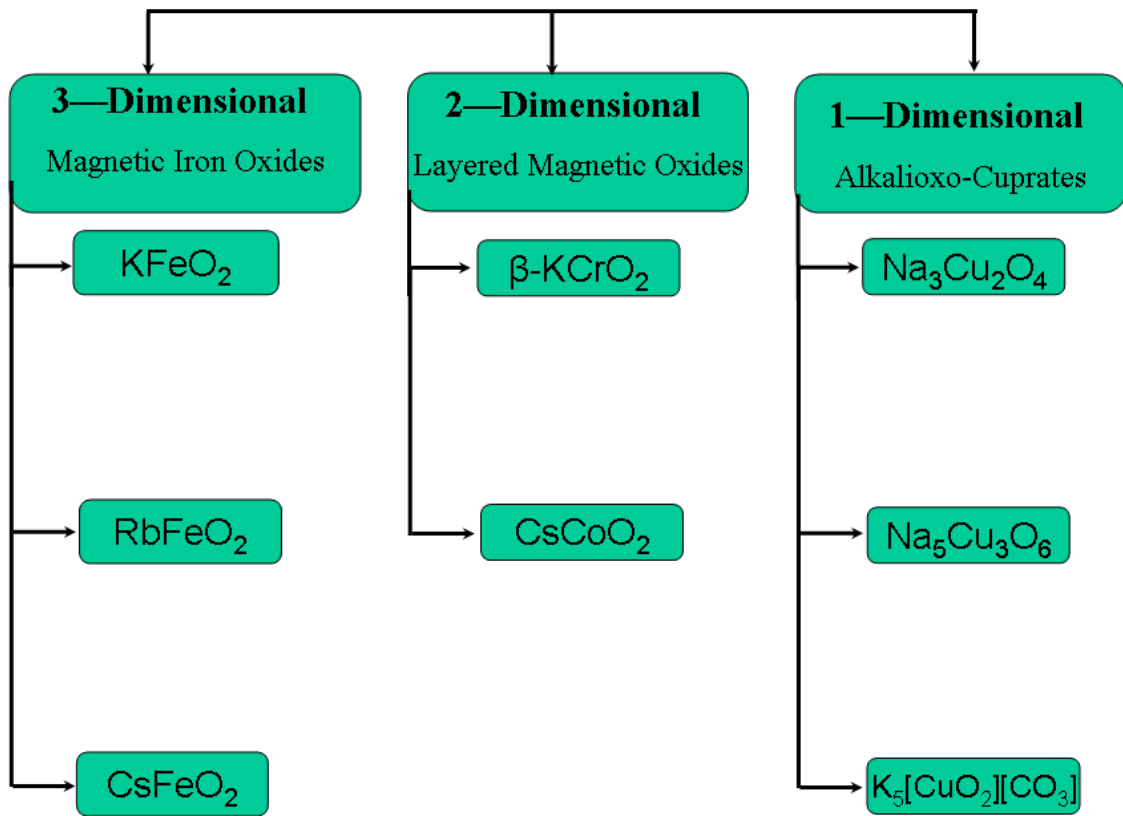
6. One-Dimensional Alkali-oxocuprates

- [75] Hisaho Nakataa, Jun Akimitsua, Susumu Katanob, Tsutomu Minamic, Norio Ogitac and Masayuki Udagawac, *Physica C: Superconductivity*, **255**, pp. 157-166 (1995).
- [76] M. Kikuchi, F. Izumi, M. Kikuchi, E. Ohshima, Y. Morii, Y. Shimojo and Y. Syono. *Physica C*, **247**, pp. 183 (1995).
- [77] G.N. Maso, V.M. Ivanov and A.V. Kumkova. *Fresenius J. Anal. Chem.* **350**, pp. 718, (1994).
- [78] [1-n] H. Shibata, K. Kinoshita and T. Yamada. *Physica C* **232**, pp. 181-183 (1994).
- [79] K .S. Aleksandrov, V. V. Beznosikov, *Phys. Solid State*, **39**, 785-808 (1997).
- [80] T. Kawashima, Y. Matsui, E. Takayama-Muromachi, *Physica C*, **233**, 143-148, (1994).
- [81] T. Kawashima, Y. Matsui, E. Takayama-Muromachi, *Physica C*, **227**, 95-101 (1994).
- [82] M. Hervieu, G. Van Tendeloo, C. Michel, D. Pelloquin, B. Raveau, *Microsc. Microanal. Microstruct.*, **7**, 107-141 (1996).
- [83] R.Hoppe, W.Losert, *Z. Anorg. Allg. Chem.*, **521**, 69 (1985).
- [84] W.Burow, J.Birx, F.Bernhardt, R.Hoppe, *Z. Anorg. Allg. Chem.*, **619**, 923 (1993).
- [85] F.Bernhardt, R.Hoppe, *Z. Anorg. Allg. Chem.*, **619**, 969 (1993).
- [86] A. Möller, *Z. Anorg. Allg. Chem.*, **627**, 2625-2629, (2001).
- [87] M. Sofin, E. M. Peters, M. Jansen, *Z. Naturforsch. B*, **57**, 1461-1463 (2002).
- [88] Further details may be obtained from Fachinformationszentrum Karlsruhe, 76344 Eggenstein-Leopoldshafen, Germany (fax: (+49)-7247-808-666; e-mail: crysdata@fiz-karlsruhe.de, [http://www.fiz-karlsruhe.de/request for deposited data.html](http://www.fiz-karlsruhe.de/request%20for%20deposited%20data.html)) on quoting the CSD number: CSD-422228.

6. One-Dimensional Alkali-oxocuprates

- [89] P. Amann, A. Möller, *Z. Anorg. Allg. Chem.*, **629**, 1643-1650 (2003).
- [90] M. H. Brooker, J. B. Bates, *Spectrochimica Acta Part A: Molecular Spectroscopy*, **30**, 2211-2220 (1974).
- [91] R. A. Nyquist, C. L. Putzig, M. A. Leugers, *Handbook of Infrared and Raman Spectra of Inorganic Compounds and Organic Salts, Vol. 2, Raman Spectra*, Academic Press Ltd., San Diego, pp. 60-63 (1997).
- [92] N. Koura, S. Kohara, K. Takeuchi, S. Takahashi, L.A. Curtiss, M. Grimsditch, M.-L. Saboungi, *J. Mol. Struct.*, **382**, 163-169 (1996).
- [93] E. T. Heyen, R. Liu, C. Thomsen, R. Kremer, M. Cardona, J. Karpinski, E. Kaldis, S. Rusiecki, *Phys. Rev. B*, **41**, 11058-11067 (1990).
- [94] Y. Yoshida, J. G. Wen, N. Watanabe, N. Koshizuka, T. Morishita, *J. Cryst. Growth*, **153**, 151-157 (1995).
- [95] M. I. Aroyo, J. M. Perez-Mato, D. Orobengoa, *Acta Crystallogr., Sect. A: Found. Crystallogr.*, **64**, C633 (2008).

Chapter 7: Summary



7. Summary

The main focus of the research work accomplished was to prepare new ternary alkali oxometallates of the first-row transition-metal elements containing, providing highly defined materials showing interesting structural and physical properties. 'Azide nitrate Route' was employed successfully for the complete synthesis, and overall **11** modifications of alkali oxometallates were characterized alongwith in depth study of their structural property relationships. Out of these, nine compounds were unknown. For all the compounds the crystal structure has been determined from single crystal data (**07**) and rest from powder data using state of the art techniques (High resolution synchrotron, neutron and advance D8-Bruker diffractometers). The "azide/nitrate route" has proven to be an efficient approach in present work for the solid state synthesis of new magnetic oxides covering the whole dimensionality, starting from 3-dimensional oxoferrates, two dimensional oxochromate and oxocobaltate respectively, and also new intrinsically doped one dimensional cuprates. We observed and illustrated, how by changing the dimensionality of a magnetic lattice, influence dramatically the thermodynamic properties by concerted study of the specific heat and magnetic susceptibility behaviour of the magnetic system particularly at low temperature. Later in order to construct a model for the spin interactions in these alkali oxometallates, the intrinsic magnetic properties of total **10** compounds have also been measured. The resulting magnetic properties were later justifiably analysed by employing various theoretical models. Thermal analysis (DSC, low and high temperature specific heat) bulk and electrical conductivity measurements, Moessbauer spectroscopy, High-resolution synchrotron powder diffractometry, neutron diffraction experiments were performed to study the structure property relation in detail and to validate the authenticity of results received.

7. Summary

A- 3-Dimensional Magnetic Oxides

KFeO₂ (Room temperature modification)

In agreement with the previously available results^[25], the KFeO₂ crystal structure at room temperature has been found to possess the orthorhombic unit cell with lattice constants $a = 5.600(1) \text{ \AA}$, $b = 11.26(2) \text{ \AA}$, $c = 15.94(2) \text{ \AA}$ (thus $a \approx \frac{1}{2}b \approx c/\sqrt{8}$), and the space symmetry $Pbca$. The structure consist of three dimensional network of corner sharing tetrahedra $[\text{FeO}_{4/2}]^-$ with monovalent potassium ion located in between. The Interatomic Fe-O distances lie in a narrow range and are in good agreement with the sum of ionic radii [$\sim 1.86 \text{ \AA}$]. The O-Fe-O bond angles indicate slightly distorted tetrahedra. Whereas the bending angles on oxygen atoms are more bent and lie in a range of $132.8(7) \leq \text{Fe-O-Fe} \leq 147.8 (8)$, differ distinctly from the idealized value (180°) reported for β -cristobalite. On the other hand, the interatomic Fe-Fe separations through these bonding are the smallest in KFeO₂ (3.45 \AA on average). The magnetic structures as determined by neutron scattering experiments at room temperature and down to 10 K is characterized by the antiferromagnetic Fe-Fe interactions in all four directions for each Fe ion, with low-temperature saturated value of the magnetic Fe³⁺ moments of $\sim 3.9 \mu_B$ (strong covalency effects). The direction of Fe³⁺ magnetic moments in KFeO₂ was found to be along the crystallographic b axis, in contrast to the previous finding of the Tomcowicz *et. al.*^[25]. However the experimentally observed Neel temperatures observed in KFeO₂ ($\sim 1001 \text{ K}$) lie close to the already reported value of 980K ^[25] and is hereby reaffirmed.

KFeO₂ (High temperature modification)

For KFeO₂ a reversible structural phase transformation takes place at 1003 K (T_{str}), as confirmed by differential scanning calorimetry and synchrotron X-ray and neutron diffraction concomitantly. The new high temperature modification of KFeO₂ (emerging at $T > T_{str}$) has been indexed on a cubic F -centered unit cell with a lattice constant $a_{cub} = 8.09171(9) \text{ \AA}$, which is related to those of the corresponding orthorhombic low-temperature modifications as: $a_{cub} \approx a_{orth} \cdot \sqrt{2} \approx b_{orth} / \sqrt{2} \approx \frac{1}{2} \cdot c_{orth}$, and the space group

7. Summary

$Fd\bar{3}m$ is adopted by the high temperature phase. The mechanism of phase transition into cubic phase is explained in detail by synchrotron data (time and space averaged structure) with the strongly anisotropic character of the atomic thermal vibrations of the oxygen atoms, and in the split atom model of our neutron investigation. The experimentally observed Néel temperatures in KFeO_2 ($T_N \sim 1001$ K) lies close to the structural phase transition ($T_{str} = 1003$ K) in contrast to the rest of the members of this compound family.

RbFeO₂ (Room temperature modification)

The new compound RbFeO_2 has been found to crystallize at room temperature with an orthorhombic unit cell (space group $Pbca$) with the lattice constants $a = 5.7197(1)$, $b = 11.5141(2)$, $c = 16.3457(2)$ Å. The unit cell contains 16 formula units. Single crystal X-ray diffraction analysis gives a reticular pseudomerohedral twinned crystal of RbFeO_2 with a pseudocubic twin lattice index of 4, because of approximate equation $a(8)^{1/2} = b(2)^{1/2} = c$. The essential feature of the crystal structure is a three dimensional network of corner sharing tetrahedra $[\text{FeO}_{4/2}]^-$ with monovalent rubidium located in between, as a consequence both heavy atoms form a three dimensional network of two interpenetrating diamond like structures built up of Rb and Fe exclusively. In principle the ${}^3[\text{FeO}_{4/2}]^-$ framework in the investigated crystal of RbFeO_2 corresponds to ${}^3[\text{SiO}_{4/2}]$ in β -cristobalite. The interatomic Fe-O distances lie in a narrow range and are in good agreement with the sum of ionic radii [~ 1.86 Å]. The O-Fe-O bond angles [$108.0(1) \leq \angle \text{O-Fe-O} \leq 113.0(2)^\circ$] indicate slightly distorted tetrahedra. Whereas the bending angles on oxygen atoms are more bent and lie in a range of $140.2(2) \leq \text{Fe-O-Fe} \leq 149.8(2)^\circ$, and differ distinctly from the idealized value (180°) reported for β -cristobalite. The interatomic Fe-Fe separations through these bondings (3.53 Å on average) are in RbFeO_2 consequently the intermediate compared to the other compounds. The magnetic structure as determined by neutron scattering experiments at room temperature and down to 10 K is characterized by the antiferromagnetic Fe-Fe interactions in all four directions for each Fe ion, with low-temperature saturated value of the magnetic Fe^{3+} moments of $\sim 3.9 \mu_B$

7. Summary

(strong covalency effects). The direction of Fe^{3+} magnetic moments in RbFeO_2 was found to be along the crystallographic c axis down to 10 K.

RbFeO₂ (High temperature modification)

The temperature evolution of the new high temperature modification of RbFeO_2 has been precisely investigated jointly by neutron and synchrotron powder diffraction techniques. This high temperature polymorph (emerging at $T > T_{str}$) has been indexed on a cubic F -centered unit cell (space group $Fd\bar{3}m$) with a lattice constant $a_{cub} = 8.24263(6)$ Å, related to those of the corresponding orthorhombic low-temperature modifications as: $a_{cub} \approx a_{orth} \cdot \sqrt{2} \approx b_{orth} / \sqrt{2} \approx \frac{1}{2} \cdot c_{orth}$. The mechanism of the phase transition into the cubic phase is explained in detail by synchrotron data (time and space averaged structure) with the strongly anisotropic character of the atomic thermal vibrations of the oxygen atoms, and in the split atom model of the present neutron investigation. The experimentally observed Néel temperature in RbFeO_2 ($T_N \sim 1029$ K) lies away from the structural phase transition ($T_{str} = 737$ K) in contrast to the respective values of KFeO_2 .

CsFeO₂ (Room temperature modification)

On the contrary to the previously reported room temperature cubic ($Fd\bar{3}m$) structure of CsFeO_2 ^[27], we found a new room temperature modification of CsFeO_2 , crystallizing in the KGaO_2 type of structure (space group $Pbca$), with lattice constants of $a = 5.915303(8)$, $b = 11.88481(2)$, $c = 16.77518(2)$ Å, which is a displacive, ordered variant of the CsAlO_2 type. The single crystal X-ray analysis performed at 100 K and 298 K reveals a multiply twinned crystal consisting of six individuals representing reticular pseudomerohedral twins with a pseudocubic twin lattice of index 4 because of approximate equations $a\sqrt{8} = b\sqrt{2} = c$. The structure consists of a three dimensional network of corner-sharing $[\text{FeO}_{4/2}]^-$ tetrahedra, with cesium atoms occupying its interstices, forming a 3D framework of two interpenetrating diamond-like networks build

7. Summary

up by cesium and iron atoms, exclusively. The interatomic Fe-O distances lie in a narrow range and are in good agreement with the sum of ionic radii. The O-Fe-O bond angles indicate slightly distorted tetrahedra. Whereas the bending angles on oxygen atoms are less bent and lie in a range of $152.2(5) \leq \text{Fe-O-Fe} \leq 161.6(4)^\circ$ as refined from single crystal X-ray diffractometry. The interatomic Fe-Fe separations through these bondings are consequently the largest in CsFeO₂ (3.63 Å on average).

CsFeO₂ (High temperature modification)

The new high temperature modification of CsFeO₂ emerging at $T \geq 350\text{K}$ has been indexed on a cubic F -centered unit cell (space group $Fd\bar{3}m$) with a lattice constant $a_{cub} = 8.406(1)$ Å as refined from single crystal data and is related to those of the corresponding orthorhombic low-temperature modification as: $a_{cub} \approx a_{orth} \cdot \sqrt{2} \approx b_{orth} / \sqrt{2} \approx \frac{1}{2} \cdot c_{orth}$. In case of CsFeO₂, because of the feasibility to achieve the transition temperature of 358 K, single crystal X-ray measurements were performed at 400 K endorsing the structural phase transition, alongwith the evolutions of this new high temperature cubic polymorph of CsFeO₂, as confirmed also by differential scanning calorimetry as well as neutron and synchrotron X-ray diffraction concomitantly. The magnetic ordering type in CsFeO₂ is antiferromagnetic ordering of magnetic Fe³⁺ ions within the system of the three-dimensional Fe-O-Fe linkages such that the Fe-Fe exchange between the nearest neighbouring ions is always antiferromagnetic. The directions of magnetic Fe moments were found to be parallel to the crystallographic c axis in CsFeO₂ in notations of the low-temperature orthorhombic modification. The experimentally found Néel temperature in CsFeO₂ (~ 1055 K) is herewith the highest ever observed in Fe oxides. Different phenomenological theoretical parameters and empirical quantities were tested to systematize the statistics on such a high Néel temperature, observed in CsFeO₂ and the rest of the members of this series. Also in a very recent study [*Phy. Rev B*]^[69], the origin of the high Neel temperatures in KFeO₂ and RbFeO₂ has been addressed by employing first-principles band-structure calculations and Monte-Carlo simulation.

7. Summary

B- 2-Dimensional Magnetic Oxides:

β -KCrO₂

β -KCrO₂ was synthesized via the azide/nitrate route by reaction between KN₃, KNO₃ and Cr₂O₃. Stoichiometric mixtures of the starting materials were heated in a special regime up to 853 K and annealed at this temperature for 50 h in silver crucibles. Single crystals have been grown by subsequent annealing of the reaction product at 773 K for 200 h in silver crucibles, which were sealed in glass ampoules under dried Ar. According to the X-ray analysis of the crystal structure at 298 K [*P*-31c (163), *Z*=2, *a*=3.0427(4) Å, *c*=11.924(2) Å, $\alpha = \beta = 90^\circ$ and $\gamma = 120^\circ$, 143 independent reflections, *R*₁= 2.6% (all data)], the structure comprises layers of edge-shared CrO₆ octahedra perpendicular to [001] with K atoms incorporated between the layers in a unique trigonal-prismatic arrangement. The thermodynamics of phase transitions was systematically investigated by high resolution X-ray powder diffraction and DSC techniques, showing transitions to occur at ~629 K from low temperature α -KCrO₂ (*R*-3m) to high temperature β -KCrO₂ (*P*-31c) with probable twisting of K⁺ cation from anti trigonal prism to trigonal prismatic structure.

CsCoO₂

CsCoO₂ was synthesized via the azide/nitrate route by reaction between CsN₃, CsNO₃ and Co₃O₄. Stoichiometric mixtures of the starting materials were heated in a special regime up to 833K and annealed at this temperature for 50 h in silver crucibles. Single crystals have been grown by subsequent annealing of the reaction product at 773K for 400 hours in silver crucibles, which were sealed in glass ampoules under dried Ar. According to the X-ray analysis of the crystal structure at 298 K [*C m c a* (64) , *Z*=8, *a*=5.9904(4) Å, *b*=12.2558(8) Å, *c*=8.2736(6)Å, $\alpha = \beta = \gamma = 90^\circ$, 1006 independent reflections, *R*₁= 1.96% (all data)], the structure consist of pairs of CoO₄ tetrahedra edge-linked to form bow-tie-shaped Co₂O₆ dimer (butterfly-motif) which share vertexes to form layered structure, a first and unique structure of its kind in the field of ternary oxide chemistry. In order to construct a model for the spin interactions in CsCoO₂, the magnetic

7. Summary

properties of CsCoO₂ have been measured. The magnetic susceptibility data is fitted by Curie Weiss law in the high temperature range of 155K to 285K, giving a Curie constant of $C = 3.016 \text{ cm}^3 \text{ K mol}^{-1}$ per Co (III) and $\theta = -490\text{K}$, $g = 2.004$ [$\mu_{\text{eff}}/\mu_B = g[S(S+1)]^{1/2}$] corresponding to Co³⁺ (d⁶) ions being in a high spin state ($S=2$), indicating a predominant intercluster antiferromagnetic interaction between Co³⁺ ions. μ_{eff} calculated from the Curie constant is $4.91 \mu_B$ which is in good agreement with the spin only value of $4.89 \mu_B$ expected for a high spin Co³⁺ (d⁶) system. However, at even lower temperature there occurs a sharp inflexion point at 7 K, which is in good agreement with the magnetic ordering transition temperature determined from the heat capacity measurements, which we presume is from the ferromagnetic coupling between Co^{III} ions within the Co₂O₆ cluster.

C- 1-Dimensional Magnetic Oxides:

Na₅Cu₃O₆

Na₅Cu₃O₆, a new member of one dimensional charge ordered chain cuprates, was synthesized via the azide/nitrate route by reacting NaN₃, NaNO₃ and CuO. According to the X-ray analysis of the crystal structures (Na₅Cu₃O₆: $P2_1/n$, $Z=4$, $a=5.7055(17)$, $b=16.795(5)$, $c=8.113(3)$ Å, $\beta=109.326(4)^\circ$, 3045 independent reflections, $R_1(\text{all})=0.065$, $wR_2(\text{all})=0.163$) the dominant feature of the crystal structure like the previous members of the family of chain cuprates Na_{1+x}CuO₂ [$x=0.5, 0.60$] is one dimensional ${}^1_{\infty}\text{CuO}_2^{n-}$ chains built up from planar, edge-sharing CuO₄ squares. From the analysis of the Cu–O bond lengths we find that the system forms a Wigner lattice. The commensurate charge order allows it to explicitly assign the valence states of either +2 or +3 to each copper atom resulting in a repetition according to $\text{Cu}^{2+}-\text{Cu}^{3+}-\text{Cu}^{2+}-\text{Cu}^{2+}-\text{Cu}^{3+}-\text{Cu}^{2+}$. Following the theoretical analysis of the previously synthesized compounds Na₃Cu₂O₄ and Na₈Cu₅O₁₀, the magnetic susceptibility was expected to show a large dimer gap. Surprisingly, this is not the case. To resolve this puzzle, we argue that the effective magnetic couplings in this compound are strongly affected by kinetic exchange contributions. By including these contributions we obtain a quantitative satisfying theoretical description of the magnetic susceptibility data.

7. Summary

Na₃Cu₂O₄

It was known from the past that the Na₃Cu₂O₄ undergoes long range antiferromagnetic ordering at 13K (T_N), however the author ^[62] also necessitates to carry out further investigation on the title compound. In much analogy we carry out again the synthesis of the title compound and studied physical properties thereof. The magnetic susceptibility data obtained recently is fitted by Curie Weiss law in the temperature range of 172 to 350 K, giving a Curie constant of $C = 0.36 \text{ cm}^3 \text{ K mol}^{-1}$ per Cu(II) and $\theta = -268 \text{ K}$, $g = 1.94$ [$\mu_{\text{eff}}/\mu_B = g[S(S+1)]^{1/2}$] corresponding to $S = 1/2$ system, indicating a predominant antiferromagnetic interaction between adjacent Cu²⁺ ions. μ_{eff} calculated from the Curie constant is $1.68 \mu_B$ which is in good agreement with the spin only value of $1.73 \mu_B$ expected for a Cu²⁺ (d^9) system. However as per author ^[62] suspicions, we reinvestigated the physical properties of the sample and conclude with confidence, keeping in view the magnetic susceptibility data endorsed with the low temperature specific heat plot that the Neel temperature of Na₃Cu₂O₄ is 22 K (T_N) in gut compliance with the rest of member of intrinsically doped sodium oxocuprates series [Na_{1+x}CuO₂], whereas the previously observed effect at 13K was due to the NaCu₂O₂ impurity.

K₅[CuO₂][CO₃]

Air and moisture sensitive K₅[CuO₂][CO₃] was prepared via the azide/nitrate route from stoichiometric mixtures of the precursors CuO, KN₃, KNO₃ and K₂CO₃. According to the single crystal X-ray analysis of the crystal structure [$P4/nbm$, $Z = 2$, $a = 7.4067(5)$, $c = 8.8764(8) \text{ \AA}$, $R_1 = 0.053$, 433 independent reflections] K₅[CuO₂][CO₃] represents an Ordered superstructure of Na₅[NiO₂][CO₃]. The structure contains isolated [CuO₂]³ dumbbells and CO₃²⁻ anions, with the latter not connected to the transition element. Raman spectroscopic measurements confirm the presence of CO₃²⁻ in the structure.

8. Zusammenfassung

Der Schwerpunkt dieser Arbeit liegt in der Synthese von neuen ternären Alkalioxometallaten der 3d-Übergangsmetalle mit interessanten Struktur und physikalischen Eigenschaft Beziehungen. Die Azid/Nitrat-Route wurde erfolgreich für die Darstellung von 11 Verbindungen angewendet, wobei 9 ganz neue Alkalioxometallate ausführlich bezüglich ihrer Eigenschaften charakterisiert wurden. Dabei zeigt sich der Ansatz mittels der Azid/Nitrat-Route sehr effizient für die Festkörpersynthese neuer magnetischer Oxide, welche die komplette Dimensionalität von dreidimensionalen Oxoferraten über zweidimensionale Oxochromaten und Oxocobaltaten bis zu neuen, dotierten, eindimensionalen Oxocupraten abdecken. Für alle dargestellten Verbindungen wurde die Kristallstruktur aus Einkristalldaten (7 Verbindungen) und Pulverdaten bestimmt.

Die Temperaturabhängigkeit der magnetischen Suszeptibilität wurde von 10 Verbindungen gemessen. Dabei erfolgte die Analyse der magnetischen Eigenschaften anhand zahlreicher theoretischer Modelle.

Darüber hinaus wurden die Proben mittels thermischer Analyse, Leitfähigkeitmessungen, hochauflösender Synchrotronpulverdiffraktometrie und Neutronenbeugung im Detail charakterisiert, um zu einem umfassenden Verständnis dieser Verbindungen zu gelangen.

A- 3-Dimensionale Magnetische Oxide

KFeO₂ (Raumtemperatur Modifikation)

In Übereinstimmung mit den Literatur Daten^[25] kristallisiert KFeO₂ bei Raumtemperatur orthorhombisch mit den Gitterparametern $a = 5.600(1) \text{ \AA}$, $b = 11.26(2) \text{ \AA}$, $c = 15.94(2) \text{ \AA}$ ($a \approx \frac{1}{2}b \approx c/\sqrt{8}$), in der Raumgruppe *Pbca*. Die Struktur besteht aus einem dreidimensionalen Netzwerk eckenverknüpfte ${}^3[\text{FeO}_{4/2}]^-$ Tetraedra mit monovalenten K Ionen in den Zwischenräumen. Der interatomare Fe-O Abstand liegt in einem engen Bereich und stimmt gut mit der Summe der Ionenradien überein. Der O—Fe—O Bindungswinkel weist auf leicht verzerrte Tetraedra hin, wobei die Fe—O—Fe Winkel starker gewinkelt sind und im Bereich von $132.8(7) \leq \text{Fe-O-Fe} \leq 147.8(8)$ liegen. Sie

8: Zusammenfassung

unterscheiden sich deutlich von dem idealen Wert (180°) wie z.B. für β -cristobalite. Andererseits ist der interatomare Fe—Fe Abstand am kürzesten in KFeO_2 (3.45 \AA gemittelt). Die magnetische Struktur, bei Raumtemperatur und bis 10 K durch Neutronen Beugungs Experimente bestimmt, ist charakterisiert durch antiferromagnetische Fe—Fe Wechselwirkungen in allen vier Richtungen für jedes Fe Ion, mit einen Tieftemperatur-Sättigungswert des magnetische Momentes für Fe^{+3} von $3.9 \mu_B$ [starke kovalence Effekte]. Die Richtung des Fe^{+3} — Fe^{+3} magnetische Momentes in KFeO_2 wurde parallel zu kristallographischen b-Achse bestimmt, was im Gegensatz zum bisherigen Ergebnis von Tomcowicz *et. Al* [25]. steht. Trotzdem liegt der beobachtetet Wert der Néel Temperatur in KFeO_2 ($T_N \sim 1001 \text{ K}$) nahe an dem bereits Literaturwert von 980 K [25].

KFeO_2 (Hochtemperaturmodifikation)

Für KFeO_2 findet ein reversibler struktureller Phasenübergang bei 1003 K statt, festgestellt sowohl durch DSC als auch durch Synchrotron-Röntgen- sowie Neutronenbeugung. Die neue Hochtemperaturmodifikation von KFeO_2 (auftretend bei $T > T_{str.}$) wurde kubisch flächenzentriert mit einer Gitterkonstante von $a_{kub} = 8.09171(9) \text{ \AA}$ indiziert, die mit der Niedrigtemperaturmodifikation über $a_{kub} \approx a_{orth} \cdot \sqrt{2} \approx b_{orth} / \sqrt{2} \approx \frac{1}{2} \cdot c_{orth}$ in Beziehung steht. Der Mechanismus des Phasenübergangs konnte im Detail mit Hilfe von Synchrotrondaten (über Zeit und Raum gemittelte Struktur) durch den stark anisotropen Charakter der thermischen Schwingungen der Sauerstoffatome und durch das Splitatommodell aus unserer Untersuchung mittels Neutronendaten aufgeklärt werden. Die experimentell gefundene Néel-Temperatur in KFeO_2 von $T_N = 1001 \text{ K}$ liegt nahe beim strukturellen Phasenübergang ($T_{str} = 1003 \text{ K}$), was im Gegensatz zu den übrigen Vertretern dieser Verbindungsgruppe steht.

RbFeO₂ (Raumtemperaturmodifikation)

Die neue Verbindung RbFeO₂ kristallisiert bei Raumtemperatur orthorhombisch in Raumgruppe *Pbca* mit den Gitterkonstanten $a = 5.7197(1)$, $b = 11.5141(2)$, $c = 16.3457(2)$ Å mit 16 Formeleinheiten pro Elementarzelle. Anhand einer Einkristallröntgenstrukturuntersuchung ergibt sich für RbFeO₂ eine retikular pseudomeroedrisch verzwilligte Kristall mit einem pseudokubischen Zwillingsgitterindex von 4, über die angenäherte Beziehung $a(8)^{1/2} = b(2)^{1/2} = c$. Das wesentliche Merkmal der Kristallstruktur ist ein dreidimensionales Netzwerk von eckenverknüpften [FeO_{4/2}]⁻-Tetraedern mit einwertigen Rb-Kationen darin. Beide Schweratomsorten bilden ein dreidimensionales Netzwerk von zwei interpenetrierenden, diamantähnlichen Strukturen ausschließlich aus Rb- und Fe-Atomen. Im Prinzip entspricht das ³_∞[FeO_{4/2}]⁻-Netzwerk in der untersuchten Kristallstruktur von RbFeO₂ dem ³_∞[SiO_{4/2}]-Gerüst in β -Cristobalit. Die interatomaren Fe-O-Abstände liegen in einem engen Bereich und stimmen sehr gut mit der Summe der Ionenradien [~ 1.86 Å] überein. Die O-Fe-O-Bindungswinkel [$108.0(1) \leq \angle \text{O-Fe-O} \leq 113.0(2)^\circ$] weisen auf nur schwach verzerrte Tetraeder hin. Dagegen sind die Bindungswinkel an den Sauerstoffatomen stärker gekrümmt und liegen im Bereich von $140.2(2) \leq \text{Fe-O-Fe} \leq 149.8(2)^\circ$, und weichen damit deutlich vom idealisierten Wert für β -Cristobalit (180°) ab. Die interatomaren Fe-Fe-Abstände über diese Bindungen (durchschnittlich 3.53 Å) bilden in RbFeO₂ daher den Mittelwert für diese Verbindungsgruppe. Die magnetische Struktur, wie sie aus Neutronenbeugungsexperimenten bei Raumtemperatur bis hinunter zu 10 K bestimmt wurde, ist charakterisiert durch die antiferromagnetischen Fe-Fe-Wechselwirkungen in alle vier Richtungen für jedes Fe-Ion, mit einem Niedrigtemperatursättigungswert der magnetischen Fe³⁺-Momente von $\sim 3.9 \mu_B$ (starke Kovalenzeffekte). Die Richtung der magnetischen Fe³⁺-Momente in RbFeO₂ liegt bis hinunter zu 10 K entlang der kristallographischen *c*-Achse.

8: Zusammenfassung

RbFeO₂ (Hochtemperaturmodifikation)

Die Temperaturabhängigkeit der neuen Hochtemperaturmodifikation von RbFeO₂ wurde präzise mittels Neutronen- und Synchrotronpulverdiffraktion untersucht. Das Hochtemperaturpolymorph (auftretend bei $T > T_{str}$) wurde mit einer kubisch F -zentrierten Elementarzelle (Raumgruppe $Fd\bar{3}m$) mit der Gitterkonstante $a_{cub} = 8.24263(6)$ Å indiziert, verwandt mit der entsprechenden orthorhombischen Niedrigtemperaturmodifikation nach $a_{cub} \approx a_{orth} \cdot \sqrt{2} \approx b_{orth} / \sqrt{2} \approx \frac{1}{2} \cdot c_{orth}$. Der Mechanismus des Phasenübergangs in die kubische Modifikation konnte detailliert durch Synchrotrondaten (zeit- und ortsgemittelte Struktur) mit dem stark anisotropen Charakter der atomaren thermischen Schwingungen der Sauerstoffatome und mit dem Splitatommodell aus den Neutronenbeugungsuntersuchungen erklärt werden. Die experimentell beobachtete Néel-Temperatur in RbFeO₂ ($T_N \sim 1029$ K) liegt entfernt vom strukturellen Phasenübergang ($T_{str} = 737$ K) im Gegensatz zum entsprechenden Wert bei KFeO₂.

CsFeO₂ (Raumtemperaturmodifikation)

Im Unterschied zu der bereits früher publizierten kubischen Raumtemperaturstruktur von CsFeO₂^[27] in Raumgruppe $Fd\bar{3}m$ haben wir eine neue, im KGaO₂-Strukturtyp (Raumgruppe $Pbca$) kristallisierende Raumtemperaturmodifikation gefunden, einer displaziv geordneten Variante des CsAlO₂-Typs. Die Gitterkonstanten sind $a = 5.915303(8)$, $b = 11.88481(2)$, $c = 16.77518$ (2) Å. Einkristallröntgenstrukturanalysen bei 100 K und 298 K ergeben einen vielfach verzwilligten Kristall bestehend aus sechs Individuen, ein retikular pseudomeroedrischer Zwillinge mit einem pseudokubischen Zwillingsgitter mit dem Index 4 aufgrund der angenäherten Beziehung $a\sqrt{8} = b\sqrt{2} = c$ darstellen. Die Struktur besteht aus einem dreidimensionalen Netzwerk eckenverknüpfter $[\text{FeO}_{4/2}]^-$ -Tetraeder, dessen Lücken mit Cäsiumatomen besetzt sind, so dass ein dreidimensionales Netzwerk aus zwei interpenetrierenden, diamantähnlichen Gerüsten ausschließlich aus Cäsium- und

8: Zusammenfassung

Eisenatomen gebildet wird. Die interatomaren Fe-O-Abstände liegen in einem engen Bereich und stimmen gut mit der Summe der Ionenradien überein. Die O-Fe-O-Bindungswinkel deuten auf kaum verzerrte Tetraeder hin. Die Bindungswinkel an den Sauerstoffatomen sind weniger gekrümmt als in den verwandten Verbindungen und liegen im Bereich von $152.2(5) \leq \text{Fe-O-Fe} \leq 161.6(4)^\circ$, wie aus Verfeinerungen der Einkristallröntgenbeugungsdaten hervorgeht. Die interatomaren Fe-Fe-Abstände über diese Bindungen sind daher auch am größten in CsFeO₂ (durchschnittlich 3.63 Å).

CsFeO₂ (Hochtemperaturmodifikation)

Für CsFeO₂ findet ein reversibler struktureller Phasenübergang bei 358 K statt, sowohl durch DSC als auch durch Neutronen- sowie Synchrotron-Röntgenbeugung bestimmt. Die neue Hochtemperaturmodifikation wurde kubisch *F*-zentriert (Raumgruppe $Fd\bar{3}m$) mit einer Gitterkonstanten von $a_{kub} = 8.406(1)$ Å indiziert und steht über $a_{kub} \approx a_{orth} \cdot \sqrt{2} \approx b_{orth} / \sqrt{2} \approx \frac{1}{2} \cdot c_{orth}$ mit der korrespondierenden orthorhombischen Niedrigtemperaturmodifikation in Beziehung. Wegen der Erreichbarkeit der Übergangstemperatur wurden im Falle von CsFeO₂ die Einkristallröntgenbeugungsmessungen bei 400 K durchgeführt und der strukturelle Phasenübergang damit bestätigt. Die magnetische Ordnung der Fe³⁺-Ionen in CsFeO₂ ist antiferromagnetischer Art innerhalb des Systems der dreidimensionalen Fe-O-Fe-Verknüpfungen, so dass der Fe-Fe-Austausch zwischen den am nächsten benachbarten Ionen immer antiferromagnetisch ist. Die Richtungen der magnetischen Momente wurden als parallel zur kristallographischen *c*-Achse (in der Notation der orthorhombischen Niedrigtemperaturphase von CsFeO₂) beobachtet. Die experimentell bestimmte Néel-Temperatur in CsFeO₂ (~ 1055 K) ist die höchste bisher in einem Eisenoxid gefundene. Verschiedene phänomenologische, theoretische Parameter sowie empirische Größen wurden geprüft, um die Statistik solch hoher Néel-Temperaturen zu systematisieren, wie sie in CsFeO₂ und den anderen Gliedern dieser Verbindungsgruppe gefunden wurden. In einer neuen Studie [*Phy. Rev B*] ^[69] wurde die Ursache der hohen Néel-Temperaturen in

8: Zusammenfassung

KFeO₂ and RbFeO₂ mit Hilfe von First-principles-Bandstrukturrechnungen und Monte-Carlo-Simulationen untersucht.

B- 2-Dimensionale Magnetische Oxide:

β -KCrO₂

β -KCrO₂ wurde über die Azid/Nitrat-Route aus stöchiometrischen Mischungen von KN₃, KNO₃ and Cr₂O₃ synthetisiert. Stöchiometrische Gemenge dieser Edukte wurden über ein spezielles Temperaturprogramm auf 853 K erhitzt und anschließend 50 Stunden in Silbertiegeln getempert. Einkristalle wurden durch Tempern dieser Produkte bei 773 K (200 Stunden, Ar) im Silbertiegel erhalten. Die Röntgeneinkristallstrukturanalyse liefert [298 K, *P*-31c (163), *Z*=2, *a*=3.0427(4) Å, *c*=11.924(2) Å, $\alpha = \beta = 90^\circ$ and $\gamma = 120^\circ$, 143 unabhängige Reflexe, *R*₁= 2.6% (für alle Daten)], Schichten von kantenverknüpften CrO₆-Oktaedern senkrecht zu (001), wobei die Kaliumatome zwischen den Schichten mit ungewöhnlicher trigonal-prismatischer Umgebung eingelagert sind. DSC-Messungen belegen einen reversiblen Phasenübergang von α -KCrO₂ [α -NaFeO₂-Typ (Raumgruppe *R*-3m)] zu β -KCrO₂ (Raumgruppe *P* $\bar{3}$ 1c) bei 629 K. Röntgenpulveruntersuchungen bestätigen diese Phasenumwandlung.

CsCoO₂

Die neue zweidimensionale Schichtverbindung CsCoO₂ wurde über die Azid/Nitrat-Route aus stöchiometrischen Mischungen von CsN₃, CsNO₃ und Co₃O₄ dargestellt. Stoichiometrischen Gemenge dieser Edukte wurden über ein spezielles Temperaturprogramm auf 833 K erhitzt und anschließend 50 Stunden im Silbertiegel getempert. Einkristalle wurden durch Tempern dieser Produkte bei 773 K (200 Stunden, Ar) im Silbertiegel erhalten. Anhand der Einkristallstrukturanalyse kristallisiert CsCO₂ orthorhombisch in der Raumgruppe *Cmca* (Nr. 64) mit *a* = 5.9904(4) Å, *b* = 12.2558(8) Å, *c* = 8.2736(6)Å, *Z* = 8, 1006 unabhängige Reflexe, *R*₁= 1.96% für alle Daten. Das

8: Zusammenfassung

Hauptmerkmal der Kristallstruktur sind Paare von kantenverknüpften CoO_4 -Tetraeder, (Co_2O_6 -Schmetterlingsmotiv) welche über Ecken zu einer Schicht verknüpft sind, eine bisher einzigartige Struktur im Bereich der ternären Oxidchemie. Um ein Modell für die interessanten Spin-Wechselwirkungen zu entwickeln, wurden die magnetischen Eigenschaften von CsCoO_2 zwischen 2K zu 300K gemessen. Die magnetische Suszeptibilität folgt dem Curie-Weiß-Gesetz für Co^{3+} (d^6)-Ionen mit high spin [$S=2$], was einer vorherrschenden antiferromagnetische Wechselwirkung zwischen Co^{3+} -Ionen entspricht.

C- 1-Dimensionale Magnetische Oxide:

$\text{Na}_5\text{Cu}_3\text{O}_6$

$\text{Na}_5\text{Cu}_3\text{O}_6$, ein neuer Vertreter gemischvalenter eindimensionaler Natriumcuprate mit ladungsgeordneten Ketten, wurde aus CuO , NaN_3 und NaNO_3 dargestellt. Es kristallisiert monoklin in der Raumgruppe $P2_1/n$ mit den Gitterparametern $a = 5.7055(17)$ Å, $b = 16.795(5)$ Å, $c = 8.113(3)$ Å, $\beta = 109.326(4)^\circ$. Die Einkristallstrukturanalyse von $\text{Na}_5\text{Cu}_3\text{O}_6$ liefert ein dimensionale CuO_2 -Ketten, gebildet aus kantenverknüpften CuO_4 -Quadraten, welches das dominierende Strukturmerkmal darstellt. Diese Ketten verlaufen entlang der b-Achse. Die Natriumatome befinden sich zwischen den CuO_2 -Ketten und bilden Reihen, die auch parallel zur b-Achse liegen. Die Cu-O Bindungsanalyse ergibt ein Wigner-Gitter für dieses System. Die Unterschiede in den Cu-O-Abständen ermöglichen es, Cu^{II} - und Cu^{III} -Ionen zu unterscheiden. Dabei wird ein komplexes Alternieren von Cu^{II} und Cu^{III} beobachtet. Ein periodisch wiederholter Abschnitt besteht aus sechs Atomen: $\text{Cu}^{2+}\text{-Cu}^{3+}\text{-Cu}^{2+}\text{-Cu}^{2+}\text{-Cu}^{3+}\text{-Cu}^{2+}$. Die theoretische Analyse zeigt, dass die effektive magnetische Kopplung in dieser Verbindung stark durch einen kinetischen Austauschbeitrag beeinflusst ist. Dieser liefert eine quantitative Beschreibung der magnetischen Suszeptibilität. Die magnetische Suszeptibilität lässt sich im Bereich 135-680 K durch das Curie-Weiß-Gesetz für $S = 1/2$ beschreiben: $\Theta = -62$ K, $g = 2,18$ ($\mu = 1,89 \mu_B$), was eine gute Übereinstimmung mit dem idealen spin-only-Wert von $1,73 \mu_B$ für das Cu^{2+} -System entspricht. Unterhalb 23 K ordnen sich die Spins

8: Zusammenfassung

antiferromagnetisch. Die exakt bestimmte Néel-Temperatur ($T_N = 23$ K) stimmt sehr gut mit den spezifischen Wärmemessungen überein. Die spezifische Wärme zeigt auch bei dieser Temperatur eine Anomalie. Die Ladungsordnung verschwindet oberhalb von 555 K, was aus den DSC- und Leitfähigkeitsmessungen folgt, und das System verhält sich wie ein eindimensionales Metall.

Na₃Cu₂O₄

Aus der Literatur ist bekannt, dass Na₃Cu₂O₄ bei 13K antiferromagnetisch ordnet, wobei die Autoren ^[62] weitere Untersuchungen an dieser Verbindungen nahelegen. Daher haben wir die Synthese dieser Verbindungen wiederholt und ihre physikalischen Eigenschaften erneut studiert. Die magnetische Suszeptibilität lässt sich im Bereich 172-350 K durch das Curie-Weiß-Gesetz für $S = 1/2$ beschreiben: $\Theta = -268$, $g = 1.94$ ($\mu = 1,68 \mu_B$), was eine gute Übereinstimmung mit dem idealen spin-only-Werte von $1.73 \mu_B$ für Cu²⁺-System entspricht. Unterhalb 23 K ordnen sich die Spins hauptsächlich antiferromagnetisch.

Die spezifische Wärme vom Na₃Cu₂O₄ zeigt eine Anomalie bei 23 K, was durch temperaturabhängige magnetische Messungen unterstützt wird. Die exakte bestimmte Néel-Temperatur ($T_N = 23$ K) steht in guter Analogie zu den Vertretern der Na_{1+x}CuO₂-Familie und stimmt mit den Messungen der spezifischen Wärme überein. In früheren Untersuchungen geben die Autoren allerdings 13 K für die antiferromagnetische Ordnung für Na₃Cu₂O₄ an. Der gefundene Effekt bei 13 K ist unserer Meinung nach auf eine Verunreinigung mit NaCu₂O₂ zurückzuführen.

8: Zusammenfassung

K₅[CuO₂]CO₃

Das neue luft- und feuchtigkeitsempfindliche Kaliumcarboxycuprat wurde über die Azid/Nitrat-Route aus stöchiometrischen Mischungen von KN₃, KNO₃, Cu₂O und K₂CO₃ dargestellt. Anhand der Einkristallstrukturanalyse kristallisiert K₅[CuO₂]CO₃ tetragonal in der Raumgruppe *P4/nbm* (Nr. 125) mit $a = 7.4067(5)$ and $c = 8.8764(8)$ Å. Die herausstechende Strukturmerkmale sind eine lineare [Cu(I)O₂]³⁻-Hantel (Cu—O-Abstand = 1.787(5) Å, O—Cu—O-Winkel = 180°) und CO₃²⁻-Anionen, Letztere sind nicht mit den Übergangsmetallen verknüpft. Die K1 Atome bilden ein verzerrtes kubisch primitives Gitter, in dem die Lücken zu je ¼ mit Cu(I)O₂-Hanteln, CO₃²⁻-Anionen und K²-Atomen gefüllt sind, und ¼ bleibt leer. Die CO₃²⁻-Anionen sind fehlgeordnet mit zwei Orientierungen auf der gleichen kristallographischen Lage mit der Symmetrie $\bar{4}2m$. Die Struktur stellt eine geordnete Variante von Na₅[NiO₂][CO₃] Strukturtyp. Ramanmessungen belegen die Anwesenheit der CO₃²⁻-Anionen in der Verbindung.

9. Addendum

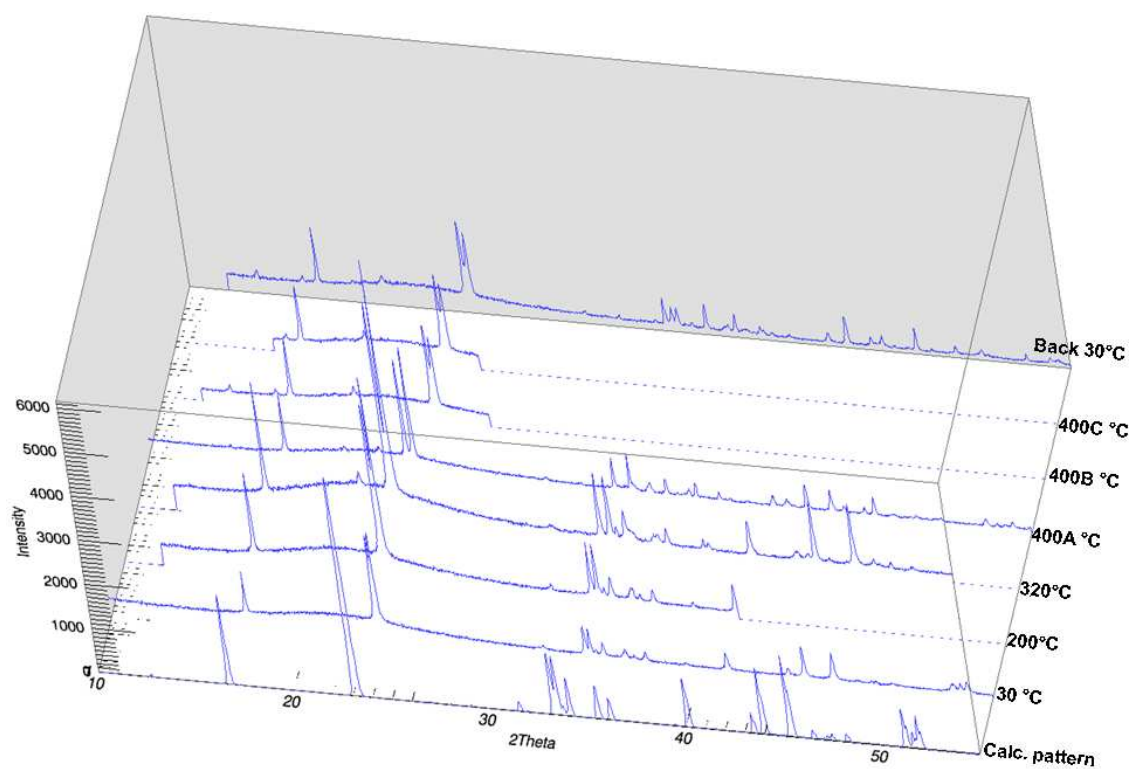


Fig. 9.1. Scattered X-ray intensity for polycrystalline sample of $\text{Na}_5\text{Cu}_3\text{O}_6$ measured on advance Bruker Mo-D8 diffractometer in rotating quartz capillary with continuous HT—XRD experiments from 298 K till 673K.

9. Addendum

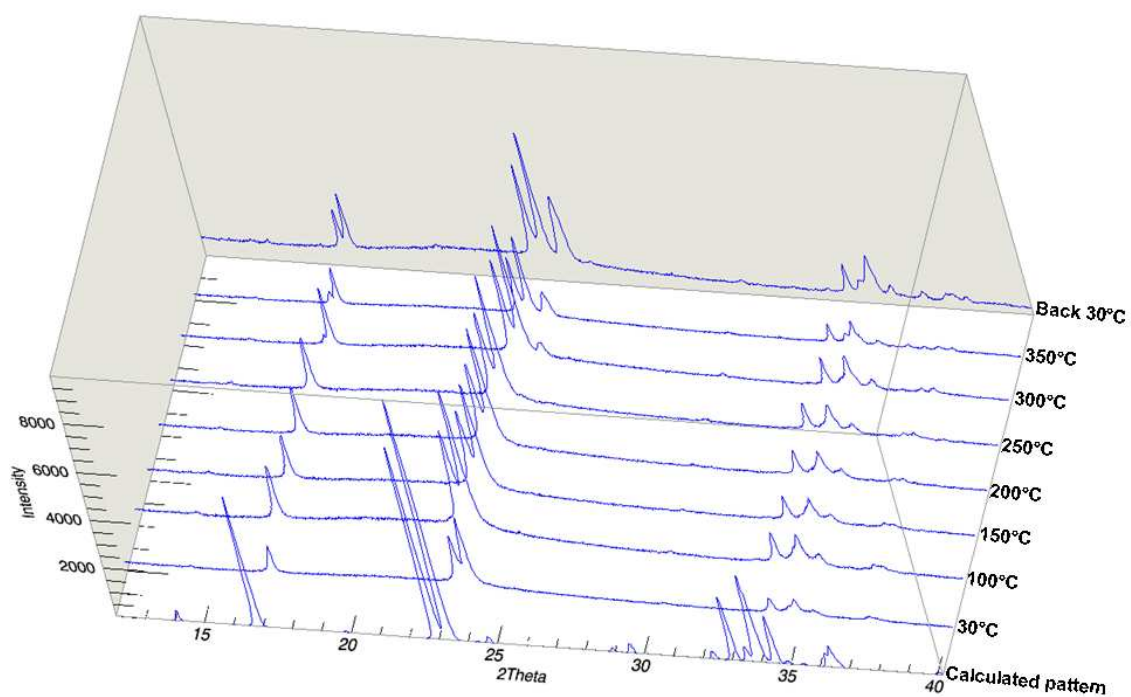


Fig. 9.2. Scattered X-ray intensity for polycrystalline sample of $\text{Na}_3\text{Cu}_2\text{O}_4$ measured on advance Bruker Mo-D8 diffractometer in rotating quartz capillary with continuous HT—XRD experiments from 298 K till 623K.

9. Addendum

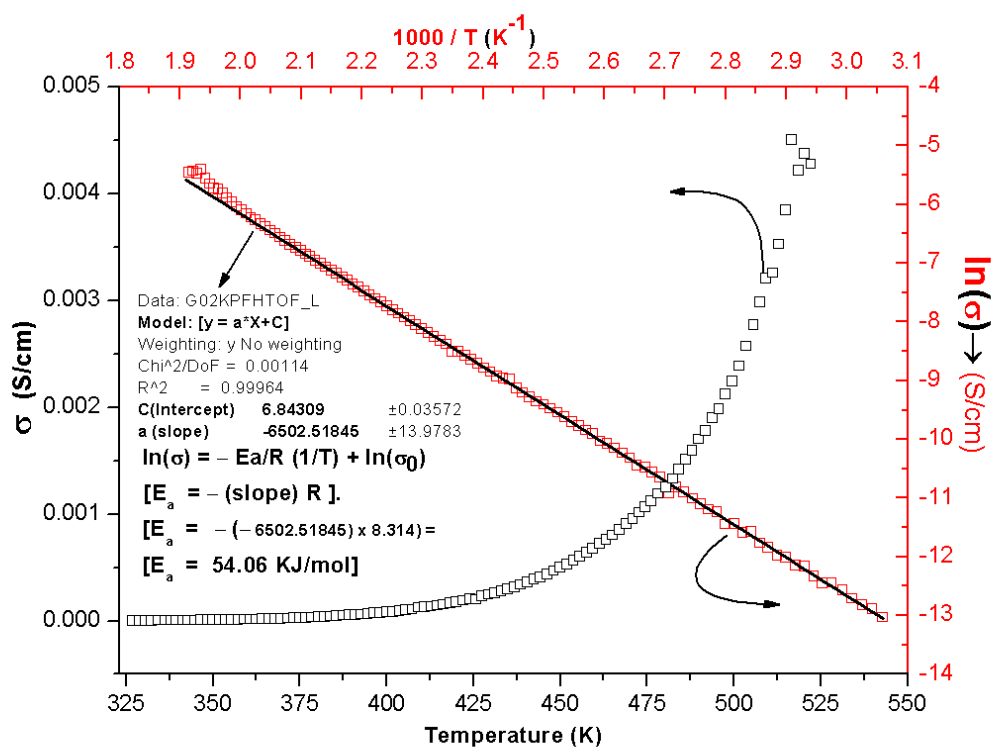


Fig. 9.3. High temperature (DC) electrical conductivity (black-squares), with corresponding Arrhenius plot (red-squares) for polycrystalline sample of Na₅Cu₃O₆

9. Addendum

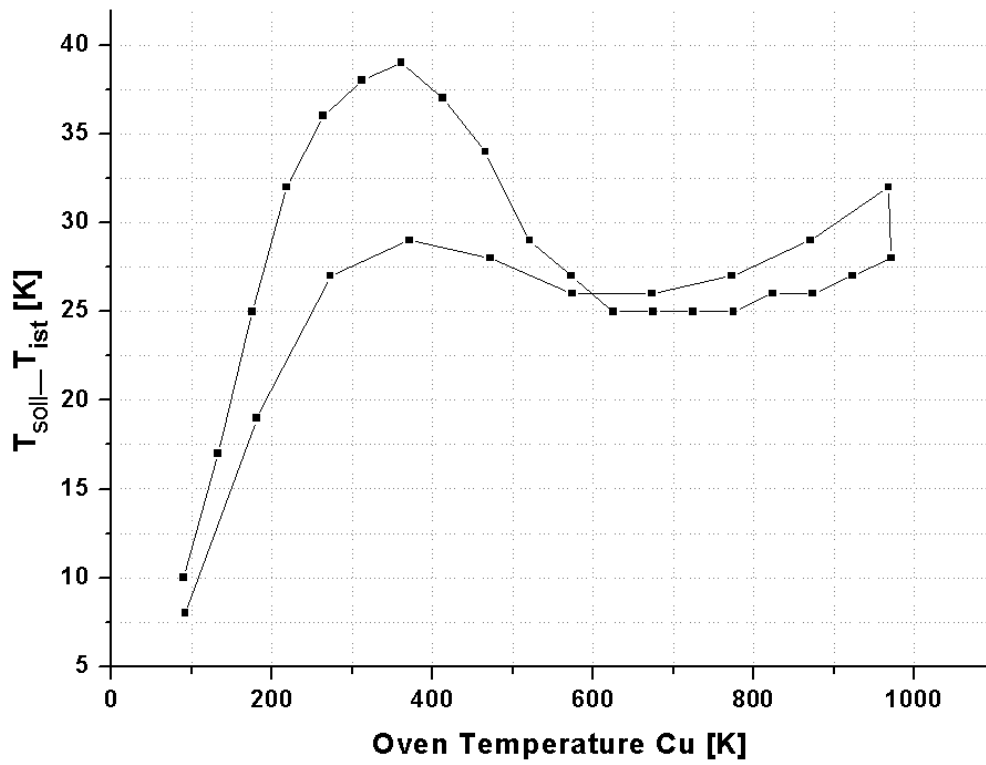


Fig. 9.4. Calibration curve for the heater stage employed on the Cu-Bruker D8 Advance diffractometer (upper curve = heating cycle, lower curve = cooling cycle)

9. Addendum

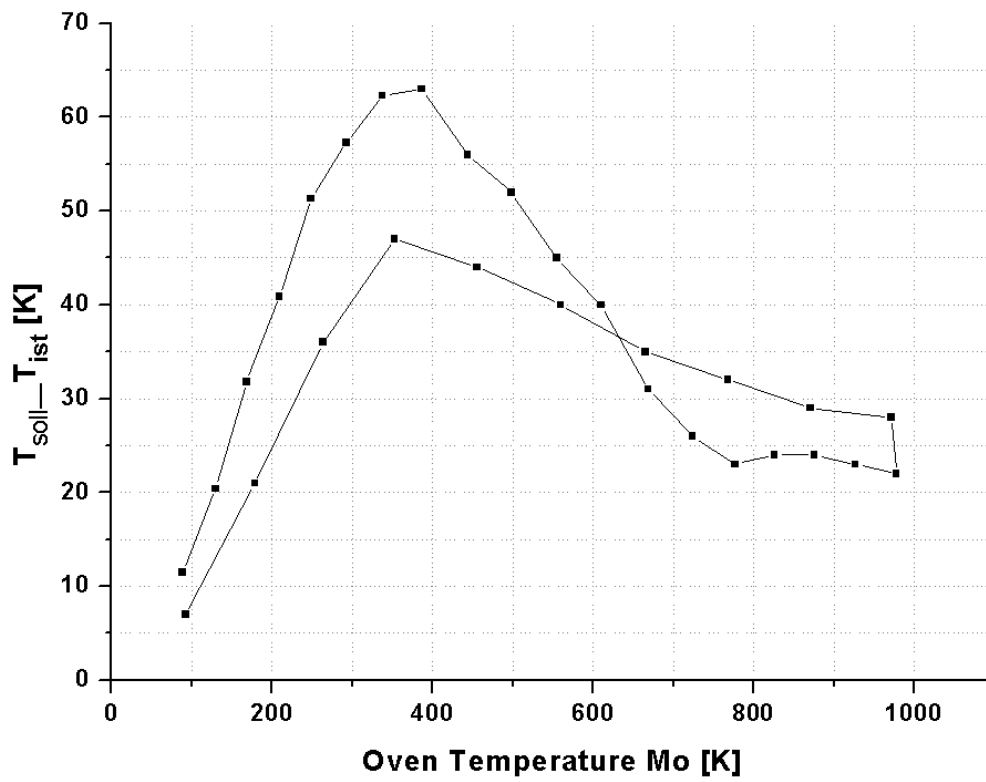


Fig. 9.5. Calibration curve for the heater stage employed on the Mo—Bruker D8 Advance diffractometer (upper curve = heating cycle, lower curve = cooling cycle)

List of abbreviations

List of Abbreviations

HT: High Temperature

RT: Room Temperature

a. u.: arbitrary units

PSD: Position Sensitive Detector

SQUID: Spin Quantum Interference Device

EDX: Energy Dispersive X-ray spectrometry

T_C: Curie Temperature

T_N: Neel Temperature

C_{max}: Maxima in Specific heat plot

g: Landé g-factor

C: Curie constant

Θ: Weiss constant

Å: Angstrom

K: Kelvin

T: Tesla

DSC: Differential Scanning Calorimetry

Oe: Oersted [1T=10000 Oe]

M: Magnetization (emu)

H: Applied magnetic field (Tesla)

χ: chi [$\chi=M/H$]

AC: Alternating current

DC: Direct current

List of Tables

List of Tables

Table 2.1: The specification of various diffractometers used in present investigation at Max Planck Institute for solid state research (FKF) Stuttgart

Table 4.1: An overview of $\alpha \rightarrow \beta$ transformation in the cristobalite family

Table 4.2: Crystallographic data for RbFeO_2 at 298 K (single crystal diffraction data).

Table 4.3: Atomic coordinates and equivalent displacement parameters (\AA^2) for RbFeO_2 .

Table 4.4: Selected bond distances and angles for RbFeO_2 (\AA , $^\circ$)

Table 4.5: Crystallographic data for single crystal of CsFeO_2 at different temperatures.

Table 4.6: Atomic coordinates and equivalent isotropic displacement parameters $U_{\text{eq}} / \text{\AA}^2$ for CsFeO_2 at different temperatures (refined from single crystal diffraction data).

Table 4.7: Bond angles $\text{Fe—O—Fe} / ^\circ$ in the orthorhombic low temperature phases of AFeO_2 ($A = \text{K, Rb, Cs}$), describing the twisting of the FeO_4 tetrahedra.

Table 4.8: The twinning matrices to transform the orthorhombic unit cells.

Table 4.9: $\Delta H_{\text{transition}}$ and T_{onset} values obtained via specific heat measurement of polycrystalline sample of AFeO_2 samples ($A = \text{K, Rb and Cs}$)

Table 4.10: Crystallographic data for AFeO_2 ($A = \text{K, Rb, Cs}$) at different temperatures (obtained from powder synchrotron data).

Table 4.11: Atomic coordinates and equivalent isotropic displacement parameters $U_{\text{eq}} / \text{\AA}^2$ for AFeO_2 ($A = \text{K, Rb, Cs}$) at different temperatures (refined from powder synchrotron data).

List of Tables

Table 4.12: Crystal structure parameters at about room temperature for KFeO_2 (320 K), RbFeO_2 (300 K) and CsFeO_2 (306 K) refined from neutron powder diffraction data. Space group $Pbca$ ($Z=16$). All atoms are located in the general (8c) sites.

Table 4.13: Crystal structure parameters for the high-temperature polymorphs of KFeO_2 (at $T \approx 1050$ K), RbFeO_2 (at $T \approx 820$ K) and CsFeO_2 (at $T \approx 400$ K) refined from neutron powder diffraction data. Space group $Fd\bar{3}m$ ($Z=8$).

Table 4.14: Isomer-shift (IS) relative to α -Fe (mm/s), half width Γ of the lines with Lorentzian shape (mm/s), quadrupole splitting QS (mm/s), internal magnetic field (H) and area A (%).

Table 5.1: Crystal data and structure refinement for CsCoO_2 .

Table 5.2: Atomic coordinates and equivalent isotropic displacement parameters (\AA^2) for CsCoO_2 .

Table 5.3: Anisotropic displacement parameters (\AA^2) for CsCoO_2 .

Table 5.4: Bond lengths [\AA] and angles [$^\circ$] for CsCoO_2

Table 5.5: Interatomic distances (in \AA), coordination numbers (CN), effective coordination numbers (ECoN) and mean fictive ionic radii (MEFIR) for CsCoO_2 .

Table 5.6: Crystal data and structure refinement for β - KCrO_2 .

Table 5.7: Atomic coordinates and equivalent isotropic displacement parameters (\AA^2) for β - KCrO_2 .

Table 5.8: Anisotropic displacement parameters (\AA^2) for β - KCrO_2 .

Table 5.9: Selected interatomic distances (\AA) and bond angles ($^\circ$) for β - KCrO_2

List of Tables

Table 5.10: MAPLE comparison [kcal/mole] of α -KCrO₂ and β -KCrO₂.

Table 6.1: X-ray and crystallographic data for Na₅Cu₃O₆

Table 6.2: Atomic coordinates and equivalent isotropic displacement parameters (\AA^2) for Na₅Cu₃O₆

Table 6.3: Anisotropic thermal displacement parameters (in \AA^2) for Na₅Cu₃O₆

Table 6.4: Interatomic distances (in \AA), CN, ECoN and MEFIR^[24] (in \AA) for Na₅Cu₃O₆

Table 6.5: Selected bond angles ($^\circ$) in Na₅Cu₃O₆

Table 6.6: Crystal data, data collection, and refinement details for K₅[CuO₂][CO₃].

Table 6.7: Atomic coordinates and equivalent isotropic displacement parameters $U_{\text{eq}}/\text{\AA}^2$ for K₅[CuO₂][CO₃].

Table 6.8: Anisotropic displacement parameters $U_{ij}/\text{\AA}^2$ for K₅[CuO₂][CO₃].

List of Figures

List of Figures

Figure 2.1: Schematic representation of vacuum assembly

Figure 2.2: *i and ii*) Schlenk tubes (upper cross section: LV of 29, remaining cross section LV 14.5: a) = ampoules sealing unit and b) = capillary filling unit. *iii*) A common drying tube (ox-Rohr).

Figure 2.3: Reaction crucibles specially designed for the azide nitrate route (hexagonal, steel 9S29-K) with Ag, Cu inlays. Double hole Crucible, (b) Single hole crucible (c) Single hole with double lining.

Figure 2.4: Schematic of commonly used quartz tube for crystal growth.

Figure 2.5: Single zone furnace (HTM Reetz GmbH, Berlin) used for synthesis in present this study.

Figure 2.6: A standard suprased quartz tube ($\varnothing = 3$ mm) with gold crucible used for high temperature magnetic susceptibility measurement.

Figure 2.7: The common Honda Owen plot of $\chi_{\text{mol}}(\text{exp})$ vs $H^{-1}(\text{Tesla}^{-1})$ at various temperatures at magnetic field approaching infinity [$H^{-1}=0$].

Figure 2.8: Setup for Mössbauer spectrometry measurements.

Fig. 3.1: A schematic view of assembly used for the preparation of alkali azides

Fig. 3.2: Measured Powder diffractograms and the calculated literature data for (a) LiN_3 (b) KN_3 (c) RbN_3 (d) and CsN_3

Fig. 3.3: The Drying Gun. (*Trockenpistole*) A) Glass round bottom flask with the dessicant / drying agent (Sicapent with indicator). B) Cotton ball for preventing

List of Figures

turbulence and to prevent the worst case of mixing the two substances during evacuation. C) Corundum crucible (boat) containing substance to be dried. D) Round glass test tube to be placed finally in the furnace.

Figure 3.4: a) Measured Powder diffractogram and the calculated literature data from Fe_2O_3 . b) Standard schematic view of temperature profile used for the synthesis of Fe_2O_3 active powder.

Figure 3.5: a) Measured Powder diffractogram and the calculated literature data of Co_3O_4 . b) Standard schematic view of temperature profile used for the synthesis of Co_3O_4 (active) powder.

Figure 3.6: a) Measured Powder diffractogram and the calculated literature data for CuO . b) Standard schematic view of temperature profile used for the synthesis of CuO powder.

Figure 3.7: a) Measured Powder diffractogram and the calculated literature data from Cr_2O_3 b) Standard schematic view of temperature profile used for the synthesis of Cr_2O_3 (active) powder.

Fig. 4.1. Crystal structure of cubic CsAlO_2 and orthorhombic KGaO_2 , with unit cells drawn in.

Fig. 4.2. Reciprocal layers $hk0$ and $hk1$ (refer to twin domain-I) constructed pixel by pixel from the original CCD-frames.

Fig. 4.3. Reciprocal layer $hk1$ (refer to twin domain I) of RbFeO_2 crystal. The reflections of the corresponding domains are emphasized by circles: $h k 1$ for domain I and II, $h -2h+1 l$ for domain III, $h 2h-1 l$ for domain IV, $h 2h+1 l$ for domain V and $h -2h-1 l$ for domain VI. The directions of the reciprocal axes of each domain are drawn in.

Fig. 4.4. a) The interrelation of lattice constants between the orthorhombic (KGaO_2) an ordered variant of the CsAlO_2 type (a_{cubic}). “[$a \approx a(\text{CsAlO}_2)/\sqrt{2}$, $b \approx a(\text{CsAlO}_2)\sqrt{2}$, $c \approx$

List of Figures

$2a(\text{CsAlO}_2)]$ ” b) Reciprocal layer $hk0$ for the orthorhombic room temperature phase, with pseudo cubic symmetry due to twinning, and the cubic high temperature phase of CsFeO_2 . The polyhedron represents the six different orientations (six colors) of the six domains.

Fig. 4.5. a) Phase transitions detected by differential scanning calorimetry (DSC).
b) Fragment of RbFeO_2 Structure with thermal motion of oxygen at high temperature.

Fig. 4.6. Group-subgroup relation between CsAlO_2 and KGaO_2 , including the coordinates of RbFeO_2 and how they arise from those of the aristotype, CsAlO_2 .

Fig. 4.7. Plot of Specific heat (C_p) versus temperature for AFeO_2 polycrystalline samples. The red dashed line a), b), c), d) and e) depicts the peak evolution in respective alkali oxoferrates.

Fig. 4.8. Plot of inverse of magnetic susceptibility vs temperature for RbFeO_2 and CsFeO_2 depicting an anomaly at around 753 K and 360 K respectively.

Fig. 4.9. Synchrotron powder pattern of KFeO_2 , RbFeO_2 , and CsFeO_2 measured at ‘Room Temperature’ at Synchrotron powder diffraction station of the Materials Sciences (MS-Powder) beamline at the Swiss Light Source [SLS] Switzerland.

Fig. 4.10. Synchrotron Powder pattern of KFeO_2 , RbFeO_2 , and CsFeO_2 measured at higher temperature [at $T > T_{\text{str}}$] at Synchrotron powder diffraction station of Swiss Light Source [SLS] Switzerland.

Fig. 4.11. a) Scattered X-ray intensity for polycrystalline sample of CsFeO_2 at $T = 303$ K (30°C) and 409 K (103°C) as a function of diffraction angle 2θ ($\lambda = 0.497 \text{ \AA}$).

Fig. 4.12. a) The bar diagram (Guinear Aufnahme) for RbFeO_2 showing clearly the onset of structural phase transition at around 737 K (460°C) as depicted by white dashed line.

List of Figures

b, c) Scattered X-ray intensity for polycrystalline sample of RbFeO₂ at T = 303 K (30 °C) and 783 K (510 °C) as a function of diffraction angle 2θ (λ = 0.497 Å).

Fig. 4.13. a, b) Scattered X-ray intensity for polycrystalline sample of KFeO₂ at T = 303 K (30 °C) and 1007 K (734 °C) as a function of diffraction angle 2θ (λ = 0.497 Å).

Fig. 4.14. A multidimensional view of structural phase transition as depicted by synchrotron X-ray powder diffraction patterns of a) CsFeO₂ b) RbFeO₂ and c) KFeO₂ taken for illustration in respective fragments.

Fig. 4.15. Temperature dependence of unit cell parameters of AFeO₂ (A = K, Rb, Cs) as refined from the synchrotron data.

Fig. 4.16. Crystal structures of KFeO₂, RbFeO₂ and CsFeO₂ near room temperature (neutron diffraction).

Fig. 4.17. Illustration of the crystal structure peculiarities of RbFeO₂ associated with the structural transition. (a): Fe1-O-Fe2 junction at T = 300 K, in the orthorhombic ordered phase. (b): Fe-O-Fe junction in the high temperature phase (T = 820 K); approach with the anisotropic thermal parameters for the oxygen atoms used in our work [*c.f.* section 4.3.3]. (c): same, the newly proposed approach based on split oxygen sites.

Fig. 4.18. Crystal structures of the high-temperature modifications of KFeO₂, RbFeO₂ and CsFeO₂. (a): From the model with the anisotropic thermal parameters for oxygen atoms. (b): approach based on split atom model with oxygen atoms being disordered on a ring. The sizes of the atoms are proportional to the refined thermal parameters of the atoms in RbFeO₂ at T = 820 K.

Fig. 4.19. a) Temperature dependences of the refined unit cell parameters and of the unit cell volumes of the orthorhombic low-temperature and cubic high-temperature crystallographic modifications of the AFeO₂ (A = K, Rb, Cs) compounds. The transition

List of Figures

temperatures are also indicated. b) Temperature dependences of the interatomic Fe-O, Fe-Fe distances and of the Fe-O-Fe bond angle (bottom) in the $A\text{FeO}_2$ compounds.

Fig. 4.20. (a): Neutron powder diffraction (NPD) patterns of the KFeO_2 compound recorded for the orthorhombic and magnetic LT phase at $T=10$ K and for the cubic and paramagnetic HT phase at 1080 K; (b): NPD patterns of the RbFeO_2 compound recorded for the orthorhombic and magnetic LT phase at $T=10$ K, for the cubic and still magnetic HT phase at 845 K; and for the cubic and paramagnetic HT phase at 1030 K; (c): NPD patterns of the CsFeO_2 compound recorded for the orthorhombic and magnetic LT phase at $T=10$ K, for the cubic and still magnetic HT phase at 400 K; and for the cubic and paramagnetic HT phase at 1050 K; (d): Colour intensity map of the temperature evolution of the diffraction patterns of CsFeO_2 (fragments of 36 diffraction patterns recorded between 10 and 1100 K in a 2Θ range from 15° to 95°).

Fig. 4.21. a) Schematic view of crystal structure of $A\text{FeO}_2$ ($A=\text{K}, \text{Rb}, \text{and Cs}$) in the low-temperature orthorhombic phase e.g. RbFeO_2 b) Illustration of the systematic increase of Fe-O-Fe angles with increasing size of A-cation. c) image of the magnetic structure of RbFeO_2 at $T=300$ K (in the low-temperature orthorhombic phase) and d) at $T=820$ K (high-temperature cubic phase).

Fig. 4.22. Rietveld refinement fit of RbFeO_2 at $T=10$ K (low-temperature orthorhombic phase). Experimental points, calculated profile and the difference curve are shown. The ticks below the graph indicate the calculated positions of the diffraction peaks. The contribution of solely the magnetic diffraction to the total diffraction intensity is shown at the bottom.

Fig. 4.23. Temperature dependences of the refined magnetic Fe^{3+} magnetic moments for $A\text{FeO}_2$ (squares for $A=\text{K}$, circles for $A=\text{Rb}$, triangles for $A=\text{Cs}$) compounds. Solid lines are fits to the formula explained in the text.

List of Figures

Fig. 4.24. Schematic plot depicting a lucid view of the various temperatures at which the structural phase transitions and magnetic ordering occurs for $A\text{FeO}_2$ ($A=\text{K, Rb and Cs}$) polycrystalline samples.

Fig. 4.25. (a): Figure^[ref: 55] showing the systematic dependence of the T_N values for the RFeO_3 compounds on $\langle \cos(\text{Fe-O-Fe}) \rangle$, (b): the similar values derived from the neutron powder diffraction data on the $A\text{FeO}_2$ ($A=\text{K, Rb, Cs}$) compounds in our study [c.f. 4.3.4]

Fig. 4.26. Temperature dependences of the $\frac{|\cos(\text{Fe-O-Fe})|}{d_{\text{Fe-Fe}}^{3.5}}$ value for the $A\text{FeO}_2$ ($A=\text{K, Rb, Cs}$) compounds.

Fig. 4.27. Mössbauer spectra of RbFeO_2 : a) at several temperatures, in streaming argon gas (except for spectrum at top, see text). b) Mössbauer spectra of RbFeO_2 taken at room temperature in closed ampoule (top) and after opening (bottom) in argon atmosphere.

Fig. 4.28. Mössbauer spectrum of CsFeO_2 in streaming argon gas: **a)** Room temperature (5 days measuring time) **b)** high temperature (37 days measuring time) **c)** comparison of Moessbauer spectra before and after heating the sample (RT).

Fig. 4.29. Isomer shifts of different Fe-X polyhedra at room temperature^[60].

Fig. 4.30. Temperature dependence of local magnetic field of ^{57}Fe in CsFeO_2 .

Fig. 4.31. Sample Holder (*self made*) for Moessbauer Spectroscopy. a) before measurement, b) after end of measurement of 37days.

Fig. 4.32. Rigid body consisting of the crystallographically independent atoms of the structure building double tetrahedron in CsFeO_2 exhibiting three internal parameters: r, tilt-1 and tilt-2.

List of Figures

Fig. 5.1. Scattered X-ray intensity for polycrystalline sample of CsCoO₂ at $T = 298$ K as a function of diffraction angle 2θ ($\lambda = 0.559407$ Å).

Fig. 5.2. a) A network of CsCoO₂ (view along b-direction) with unit cell drawn.

b) Crystal structure of CsCoO₂ viewed along a-direction comprises of pairs of CoO₄ tetrahedra edge-linked to form bow-tie-shaped Co₂O₆ dimer units and these units condense by vertex sharing to form two dimensional layered structure of CsCoO₂ with Cs atoms incorporated in between.

Fig. 5.3 a) The pictorial view of selected bond angles in CsCoO₂

b) The pictorial view of selected bond distances in CsCoO₂

Fig. 5.4. Phase transition as detected by differential scanning calorimetry.

Fig. 5.5. Scattered X-ray intensity for HT-CsCoO₂ as a function of diffraction angle 2θ ($\lambda = 0.709300$ Å).

Fig. 5.6 Temperature dependence of electrical conductivity [■] electrical resistivity [□] for polycrystalline sample of CsCoO₂.

Fig. 5.7 Temperature dependent magnetic susceptibility (χ -□open black square) and inverse magnetic susceptibility (χ^{-1} -■ filled grey square) plot of CsCoO₂ at 7 T with a respective Curie Weiss fit.

Fig. 5.8 a) Specific heat (C_p/T^2) at zero field as a function of T of polycrystalline sample of CsCoO₂. b) The inset at the top right shows zoomed in part of plot (a), c) the lower right inset shows $d/dT(\chi_{\text{mol}} \times T)$ (Fisher's heat capacity).

Fig. 5.9. Polyhedral view of the crystal structure of a) α -KCrO₂ (left) and b) β -KCrO₂ (right).

List of Figures

Fig. 5.10. Phase transitions detected by differential scanning calorimetry (DSC).

Fig. 5.11. The effect of the structural phase transition on the X-ray diffraction patterns sporadically collected and measured on Bruker Mo D8-Diffractometer ($\lambda = 0.709300 \text{ \AA}$).

Fig. 5.12. Phase transitions as detected by continuous HT XRD experiments in quartz Capillary (on Bruker Mo D8-Diffractometer).

Fig. 5.13. Temperature dependence of the magnetic susceptibility (χ and $1/\chi$ vs T) for

β -KCrO₂. The solid line represents the fit of the data to the Curie–Weiss law. The inset in the top-left corner presents the $1/\chi$ vs T plot to show the magnetic field independence of the powder sample with temperature.

Fig. 5.14. a) Specific heat (C_p) at zero field as a function of T of polycrystalline sample of KCrO₂. The inset at the top b) C_p/T and inset c) bottom shows C_p/T^2 both as a function of T whereas inset d) plot C_p/T^2 vs T^2 with lucid view around the respective magnetic ordering temperatures.

Fig. 6.1. Crystal structure with unit cell of Na₅Cu₃O₆: (left) showing the periodicities of Na and CuO₂ units with Na ions forming a honeycomb pattern (emphasized by white sticks) with the voids occupied by cuprate ribbons; (right) CuO₂ chains in Na₅Cu₃O₆: Cu³⁺—red squares, Cu²⁺—blue squares.

Fig. 6.2. a). Thermal behaviour of Na₅Cu₃O₆ as detected by differential scanning calorimetry (DSC) (b). High temperature conductivity of polycrystalline sample of Na₅Cu₃O₆.

Fig. 6.3. Comparison of crystal structures of a) NaCuO₂ with b) Na₅Cu₃O₆

Fig. 6.4. Scattered X-ray intensity for polycrystalline sample of Na₅Cu₃O₆ at $T = 298 \text{ K}$ as a function of diffraction angle 2θ ($\lambda = 1.54059 \text{ \AA}$).

List of Figures

Fig. 6.5. Specific heat (C_p) at zero field as a function of T of polycrystalline sample of $\text{Na}_5\text{Cu}_3\text{O}_6$. The inset at the bottom shows C_p/T^2 as a function of T around T_N , and the upper inset shows $d/dT(\chi_{\text{mol}} \times T)$ (Fisher's heat capacity).

Fig. 6.6(a). Temperature dependence of the magnetic susceptibility (χ and $1/\chi$ vs T) for polycrystalline sample of $\text{Na}_5\text{Cu}_3\text{O}_6$. The solid green line represents the fit of the data to the Curie–Weiss law in the temperature range of 135 to 680 K.

Fig. 6.6(b). Measured susceptibility (symbols) compared to a Curie law fit (dashed line) for $100 \text{ K} < T < 700 \text{ K}$ with $C = 0.42 \text{ K emu/mol}$ and $\theta = -60.2 \text{ K}$ and to an independent dimer model (solid line) with exchange constant $J_2 = 145 \text{ K}$ and $\chi_0 = -9 \times 10^{-5} \text{ emu/mol}$.

Fig 6.7. (a) Chain with Cu^{2+} (filled circles) and Cu^{3+} ions and magnetic exchange couplings J_1, J_2, J_3 . (b) Simplified magnetic structure showing only magnetic Cu^{2+} ions and couplings J_1, J_2 . In this approximation the model is an alternating ferro-antiferromagnetic Heisenberg chain. (c) Taking also J_3 into account the magnetic model is a Heisenberg ladder. (d) Nearest neighbour ferromagnetic interaction (J_1), $\sim 90^\circ$ Cu-O-Cu angle (mainly direct d-d overlap). Next nearest neighbour Cu-O-O-Cu ($J_2 \gg J_1$) dominant overlap of oxygen p-orbitals with the d-orbitals of Cu ions.

Fig. 6.8. (a) Kinetic exchange term giving a contribution $\sim t_1^2 t_2 / D^2$ to J_2 . (b) mixed exchange process yielding a contribution $J_2 \sim t_1^2 t_2 / (UD)$.

Fig. 6.9. Exchange constants, as a function of the energy scale for charge fluctuations D for hopping parameters and Coulomb interaction strengths as given in the text. Shown are the total exchange constants (solid lines), the superexchange contributions involving U (dashed lines), and the kinetic exchange terms (dot-dashed lines).

Fig. 6.10. Experimental data for the susceptibility (symbols) compared to the susceptibility for a Heisenberg model with $J_1 = -86 \text{ K}$, $J_2 = 0 \text{ K}$, $J_3 = 138 \text{ K}$ as calculated numerically using a TMRG algorithm.

List of Figures

Fig. 6.11. Measured (blue) and calculated (red lines) powder diffractogram of polycrystalline sample of $\text{Na}_3\text{Cu}_2\text{O}_4$.

Fig. 6.12. (a) Temperature dependent Magnetic Susceptibility (χ -□ open black square) and inverse magnetic susceptibility (χ^{-1} -■ filled black square) plot of $\text{Na}_3\text{Cu}_2\text{O}_4$ at 3 T with a respective Curie Weiss fit. (b) Plot of inverse magnetic susceptibility versus temperature at 1, 3 and 7 T focusing the field (H) independency of pristine sample of $\text{Na}_3\text{Cu}_2\text{O}_4$.

Fig. 6.13. Comparison of temperature dependent Magnetic Susceptibility (χ -□ open black square) and inverse magnetic susceptibility (χ^{-1} -■ filled black square) plot of $\text{Na}_3\text{Cu}_2\text{O}_4$ with old data red squares.

Fig. 6.14. Specific heat (C_p) at zero field as a function of T of polycrystalline sample of $\text{Na}_3\text{Cu}_2\text{O}_4$. The upper black line shows plot of C_p/T as a function of T and the blue line symbolizes a lucid plot of C_p/T^2 as a function of T around T_N (22.5K).

Fig. 6.15. Wigner charge order and associated Heisenberg spin structure showing periodicities of CuO_2 chains in $\text{Na}_5\text{Cu}_3\text{O}_6$ (right), $\text{Na}_8\text{Cu}_5\text{O}_{10}$ (middle) and $\text{Na}_3\text{Cu}_2\text{O}_4$ (left).

Fig. 6.16. a) Perspective representation of the crystal structure of $\text{K}_5[\text{CuO}_2][\text{CO}_3]$. The margins of the unit cell are shown in dotted lines. b) The disordered carbonate group found to be in two distinguished orientations on the same crystallographic site.

Fig. 6.17. Single crystal Raman spectrum of $\text{K}_5[\text{CuO}_2][\text{CO}_3]$.

Fig. 9.1. Scattered X-ray intensity for polycrystalline sample of $\text{Na}_5\text{Cu}_3\text{O}_6$ measured on advance Bruker Mo-D8 diffractometer in rotating quartz capillary with continuous HT—XRD experiments from 298 K till 673K.

List of Figures

Fig. 9.2. Scattered X-ray intensity for polycrystalline sample of $\text{Na}_3\text{Cu}_2\text{O}_4$ measured on advance Bruker Mo-D8 diffractometer in rotating quartz capillary with continuous HT—XRD experiments from 298 K till 623K.

Fig. 9.3. High temperature (DC) electrical conductivity (black-squares), with corresponding Arrhenius plot (red-squares) for polycrystalline sample of $\text{Na}_5\text{Cu}_3\text{O}_6$.

Fig. 9.4. Calibration curve for the heater stage employed on the Cu-Bruker D8 Advance diffractometer (upper curve = heating cycle, lower curve = cooling cycle)

Fig. 9.5. Calibration curve for the heater stage employed on the Mo—Bruker D8 Advance diffractometer (upper curve = heating cycle, lower curve = cooling cycle)

Acknowledgments

Acknowledgments

With deepest gratitude, I would like to thank (شکر یہ) my 'DoktorVater' Prof. Dr. Dr. h. c. M. Jansen, who gave me the sheen of confidence and encouraged me to strive for independence and excellence in my scientific research, as well as providing personal support in my comings and goings. I would like to thank my dissertation committee members Prof. Dr. Robert Ernst Dinnebier and Prof. Dr. Thomas Schleid for their willingness to act as my examiners.

Moreover I would also like to express my gratitude to:

- Dr. Jürgen Nuss not only for measurement and solution of single-crystal data, but also for his preliminary scientific training.
- Dr. Denis Sheptyakov for his excelsior approach in neutron and synchrotron experiments related to alkali oxoferrates study.
- Prof. Dr. Robert Dinnebier for precious tips and tricks in solving and refining crystal structures from powder diffraction data using Topas software.
- Ms Sabine Paulsen for guidance in bureaucratic and administrative works.
- Dr. Dieter Fischer for being my tutor and for technical support throughout.
- Dr. Reinhard. K. Kremer and Dr. Hanne Nuss for sharing their expertise in interpretation of magnetic susceptibility data.
- Mrs. Eva Brücher for susceptibility measurements, and Mrs. Gisela Siegle for heat capacity measurement (MPI-FkF).
- Mr. Claus Mühle for technical support and for lively lab atmosphere.
- Mr. Werner Giering for Laue precession photographs.
- Mr. Ewald Schmitt and Mr. Moritz Stahl for DSC measurements
- Mr. Armin Schulz for I.R. & Raman spectroscopy.
- Mr. Frank Adams & Ms Christine Stefani for support in the X-ray diffraction laboratory. And Mr., P. Rajiv for guiding in using Powder 3-D software.
- Dr. Thomas Locherer and Mr. Frank Falkenberg for assisting in my attempts to do high-pressure experiments.
- Ms Sabine Prill-Diemer for SEM/EDX analysis.
- Mr. Helmut Kammerlander and his team for glass blowing related tasks.

Besides I am extremely indebted to all members and ex-members of the Jansen's Department, their friendliness and competence make working in the department, a pleasure. I am extremely indebted for the financial support from the Higher Education Commission (HEC) Pakistan and the German Academic Exchange Service (DAAD) in the form of a fellowship. And also financial support from Max Planck Institute for solid state research in the form of scholarship is gratefully acknowledged.

Resume

CURRICULUM VITAE

Personal Data:

Name : NAVEED ZAFAR ALI
Date of Birth : Tuesday, February 01, 1977
Place of Birth : Islamabad Pakistan.
Email : naveednik@hotmail.com
Marital Status : Married to Shazia Naveed,



Education:

Qualification	Subject	Time duration	Institution
Ph.D	Material Chemistry	from: April 2006 to: March 2011	Max Planck Institute for Solid State Research MPI-FKF Stuttgart, Deutschland.
M.Phil	Inorganic Chemistry	from: 2001 to: 2003	Quaid-i-Azam University, Islamabad, Pakistan.
M.Sc.	Inorganic Chemistry	from: 1999 to: 2001	Quaid-i-Azam University, Islamabad, Pakistan.
B.Sc.	Chemistry	from: 1995 to: 1997	F.G. Post Graduate College for Men, H-8 Islamabad, Pakistan.
HSSC.	Science	from: 1993 to: 1995	I.M.C.B, F-8/4, Islamabad, Pakistan.
SSC.	Pre- Science	from: 1982 to: 1992	I.M.C.B, F-8/4, Islamabad, Pakistan.

Distinction:

- ☉ DAAD-HEC scholarship holder for doctoral studies in Germany (Ref:442-A/05/58011)
- ☉ M. Phil. Merit-scholarship holder (granted by Quaid-i-Azam University Islamabad, Pakistan)
- ☉ Scientific Talent Scholarship holder (granted by University Grants Commission, Islamabad)
- ☉ Member Chemical Society of Pakistan (Membership no. I-0143)
- ☉ Member Gesellschaft Deutscher Chemiker e.V., GDCH (Membership no. GDCH-94772)
- ☉ Recipient of Lady Noon Scholarship for Doctor of Philosophy in Inorganic Chemistry at University of Oxford, United Kingdom. (Offer declined over Max Planck Institute).

Work Experience:

- ☉ Assistant Manager (Technical) at National Engineering and Scientific Commission (NESCOM) Islamabad, Pakistan. Jan 2004-Dec 2005

Resume

Ph.D Project:

- ☉ New ternary alkaliometallates of the first-row transition-metal elements through the Azide Nitrate Route

M.Phil Project:

- ☉ Speciation of chromium in tanneries contaminated soils by using Cr-DPC based spectrometric methods

M.Sc. Project:

- ☉ Environmental Impact assessment and monitoring of Essential/Non Essential heavy metals in edible liver using spectroscopic techniques.

Publications:

- ☉ **Naveed Zafar Ali**, Robert E. Dinnebier and Martin Jansen, The Crystal Structure of CsCoO₂ at High Temperature, Paper in progress.
- ☉ **Naveed Zafar Ali**, Jürgen Nuss, Robert E. Dinnebier and Martin Jansen, Synthesis, crystal structure, structural phase transitions and magnetic properties of an unusually new coordination of Potassium in β -KCrO₂ with layered structure, Paper in progress.
- ☉ **Naveed Zafar Ali**, Jürgen Nuss and Martin Jansen, Synthesis, crystal structure and magnetic properties of a new oxocobaltate with layered structure, Paper in progress.
- ☉ **Naveed Zafar Ali**, Jesko Sirker, Jürgen Nuss and Martin Jansen, Synthesis, crystal structure and magnetic properties of Na₅Cu₃O₆ a new member of chain cuprates, *Phys. Rev. B*, submitted, March 2011. <http://arxiv.org/abs/1103.1588>
- ☉ **Naveed Zafar Ali**, Jürgen Nuss and Martin Jansen, Crystal structure and raman spectroscopy study of K₅[CuO₂]CO₃, *Z. Anorg. Allg. Chem.* (2011) **637**, 183-185. [doi:10.1002/zaac.201000377](https://doi.org/10.1002/zaac.201000377)
- ☉ Denis Scheptyakov, **Naveed Zafar Ali** and Martin Jansen, A neutron diffraction study of structural and magnetic transformations in AFeO₂ (A = K; Rb and Cs), *Journal of Physics: Condensed Matter* (2010) **22**, 426001. [doi: 10.1088/0953-8984/22/42/426001](https://doi.org/10.1088/0953-8984/22/42/426001)
- ☉ Melanie Müller, Robert E. Dinnebier, **Naveed Z. Ali**, Branton J. Campbell and Martin Jansen, Direct access to the order parameter: parameterized symmetry modes and rigid body movements as a function of temperature, *Materials Science Forum*, (2010) **651**, 79-95. <http://www.scientific.net/MSF.651.79>
- ☉ **Naveed Zafar Ali**, Jürgen Nuss, Denis Sheptyakov and Martin Jansen, The AFeO₂ (A = K, Rb and Cs) family: A comparative study of structures and structural phase transitions, *Journal of Solid State Chemistry*, (2010) **183** (3), 752-759. Appeared on the cover letter of Journal [doi:10.1016/j.jssc.2010.01.022](https://doi.org/10.1016/j.jssc.2010.01.022)

Resume

- ☉ Jurgen Nuss, **Naveed Zafar Ali**, and Martin Jansen, Structure of RbFeO₂, refined from a reticular pseudomerohedrally twinned crystal with six domains. *Acta crystallographica. Section B*, Structural science (2007), **63**(Pt 5), 719-25. [doi:10.1107/S0108768107037147](https://doi.org/10.1107/S0108768107037147)
- ☉ Fiaz Ahmad, Arshad Munir, Zafar-uz-Zaman and **Naveed Zafar Ali**, Distribution of essential and non-essential elements on the surface of roadside leaves and in the bulk of various fruits by atomic absorption spectrophotometry, *Nutrition & Food Science*, (2009) **39**(2), 160-167. [doi:10.1108/00346650910943262](https://doi.org/10.1108/00346650910943262)
- ☉ **Naveed Zafar Ali**, Muhammad Jaffar, Environmental assessment and monitoring of chromium in tanneries' polluted soils by spectrometric techniques. *International Journal of Environmental Studies* (2005), **62**(4), 365-366. [doi: 10.1080/00207230500110733](https://doi.org/10.1080/00207230500110733)

Conference Papers/ Poster Abstracts:

- ☉ Naveed Zafar Ali, Juergen Nuss and Martin Jansen, 18th Meeting of the Scientific Advisory Board, Max Planck Institute for Solid State Research, Stuttgart, Germany (Nov. 9, 2010).
- ☉ Naveed Zafar Ali, J. Nuss, D. Scheptyakov and M. Jansen. Gordon Research Conference: Solid State Chemistry, Oxford, United Kingdom (Sept-2009).
- ☉ Naveed Zafar Ali, Hirscheegg Seminar, Kleinwalsertal, Austria (May22-25, 2008).
- ☉ Naveed Zafar Ali, M. Jaffar, Zafar uz Zaman and Fiaz Ahmad, 5th International and 15th National Chemistry Conference of the Chemical Society of Pakistan, Quaid-I-Azam University, Islamabad, Pakistan (24-28 Nov. 2004)
- ☉ Naveed Zafar Ali and M. Jaffar, International Biotech and Lab Automation Europe, London, UK, 51, (25-26 Nov, 2003)
- ☉ Naveed Zafar Ali and M. Jaffar, 3rd International and 13th National Chemistry Conference of the Chemical Society of Pakistan, University Of Karachi, Pakistan (28-31 Dec, 2002)

Language Skills:

- ☉ **IELTS Score (Int'l English Language Testing System):**
Overall Band=6.5
Listening: 7.0 Reading: 5.5 Writing: 7.0 Speaking: 6.0
- ☉ **Deutsch Sprachkenntnisse [German Language Skills]:**
Sixth Month Intensive German Language Course:
Sept 01, 2006-November 30, 2005 Goethe Institute **Karachi** A2 Level
January 01, 2007- March 31 2006 Goethe Institute **Mannheim** A2 and B1
Zertifikat Deutsch: March 20 2006 Goethe Institute **Mannheim** 240/300 (Gut)

Declaration

Hiermit erkläre ich an Eides statt, dass ich die vorliegende Dissertation unter Verwendung der angegebenen Hilfsmittel selbständig verfasst habe und bisher noch keinen Promotionsversuch unternommen habe.

Stuttgart, den 16 / 03 / 2011

Naveed Zafar Ali